Development of pH-responsive microgels and nanogels with gold nanoparticles based on the design of particle structure and gel network

A thesis submitted to the University of Manchester for the degree of

Doctor of Philosophy

in the Faculty of Science and Engineering

Submitted 2020

Shanglin Wu

Department of Materials

School of Natural Sciences

The University of Manchester

Table of contents

Word Count: 61077

List of Publications

Published works

1. Wu, S.; Zhu, M.; Lian, Q.; Lu, D.; Spencer, B.; Adlam, D. J.; Hoyland, J. A.; Volk, K.; Karg, M.; Saunders, B. R. Plasmonic and Colloidal Stability Behaviours of Au-Acrylic Core-Shell Nanoparticles with Thin pH-Responsive Shells. *Nanoscale* **2018**, 10, 18565–18575.

2. Wu, S.; Zhu, M.; Lu, D.; Milani, A. H.; Lian, Q.; Fielding, L. A.; Saunders, B. R.; Derry, M. J.; Armes, S. P.; Adlam, D.; et al. Self-Curing Super-Stretchable Polymer/Microgel Complex Coacervate Gels without Covalent Bond Formation. *Chem. Sci*. **2019**.

Co-authored works

3. Schmidt, M. M.; Wu, S.; Cui, Z.; Nguyen, N. T.; Faulkner, M.; Saunders, B. R. How Gold Nanoparticles Can Be Used to Probe the Structural Changes of a pH-Responsive Hydrogel. *Phys. Chem. Chem. Phys.* **2017**, 19, 5102–5112.

4. Cui, Z.; Wang, W.; Obeng, M.; Chen, M.; Wu, S.; Kinloch, I.; Saunders, B. R. Using Intra-Microgel Crosslinking to Control the Mechanical Properties of Doubly Crosslinked Microgels. *Soft Matter* **2016**, 12, 6985–6994.

5. Zhu, M.; Lu, D.; Wu, S.; Lian, Q.; Wang, W.; Lyon, L. A.; Wang, W.; Bártolo, P.; Saunders, B. R. Using Green Emitting pH-Responsive Nanogels to Report Environmental Changes within Hydrogels: A Nanoprobe for Versatile Sensing. *Nanoscale* **2019**, 11, 11484–11495.

6. Zhu, M.; Lu, D.; Wu, S.; Lian, Q.; Wang, W.; Milani, A. H.; Cui, Z.; Nguyen, N. T.; Chen, M.; Lyon, L. A.; et al. Responsive Nanogel Probe for Ratiometric Fluorescent Sensing of pH and Strain in Hydrogels. *ACS Macro Lett.* **2017**, 6, 1245–1250.

7. Lu, D.; Zhu, M.; Wu, S.; Wang, W.; Lian, Q.; Saunders, B. R. Triply Responsive Coumarin-Based Microgels with Remarkably Large Photo-Switchable Swelling. *Polym. Chem.* **2019**, 10, 2516–2526.

8. Lu, D.; Zhu, M.; Wang, W.; Wu, S.; Saunders, B. R.; Adlam, D. J.; Hoyland, J. A.; Hofzumahaus, C.; Schneider, S.; Landfester, K. Do the Properties of Gels Constructed by Interlinking Triply-Responsive Microgels Follow from Those of the Building Blocks? *Soft Matter* **2019**, 15, 527–536.

9. Lian, Q.; Chen, M.; Mokhtar, M. Z.; Wu, S.; Zhu, M.; Whittaker, E.; O'Brien, P.; Saunders, B. R. Surface Structure, Optoelectronic Properties and Charge Transport in ZnO Nanocrystal/MDMO-PPV Multilayer Films. *Phys. Chem. Chem. Phys.* **2018**, 20, 12260–12271.

10. Lu, D.; Zhu, M.; Wu, S.; Lian, Q.; Wang, W.; Adlam, D.; Hoyland, J. A.; Saunders, B. R. Programmed Multiresponsive Hydrogel Assemblies with Light-Tunable Mechanical Properties, Actuation, and Fluorescence. *Adv. Funct. Mater.* **2020**, *30.*

List of Figures

List of Tables

List of Abbreviations

AcSEMA	2-(acetylthio)ethyl methacrylate
APS	Ammonium persulfate
ATR	Attenuated total reflectance
ATRP	Atomic transfer radical polymerisation
Au NP	Gold nanoparticle
B-en-A	3-Butenylamine
BSA	Bovine serum albumin
BSE	Backscattered electrons
CCC	Critical coagulation concentration
CEA	2-carboxyethyl acrylate
CMC	Critical micelle concentration
DLS	Dynamic laser scattering
DLVO	Derjaguin–Landau–Verwey–Overbeek
DMEM	Dulbecco’s modified Eagle’s medium
DVB	Divinylbenzene
DX	Doubly crosslinked
EA	Ethyl acrylate
EGDMA	Ethylene glycol dimethacrylate
FDTD	Finite difference time domain
FE	Field emission
FTIR	Fourier transform infrared
GMA	Glycidyl methacrylate

IR	Infrared
IRE	Internal reflection element
IVD	Intervertebral disc
LSPR	Localised surface plasmon resonance
MAA	Methacrylic acid
MEO_2MA	2-(2-methoxyethoxy)ethyl methacrylate
MG	Microgel
MMA	Methyl methacrylate
MR	Mass ratio
Na_3Cit	Sodium citrate
NG	Nanogel
PBS	Phosphate buffered saline
PE	Polyelectrolyte
PEI	Polyethyleneimine
PMCC	Polymer/microgel complex coacervate
PML	Perfectly matched layer
Poly(EA-MAA-DVB)	Poly(ethyl acrylate-methacrylic acid-divinylbenzene)
Poly(MMA)	Poly(methyl methacrylate)
Poly(MMA-MAA-EGDMA)	Poly(methyl methacrylate-methacrylic acid-ethylene glycol dimethacrylate)
Poly(NIPAM)	Poly(*N*-isopropylacrylamide)
PTFE	Poly(tetrafluoroethylene)
RAFT	Reversible addition fragmentation chain transfer
rcf	Relative centrifugal force

rpm	Revolutions per minute
SDS	Sodium dodecyl sulfate
SE	Secondary electrons
SEM	Scanning electron microscope
TEM	Transmission electron microscope
TEMED	*N*,*N*,*N′*,*N′*-tetramethylethylenediamine
TFSF	Total-field scattered-field
UV-Vis	Ultraviolet–visible
XPS	X-ray photoelectron spectroscopy

List of Symbols

α	Particle radius
α_e	Extension ratio
α_{ion}	Degree of ionisation
A	Absorbance
A_{eff}	Effective Hamaker constant
A_1	Hamaker constant for particle
A_3	Hamaker constant for medium
C	Concentration
C_{Au}	Molar particle concentration of Au NP
C_e	Concentration of electrolyte
C_{ext}	Extinction cross section
d_c	Core particle diameter
d_{cs}	Core-shell particle diameter
d_h	Hydrodynamic diameter
d_{TEM}	TEM-based diameter
d_z	Z-average diameter
D	Diffusion coefficient
D_p	Particle diameter
E	Elasticity
$E(t)$	Scattered electric field at time t
f	Number of counterions per chain
f_i	Initiator efficiency

$g_1(\tau)$	Normalised electric field correlation function
$g_2(\tau)$	Normalised intensity correlation function
H	Separation between particles
$I(t)$	Scattered intensity at time t
k	Boltzmann constant
k_c	Rate coefficient for combination
k_d	Rate coefficient for initiator dissociation
k_{dp}	Rate coefficient for disproportionation
k_p	Rate coefficient for propagation
k_t	Rate coefficient for termination
K_a	Acid dissociation constant
M	Molecular weight
$\overline{M}_c$	Number-average molecular weight of chain segments
n	Refractive index
n_m	Refractive index of medium
N	Electron density
N_A	Avogadro’s constant
N_c	Effective number of polymer chains in gel volume
N_p	Number of atoms per particles
N_{SUM}	Number of atoms in dispersion
q	Scattering wave vector
R	Gas constant
R_i	Rate of initiation

R_p	Rate of propagation
R_t	Rate of termination
t	Time
T	Temperature
v_s	Molar volume of solvent
V_0	Collapsed volume of MG
V_A	Attractive interaction energy
V_d	Total volume of dispersion
V_R	Repulsive interaction energy
V_T	Total interaction energy
z	Charge number
Z	Atomic number
ρ	Density
ρ_{Au}	Density of Au NP
ρ_p	Density of polymer
ε	Dielectric function
ε_m	Medium dielectric function
$\varepsilon_r + i\varepsilon_i$	Complex metal dielectric function
λ	Wavelength of incident light
λ_0	Wavelength of incident laser in vacuum
λ_{max}	LSPR peak wavelength
λ_p	Bulk metal plasmon wavelength
τ	Delay time

$\mathit{\Gamma}$	Decay constant
θ	Scattering angle
η	Viscosity of medium
κ	Debye constant
ϕ	Volume fraction in swollen state
ϕ_0	Volume fraction in collapsed state
δ	Thickness
δ_{DLS}	DLS-based thickness
δ_{Shell}	Shell thickness
δ_{TEM}	TEM-based thickness
Π_{don}	Donnan equilibrium
Π_{elas}	Elastic osmotic pressure
Π_{mix}	Solvent-polymer mixing osmotic pressure
Π_{total}	Total osmotic pressure of polymeric network
χ	Flory polymer-solvent interaction parameter
χ_s	Shape factor
ζ	Zeta potential
$\mathit{\Psi}_{\delta}$	Stern potential

Abstract

This thesis presents a study of pH-responsive nanogel (NG) or microgel (MG) based systems, which aimed to achieve improved functionality and gel performance for future biomedical applications. Doubly crosslinked (DX) MGs have already been studied and suggested in the recovery of degenerated intervertebral discs. The next generation of gel could focus on the improvement in therapeutic and diagnostic treatment. In the first study of this thesis, gold nanoparticles (Au NPs) were synthesised to generate the localised surface plasmon resonance (LSPR) property for NGs using core-shell approaches. The colloidal stability of Au NPs relies on the electrostatic repulsion due to a citrate reduction. Therefore, the aggregation of Au NPs is unavoidable for the preparation of DX MGs. This result was observed in the study of poly(ethyl acrylate-methacrylic acid-divinylbenzene) MGs (poly(EA-MAA-DVB) MGs). Precipitation polymerisation is a powerful method to construct a temperature-responsive poly(N-isopropylacrylamide) copolymer shell for Au NPs. However, a functionalisation step is usually required to facilitate shell growth. I evaluated three core-shell approaches and created a new methodology of precipitation polymerisation without using any pre-functionalisation steps. Finally, a well-defined core-shell structure was synthesised by constructing a NG shell of poly(methyl methacrylate-methacrylic acid-ethylene glycol dimethacrylate). Those new core-shell particles had excellent colloidal stability in electrolytes. LSPR properties of the Au NP core-shell dispersion were restorable from salt-triggered sediments or oven-dried solids.

The facile methodology of core-shell syntheses allowed the investigation of pH-response and shell thicknesses dependent LSPR properties in the second study. I synthesised five types of acrylic-based core-shell particles with tuneable shell thicknesses. The shell composition was mainly varied by the content of either 2-carboxyethyl acrylate (CEA) or methacrylic acid (MAA). The resultant NG shells were thin and ranged from 2 – 18 nm based on measurements from TEM. All swelling and LSPR properties were recorded and compared for the analysis. LSPR peak wavelengths were strongly dependent on the NG shell thickness. The maximum peak wavelength of core-shell particles achieved 529 nm, which had a 10 nm red-shift compared to the parent Au NPs. The spectral change and near-field map were subsequently provided using finite difference time domain (FDTD) simulations. The experimental data of

LSPR properties fitted well with those predictions. The pH-dependent change of LSPR peak wavelengths was also found in a highly swellable MAA-containing core-shell particle. A visible colour transition was observed from pH 6 to pH 11. Importantly, pH-triggered reversible aggregation existed in a CEA-containing core-shell particle. Their thin NG shells provided an effective coupling effect for the Au cores. The internalisation study of HeLa cell culture further proved CEA-containing core-shell particles have the potential in sensing the intracellular pH for future biomedical uses.

The mechanical property of DX MGs is not ductile enough to enable a useful investigation of core-shell particles (e.g. a remote probe of gel environments or mechanics). The development of the gel network is also important. Therefore, the last piece of work focused on the generation of new gel using pH-responsive poly(EA-MAA-DVB) MGs. I developed a new methodology by constructing a physical gel network with branched polyethyleneimine (PEI). A complex coacervate was formed due to a strong interaction between anionic MGs and cationic PEI. This polymer/MGs complex coacervate (PMCC) system showed outstanding gel property performance, including super-stretchability, self-healing, super-swellability and strong adhesion. A highly deformable and injectable pre-gel could be transformed to an elastic and stable gel by simply tuning the annealing temperature (≥ 37 °C). Moreover, the stiffness of elastic gel can largely increase up to 34 MPa after introducing Ca^{2+} crosslinking. The work provides the basis for new gels, which could be used to monitor biomechanical properties remotely.

Declaration

I declare that no portion of the work referred to in the thesis has been submitted in support of an application for another degree or qualification of this or any other university or other institute of learning.

Shanglin Wu

Copyright Statement

i. The author of this thesis (including any appendices and/or schedules to this thesis) owns certain copyright or related rights in it (the "Copyright") and s/he has given The University of Manchester certain rights to use such Copyright, including for administrative purposes.

ii. Copies of this thesis, either in full or in extracts and whether in hard or electronic copy, may be made only in accordance with the Copyright, Designs and Patents Act 1988 (as amended) and regulations issued under it or, where appropriate, in accordance with licensing agreements which the University has from time to time. This page must form part of any such copies made.

iii. The ownership of certain Copyright, patents, designs, trademarks and other intellectual property (the "Intellectual Property") and any reproductions of copyright works in the thesis, for example graphs and tables ("Reproductions"), which may be described in this thesis, may not be owned by the author and may be owned by third parties. Such Intellectual Property and Reproductions cannot and must not be made available for use without the prior written permission of the owner(s) of the relevant Intellectual Property and/or Reproductions.

iv. Further information on the conditions under which disclosure, publication and commercialisation of this thesis, the Copyright and any Intellectual Property and/or Reproductions described in it may take place is available in the University IP Policy (http://documents.manchester.ac.uk/DocuInfo.aspx?DocID=2442 0), in any relevant Thesis restriction declarations deposited in the University Library, The University Library's regulations (http://www.library.manchester.ac.uk/about/regulations/) and in The University's policy on Presentation of Theses

Acknowledgements

I feel very fortunate to spend my PhD life with so many nice and lovely people in Manchester. I could not finish my thesis writing without all your help and support. I would like to particularly express my gratitude to my supervisor, Prof. Brian Saunders. He helped me get through a lot of difficulties and built my confidence at the start point. His expertise and guidelines always keep my research in the right direction. The most important thing I have learnt from him is the self-discipline and professional attitude towards academic research. It enlightens me in thinking and planning of my future career. I would also thank my co-supervisor Dr. Stephen Edmondson for his valuable advice in 2nd and 3rd year progressions.

I would like to express my sincere appreciation to Daman Adlam, Dr. Ben Spencer, Dr. Kirsten Volk, Dr. Matthew Derry, Dr. Lee Fielding, Prof. Matthias Karg, Prof. Judith Hoyland and Prof. Steven Armes. I have received a lot of academic support from those experts in various areas. They have shown me the importance of multidisciplinary works for producing high-quality and innovative research. I would also like to thank Jasmine Fernley, Polly Greensmith and Dr. Chloe Loveless for maintaining a good laboratory environment and generously providing technical support all the time.

Many appreciations go to all the colleagues, who have spent a lot of time with me in the lab over the past four years. Particularly to Dr. Zhengxing Cui, who taught me to set up my first experiment and keep providing background support in my PhD life. I would like to thank Mingning Zhu, Qing Lian, Dongdong Lu, Chotiros Dokkhan, Hannah Shanks, James Turton, Tong Wu, Zixuan Dou, Dr. Muhamad Sharan Musa, Dr. Mu Chen, Dr. Wenkai Wang, Dr. Syazwani Mohd Zaki and Dr. Jennie Saunders for all your generous assistance and discussions. Many thanks also to our postdocs: Dr. Junfeng Yan, Dr Amir Milani, Dr Nam Nguyen and Dr. Muhamad Zulhasif Mokhtar. I am grateful to Densen, Chen, Siming, Yin, Shi, Xueqian, Dalang, Yunfan and Tong for sharing the joys and warmth with me through my PhD life.

Importantly, I am deeply indebted to my parents, my brother and my girlfriend’s family for their continuous encouragement. Although none of you understands my research, I can still feel a lot of love and wishes from you, in particular, my girlfriend Jingwei. Thank you and love you all!

Chapter 1: Introduction

1.1 Motivation

In the past decades, stimuli-responsive polymers have been widely explored in biomedical applications due to their superior performance for drug release, sol-gel transition and bio-sensing.[1–5] Microgels (MGs) or nanogels (NGs) composed of stimuli-responsive polymers have a pre-formed particulate gel phase with tuneable size, large surface area, high swellability and colloidal stability.[6–10] These features are highly desired in making drug carriers [11–14] or regenerative biomaterials[15–18]. Moreover, pH-responsive NGs or MGs are one of the most successful bio-candidate, because they can spontaneously tailor their properties at different body environments. They have been shown to be potentially useful for cancer cell therapy[19–21] and load-bearing tissue repair.[22,23] In contrast to spinal fusion or disc replacement for treating the degeneration of intervertebral discs (DIVD), injectable pH-responsive doubly crosslinked (DX) MGs can restore the disc height and mechanical properties through a minimally-invasive therapy.[24,25] Swollen MGs readily form a physical gel phase at physiological pH. Subsequent crosslinking can prevent these MGs from redispersion over the long-term application. Those features highlight the advantages of pH-responsive MGs as the pre-formed gel phase compared to other candidates, such as alginate,[26] hyaluronan,[27] and preformed composite hydrogels.[28]

The further development of these pH-responsive polymer colloids requires more functionalities towards diagnostic areas, which can monitor the disease and achieve a successful therapy (e.g. for DIVD treatment). The remote detection method offers a potential solution to report the internal environmental changes inside cells or tissues.

This function could be crucial to establish non-invasive and theranostic colloids for the next generation of pH-responsive biomaterials. MGs or NGs have facile fabrication, which provides practical advantages as functional colloids.[29,30] A smart design (e.g. pH-responsiveness) can manipulate and monitor the behaviours of swellable colloids at intracellular level, such as pH-triggered drug carriers.[21,31,32] In load-bearing materials, an appropriate sensing mechanism (e.g. a readable distance-dependent response) should also enable MGs or NGs to report the internal strain/stress information.[22,33,34] Gold nanoparticles (Au NPs) possess a powerful localised surface plasmon resonance (LSPR) property, which meets both cellular and macroscopic transduction requirements. The local field enhancement, noble metal property, electrical conductivity, strong absorption and scattering cross section of Au NPs provide high flexibility in clinical treatments. These include refractive index sensing, surface enhanced Raman scattering, fluorescence quenching, photothermal therapy, colorimetric sensing, conductivity enhancement and catalysis.[35–42]

For the current repair therapy from the Saunders group, DX MGs act as the load-bearing material which can be tuned to adapt the surrounding soft tissues under the compressive stress.[24,25,43,44] However, the lack of stretchability, tackiness and strong elasticity also limits their advantages as a regenerative material in other areas, such as cartilage repair, hip-joint replacement or tissue glue. This thesis aims to investigate the next generation of pH-responsive NGs or MGs with high flexibility and improved functionality. Current colloidal and gel platforms require further improvement, which should not only provide the theranostic potential for DIVD but also show the capability of solving other biological challenges. The thesis provides evidence for a new research direction in developing these materials. The study includes a facile strategy to incorporate Au NPs in NGs and potentially improve gel performance in practice. Potential intracellular pH reporters are created for cancer cells. A promising and multifunctional gel is designed and studied using pH-responsive MGs. The overall investigation should improve understanding and lead to more favourable uses of pH-responsive NGs and MGs in the biomedical field.

1.2 Survey of thesis

The content of thesis starts with a literature review in Chapter 2. This section introduces the characteristic of Au NPs and MGs. Both the theory and history of essential processes are discussed with emphasis on transduction methods, citrate reduction, free-radical polymerisation, emulsion polymerisation and colloidal stability. In addition, the characterisation methods are discussed for each important instrument or technique used. Research and discussion topics are divided into three experimental sections from Chapter 3 to Chapter 5. Core-shell particles (Au cores and NG shells) and their syntheses are studied in Chapter 3 and Chapter 4. Chapter 5 introduces a new and robust MG-based gel network without the formation of covalent bonds. At the end of the thesis, the conclusions and future work are presented in Chapter 6.

Chapter 3 begins with the synthesis of Au NPs and core-shell approaches. Citrate stabilised Au NPs were prepared using a citrate reduction method (Scheme 1.1(i)). Those particles had poor colloidal stability in electrolytes. The aim of this chapter is to establish a core-shell structure which can be adapted for our pH-responsive NGs or MGs. A NG shell composed of poly(methyl methacrylate-methacrylic acid-ethylene glycol dimethacrylate) (poly(MMA-MAA-EGDMA) (Scheme 1.1(ii)) was selected and synthesised using precipitation polymerisation. Scheme 1.1 (iii) depicts three core-shell structure approaches that were applied to different surface properties of Au NPs. After carefully evaluating these approaches, the synthesis produced a well-defined core-shell structure using a new protocol without any prefunctionalisation steps. The new synthesis is simple, scalable and has high efficiency. Further improvement in colloidal stability of core-shell particles was investigated in comparison to Au NPs (Scheme 1.1(iv)).

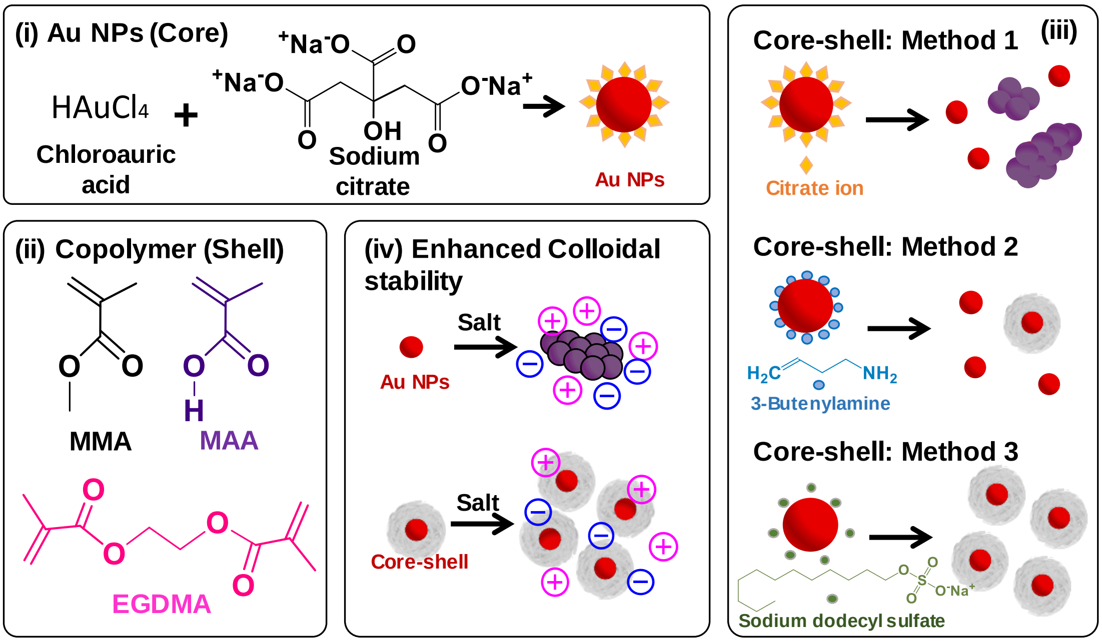

Scheme 1.1 (i) Schematic depiction of the Au NPs synthesis using Turkvich method and the copolymer shell growth using (ii) MMA, MAA and EGDMA through three approaches (iii). The enhanced colloidal stability of core-shell particles is depicted in (iv).

Following the new and facile precipitation polymerisation proposed in Chapter 3, five kinds of core-shell particles were synthesised with different compositions and shell thicknesses in Chapter 4 (Scheme 1.2(i)). The subscript of sample code denotes the shell thickness in nanometres measured by TEM. An acidic monomer 2-carboxyethyl acrylate (CEA) was also selected for the core-shell particle synthesis. The changes of swelling, zeta potential and shell thicknesses dependent LSPR properties are studied in Chapter 4. All the resultant copolymer shells were thin and closely coincided with a regime where LSPR was strongly affected. As a result, tuneable optical properties were found in a shell thickness range of 2 – 18 nm. The experimental data help to improve the understanding of thin NG shells on Au NP with the supporting information from finite different domain simulation. Importantly, a pH-dependent LSPR shift and pH-triggered aggregation were observed and discussed (Scheme 1.2(ii)&(iii)) as the potential sensors. In addition, the pH-triggered aggregation was carried in the HeLa cell culture and an internalisation study conducted for potential biomedical imaging use.

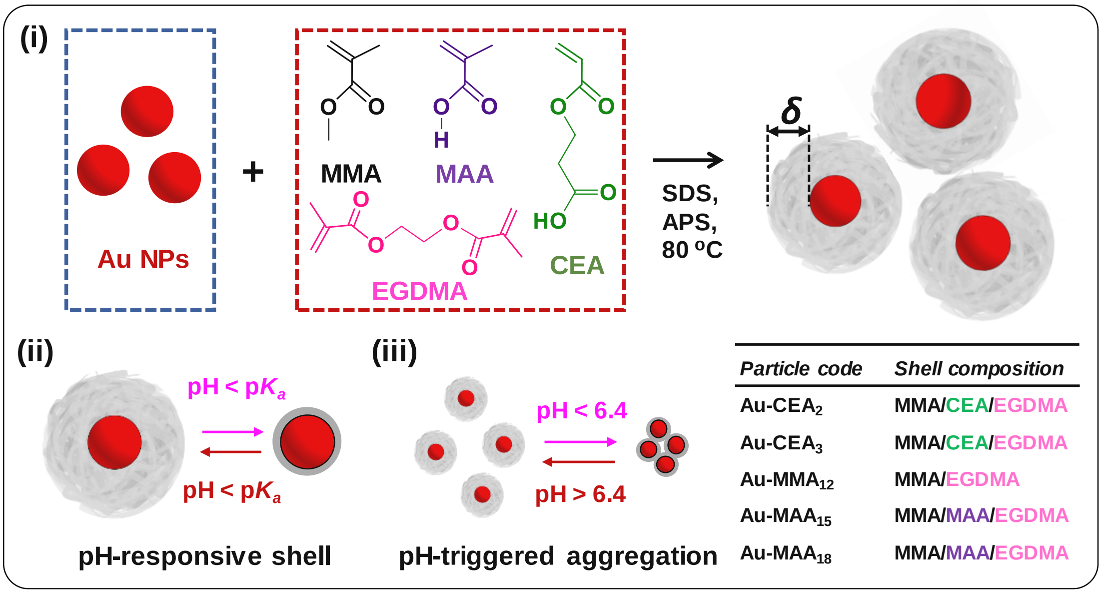

Particle code	*Shell composition*
Au-CEA$_2$	MMA/CEA/EGDMA
Au-CEA$_3$	MMA/CEA/EGDMA
Au-MMA$_{12}$	MMA/EGDMA
Au-MAA$_{15}$	MMA/MAA/EGDMA
Au-MAA$_{18}$	MMA/MAA/EGDMA

Scheme 1.2 (i) Schematic depiction of five types of acrylic core-shell syntheses using precipitation polymerisation. The particle codes are listed in the table. δ is the subscript and denotes the shell thickness. (ii) The core-shell particles show swellable copolymer shells by varying the pH. (iii) A pH-triggered reversible aggregation is established for CEA containing particles.

A new multifunctional and superstretchable gel was explored from the mixture of anionic poly(ethyl acrylate-methacrylic acid-divinylbenzene) (poly(EA-MAA-DVB)) MGs and cationic branched polyethyleneimine (PEI) in Chapter 5. This physical gel was easily prepared by the preformed components without using free-radical or chemical crosslinking. The new methodology provided a highly deformable pre-gel from the complex coacervate at physiological pH. When the temperature increased above 37 °C, a highly elastic and robust T-gel (> 1000% breaking strain) was obtained without the formation of covalent bonds (Scheme 1.3). This new physical gel was well characterised with different mass ratios and annealing temperatures. Swelling, adhesiveness, self-healing, mechanical properties and responses to ions were investigated to examine the performance of this extraordinary gel. The biocompatibility assays showed low cytotoxicity of PEI/MG gel, which may offer the opportunity to develop the gel performance for the current load-supporting bio-candidates in the future (e. g. DX MGs).

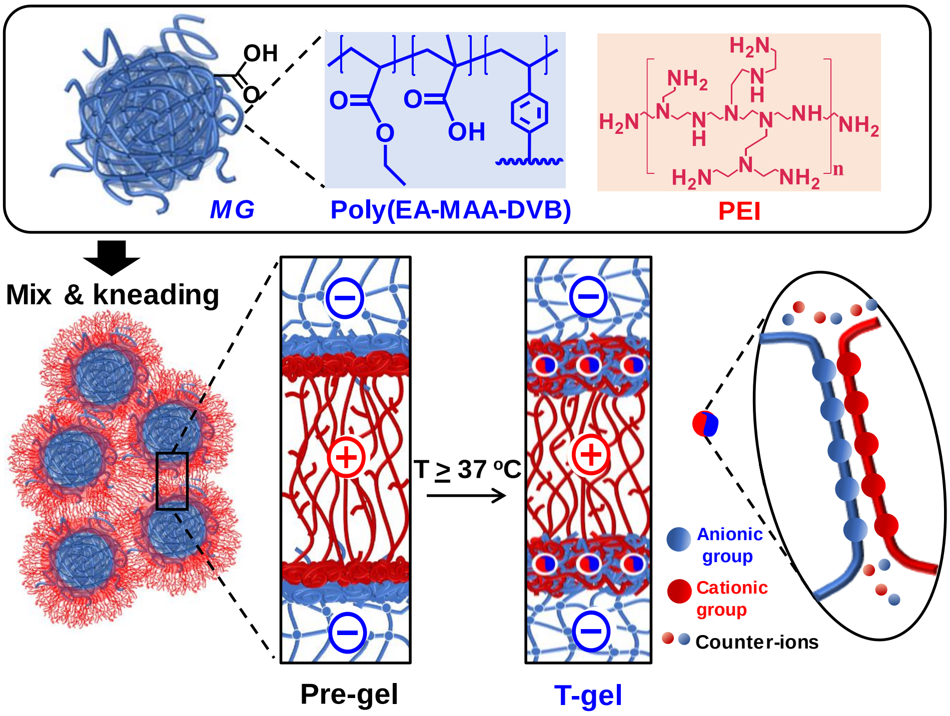

Scheme 1.3 Schematic depiction of PEI/MG pre-gel and T-gel preparation with cooperative ionic bonding using a simple mix and kneading method.

1.3 References

1. Cayre, O. J.; Chagneux, N.; Biggs, S. Stimulus Responsive Core-Shell Nanoparticles: Synthesis and Applications of Polymer Based Aqueous Systems. *Soft Matter* **2011**, *7*, 2211–2234.

2. Cabane, E.; Zhang, X.; Langowska, K.; Palivan, C. G.; Meier, W. Stimuli-Responsive Polymers and Their Applications in Nanomedicine. *Biointerphases* **2012**, *7*, 1–27.

3. Guan, G.; Wu, M.; Han, M. Y. Stimuli-Responsive Hybridized Nanostructures. *Adv. Funct. Mater.* **2019**, *1903439*, 1–27.

4. Amaral, A. J. R.; Pasparakis, G. Stimuli Responsive Self-Healing Polymers: Gels, Elastomers and Membranes. *Polym. Chem.* **2017**, *8*, 6464–6484.

5. Kocak, G.; Tuncer, C.; Bütün, V. PH-Responsive Polymers. *Polym. Chem.* **2017**, *8*, 144–176.

6. Plamper, F. A.; Richtering, W. Functional Microgels and Microgel Systems. *Acc. Chem. Res.* **2017**, *50*, 131–140.

7. Smith, M. H.; South, A. B.; Lyon, L. A. Microgels and Biological Interactions. *Hydrogel Micro and Nanoparticles* **2012**, 209–235.

8. Klinger, D.; Landfester, K. Stimuli-Responsive Microgels for the Loading and Release of Functional Compounds: Fundamental Concepts and Applications. *Polymer (Guildf).* **2012**, *53*, 5209–5231.

9. Lyon, L. A.; Meng, Z.; Singh, N.; Sorrell, C. D.; St. John, A. Thermoresponsive Microgel-Based Materials. *Chem. Soc. Rev.* **2009**, *38*, 865–874.

10. Pelton, R.; Hoare, T. *Microgels and Their Synthesis: An Introduction, in Microgel Suspensions: Fundamendtals and Applications*; Wiley-VCH Verlag GmbH & Co. KGaA, **2011**.

11. Town, A. R.; Giardiello, M.; Gurjar, R.; Siccardi, M.; Briggs, M. E.; Akhtar, R.; McDonald, T. O. Dual-Stimuli Responsive Injectable Microgel/Solid Drug Nanoparticle Nanocomposites for Release of Poorly Soluble Drugs. *Nanoscale* **2017**, *9*, 6302–6314.

12. Zhang, Q.; Colazo, J.; Berg, D.; Mugo, S. M.; Serpe, M. J. Multiresponsive Nanogels for Targeted Anticancer Drug Delivery. *Mol. Pharm.* **2017**, *14*, 2624–2628.

13. Oh, J. K.; Drumright, R.; Siegwart, D. J.; Matyjaszewski, K. The Development of Microgels/Nanogels for Drug Delivery Applications. *Prog. Polym. Sci.* **2008**, *33*, 448–477.

14. Serpe, M. J.; Yarmey, K. A.; Nolan, C. M.; Lyon, L. A. Doxorubicin Uptake and Release from Microgel Thin Films. *Biomacromolecules* **2005**, *6*, 408–413.

15. Jiang, W.; Li, M.; Chen, Z.; Leong, K. W. Cell-Laden Microfluidic Microgels for Tissue Regeneration. *Lab Chip* **2016**, *16*, 4482–4506.

16. Newsom, J. P.; Payne, K. A.; Krebs, M. D. Microgels: Modular, Tunable Constructs for Tissue Regeneration. *Acta Biomater.* **2019**, *88*, 32–41.

17. Jia, X.; Yeo, Y.; Clifton, R. J.; Jiao, T.; Kohane, D. S.; Kobler, J. B.; Zeitels, S. M.; Langer, R. Hyaluronic Acid-Based Microgels and Microgel Networks for Vocal Fold Regeneration. *Biomacromolecules* **2006**, *7*, 3336–3344.

18. Saxena, S.; Hansen, C. E.; Lyon, L. A. Microgel Mechanics in Biomaterial Design. *Acc. Chem. Res.* **2014**, *47*, 2426–2434.

19. Gil, M. S.; Thambi, T.; Phan, V. H. G.; Kim, S. H.; Lee, D. S. Injectable Hydrogel-Incorporated Cancer Cell-Specific Cisplatin Releasing Nanogels for Targeted Drug Delivery. *J. Mater. Chem. B* **2017**, *5*, 7140–7152.

20. Song, Q.; Yin, Y.; Shang, L.; Wu, T.; Zhang, D.; Kong, M.; Zhao, Y.; He, Y.; Tan, S.; Guo, Y.; et al. Tumor Microenvironment Responsive Nanogel for the Combinatorial Antitumor Effect of Chemotherapy and Immunotherapy. *Nano Lett.* **2017**, *17*, 6366–6375.

21. Das, M.; Mardyani, S.; Chan, W. C. W.; Kumacheva, E. Biofunctionalized PH-Responsive Microgels for Cancer Cell Targeting: Rational Design. *Adv. Mater.* **2006**, *18*, 80–83.

22. Freemont, T. J.; Saunders, B. R. PH-Responsive Microgel Dispersions for Repairing Damaged Load-Bearing Soft Tissue. *Soft Matter* **2008**, *4*, 919–924.

23. Nguyen, N. T.; Milani, A. H.; Jennings, J.; Adlam, D. J.; Freemont, A. J.; Hoyland, J. A.; Saunders, B. R. Highly Compressive and Stretchable Poly(Ethylene Glycol) Based Hydrogels Synthesised Using PH-Responsive Nanogels without Free-Radical Chemistry. *Nanoscale* **2019**, *11*, 7921–7930.

24. Milani, A. H.; Freemont, A. J.; Hoyland, J. A.; Adlam, D. J.; Saunders, B. R. Injectable Doubly Cross-Linked Microgels for Improving the Mechanical Properties of Degenerated Intervertebral Discs. *Biomacromolecules* **2012**, *13*, 2793–2801.

25. Saunders, J. M.; Tong, T.; Le Maitre, C. L.; Freemont, T. J.; Saunders, B. R. A Study of PH-Responsive Microgel Dispersions: From Fluid-to-Gel Transitions to Mechanical Property Restoration for Load-Bearing Tissue. *Soft Matter* **2007**, *3*, 486–494.

26. Chou, A. I.; Nicoll, S. B. Characterization of Photocrosslinked Alginate Hydrogels for Nucleus Pulposus Cell Encapsulation. *J. Biomed. Mater. Res. - Part A* **2009**, *91*, 187–194.

27. Su, W. Y.; Chen, Y. C.; Lin, F. H. Injectable Oxidized Hyaluronic Acid/Adipic Acid Dihydrazide Hydrogel for Nucleus Pulposus Regeneration. *Acta Biomater.* **2010**, *6*, 3044–3055.

28. Schmocker, A.; Khoushabi, A.; Frauchiger, D. A.; Gantenbein, B.; Schizas, C.; Moser, C.; Bourban, P. E.; Pioletti, D. P. A Photopolymerized Composite Hydrogel and Surgical Implanting Tool for a Nucleus Pulposus Replacement. *Biomaterials* **2016**, *88*, 110–119.

29. Karg, M.; Pich, A.; Hellweg, T.; Hoare, T.; Lyon, L. A.; Crassous, J. J.; Suzuki, D.; Gumerov, R. A.; Schneider, S.; Potemkin, I. I.; et al. Nanogels and Microgels: From Model Colloids to Applications, Recent Developments, and Future Trends. *Langmuir* **2019**, *35*, 6231–6255.

30. Thorne, J. B.; Vine, G. J.; Snowden, M. J. Microgel Applications and Commercial Considerations. *Colloid Polym. Sci.* **2011**, *289*, 625–646.

31. Gao, Y.; Ahiabu, A.; Serpe, M. J. Controlled Drug Release from the Aggregation-Disaggregation Behavior of PH-Responsive Microgels. *ACS Appl. Mater. Interfaces* **2014**, *6*, 13749–13756.

32. Yang, H.; Wang, Q.; Huang, S.; Xiao, A.; Li, F.; Gan, L.; Yang, X. Smart PH/Redox Dual-Responsive Nanogels for On-Demand Intracellular Anticancer Drug Release. *ACS Appl. Mater. Interfaces* **2016**, *8*, 7729–7738.

33. Steiner, A. M.; Mayer, M.; Seuss, M.; Nikolov, S.; Harris, K. D.; Alexeev, A.; Kuttner, C.; König, T. A. F.; Fery, A. Macroscopic Strain-Induced Transition from Quasi-Infinite Gold Nanoparticle Chains to Defined Plasmonic Oligomers. *ACS Nano* **2017**, *11*, 8871–8880.

34. Zhu, M.; Lu, D.; Wu, S.; Lian, Q.; Wang, W.; Milani, A. H.; Cui, Z.; Nguyen, N. T.; Chen, M.; Lyon, L. A.; et al. Responsive Nanogel Probe for Ratiometric Fluorescent Sensing of PH and Strain in Hydrogels. *ACS Macro Lett.* **2017**, *6*, 1245–1250.

35. Yang, Y.; Zhu, J.; Zhao, J.; Weng, G. J.; Li, J. J.; Zhao, J. W. Growth of Spherical Gold Satellites on the Surface of Au@Ag@SiO 2 Core-Shell Nanostructures Used for an Ultrasensitive SERS Immunoassay of Alpha-Fetoprotein. *ACS Appl. Mater. Interfaces* **2019**, *11*, 3617–3626.

36. Baei, P.; Jalili-Firoozinezhad, S.; Rajabi-Zeleti, S.; Tafazzoli-Shadpour, M.; Baharvand, H.; Aghdami, N. Electrically Conductive Gold Nanoparticle-Chitosan Thermosensitive Hydrogels for Cardiac Tissue Engineering. *Mater. Sci. Eng. C* **2016**, *63*, 131–141.

37. Nam, J.; Won, N.; Jin, H.; Chung, H.; Kim, S. PH-Induced Aggregation of Gold Nanoparticles for Photothermal Cancer Therapy. *J. Am. Chem. Soc.* **2009**, *131*, 13639–13645.

38. Maltez-Da Costa, M.; De La Escosura-Muñiz, A.; Nogués, C.; Barrios, L.; Ibáñez, E.; Merkoçi, A. Detection of Circulating Cancer Cells Using Electrocatalytic Gold Nanoparticles. *Small* **2012**, *8*, 3605–3612.

39. Wu, Y.; Ali, M. R. K.; Chen, K.; Fang, N.; El-Sayed, M. A. Gold Nanoparticles in Biological Optical Imaging. *Nano Today* **2019**, *24*, 120–140.

40. Carnevale, K. J. F.; Riskowski, R. A.; Strouse, G. F. A Gold Nanoparticle Bio-Optical Transponder to Dynamically Monitor Intracellular PH. *ACS Nano* **2018**, *12*, 5956–5968.

41. Tang, L.; Li, J. Plasmon-Based Colorimetric Nanosensors for Ultrasensitive Molecular Diagnostics. *ACS Sensors* **2017**, *2*, 857–875.

42. Wu, C.; Xu, Q.-H. Stable and Functionable Mesoporous Silica-Coated Gold Nanorods as Sensitive Localized Surface Plasmon Resonance (LSPR) Nanosensors. *Langmuir* **2009**, *25*, 9441–9446.

43. Saunders, B. R. Doubly Crosslinked Microgels. *Hydrogel Micro and Nanoparticles* **2012**, 141–167.

44. Milani, A. H.; Bramhill, J.; Freemont, A. J.; Saunders, B. R. Swelling and Mechanical Properties of Hydrogels Composed of Binary Blends of Inter-Linked PH-Responsive Microgel Particles. *Soft Matter* **2015**, *11*, 2586–2595.

Chapter 2: Literature review

2.1 Transduction mechanisms

Numerous research studies have been conducted in sensing and imaging applications, which aim to solve clinical challenges through diagnostic methods.[1–3] The continuous development of nanomaterials promotes new designs at the cellular and biomolecular level due to their high surface area to volume ratio, tunability and sensitivity.[4–6] In this thesis, a remote detection system is a target for minimally invasive and fast response diagnosis. In order to accommodate pH-responsive microgel (MG) or nanogel (NG) based therapies, a suitable transduction mechanism should be considered to transform any responsive features into detectable signals. Relevant research directions include the electrical, magnetic and optical detection. This thesis focuses on the latter.

2.1.1 Electrical methods

The detection of potentiometric, amperometric, or coulometric electrical responses is a well-known method to report local changes, redox reactions and binding events in the biological field.[4,7] The strategy usually needs to include highly conductive materials in the design, such as metallic, ionic or carbon-based components. Although their sensitivity may show limitations in the complex salt environments, the fast signal response and bioelectronic potential make them one of the most thriving diagnostic approaches.[7–9] In particular, the study of skin wearable devices shows an accelerating trend in recent years.[10] As shown in Fig. 2.1 (A)-(B), a detectable strain change can be measured by recording the ratio of relative resistance or capacitance changes in conductive gel devices (piezoresistant materials or ionic gels).[11,12] Further skin attachment is suitable to record the real time body motion, which is advantageous for the construction of bioelectronic devices and soft robotics.[13,14] Similar resistance sensing has been also used to detect the presence of small biomolecules and oligonucleotides, which is targeted at the electrochemical biosensing.[15,16] As shown in Fig. 2.1(C), the swelling degree of conductive DNA-incorporated hydrogel can be controlled by breaking complementary crosslinks in the analyte solution. As a consequence, the increased volume lowered the relative density of conductive species (e.g. carbon powders) and the detectable resistance change was measured in the swollen network.[16]

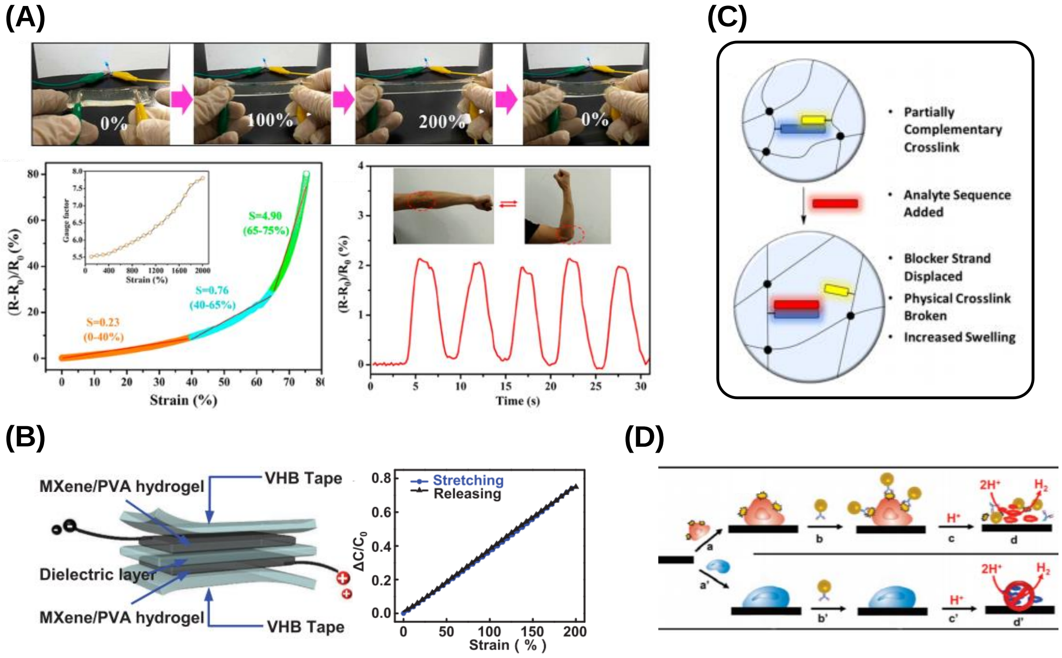

Figure 2.1 (A) A tannic acid-coated cellulose nanocrystal ionic gel showed the capability of strain sensing and elbow bending recognition by monitoring the ratio of relative resistance changes.[11] (B) A MXene/polyvinyl alcohol hydrogel capacitor sensor showed the capability of strain sensing at the loading and unloading condition by monitoring the relative capacitance changes.[12] (C) The scheme illustrates an increased swelling effect in a morpholino oligonucleotide cross-linked hydrogel after detecting the analyte.[15] (D) The scheme illustrates the cell detection in an acidic environment based on the electrocatalytic process of antibody functionalised Au NPs.[17]

In a cellular approach, sensitive detection can be achieved by a electrocatalytic method.[18,19] An example (Fig. 2.1 (D)) shows that the specific protein recognition allowed the binding between the targeting cell line and antibody modified gold nanoparticles (Au NPs).[17] Those cells were seeded on the electrode in an acidic environment. The catalytic hydrogen reduction occurred around Au NPs under an applied voltage. Therefore, a measurable current could be generated and detected to identify the number of targeting cells. Such an electrocatalytic strategy is also capable of measuring the extracellular pH using the concentration of H^+. Intracellular pH sensing may further require the construction of a miniaturised pH electrode.[20]

2.1.2 Magnetic methods

The magnetic detection has a high importance in developing non-invasive clinical monitoring, especially as bioimaging and cancer therapies.[21–23] Magnetic nanomaterials have high contrast in the body due to the natural absence of strong magnetic fields.[3,24] The movement and delivery of nanoparticles can be guided by an external magnetic field, which facilitates the targeting process.[25] In contrast to other transduction methods, magnetic resonance contrast imaging can be used to label the position of magnetic nanoparticles in vivo.[26–28] However, the detection may suffer from the long-processing time and low sensitivity in practice.[29]

As shown in Fig. 2.2, an antibody functionalised nanohybrid was produced by combining a number of magnetic nanocrystals and amphiphilic block polymers in an early approach for cancer therapy.[30] These functionalised nanohybrids showed enhanced permeability and retention effect. After injecting nanohybrids into a mice tail, magnetic resonant imaging confirmed the detection and delivery of magnetic nanohybrids by monitoring the relaxivity change. In a recent study, Lin et al. reported a continuous theranostic development for the tumour-bearing mice using magnetic-plasmonic hybrid nanostructures of Au and Fe_3O_4.[31] These nanoparticles showed a tumour accumulation effect by controlling their size and prolonging the circulation time. The targeting tumour was then detected using magnetic resonance imaging. The combination of the photothermal effect (Au shell) and anticancer drugs together gave a superior tumour regression, which is appealing as a non-invasive cancer therapy.

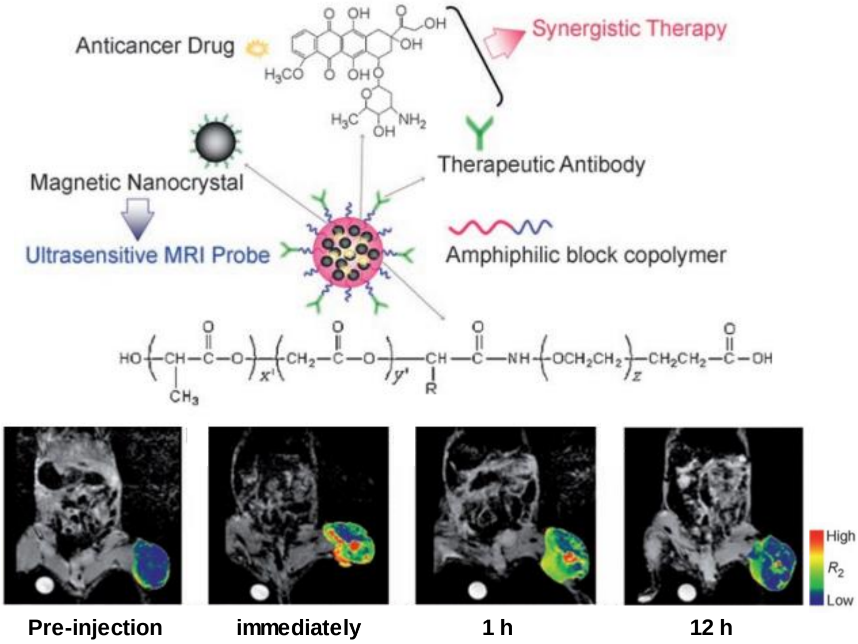

Figure 2.2 An antibody functionalised nanohybrid was used as the magnetic resonance imaging probe for the detection of breast cancer cell line in mice. The images and colour maps showed the cancer-targeting events at different steps of the injection process.[30]

2.1.3 Optical methods

Optical detection (which is a subject of this thesis) is advantageous for the remote theranostic treatment due to its high safety, fast response, non-invasiveness and ease of use.[7,32,33] The continuous research for improved nanomaterials stimulated the growth of this area in the past few decades, especially for colorimetric,[34–36] fluorescence[37–40] and Raman[41–43] methodologies. Natural high tuneability of these candidates offers numerous options in designing improved optical strategies, such as the ratiometric sensing,[44] biomolecular detection,[45] bioimaging,[41] light-triggered therapies[46] and pH reporting.[47]

Target-induced aggregation is a well-known approach as a colorimetric biosensor.[48,49] It was first suggested by Mirkin in 1996.[50] The authors modified two batches of Au NPs with two specified DNA oligonucleotides respectively (Fig. 2.3(A)). The addition of "target" (a duplex oligonucleotides) triggered the aggregation which was observed by a visual colour/UV-Vis spectral change due to the coupling effect.[51] The coupling effect makes plasmonic nanoparticles appealing for a colorimetric approach, especially for the rapid detection of proteins, DNAs and ions.[52–54] In Fig. 2.3(B), an example of thermo-responsive colorimetric sensor was constructed by synthesising and incorporating raspberry-shaped plasmonic poly(N-isopropylacrylamide) (poly(NIPAM)) MGs in a polyacrylamide hydrogel matrix.[55] The distance-dependent plasmonic coupling produced a visible colour change upon swelling or shrinking of the MGs at different temperatures. This colorimetric hydrogel could be attached to the body and monitor real-time temperature changes because of its thermo-responsiveness.

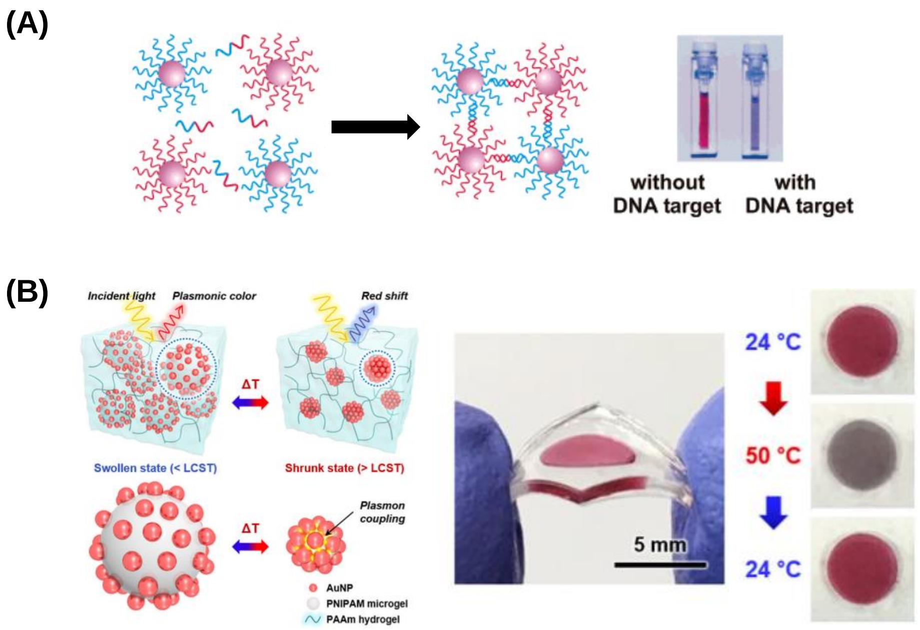

Figure 2.3 (A) The aggregation of oligonucleotides functionalised Au NPs occurred in the presence of DNA targets.[56] (B) The raspberry-shaped plasmonic poly(N-isopropylacrylamide) MGs showed the thermo-responsive plasmon coupling effect. A colorimetric sensor was produced by incorporating MGs into the polyacrylamide hydrogel matrix.[55]

The detection of fluorescence signals is the most common method used in the biomedical area due to the versatility of fluorescent materials and sensitivity of spectral information.[33,57] In the study of intracellular reporters, ratiometric pH sensing can be designed using Fourier resonance energy transfer mechanism (FRET).[47,58,59] In Fig. 2.4, an example of fluorescent protein conjugated quantum dots shows the intensity of FRET signals changed with the intracellular pH in endosomes.[59] Quantum dots acted as the photostable donor and conjugated fluorescent proteins acted as the pH-sensitive acceptor. The variation of pH was detected and visualised in HeLa cells by the cellular imaging. Similar resonance energy transfer has also been explored with Au NPs based on the strong enhancement of the local electromagnetic field around gold surfaces. This may reduce the quantum yield of fluorophores with an increase of non-radiative decay rate.[60–62] In a biomedical application, an aptamer could be chosen to link the fluorescent species and Au NPs.[63] A detrimental antigen can induce the conformational change of aptamer, which breaks the link and prohibits quenching. Importantly, this quenching process adapts to a range of designs (using spacer and DNA origami), where the fluorescence signals are highly sensitive to distance.[64–67] A useful strategy can enable the application of Au NPs in sensing and imaging areas, such as nanogels based cell apoptosis imaging,[68] intracellular uptake monitoring[69] and enzyme activity sensing.[70]

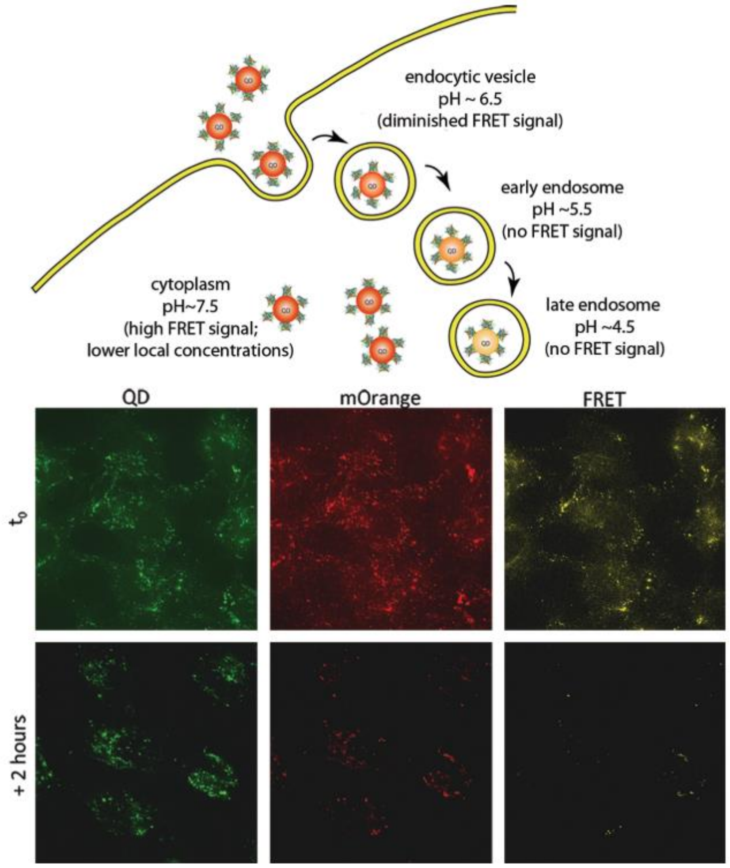

Figure 2.4 The cellular imaging of fluorescent protein conjugated quantum dots showed the growth of endosomes with the decrease of FRET efficiency after 2 hr in HeLa cells.[59]

In comparison to other transduction methods, optical transduction offers a feasible and cost-effective solution for remote detection.[32,33,57] The use of absorption, scattering or fluorescence spectroscopy is versatile for theranostic designs, which are suitable for laboratory or in vivo requirements. As introduced in a pH-responsive MG study, the injectable doubly crosslinked MGs were beneficial from the minimally invasive therapy of degenerated intervertebral disc (DIVD) treatments.[71,72] A new transduction system (as prepared in thesis study) may improve the therapeutic advantages.

As described in Chapter 1, the objective of this thesis is to create a system for remote detection approach and advance the bio-applications in theranostic MGs or NGs. A distance-dependent sensing process is potentially appealing due to its effectiveness in reporting the environmental changes (in gels) and pH-responsiveness (in cells). There are a range of optical candidates which can meet these reporting requirements, such as dye molecules,[73,74] quantum dots,[64,65] polymer dots,[75,76] carbon[77,78] and plasmonic nanomaterials[79,80]. The use of Au NPs is attractive due to their multifunctionality, signal amplification potential, high tuneability, facile synthesis, strong inertness, non-cytotoxicity and high cell membrane permeability.[81–86] The plasmonic behaviours of Au NPs show strong light absorption and scattering properties with a local field enhancement effect.[87] The spectral information is highly sensitive to the local refractive index and aggregation (interparticle distances). They are suitable for various media. In contrast to purely fluorescent-based technique, the reduction of photobleaching for Au NPs makes the detection more reliable and consistent.[88,89] Au NPs also offer multiple diagnostic methodologies, including as colorimetric sensing,[90] fluorescence quenching,[91] surface enhanced Raman scattering[92] and dark field imaging.[46,93] Their applications are not limited to sensing and imaging areas owing to the strong plasmonic effect (Fig. 2.5). The photothermal effect,[94,95] bioconjugation,[96] catalysis[97] and light capture enhancement[98] for Au NPs enlarge their potential in the development of new therapeutic solutions. As reported by Chen et al. in 2016, the future investigation of those materials needs to focus on core-shell nanoparticle construction, multimodal imaging, light-regulated drug release and theranostics.[99] This research trend coincides well with the major objective of this thesis, which involves further improvement of pH-responsive NGs with theranostic potential. The research (and publications) from this PhD project should also provide a useful contribution to the plasmonic research field.

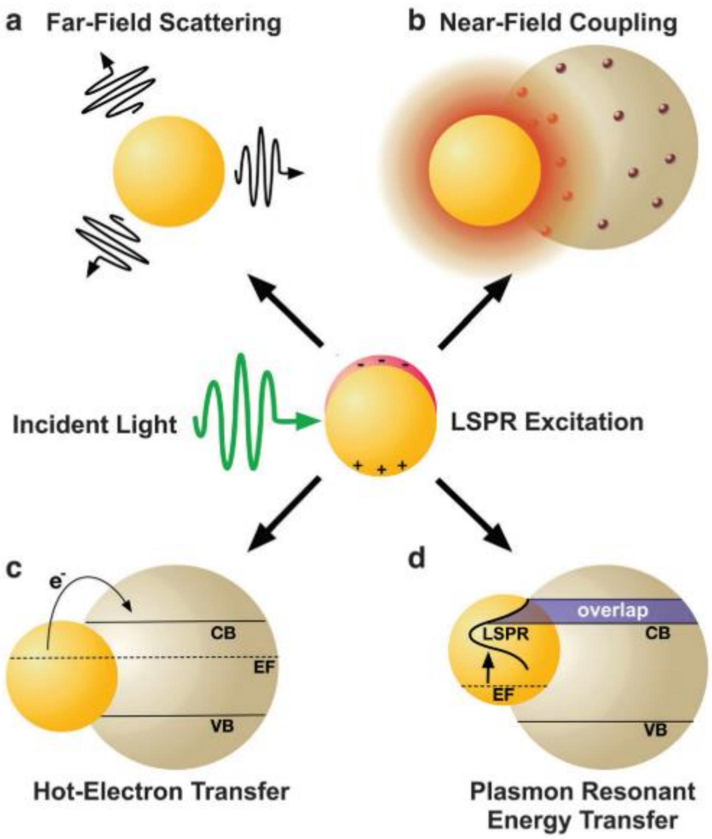

Figure 2.5 Representative mechanisms for plasmonic effects.[98]

2.2 A brief review of Gold

2.2.1 Features and theories

Gold is one of the noble metals and has the very strong chemical inertness. Its shiny appearance is due to the reflection of visible light at high wavelength.[100,101] When gold materials are scaled down to a nanometre size, their optical properties can completely change compared to its bulk state.[102] In 1857, Faraday reported the first research involving colloidal gold.[103] He obtained a ruby gold dispersion from a two-phase system, which contained an aqueous gold chloride solution and phosphorus in CS_2. The unusual optical property of these colloids was quantitatively analysed by Mie in 1908.[87,104] According to his theory, the strong light scattering and absorption cause the variation of colours in the colloidal gold dispersion (Fig. 2.6(A)). These effects are contributed by a process, called the localised surface plasmon resonance (LSPR).[87,105] The LSPR of metallic nanoparticles describes the interaction between light and conduction electrons at a resonant frequency. As illustrated in the below Fig. 2.6(B), the conduction electrons collectively oscillate with the guidance of the electromagnetic wave and form the surface plasmon against the restoring force from lattice atoms. Consequently, a certain number of photons will be scattered and absorbed as a function of the wavelength and particle size.[81] The optical property highly relies on the particles size, which has a strong impact for desired applications. Fig. 2.6(C) shows the variation of light absorption and scattering for the spectra of Au NPs. The scattering regime overweighs the absorption regime with increasing the particle diameter. The intense light scattering is appealing for the design of enhanced light trapping in solar cells[98] or contrast agents in bioimaging[106].

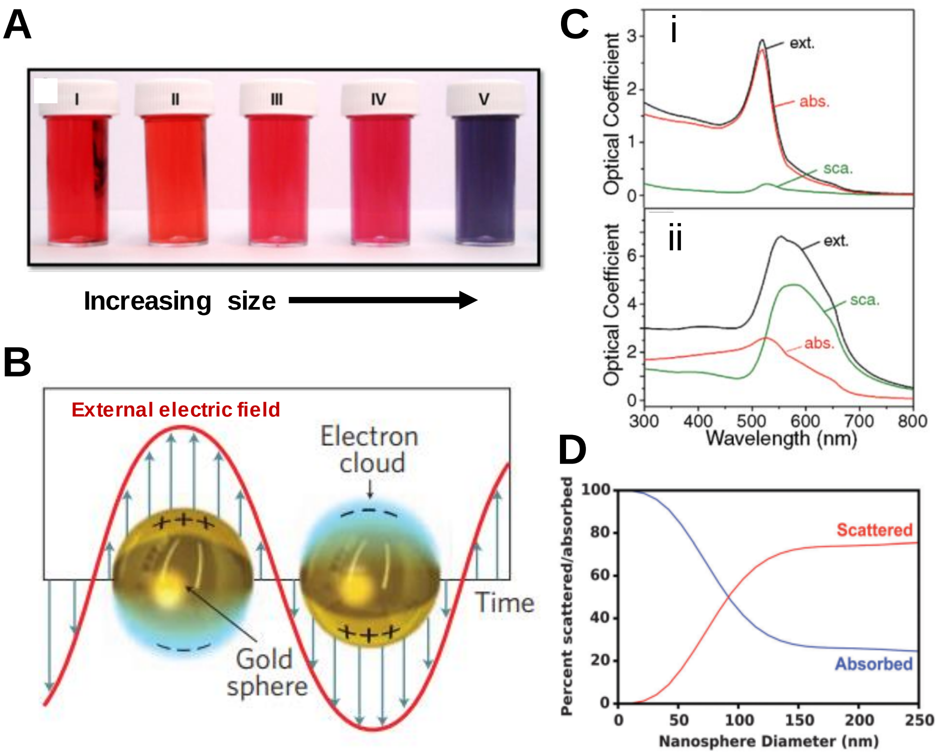

Figure 2.6 (A) The colour of colloidal gold solutions changed with an increase of nanoparticle size from left to right.[107] (B) Large gold spheres show the localised oscillation of electrons upon encountering an electromagnetic wave.[108] (C) The calculated absorption, scattering and extinction spectra for gold spheres (i) radius = 20 nm and (ii) radius = 50 nm.[106] (D) The percentage of light absorption and scattering changed with the size of gold sphere over 300 – 800 nm wavelength.[98]

In this thesis, I aim to synthesise small Au NPs which reside in the dominant light absorption regime and potentially permit stimulus-triggered ensemble scattering methods (Dark field imaging).[87] The excitation of multipoles (high order plasmons) modes in inhomogeneous polarisation will not be significant if the diameter of the Au NPs is less than 25 nm.[51,109] A study showed small Au NPs (< 45 nm) can optimise the efficiency of endocytosis in the lung cancer cell line and HeLa cell.[110] The later cells were applied to the internalisation study in Chapter 4. Typically, 15 nm Au NPs are relatively noncytotoxic[111] and potentially have broad biodistribution.[112] This diameter of Au NPs was selected as a suitable biocandidate in Chapter 3 and Chapter 4. As shown in Fig. 2.6(C) and Fig. 2.6(D), the colour of 15 nm Au NP solution is contributed mainly by a light absorption effect from LSPR.[113,114]

According to Mie's theory, the extinction cross section (C_{ext}) of a small nanoparticle (Size << wavelength of incident light) can be described by Equation 2.1:[87,105]

$$C_{ext} = \frac{24\pi^2\alpha^3\varepsilon_m^{3/2}}{\lambda}\frac{\varepsilon_i(\lambda)}{\left[\varepsilon_r(\lambda)+\chi_s\varepsilon_m\right]^2+\varepsilon_i{}^2} \qquad (2.1)$$

Where α is the radius of nanoparticles. λ represents the wavelength of incident light. ε_m is the medium dielectric function, and $\varepsilon = \varepsilon_r + i\varepsilon_i$ describes the complex metal dielectric function. The dielectric constant of metal is strongly dependent on the wavelength, and has been experimentally determined by Johnson and Christy.[115,116] χ_s accounts for a shape factor which is equal to 2 for spherical nanoparticles. The extinction coefficient (in M^{-1} cm^{-1}) of nanoparticles can be represented by $N_A C_{ext}/2.303$,[117] where N_A is the Avogadro's constant. The parameter C_{ext} is a sum of the scattering cross section and absorption cross section. The light absorption acts as the only dominant term in determining the extinction spectrum when the diameter of Au NPs is less than 20 nm.[106,113] These nanoparticles will start to resonant, if:[87,105]

$$\varepsilon_r = -2\varepsilon_m \qquad (2.2)$$

This condition minimises the denominator in Equation 2.1. Therefore, the maximum C_{ext} can be obtained. The combination of Equation 2.1 and Equation 2.2 highlights the importance of the local dielectric environment around Au NPs. These equations can determine the resonant condition as a function of λ, which provides the fundamental information for the finite difference time domain simulation of Au NPs used in Chapter 4.

The plasmonic interactions can be revealed on a single metallic nanoparticle using electron energy-loss spectroscopy, which directly observes spectral and surface plasmonic changes at the vacuum state (Fig. 2.7(A)).[118–121] The dark-field scattering spectra can be also used to observe plasmonic changes of large individual nanoparticles.[80] In proximity to the edge of nanoparticles, the surface plasmons concentrates the electromagnetic wave and generates the strong local near-field enhancement as shown in Fig. 2.7(B).[105,122] This feature offers the opportunity for detection, such as surface enhanced Raman scattering and photoluminescence.[123,124]

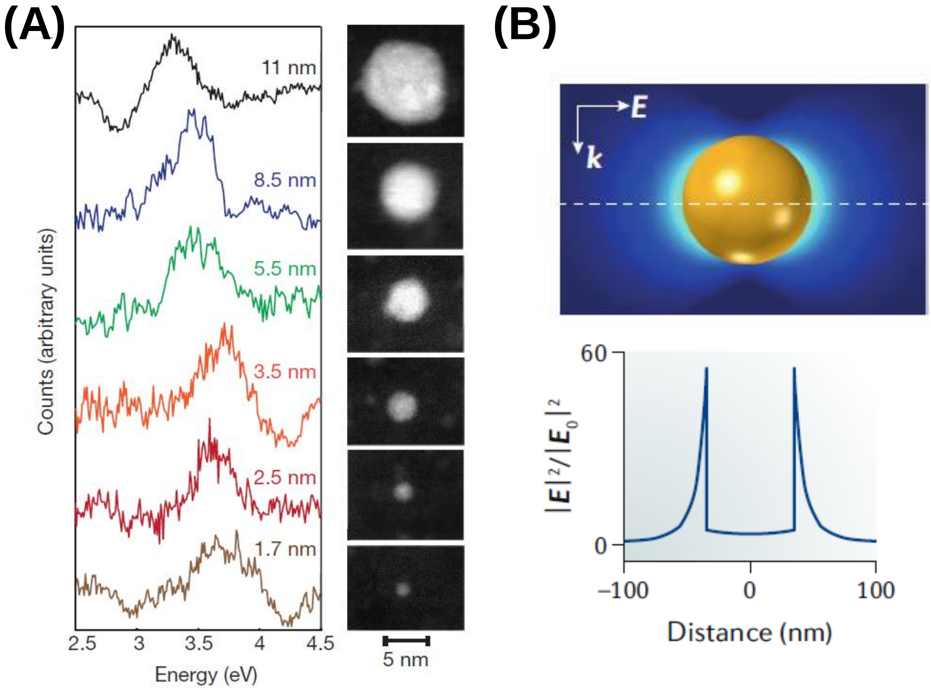

Figure 2.7 (A) The electron energy-loss spectroscopy data of silver nanoparticles was measured with a range of diameters. The inset pictures show the corresponding STEM images.[119] (B) The electromagnetic field distribution of gold nanoparticles. E and k represent the electromagnetic field and wave vector of incident light, respectively. $|E|^2$ and $|E^0|^2$ represent the amplitude of local and incident electromagnetic field, respectively.[122]

Most importantly, the sensitivity of local environmental changes also relies on the near-field property of Au NPs and it gains the attention in theranostic research.[49,125] The variation of refractive index around Au NPs can trigger LSPR peak wavelength shift. This is described by the Drude model:[87,126,127]

$$\lambda_{max} = \lambda_p\sqrt{2{n_m}^2 + 12.2} \qquad (2.3)$$

Where n_m is the refractive index of the medium, and $\varepsilon = n^2$. λ_p is the bulk metal plasmon wavelength for Au (131 nm).[126] The selection of appropriate adsorbed species and solvents can give a strong impact on its optical property.[116,117] The growth of copolymer shells around Au NPs is one of the major targets in Chapter 3 and Chapter 4. The copolymer shell can increase n_m and lead to a red-shift of the resonant peak. Further control of shell composition and stimulus-responsiveness can determine their peak positions, which reveal the information of the local environment. This sensitivity to the refractive index makes Au nanomaterials ideal for sensing.[49]

2.2.2 Synthesis of gold nanoparticles

A facile preparation of Au NPs was firstly introduced by Turkvich in 1951.[128,129] He obtained a colloidal gold dispersion by mechanically stirring the chloroauric acid ($HAuCl_4$) solution with different reducing agents. In his study, the addition of sodium citrate at boiling conditions provided the best colloidal gold and was analysed by TEM. These Au NPs had a consistent shape with highly controllable and reproducible properties. The citrate ions not only act as an efficient reducing agent, but also provide electrostatic stabilisation to the Au NPs.[129,130] As shown in Fig. 2.8(A), a citrate ion layer is built up through the coordination of carboxylate groups on the gold surface. The interaction of such a coordination is weak ~ 2 kcal mol^{-1} ($Au\text{-}O_{COOH}$), and easily ligand exchanged by other molecules with high affinity for gold (thiol or amine).[96,131] The actual binding modes of citrate ions are complicated and variable in dispersion.[132] AI-Johani introduced three possible coordinating patterns in the interaction with Au atoms,[133] as illustrated in Fig. 2.8(B).

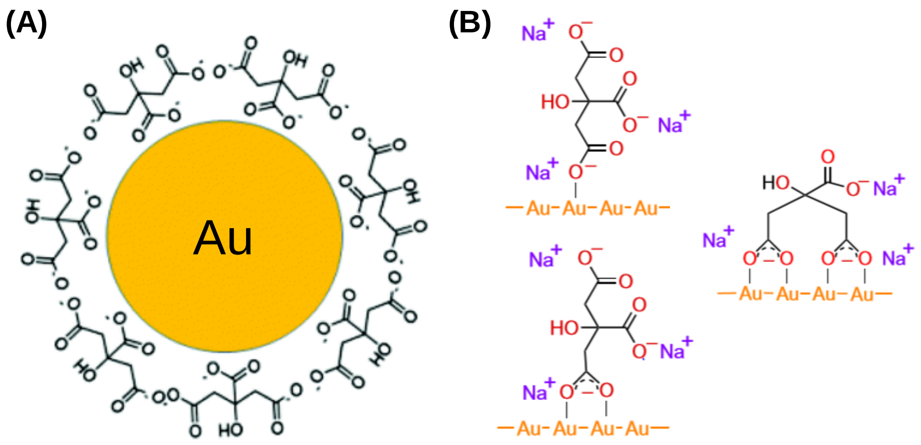

Figure 2.8 (A) The citrate stabilising gold nanoparticle.[134] (B) The potential binding modes of citrate ions on the gold surface.[133]

Fren's study concluded that the number of nuclei could be manipulated by varying the ratio between sodium citrate and $HAuCl_4$.[135] The size of Au NPs was tuned from 147 nm to 16 nm by steadily increasing the volume of sodium citrate at a fixed concentration of Au^{III}. The results showed a good agreement with the nucleation-growth mechanism. In Fig. 2.9(A), the diameter of particle started to increase after reaching a molar ratio = 3.5.[136] Ji et al. found the initial colour change was retarded for high molar ratio synthesis.[136] After examining the pH of the precursor, he concluded the change of the Au^{III} complex gave strong impacts to the nucleation process in the aqueous medium (Fig. 2.9(B)).

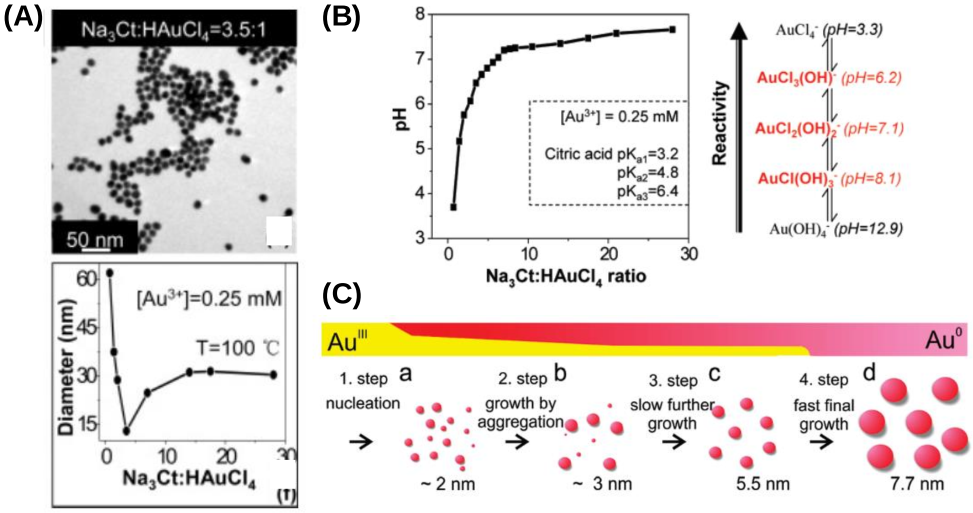

Figure 2.9 (A) The diameter of gold nanoparticles changed with the molar ratio of sodium citrate to $HAuCl_4$. A TEM image of gold nanoparticles was captured at molar ratio = 3.5.[136] (B) The variation of solution pH with different molar ratios of the reactants. A range of Au^{III} complexes appeared as a function of pH. The increase of the reactivity is labelled by a black arrow. The most dominating species are highlighted in red.[136] (C) The schematic illustration shows the formation of gold nanoparticles at ~ pH 6 with a final diameter = 15.4 nm.[137]

Turkvich method could be divided into a four-step process at pH ~ 6.[137] As shown in Fig. 2.9(C), the conversion of Au^{III} to Au^{0} rapidly builds up small nuclei for the initial step. The nucleation is followed by the coalescence of these nuclei in step 2. Step 3 is a slow diffusional growth process due to the low concentration of Au^{III} in solution and the conversion of Au^{III} to Au^{0} acts as a rate determining step.[137,138] The final step involves a fast consumption of the remaining Au^{III}. The size dispersity of the particles continuously reduced to a final value of 10% after completing step 4.[137]

The Turkvich method is used for the study in this thesis. The facile synthesis, tuneable size, good dispersity and citrate stabilisation highlight its advantages for the subsequent particle surface modification and core-shell synthesis. Negatively charged citrate stabilised Au NPs is also compatible with an anionic NGs or MGs system employed. In Chapter 3 and Chapter 4, the synthesis of Au NPs was conducted at molar ratio = 4.1 (pH ~ 6) following Turkvich method. The final diameter was around 15 nm and comparable to the work from Polte et al.

2.2.3 Gold core-shell particle structure

Core-shell nanoparticles are used in materials chemistry due to their highly tailorable properties.[139] There have been several studies on making core-shell structures of Au NPs. Silica hard shells have been found as an effective material to provide a good photothermal stability on gold nanorods.[140] The LSPR of Au NPs is tuneable by changing the thickness of the silica shell,[141] which makes the core-shell particles flexible for biosensing and photothermal therapy. Such silica shells were further used as an effective spacer for the study of distance-dependent fluorescent process.[91] The high sensitivity of local refractive index change can be also generated by a mesoporous silica shell in the detection of biological molecules.[142] The successful investigation of silica gold core-shell structures helps to develop the smart products, and further extends the relevant structural research in other directions.

The thermo/pH-responsive plasmonic effect can be added to Au NPs by growing a soft shell, which indicates a lot of potential for clinical treatments. Poly(NIPAM) is one of the polymer shells that have been extensively studied on Au NPs. When the temperature exceeds its lower critical solution temperature, poly(NIPAM) shells can change from hydrophilic to hydrophobic. The directional growth of the poly(NIPAM) shell has been established by connecting a sulphur-containing initiator to the surface of Au NPs.[143] Atomic transfer radical polymerisation (ATRP) was subsequently carried out to build a brush-like core-shell structure. However, it is difficult to ensure an effective crosslinking network through this kind of growth. The study of layer-by-layer approaches also introduces a novel way to synthesise the poly(NIPAM) shell.[144] The protocol employed showed that CTAB stabilised Au NPs were positively charged. A negative charged allylamine-containing polyacrylic acid was added onto the Au NPs by the electrostatic interaction. The attachment of vinyl group could finally facilitate the growth of the poly(NIPAM) shell.

All the above poly(NIPAM) shell synthesis have used the relatively complicated methodologies and are difficult to use for the large-scale production. The precipitation polymerisation is an attractive approach for the crosslinked and responsive shell synthesis and may have the potential to solve these issues. This method potentially requires less synthesis steps and generates more efficient shell growth compared to other pathways (e.g. Layer-by-layer, ATRP).[145–147] An early strategy employed precipitation polymerisation to pre-grow a thin polystyrene shell on the CTAB stabilised Au NPs.[148] Such shells endowed the stability to Au NPs and provided a compatible surface for the subsequent polymerisation. The resultant particles had a well-defined core-shell structure with the thermo-responsive property. Later, the methodology was further improved by pre-functionalising Au NPs with the butenylamine instead of the polystyrene shell.[149–151] The new functionalising agent provided a favourable surface for the adsorption of NIPAM monomer or oligomer which highly yielded core-shell particles without showing uncoated Au NPs (Fig. 2.10(A)).

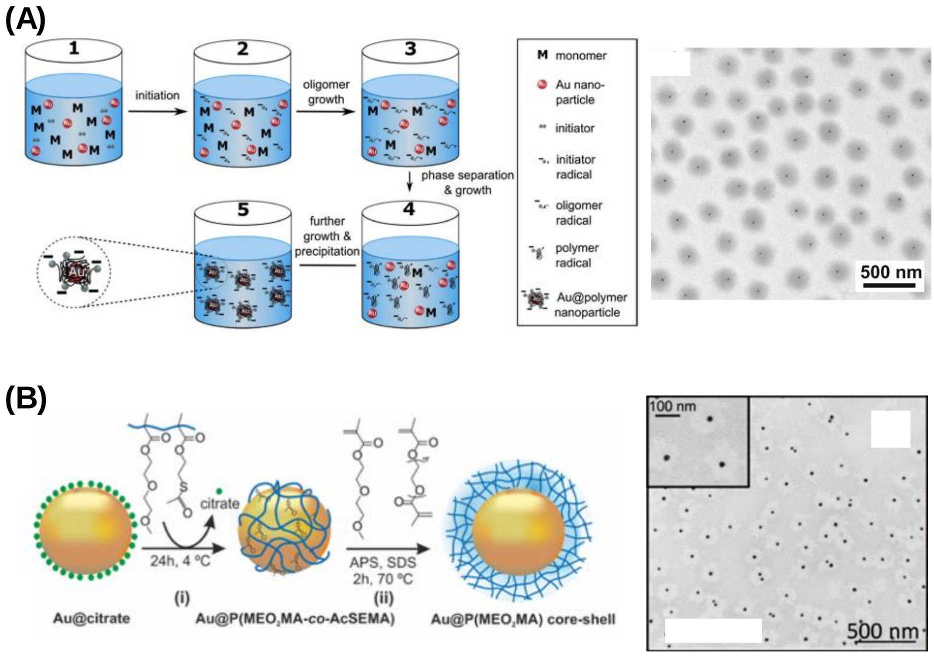

Figure 2.10 (A) The schematic depiction of precipitation polymerisation. The TEM image showed a well-defined gold-poly(NIPAM) core-shell product after applying the butenylamine in the functionalisation step.[149] (B) The schematic depiction of the precipitation polymerisation by functionalising the Au NPs with a preformed copolymer. The TEM image showed a well-defined Au-poly(MEO_2MA) core-shell particle product.[152]

Apart from the poly(NIPAM), other monomers have also been applied to the core-shell structure synthesis using the precipitation polymerisation. As shown in Fig. 2.10(B), Guarrotxena et al. introduced a thiol-containing monomer 2-(acetylthio)ethyl methacrylate (AcSEMA),[153] which can self-attach to the Au NP surface due to the strong interaction between thiol and Au.[152] AcSEMA was used for the synthesis of copolymers with 2-(2-methoxyethoxy)ethyl methacrylate (MEO_2MA) by ATRP process. Such a new copolymer successfully mimicked the surface of the colloidal seed before the polymerisation. As a result, the precipitation polymerisation also proceeded the thermo-responsive poly(MEO_2MA) shell growth. In this thesis, a pH-responsive NG shell was grown around Au NPs by appropriately controlling the surface hydrophobicity and reaction conditions. The successful synthesis can realise enhanced colloidal stability, tuneable LSPR and potential pH-responsive plasmonic effect as shown in Chapter 3 and Chapter 4.

2.3 Background of Microgels

MGs are crosslinked colloidal polymer particles which can swell in a good solvent, or with the presence of stimuli.[154–156] The term “microgel” was first introduced by Baker for crosslinked polybutadiene particles in 1949.[157] MGs allow the entrapment of solvent or solute in the swollen network[158–160] in contrast to other dense structures, such as silica or metallic particles. As shown in Fig. 2.11, the schematic cartoon exhibits the MGs as a core-corona model, which possesses the loosely connected polymer chains after swelling.[161] This swelling relies on the composition of MGs and can be manipulated by a range of stimuli,[162–164] such as temperature, pH and light. The size of these crosslinked colloidal polymers is also highly scalable in the synthesis. MGs have a diameter up to the micrometre-range. Smaller gel particles are less than 100 nm and are usually described as nanogels (NGs).[165] The soft, permeable and functionable features[165,166] of these particles facilitate their use in a wide range of applications, including as colloidal building blocks,[155] purification,[167] food science,[168] drug delivery[169] and solar cell fabrication.[170] In both industrial and biomedical fields, the MGs and NGs are attractive because of their large specific surface area, colloidal stability and ease of fabrication.[165,169] The highly tailorable composition, encapsulation capabilities, swellability and injectability highlight their advantages in the design of therapeutic dispersions.[171–174]

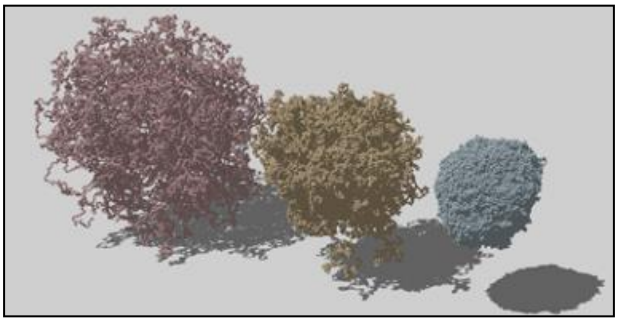

Figure 2.11 In silico MGs exhibit a volume phase transition from swollen to compact.[161]

2.3.1 pH-responsive microgels

Stimuli-responsive MGs are classified as a "smart" material, which are sensitive to the change of the environment.[164] Thermo- or pH-responsive MGs attract a lot of interest due to their facile control over swelling and deswelling behaviours at physiological conidtions.[166,169] The incorporation of ionic side groups can endow a pH-responsive property to MGs. These particles tend to swell or de-swell when the pH approaches pK_a in the solution.[154] Either anionic or cationic systems can be prepared varying the composition of crosslinked polymers toward different preferable applications.[169,175,176] In the Saunders's group, a wide range of pH-responsive NGs or MGs has been reported and explored for potential biomedical applications.[71,159,160,177–181] Two systems of poly(ethyl acrylate-methacrylic acid-1,4-butanediol diacrylate) and poly(methyl methacrylate-methacrylic acid-ethylene glycol methacrylate) intra-crosslinked colloidal polymers were able to form the free-standing physical gel at high pH upon swelling, and further inter-crosslinked to form a load-bearing chemical gel as illustrated in Fig. 2.12.[178] This study introduced the injectable doubly crosslinked MG system as a potential solution for IVD repair.[71,72,178] In order to avoid invasive surgery, the injectable hydrogel has been studied and developed to locally replace nucleus pulposus over past decades.[182–184] The adjustable swelling behaviours and mechanical properties make MGs an excellent candidate for a load-bearing substitute. Several types of hydrogels have been tested in developing therapeutic solution for DIVD, such as chitosan based hydrogels, hyaluronan-based hydrogels and synthetic gels.[185–188] To restore the function of IVD, it is necessary to meet several requirements in the selection of gels. The materials should be biocompatible, injectable, and be able to be solidified immediately after the injection without leakage. Acceptable mechanical and swelling properties should be achieved at the physiological environment under the loading condition.[184] The doubly crosslinked MG system is one of the most successful candidates, which potentially meet all the requirements in this application.[71,72,178] (It has now entered clinical trials) The published results showed methyl methacrylate and methacrylic acid-based doubly crosslinked MGs successfully improved the modulus, toughness and compressive resilience in the degenerated bovine bone IVD.[72] Moreover, the injectable single crosslinked gel can readily form the doubly crosslinked gel, which did not show any indications of redispersion.

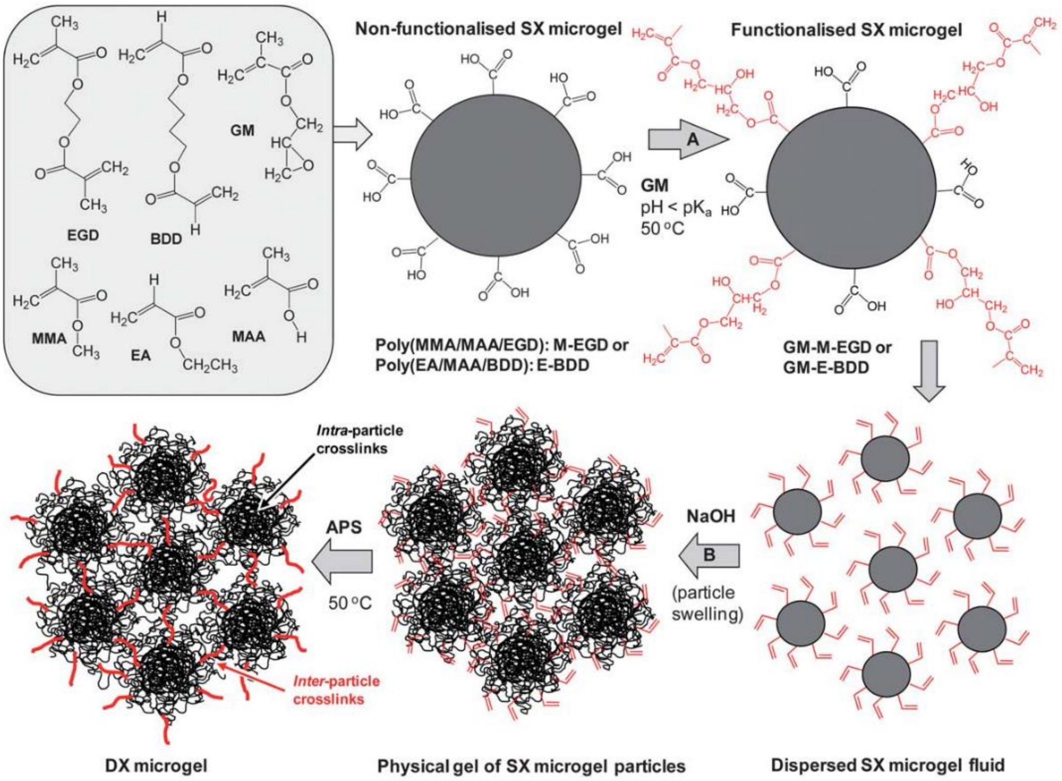

Figure 2.12 The schematic depiction of the formation of single crosslinked MG and doubly crosslinked MG using the pH-responsive MG.[178]

However, most doubly crosslinked MGs were not stretchable, and could fracture at the inter-MGs crosslinks. The study of pH-triggered polyacid nanoparticle disassembly showed the removal or decrease of intra-MGs crosslinks could enhance the stretchability to ~ 420%.[189] The improvement was caused by increasing the average number of segments between crosslinks. Some MG studies also showed the stretchability and toughness can be further improved by introducing a matrix phase and interpenetrating polymer networks through the swollen MGs.[190,191] The matrix phase (polyacrylamide) was constructed by UV polymerisation, and the chain entanglement within MGs acts as additional physical crosslink sites. In Chapter 5 of this study, I introduce a new strategy to improve the stretchability and multifunctionality of pH-responsive anionic MGs based gels using physical crosslinking with a cationic polymer. Different curing temperature is shown to alter the number density of elastically effective ionic crosslinks, which determines the modulus and stretchability of this new gel. Tensile measurements revealed the temperature dependent mechanical properties in Chapter 5. The difference can be explained by a rubber elasticity theory (below).

In a three-dimensional network of rubber-like material, an elastic polymeric system can be constructed by incorporating crosslinks with the high degree of flexibility.[192,193] Goodyear firstly introduced such a system through vulcanisation in 1839.[194] According to Kuhn, the elastic modulus (E) of a crosslinked polymer for the small deformation can be described as:[195–197]

$$E = \frac{3\rho_p RT}{\bar{M}_c} \qquad (2.4)$$

Where ρ_p is the density of the polymer, R is the gas constant and T is the temperature. $\bar{M}_c$ stands for the number averaged molecular weight between consecutive crosslinks. If elongation is considered in the analysis, the equation can be expressed as:[195]

$$E = \frac{\rho RT}{\bar{M}_c}\left(1 + \frac{2}{{\alpha_e}^3}\right) \qquad (2.5)$$

Where α_e is the extension ratio of the polymer. Both Equation 2.4 and 2.5 clearly exhibit the impact of $\bar{M}_c$ on the modulus for a crosslinked material. The increase of crosslinks lowers $\bar{M}_c$, which results in the increase of elastic modulus. The theory also applies in the analysis of hydrogel networks, including various types of crosslinks.[178,179,198]

At the cellular level, pH-responsive NGs also act as a powerful bio-candidate for cancer therapy and drug delivery. Both natural derived and synthetic polymers have been widely investigated for the smart design of NGs. Song et al. reported a chitosan based pH-responsive NGs for the antitumor treatment.[199] Two oppositely charged chitosan derivatives were used to construct the network of NGs by electrostatic interactions (Fig. 2.13(A)). After the UV irradiation, a drug loaded solubilising excipient was crosslinked into the NGs. In a weak acidic tumour microenvironment, these NGs were disintegrated due to the protonation of $-COO^-$ groups and the repulsive force from positively charge groups. As a result. the loaded drug could be spontaneously released to tumour sites through the blood circulation. Similar pH-triggered strategies has been also applied to a range of swellable NGs, such as poly(methyl methacrylate-methacrylic acid),[200,201] poly(N-isopropylacrylamide-co-acrylic acid),[202–204] polypeptide[205–207] and poly(2-diethylaminoethyl methacrylate)[208–210] NGs. Wu et al. also reported a sensing design of pH-responsive hydroxypropylcellulose poly(acrylic acid) NGs (Fig. 2.13(B)).[211] The particles showed the reversible swelling and shrinking transition in a size range between ~ 30 nm and ~ 100 nm. The incorporation of fluorescent quantum dots endowed these NGs with imaging and sensing properties, which may facilitate the pH-regulated systems for cancer therapy. As reported in the previous study, methyl methacrylate and methacrylic acid based NGs showed non-cytotoxicity and good swellability in the construction of injectable load-bearing hydrogels.[181] Herein, the combination of Au NPs and those swellable NGs should also provide the opportunity in developing a theranostic system at cellular level. In Chapter 4, I describe the feasibility of pH-triggered intracellular imaging in HeLa cells using the pH-responsive core-shell particles.

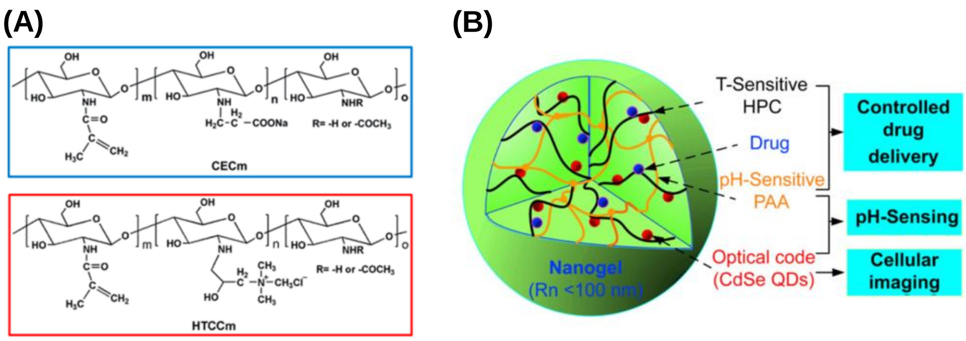

Figure 2.13 (A) Two modified oppositely charged chitosans for constructing pH-responsive NGs.[199] (B) A design of hydroxypropylcellulose-poly(acrylic acid)-CdSe hybrid NGs for drug delivery, sensing and imaging.[211]

2.3.2 The swelling of microgel particles

The swelling process for MGs is driven by the difference of osmotic pressures between the internal and external environments of the particles.[212] According to Flory−Huggins thermodynamic theory,[212,213] the net equilibrium of osmotic pressure inside the gel particles can be expressed as:[213]

$$\Pi_{total} = \Pi_{mix} + \Pi_{elas} \qquad (2.6)$$

Where Π_{mix} represents the solvent-polymer mixing contribution inside the crosslinked polymer, and Π_{elas} represents the elasticity which constrains the network. Π_{total} is the total osmotic pressure of the polymeric network. When Π_{total} is equal to zero, the equilibrium condition is achieved upon the swelling or deswelling of MG particles. However, Equation 2.6 should be modified if the ionic polymer is involved in the study.[214,215] The mobile counter ions of polymer generate a new term as shown in below:[214–216]

$$\Pi_{ext} = \Pi_{mix} + \Pi_{elas} + \Pi_{don} \qquad (2.7)$$

Where Π_{don} is a Donnan equilibrium term,[212,215] and stands for the osmotic pressure from the counterions on the gel-solvent interface.[217] The new equation takes the ions into the consideration.[214,216] The equations could be further modified if electrostatic interactions and salt media are considered.[215]

Π_{mix} and Π_{elas} can be shown as:[214,216,217]

$$\Pi_{mix} = -\frac{N_A kT}{v_s}\ [\phi + \ln(1-\phi) + \ \chi\phi^2] \qquad (2.8)$$

$$\Pi_{elas} = \frac{N_c kT}{V_0}\ [\frac{\phi}{2\phi_0} - \left(\frac{\phi}{\phi_0}\right)^{1/3}] \qquad (2.9)$$

$$\Pi_{don} = \frac{f N_c kT}{V_0}\ \frac{\phi}{\phi_0} \qquad (2.10)$$

Where N_A and k are the Avogadro number and Boltzmann constant, respectively. N_c stands for the effective number of polymer chains in the gel volume. V_0 and v_s represent the collapsed volume of MGs and molar volume of solvent, respectively. ϕ_0 is the volume fraction of polymer in the collapsed state, and ϕ is the volume fraction in the swollen state. T is the temperature. f is the number of counterions per chains, which describes the contribution of ionic group in MGs. χ is the Flory polymer-solvent interaction parameter. The conformation of polymer chains converts from a compact globule to an extended coil, when χ is lower than 0.5.[216,217]

2.3.3 Free-radical polymerisation

Free-radical polymerisation is a chain reaction of monomers. The basic mechanism was first introduced and developed in the 1940s and 50s.[218] The polymerisation begins with the generation of free-radicals. Free-radicals are the atoms or molecules or ions with a unpaired electron. They are highly reactive and short-lived, which are responsible for creating the "active centre" in the double carbon bonds containing compound.[219,220] Free-radical polymerisation can be divided into three steps, which are initiation, propagation and termination processes. Acrylic monomers could be favourably used in the construction of pH-responsive MGs or NGs for both load-bearing materials and pH-triggered therapies as shown in Section 2.3.1. Methyl methacrylate, which is used here, is also suitable for making bone cements and dental appliances.[221–224] This thesis involves the theranostic development of these acrylates, which requires the synthesis of MGs or NGs using a pH-responsive formulation (e.g. poly(methyl methacrylate-methacrylic acid-ethylene glycol methacrylate)[225]). Conventional emulsion polymerisation is selected to prepare the stable colloidal dispersion in an aqueous medium.[226] In this kind of synthesis, persulfate compounds act as a common water-soluble initiator for a range of latex, MG and core-shell particle preparation.[226–230]

The initiation step describes the formation of free radicals at the beginning of polymerisation. Free radicals can be formed through either homolysis or redox reaction. They require the heat or radiative energy to trigger the reaction based on different types of initiators.[220] Here, a thermal initiator and strong oxidising agent, ammonium persulfate (APS) is used to synthesise swellable polymer shells or colloids in Chapter 3 to 5. This initiator and a tetramethylethylenediamine catalyst have been widely used together to prepare different hydrogels at relatively low temperature.[181,231–234] In MGs synthesis, persulfate can be thermally degraded into free-radicals at elevated temperature, as shown in Fig. 2.14.

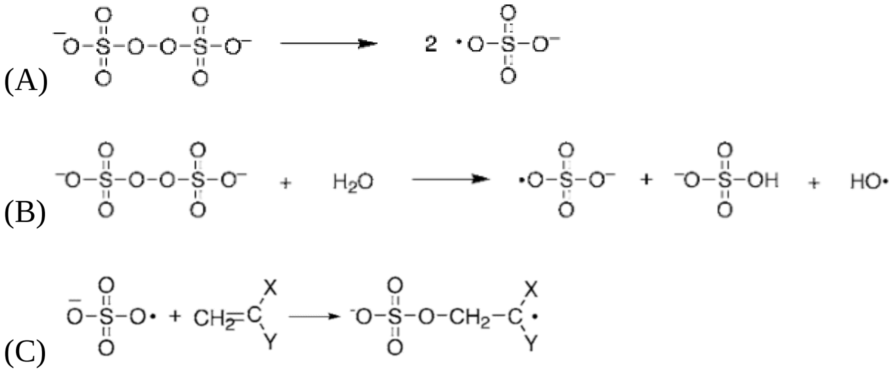

Figure 2.14 (A) & (B) The persulfate ion shows the generation of free radicals through two different pathways at the initiation step. (C) The sulfate radical anion attacks the monomer through direct addition.[218]

Subsequently, the radicals attack the carbon double bonds of monomers which are relatively weak. The breakage of double bonds creates a "active centre" in the neighbouring atom.[218,220] An example is shown in Fig. 2.14, a sulfate radical can react with a monomer. As a result, a radical anion is formed through direct addition.[218] The concentration of initiators, $[I]$ is an important factor in determining the rate of initiation, which can be expressed as:[218,220]

$$R_i = 2k_d f_i [I] \tag{2.11}$$

Where R_i is the rate of initiation and k_d is rate coefficient for initiator dissociation. f_i stands for initiator efficiency, which can decrease with conversion. In order to avoid the inhibition effect,

The previous "active centre" of monomers start to grow with the feeding of monomers. A chain reaction is built up by continuous relocation of the "active centre", and it is a rapid and controllable process.[220] As shown in Fig. 2.15, the growth of polymers can be either head to tail or head to head addition during the propagation step.

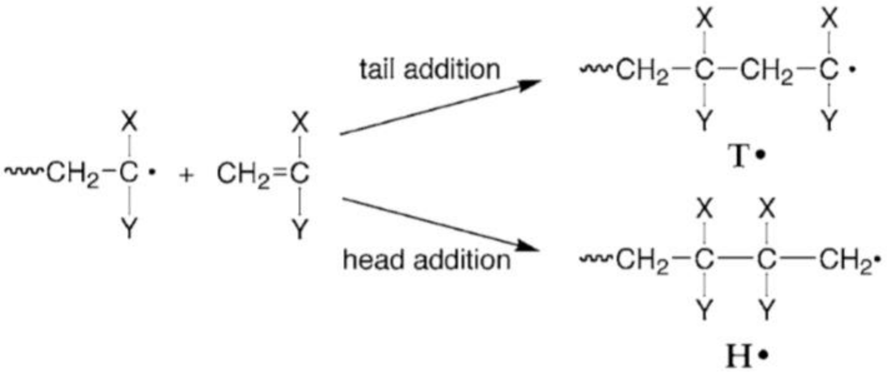

Figure 2.15 The growth of polymer chain in the propagation step with head to tail addition and head to head addition.[218]

The growth kinetics depends on the concentration of monomers and “active centre”. The reactivity of the propagation can be described by the equation:[218,220]

$$R_p = k_p[P\,\bullet][M] \qquad (2.12)$$

Where R_p is the rate of propagation. $[P\,\bullet]$ and $[M]$ stand for concentration of propagating radicals and monomers, respectively. k_p is the rate coefficient for propagation, which could be affected by the length of polymer chain.[218] As shown in early research[178,225] and Chapter 3 to 5, a series of methacrylates and acrylates were used to synthesise pH-responsive MG or NG components. The head to tail addition is statistically favourable in the propagation growth of acrylate polymers.[235] The addition of polymer chains is less sterically hindered at the β carbon.[236–238] In addition, free-radicals can be more stabilised at the α carbon, which show hyperconjugation and conjugation effects with the substituted groups (e.g. alkyl groups and carbonyl linkage).[236–238] Therefore, the reactivity of monomers and polymeric radicals also relies on their structures.[220] The copolymerisation can be easily controlled by the monomers with similar reactivity (methacrylates and acrylates are used to prepare NGs or MGs in this thesis).

Termination can occur between two radicals-containing polymer chains. It stands for the end of polymerisation. Combination and disproportionation are two standard pathways to bring the radical form of polymer chains back to its bonding state, as shown in Fig. 2.16. Both pathways could occur simultaneously in the termination step. Substantial disproportionation likely appears in the polymerisation of methyl methacrylate. Sometimes, the inhibitor can be also used to selectively terminate the growth of polymers.

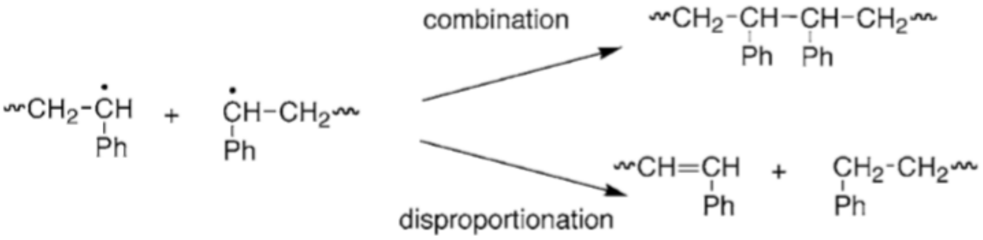

Figure 2.16 The end of polymerisation in the termination step with combination and disproportionation pathways.[218]

The rate (R_t) and rate coefficient (k_t) of termination are calculated based on the sum of the rate coefficient for combination (k_c) and disproportionation (k_{dp}), as shown below:[218,220]

$$k_t = k_{dp} + k_c \tag{2.13}$$

$$R_t = 2k_t[P\bullet]^2 \tag{2.14}$$

If the steady-state and long chain are assumed in the polymerisation, the generation and consumption of the free radical are constant. Then, Equation 2.15 can be further expressed as:[218,220]

$$R_p = k_p\left(\frac{k_d f_i}{k_t}\right)^{0.5}[I]^{0.5}[M] \tag{2.15}$$

2.3.4 Emulsion polymerisation

A conventional emulsion polymerisation is used to prepare MGs in Chapter 3 and Chapter 5. Emulsion polymerisation acts as a common method for the formation of polymer latex, which is applied to a wide range of applications due to the simplicity, high reaction rate and low viscosity of the polymerisation.[239,240] The method was first introduced as an industrial scale production in mid-1930s.[226] The reaction proceeds in an aqueous continuous phase with low water-soluble monomers, water-soluble initiators and emulsifiers (surfactants).[239–241] The formation of colloids follows the classic nucleation and growth processes based on the free-radical polymerisation mechanism with an oil-water interface.

The addition of surfactants enhances the stability of polymer colloids during the emulsion polymerisation. The stabilisation could be either ionic or non-ionic. When the quantity of surfactants exceeds the critical micelle concentration (CMC), the micelles will form in the solution.[226] These micelles act as effective nucleation sites for the polymer particles.[226] In an emulsified system, the monomers could be distributed to the emulsified monomer droplet and monomer swollen micelles or dissolve in the aqueous phase. As shown in Fig. 2.17, the micellar nucleation model can be divided into three intervals: (I) Nucleation of monomer-swollen micelles, (II) Growth of latex particles and (III) Consumption of residual monomer.[226,239]

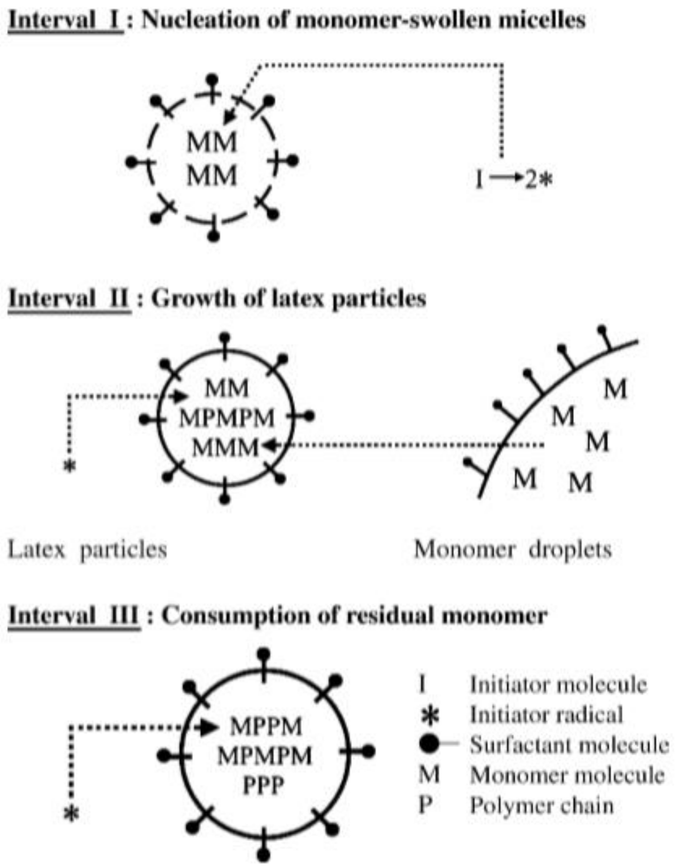

Figure 2.17 The formation of a polymer colloid based on the micellar nucleation model with three intervals.[239]

In interval I, the monomer-swollen micelles and free radicals are formed in water. As a result of their high oil-water interfacial areas, these micelles capture the free radicals or oligomeric radicals and gradually transfer to particle nuclei by the polymerisation.[239] Less surfactants in solution will generate larger and narrower particle size distributions at the nucleation step.[239] After the exhaustion of monomer swollen micelles, the surfactant adsorbed monomers droplet acts as a reservoir to continuously enable the growth of particle nuclei in interval II. The number of nuclei remains constant and the growth relies on the rapid diffusion of monomers from the droplet. In Fig. 2.18, the polymerisation rate becomes relatively steady due to the constant monomer concentration within the particles.[239,240] When all the monomer droplets are exhausted, the particles will consume all the remaining monomers, which result in a decrease of the polymerisation rate in interval III.

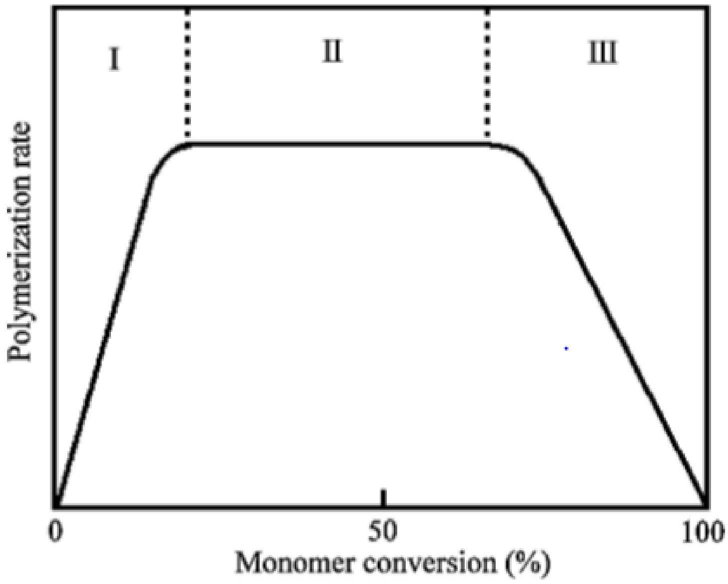

Figure 2.18 The emulsion polymerisation rate as a function of monomer conversion with three intervals.[239]

When the quantity of surfactants is lower than the CMC, emulsion polymerisation may undergo homogeneous nucleation.[226] The radicals can react with monomers and produce water-soluble oligomeric radicals. The solubility of theses oligomers is limited and they precipitated after a period of growth. The surfactant can stabilise the precipitates and particle growth can proceed continuously with effective monomer adsorption. The small size precipitates may also aggregate together to form a mature particle, which is large enough to take up the monomers.[226]

2.3.5 Colloidal properties and stability

A colloidal dispersion describes a two-phase system, where the dispersed phases (β_i) show Brownian motion and can be distributed uniformly in a continuous phase (α_i) as shown in Fig. 2.19.[242,243] The dispersed phase is usually 1 nm – 10 μm in size and are droplets, bubbles or particles.[243] They accommodate a range of shapes and applications through daily life.[244–246] The dimensional effect and the high surface-to-volume ratio make the particles perform different properties compared to their bulk states. Examples of colloids are the aqueous dispersions of Au NPs and MG or NG particles in this thesis.

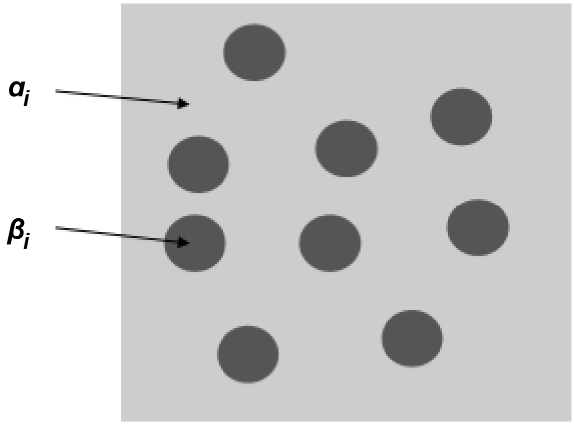

Figure 2.19 The schematic depiction of the dispersed phase (β_i) and the continuous phase (α_i).[243]

There are different types of forces around the particles, which can determine the property and stability of colloidal dispersions. Normally, the presence of inertial forces (negligible for small colloidal particles[247]), external field forces, shear forces, inter-particle forces and interfacial tension together describe the state of a dilute colloidal dispersion.[243] The inter-particle force is a key parameter controlling the colloidal stability of charged particles. The study of a long-range repulsive forces (overlap of electrical double layers) and a short-range attractive force (London-van der Waals forces) give the fundamental understanding of well-dispersed particles.[248] The study is known as Derjaguin–Landau–Verwey–Overbeek (DLVO) theory.[249,250] The imbalance of these inter-particle forces can cause direct aggregation by short-range thermodynamic interactions.[251]

2.3.5.1 Van der Waals force

The van der Waals force describes the emergence of attractive intermolecular force as a result of dipole formation, when two particles are close to each other.[252] Keesom interactions (permanent dipole-permanent dipole), Debye interactions (induced dipole-permanent dipole) and London dispersion forces (fluctuating dipoles) are three types of van der Waals force.[252,253] An instantaneous fluctuating dipole formation gives rise to the attractive interaction between two particles. This process has been theoretically investigated by Hamaker[254] and de Boer.[255] If two spherical particles have the same radius (a) with a small separation (H), this attractive interaction energy (V_A) can be expressed as:[248,253]

$$V_A = -\frac{A_{eff}}{12}\left[\frac{1}{x(x+2)} + \frac{1}{(x+1)^2} + 2\,ln\frac{x(x+2)}{(x+1)^2}\right] \qquad (2.16)$$

$$x = \frac{H}{2a} \qquad (2.17)$$

Where A_{eff} is the effective Hamaker constant. If these particles meet the requirement of H << a (i.e. x << 1), Equation 2.16 can be further simplified as:[248,253]

$$V_A = -\frac{A_{eff}}{12} \cdot \frac{1}{2x} = -\frac{A_{eff}a}{12H} \qquad (2.18)$$

According to Equation 2.18, the attractive interaction between particles is dependent on A_{eff}, which is controlled by the electronic polarisability and the density.[248] The calculation of A_{eff} needs to consider the sum of interactions among particle-to-particle, particle-to-medium and medium-to-medium, with particle 1, particle 2 and medium 3 as illustrated in Fig. 2.20. The Hamaker constants (A) of these interactions are A_{13}, A_{23}, A_{12}, and A_{33} (or A_3). The replacement of particle-medium interactions (A_{13}, A_{23}) could be required, if the particles are closer to each other. Therefore, the A_{eff} can be described as:[248,256]

$$A_{eff} = A_{12} + A_{33} - A_{13} - A_{23} \tag{2.19}$$

The Hamaker constant of the interaction between different phases is estimated by the geometric means.[248,256] When the same type of materials (particle $A_1 = A_2$) dispersed in the medium 3, Equation 2.19 becomes:

$$A_{eff} = \left(\sqrt{A_1} - \sqrt{A_3}\right)^2 \tag{2.20}$$

Usually the Hamaker constant has a magnitude of around $10^{-19} - 10^{-20}$ J.[248,253,256] The positive value of A_{eff} represents the inherent attractive interaction of particles in dispersion. In Chapter 3, A_{eff} values were calculated for both Au NP and core-shell dispersions. The calculated values are used to support an explanation of an enhanced colloidal stability in the core-shell particles.

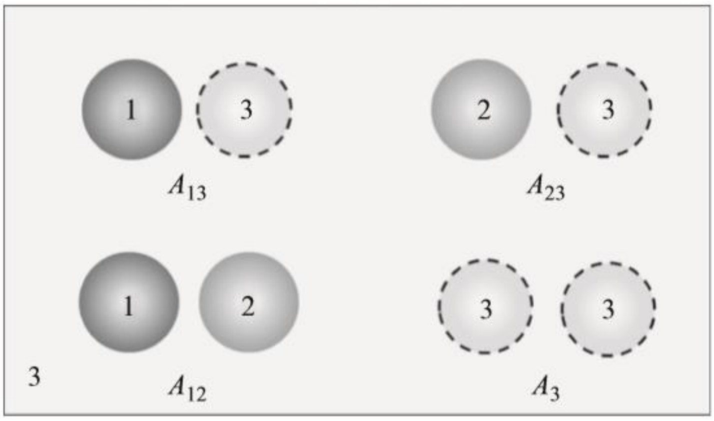

Figure 2.20 The interaction among particle 1, particle 2 and medium 3, with the corresponding Hamaker constants.[256]

2.3.5.2 Electrical double layer

Besides the attractive van der Waals force, charged colloidal particles develop an electrostatic repulsion in polar media, such as water. Ionisation or dissociation of surface groups and adsorption of ions are two common routes to generate the surface charges on particles. Representative examples of MG particles (carboxylic acid group incorporated copolymer) and Au NPs (citrate ions stabilising layer) are introduced in this thesis. These particles can interact and redistribute the ions around the charged surface, where they repel co-ions and attract counterions in the medium. As shown in Fig. 2.21, this redistribution of ions builds up a hierarchical structure, called an electrical double layer.[248,252,257]

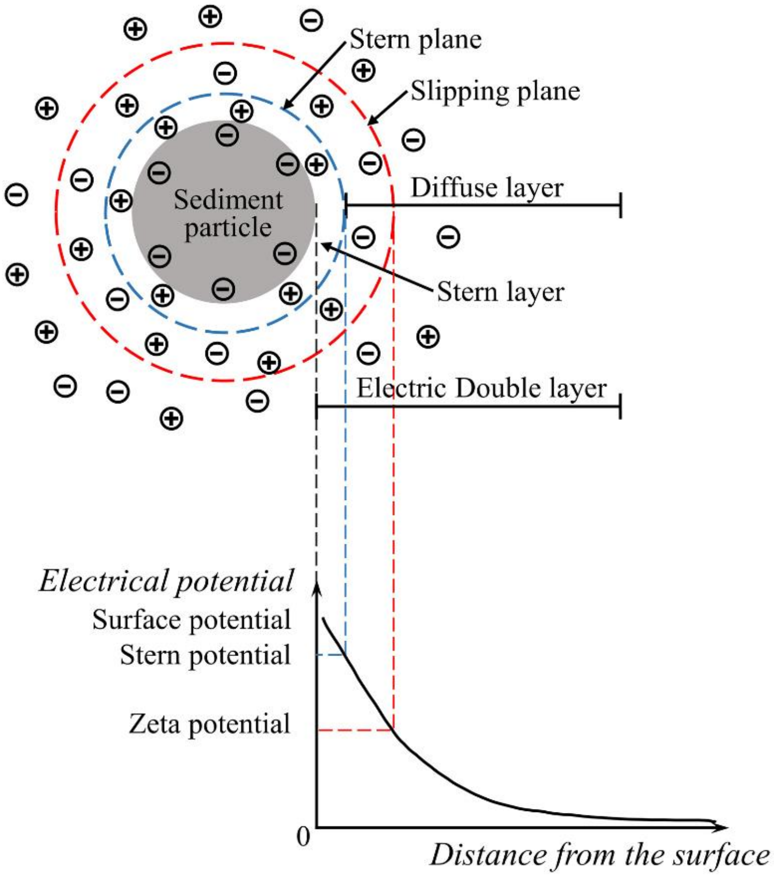

Figure 2.21 The structure of electrical double layer for a negatively charged particle, showing the corresponding electrical potentials as a function of distance from the particle surface.[258]

As described by Stern in 1924,[259] the ion distribution can be divided into a Stern layer and a diffuse layer near the particle surface. The Stern layer is constructed by accumulative counterions, which are closely adsorbed on the particle surface. The diffuse layer contains a mixture of counterions and co-ions. The configuration of the diffuse layer can be affected by the electrical force and random thermal motion.[248] The surrounding mobile ions with a particle will form an integral structure and move together in the medium. The boundary of this structure is defined by the slipping plane (shear plane).[248,260] The zeta potential of the particles can be acquired from this slipping plane, which is a valuable parameter for the analysis of colloidal stability and charges. The electrical potential is a maximum over the particle surface and exponentially drops toward the outer region as a function of distance. A characteristic distance 1/κ (Debye length) describes the "thickness" of the diffuse double layer,[248,253] which largely relies on the electrolyte concentration. The Debye length can be determined by:[261,262]

$$\kappa^{-1} = \left(\frac{\varepsilon_m \varepsilon_0 k_B T}{2e^2 z^2 c_e}\right)^{1/2} \qquad (2.21)$$

Where C_e is the concentration of the electrolyte in solution. *e* is the charge of an electron. *z* is the valence of the ion species in solution. ε_m and ε_0 represent the permittivity of the medium and free space, respectively. k_B is the Boltzmann constant and T is the temperature. Overlapping of electrical double layers occurs between two spherical particles as they approach one another. The process generates a repulsive interaction due to the increased concentration of ions. For particles with constant surface potential and separation H, such that $exp(-\kappa H)$ << 1, the repulsive interaction energy can be expressed as:[248,253]

$$V_R = 2\pi\varepsilon_m a \Psi_\delta^2 exp(-\kappa H) \qquad (2.22)$$

Where ε_m is the permittivity of the medium and a is the radius of the spherical particle. Ψ_δ stands for the Stern potential.

2.3.5.3 Total potential

The total interaction energy (V_T) can be calculated as a sum of the repulsive and attractive interaction energies (V_R and V_A) between two identical particles (spheres), as described by the DLVO theory:[248,253,256]

$$V_T(H) = V_R(H) + V_A(H) \qquad (2.23)$$

The resultant potential energy curve exhibits several characteristic features including a maximum, a primary minimum and a secondary minimum as shown in Fig. 2.22(A). For large particles (approximately > 10 nm), a secondary minimum may develop due to the weak repulsive potential or high electrolyte concentration.[248,253,256,260] When the depth of this minimum is comparable to the thermal energy (described by $k_B T$), flocculation may occur between the particles.[248] If two particles continuously approach each other, a repulsive energy maximum appears in the total potential curve. This maximum acts as the energy barrier to prevent particles from coagulating. Here, the electrostatic interaction is dominant in a stable colloidal dispersion. The Debye length and Stern potential determine the magnitude of this maximum.[248] In other words, the energy barrier is also controlled by the electrolyte concentration. If the thermal energy of particles overcomes the energy barrier, a dramatic increase of attractive interaction will cause the irreversible aggregation with further reduction of H. This process is called the reaction limited aggregation.[262] As shown in Fig. 2.22(B), the continuous addition of electrolytes keeps decreasing the maximum of the total potential curve. As a result, reaction limited aggregation shifts to diffusion limited aggregation at the vanishing point of the energy barrier. The interaction potential becomes completely attractive in such circumstances.

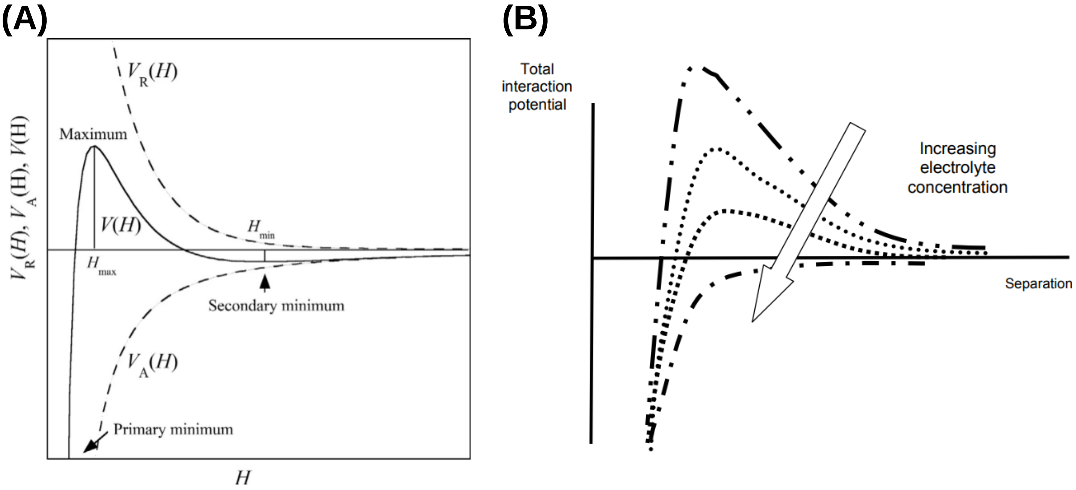

Figure 2.22 (A) The interaction energy curve of two identical particles (spheres) changes as a function of separation.[256] (B) The total interaction potential changes with the electrolyte concentration.[247]

2.3.5.4 Steric stabilisation

Some dispersions maintain their colloidal stability in the absence of the electrical double layer. Usually, steric stabilisation gives additional protection to these dispersions. Such stabilisation was applied to store ink (carbon black particles) by mixing with a natural polymeric solution (casein or gum Arabic) in ancient times (2500 BC).[263,264] Polymeric structures and macromolecules can generate this stabilising mechanism through the extension of their chains.[248,265] When the particles approach each other, the interpenetration of polymeric chains may occur after the collision. However, the process can be unfavourable or reversible, if the Gibbs free energy is positive due to the release of solvent molecules (change in enthalpy) and the change of configuration freedom (change in entropy) in polymeric chains.[248,265] The presence of this steric repulsive force maintain a well-dispersed state for these particles. In addition, the elastic repulsion (entropy-based) responses to the compressive change may also contribute to the stabilising mechanism for the soft periphery.[248,263,265,266] Steric stabilisation is less sensitive to electrolyte concentration in contrast to electrostatic stabilisation.[248,264] For some MGs, the coexistence of both mechanisms gives rise to electrosteric stabilisation in the dispersion.[154,267] The pH-responsive MGs contain electrosteric stabilisation due to their chain-like periphery, ionic charged groups and swollen state at high pH. The swollen MG particles reduce the effective Hamaker constant, which makes it comparable to the value of surrounding solvent and A_{eff} approaches zero. This effect also lowers the attractive interaction between particles.[154,268]

2.4 Instrumentation

2.4.1 Potentiometric titration

In the study of anionic MGs, potentiometric titration was applied to measure the pK_a and the molar content of charged groups using a strong base.[169,179,216] The pK_a describes the ionisability of carboxylic acid groups in aqueous MG dispersions.[269] These polyacid groups are weak acids. In a weak acid reaction, the dissociation of RCOOH can be expressed following the Henderson–Hasselbalch Equation:[160,270,271]

$$\mathrm{RCOOH} + \mathrm{H_2O} \rightleftharpoons \mathrm{RCOO^-} + \mathrm{H_3O^+} \qquad (2.24)$$

$$K_a = \frac{[\mathrm{H_3O^+}][\mathrm{RCOO^-}]}{[\mathrm{RCOOH}]} \qquad (2.25)$$

Where K_a is the dissociation constant. $[\mathrm{H_3O^+}][\mathrm{RCOO^-}]$ and $[\mathrm{RCOOH}]$ represent the concentrations. When pH = $-log\,[H^+]$ and α_{ion} is the degree of ionisation ($[\mathrm{RCOO^-}]$/($[\mathrm{RCOO^-}]$+$[\mathrm{RCOOH}]$)), the equation can be further expressed as:[272]

$$\mathrm{pH} = \mathrm{p}K_a + log\,\frac{[\mathrm{RCOO^-}]}{[\mathrm{RCOOH}]} = \mathrm{p}K_a + log\,\frac{\alpha_{ion}}{1-\alpha_{ion}} \qquad (2.26)$$

According to Equation 2.26, 50% degree of ionisation is recognised as a stoichiometric inflection point (equivalence point), where pH = pK_a can be extracted from the titration data curve. pK_a indicates an intermediate swelling point for pH-responsive MGs. The control of swelling is important to meet criteria for MG applications, such as physiological pH-triggered gelation.[165,187] As shown in Fig. 2.23, the titration data of multiple pH-responsive MGs was acquired using strong base. These poly(1,3-butadiene-methacrylic acid) MGs gave different swelling pK_a by altering the composition during the synthesis.[160] Increasing methacrylic acid content (6 wt% - 20 wt%) lowered the pK_a from 10 to 8.8 in MG dispersions, and pure linear poly(methacrylic acid) had the lowest pK_a ~ 6. The change of inter-segment MG hydrophobicity could be one of reasons for their differences. If the solid content of MG dispersions is known, the molar content of -COOH can be also calculated based on the recorded volume of strong base at 100% neutralisation. In the study of doubly crosslinked MGs, the modified groups were quantified by the difference of -COOH content before and after glycidyl methacrylate functionalisation.[72,180] This method provided a fast and simple way to estimate the number of non-charged functionalised groups on pH-responsive MGs. In Chapter 5, potentiometric titration is used to obtain the pK_a and acidic group content in pH-responsive MG dispersions.

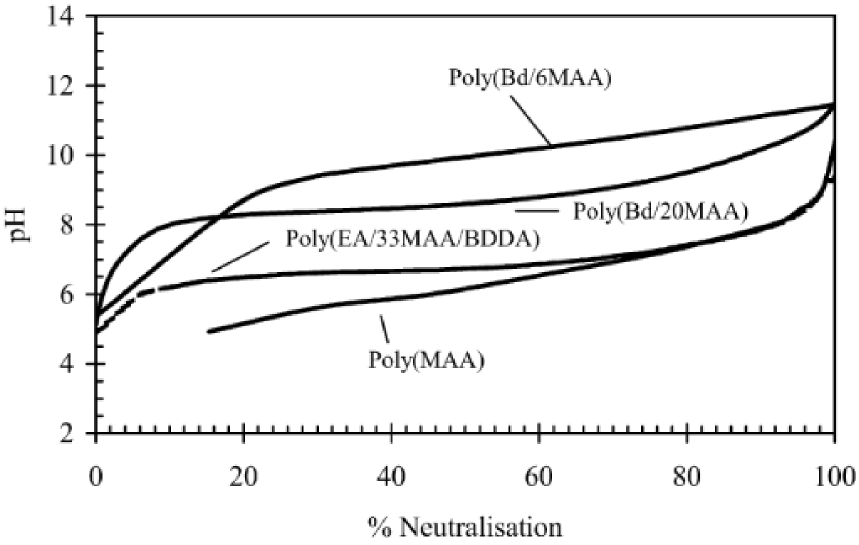

Figure 2.23 Potentiometric titration data of poly(1,3-butadiene-methacrylic acid) MGs, poly(ethyl acrylate-methacrylic acid-1,4-butanediol diacrylate) MGs and poly(methacrylic acid).[160]

2.4.2 Dynamic light scattering

Dynamic light scattering (DLS, also known as photo correlation spectroscopy) is an important size measurement technique for the analysis of colloidal particles.[273] These fine suspensions show Brownian motion.[274] A laser source generates coherent monochromatic radiation, which is effectively scattered (Fig. 2.24(A)). The change of the relative position of particles interferes with the travel distance of scattered light to the detector. Therefore, the fluctuated light intensity is detected as a result of the random movement of particles. The principle of DLS relies on monitoring the time dependent change of signal, which indicates the importance of the particle diffusion rate. Small particles diffuse faster than large particles, so their intensity signals fluctuate more rapidly as shown in Fig. 2.24(B).[274] The information can be quantitatively analysed using a signal processing technique, called autocorrelation. The normalised intensity correlation ($g_2(\tau)$) function can be expressed by:[275,276]

$$g_2(\tau) = \frac{\langle I(t)I(t+\tau)\rangle}{\langle I(t)\rangle^2} \tag{2.27}$$

Where $I(t)$ represents the scattered intensity at time t, and $I(t+\tau)$ is the signal after a delay time τ. In addition, an electric field correlation function can be applied to describe the motion of particles relative to each other through the medium. The normalised electric field correlation function is expressed as:[275,276]

$$g_1(\tau) = \frac{\langle E(t)E(t+\tau)\rangle}{\langle E(t)E(t)\rangle} \tag{2.28}$$

Where $E(t)$ and $E(t+\tau)$ account for the scattered electric field at t and $t+\tau$, respectively. Two correlation functions ($g_1(\tau)$ and $g_2(\tau)$) can be connected using the Siegert relationship if photon counting is a random Gaussian process and only scattered light can be recorded at the detector.[277] Then, the two correlation functions are related as:[275,276]

$$g_2(\tau) = 1 + \beta|g_1(\tau)|^2 \tag{2.29}$$

Where β is a constant determined by the experimental conditions (detector areas, optical alignment, scattering properties of particles).[277] If a monodisperse suspension is analysed and the movement of particles follows Brownian diffusion, the $g_1(\tau)$ will decay exponentially as:[275,276]

$$g_2(\tau) = 1 + \beta exp(-2\Gamma\tau) = 1 + \beta exp(-2Dq^2\tau) \qquad (2.30)$$

Where Γ is the decay constant and equal to Dq^2. D represents the diffusion coefficient of particles. q is the scattering wave vector and can be expressed as:[275,276]

$$q = \frac{4\pi n_m}{\lambda_0} sin\frac{\theta}{2} \qquad (2.31)$$

Where n_m is the refractive index of the medium and λ_0 is the wavelength of the incident laser in vacuum. θ represents the scattering angle. According to the Stokes-Einstein relationship, the hydrodynamic diameter (d_h) of spherical particles can be extracted from its diffusion coefficient as described in Equation 2.32:[275,276]

$$D = \frac{k_B T}{3\pi\eta \mathrm{d}_h} \qquad (2.32)$$

Where k_B is the Boltzmann constant and T is the temperature. η is the viscosity of the medium.

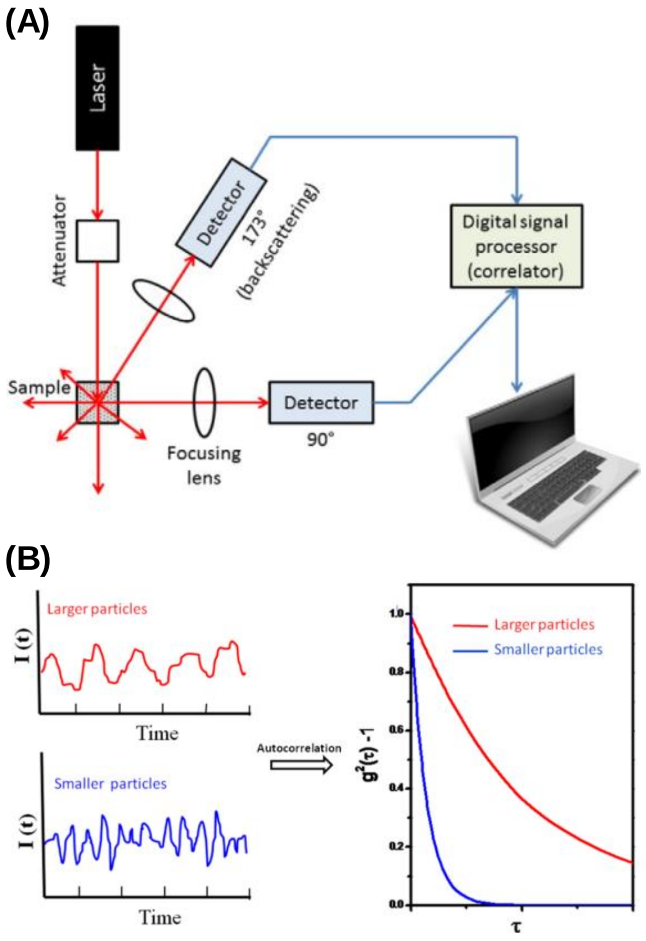

Figure 2.24 (A) The schematic diagram of DLS instrument.[276] (B) The fluctuation of the scattered light intensity and the autocorrelation functions for two different particle sizes.[274]

DLS is used to measure the hydrodynamic size for a range of colloidal particles in Chapter 3 to 5, including Au NPs, core-shell particles, pH-responsive NGs and MGs. The method is widely used for determining the size of colloidal particles in dispersion. For example, MG growth can be monitored by DLS and tuned by controlling the monomer feed at time interval during the synthesis. Fig. 2.25(A) shows an example of poly(NIPAM) MGs measured by DLS.[278] Long decay time suggested the large particles were present. A relatively monodisperse size distribution was obtained from $g_2(\tau)$ correlation function, which showed a radius ~ 298 nm at 31.3°C. This calculated size is broadly used and known as the z-average size (harmonic mean size).[279] The swelling study of MGs can be easily recorded by DLS. As shown in Fig. 2.25(B), three types of pH-responsive poly(ethyl acrylate-methacrylic acid) MGs were synthesised with different crosslinkers (divinyl benzene, 1,4-butanediol diacrylate and their mixtures).[179] A swelling trend was plotted by altering pH in MG dispersions. The trend clearly revealed differences in the maximum swollen volume of these MGs at pH > 7. Less efficient intra-particle crosslinking of divinyl benzene was concluded from the DLS results. In an adsorption study, DLS measurements also showed the capability in reporting bioconjugation events on Au NPs. In Fig. 2.25(C), bovine serum albumin (BSA) was incubated with Au NPs (diameter ~ 108 nm) at different pH environments. The full coverage of BSA increased the particle size by ~ 30 nm, and the result was confirmed by DLS.[280] Therefore, the optimal environment of BSA conjugation was found between pH 7 and 9 for Au NPs, which showed a similar size increase compared to the full coverage state. In other fields, DLS measurements also provide a convenient way to estimate the aggregation and degradation of colloidal particles. Multiple size distributions and increase of the z-average diameter may indicate the presence of aggregates in many studies, such as Au NPs.[281–283] DLS can detect a small increase of diameter (~ 10%).[280] In Fig. 2.25(D), DLS measurements of poly(methyl acrylate-methacrylic acid) particles showed a broad and disorder size distribution after increasing pH to 6.8.[189] This feature may indicate the disruption of particles due to the absence of effective crosslinkers. This electrostatic repulsion triggered disassembly was later confirmed by electron microscopy.

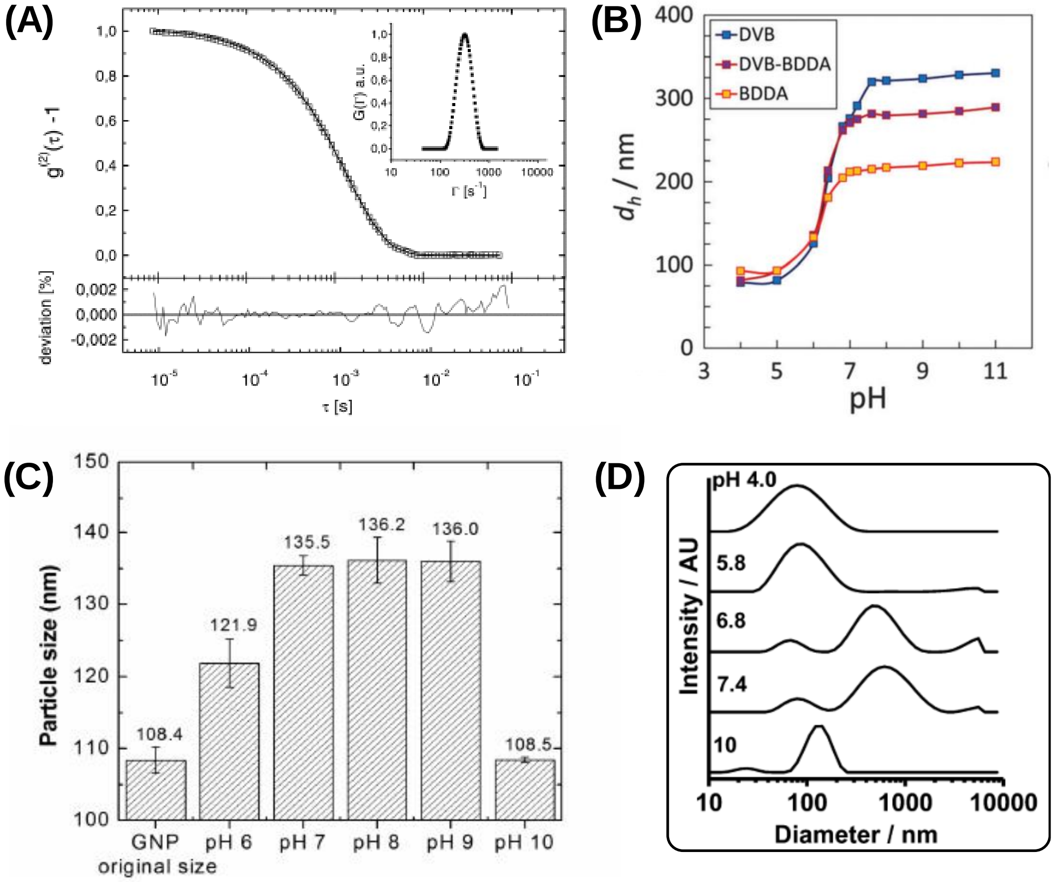

Figure 2.25 (A) DLS results for poly(NIPAM) MGs.[278] (B) Swelling data of poly(ethyl acrylate-methacrylic acid) MGs with three different crosslinkers: divinyl benzene, 1,4-butanediol diacrylate and their mixtures.[179] (C) The size change of Au NPs bioconjugation at different pH.[280] (D) The size distribution of poly(methyl acrylate-methacrylic acid) particles at different pH.[189]

2.4.3 Fourier transform infrared spectroscopy

Fourier transform infrared (FTIR) spectroscopy is a powerful characterisation method for analysing the structural information and chemical composition of unknown specimens. Both transmission and absorption processes can occur when specimens are exposed to the infrared (IR) radiation. IR radiation induces the molecular vibration of materials, which originates from their chemical bonds and functional groups containing the dipole moment.[284] The photons excite the molecules to a higher energy level as a result of the transition between the quantised vibrational energy states.[285] The energy of transition usually occurs in the mid-infrared spectrum (400 to 4000 cm^{-1}).[286] As shown in Fig. 2.26(A), the possible vibrational modes include bond stretching (symmetric and asymmetric) and bond bending (scissoring, rocking, wagging and twisting), which respond to the specific frequencies of IR radiation.[285] Consequently, each material has its own "fingerprint" on the FTIR spectrum. This allows one to monitor and examine the evolution of chemical structure, especially as bonding changes.

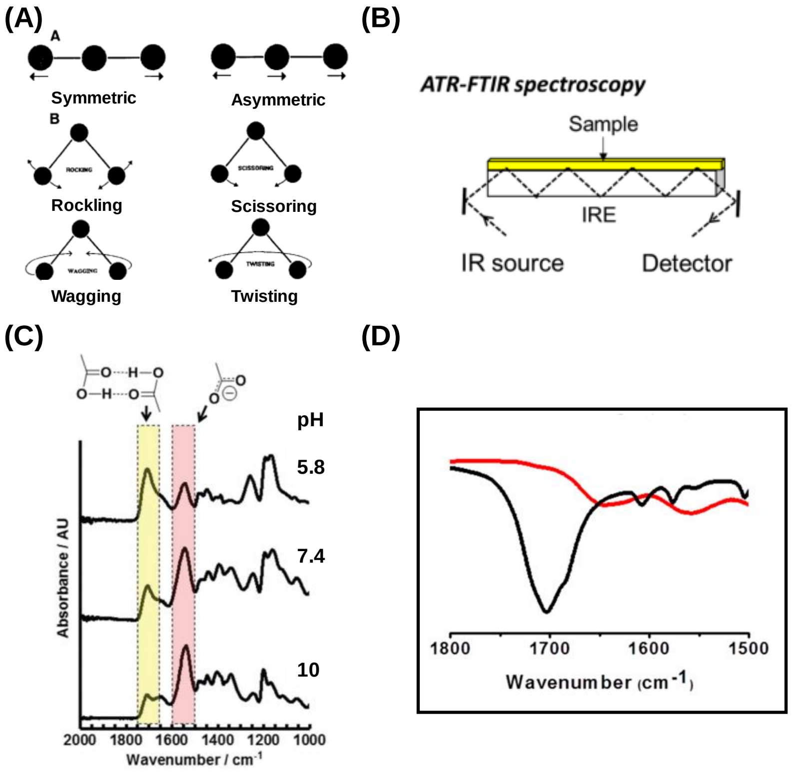

Figure 2.26 (A) The possible vibrational modes of molecules.[285] (B) The analysis modes of transmission attenuated total reflectance-FTIR spectroscopy.[287] (C) FTIR spectra of poly(methyl methacrylate-methacrylic acid-glycidyl methacrylate) gels (prepared at different pH).[189] (D) FTIR spectra of aldehyde-displaying carbon dots (Black) and their assembled polyethyleneimine gels (Red).[288]

FTIR spectroscopy has the advantages of fast and facile measurement. Mixture pellets of KBr (IR transparent) and pulverised specimens need to be prepared in the transmission FTIR spectroscopy. Usually, the sample is limited to 0.5-1 mm thick to maintain its translucent property for the IR beam.[287] ATR-FTIR spectroscopy (Fig.

2.26(B)) has the short effective pathlength (<< 1 mm), which relies on the internal reflection in a high refractive-index crystal (internal reflection element (IRE)).[285] The IR radiation is attenuated exponentially from the surface of IRE to the sample. This can be applied to measure the aqueous solution as an advantage.[285,287] In Chapter 5, ATR-FTIR spectroscopy is used to analyse the evolution of chemical structure in a new gel system. The spectral study included anionic poly(ethyl acrylate-methacrylic acid-divinyl benzene) MGs, cationic branched polyethyleneimine and their gel mixture. In some amine functionalised or incorporated MG research, the spectra may generate characteristic R-NH_2 bands at ~ 1590 cm^{-1} and ~ 3300 cm^{-1}.[289,290] These bands act as one of indications in justifying the MG composition. Chitosan and polyethyleneimine also showed a N-H stretch at similar position ~ 3400 cm^{-1}.[291–293] Hydrogen bonding interactions may slightly lower the wavenumber of N-H stretch.[294–296] Similar spectral information is widely used to study physical bonding and ionic interactions in FTIR spectroscopy. As shown in Fig. 2.26(C), a study of poly(methacrylic acid) containing gels showed two characteristic bands of -COOH (~ 1710 cm^{-1}) and -COO^- (~ 1544 cm^{-1}) in spectra.[189] The ratio of -COOH to -COO^- decreased by increasing the degree of ionisation. At different gel preparation pH, this ratio can be related to the mechanical analysis of the gel networks. In a chitosan and poly(acrylic acid) based membrane, the presence of ionic interactions was also proven by FTIR spectral information.[297] The sample exhibited new band formation at 1553^{-1} and 1637 cm^{-1}, which represented -COO^- (symmetrical stretch) and -NH_3^+, respectively. The strong interaction supported the construction of interpenetrating polymeric network in the membrane. This study provided an indication of physical bonding patterns in Chapter 5. FITR spectroscopy can be also used to explain some typical processes in self-healing gels, such as Schiff base reaction. FTIR spectral studies showed dynamic covalent bonding processes between aldehyde groups and amine groups.[288,298] As shown in Fig. 2.26(D), the formation of imine bonds became dominant at ~ 1650 cm^{-1}. In the meantime, aldehyde groups were consumed, and their bands started to diminish at ~ 1700 cm^{-1}. The spectral evolution showed a direct evidence for Schiff base reaction, which was responsible for the robust gel network and self-healing property.

2.4.4 Scanning electron microscopy

The visual inspection of particle size, dispersity and morphology provides valuable information describing colloidal dispersions.[299] However, small colloids are difficult to distinguish by human eye, which only has a resolution ~ 0.1 mm at 25 mm viewing distance.[300] The resolution of optical microscope is also limited.[300] Therefore, it is not possible to observe any nano-colloids using common inspection methods. Scanning electron microscopy (SEM) is a powerful imaging technique in analysing MG particles and microstructures.[178,180] The focused electron beam generates information at each spotted place scanning across a selected area. A thermionic (Tungsten, Lanthanum Hexaboride) or field emission source can be used to generate the electron beam.[300,301] The electrons are extracted by anodes in the field emission (FE) source, which is usually selected for the modern SEM due to its higher brightness and resolution compared to the traditional filament heating method. The electrons can be accelerated to 0.1–30 keV and subsequently pass through a condenser and objective lens (Fig. 2.27).[300,301] Although the high accelerating voltage might optimise the structural information, the inappropriate control of the electron beam could damage thermally vulnerable specimens.[299] This issue was widely found in SEM of gel networks or MG dispersions. In order to avoid severe damages, the maximum accelerating voltage did not exceed 20 keV for the data presented in this thesis. The condenser lens controls the convergence of the electron beam and discards the unnecessary electrons through the aperture. The objective lens can determine the spot size of the beam, which has an impact on the resolution of images. After reaching the sample, the primary electron beam produces multiple useful interacting sources, such as secondary electrons (SE), backscattered electrons (BSE), Auger electrons, cathodoluminescence and X-rays.[300]

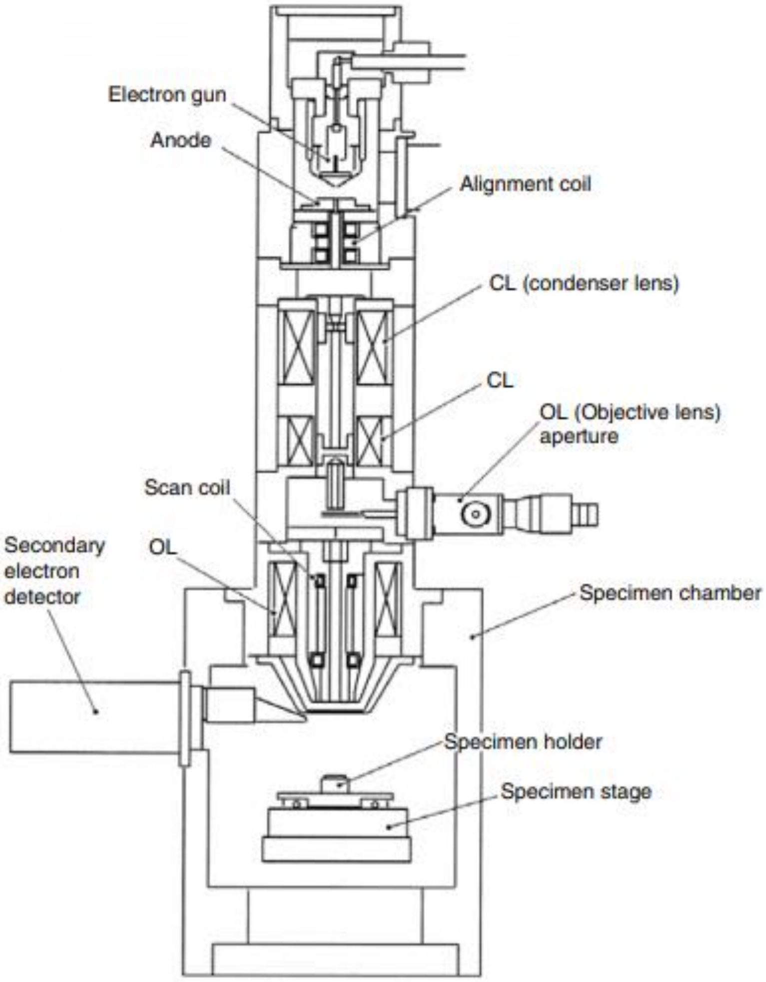

Figure 2.27 The schematic diagram of a scanning electron microscope.[300]

For sample preparation, a few nanometre coating (of metal or carbon) is usually applied onto dried MGs or gels on stubs. The enhancement of conductivity prevents charge accumulation and improves the overall image quality. The topographic information of samples is obtained from SE. Those electrons have a low escape depth and are generated from the inelastic scattering near the surface of materials. SEs have a low energy < 50 eV, and are typically within a range of 3-5 eV.[300,301] The contrast difference of signals depends on the number of detected SEs and finally reveals the surface structure. Such SE imaging is widely used to define the morphology of MGs and porous gel matrix.[178,180] As shown in Fig. 2.28(A), SEM images of hybrid chitosan-polyacrylamide hydrogels revealed the microscopic gel network after freeze-drying.[302] The reduction of pore size was observed in salt immersed gels, which possessed an ionic crosslinking chitosan network through SO_4^{2-} or citrate^{3-} anions. Extra crosslinking produced a much denser microstructure (< 180 nm pore size) compared to its original gel network. The variation of microstructures tightly related to their macroscopic properties, such as stiffness and tensile strength. For example, the stiffness of these gels increased from ~ 60 kPa to ~ 1 MPa and the microstructure pore size decreased. SE imaging can be also used to locate structural differences in the gel network. In Fig. 2.28(B), the freeze-dried composite gel of carbon nanotubes and pH-responsive MGs was studied under SE mode.[303] Such a system was targeted to improve electrical and mechanical properties of doubly crosslinked gel networks. The successful incorporation of carbon nanotubes was confirmed by the tube-like features. After the gel formation, particle-like MGs were unobservable, and the distribution of carbon nanotubes was randomly orientated in the gel matrix. In a study of cellulose incorporated poly(acrylic acid) gels, the tannic acid-coated cellulose nanocrystals could form a thick fibril-like structure and other ionic interactions in the presence of metal ions.[11] SE imaging directly visualised the stretching cellulose bundle at a crack tip of a freeze-dried sample (Fig. 2.28(C)). The feature contributed to the mechanical reinforcement in the gel network.

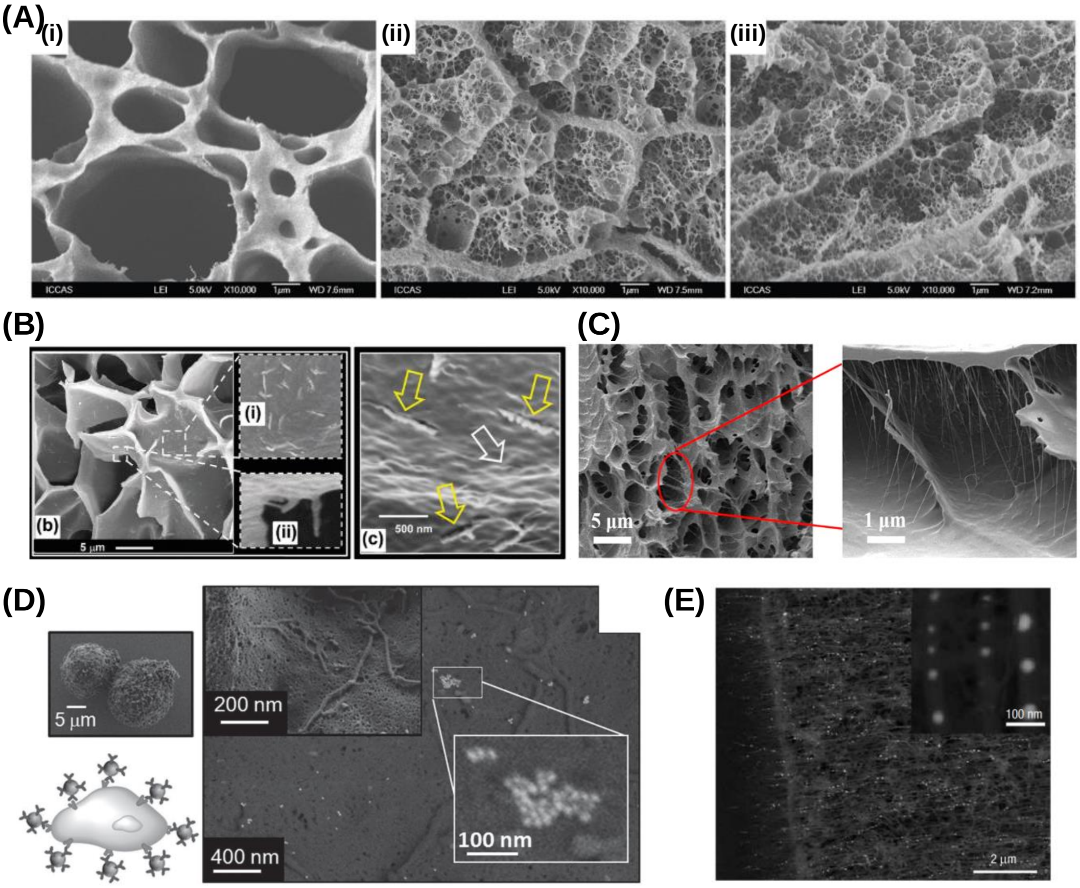

Figure 2.28 Secondary electron mode: (A) SEM images of hybrid chitosan-polyacrylamide hydrogels.[302] (i) Original. (ii) Immersed in Na_2SO_4 solution. (iii) Immersed in sodium citrate solution. (B) SEM images of carbon nanotubes incorporated doubly crosslinked MGs.[303] (C) SEM images of cellulose incorporated poly(acrylic acid) gels.[11] Backscattered electron mode: (D) SEM images of Au NPs adhered human colon adenocarcinoma cell line.[19] (E) SEM images of gold and silica hybrid nanostructures.[304]

Backscattered electrons (BSE) are the other important source, which is generated from the elastic scattering (> 50 eV) of electrons.[300,301] They have much larger interaction volumes compared to SEs. The electron beam penetrates further and directly interacts with heavy atomic nuclei. The generation of BSEs depends on the atomic number of elements. In comparison, the beam electrons might produce ~ 6% BSEs for carbon and ~ 50% BSEs for gold at the same experimental condition.[300] Therefore, imaging can distinguish the compositional contrast difference by recording the density of BSEs. Such a technique is very useful for visualising the composite structure, which possesses heterogeneous components. In a cellular study, antibody functionalised Au NPs were used to target human colon adenocarcinoma cell line.[19] Specific recognition was achieved by interacting the epithelial cell adhesion molecule on the cell surface. Such a strategy is widely used in electrochemical sensing, which relies on electrocatalytic activity from Au NPs. In BSE mode, bright Au NPs were clearly identified on the cell surface which could suggest the successful targeting (Fig. 2.28(D)). Such an imaging is also useful in distinguishing hybrid nanostructures. As shown in Fig. 2.28(E), many shiny dots were distributed in a loose wire-like microstructure.[304] These features represented heavy gold cores and silica nanowires, which gave a strong contrast difference due to BSEs. In Chapter 3, BSE imaging is used to investigate the distribution of Au NPs in a DX MG network. A high electron contrast difference was present between these two materials.

2.4.5 Transmission electron microscopy

Transmission electron microscope (TEM) was designed and first used in 1931.[305] This technique has been continuously developed to resolve fine structures or matter, and has shown the importance in characterising colloidal particles (polymer latex, core-shell particles, nanocrystal).[299] In general, TEM has a much higher magnification and resolution compared to other common microscopes. An example of Phillips CM200 FEG TEM shows a maximum image resolution up to 0.1 nm with a magnification range from 25× to 1100000×.[305] According to the Rayleigh's formula, the resolution of microscopes is related to the wavelength of optic/electron beams.[306] The high accelerating voltage of source emits the short wavelength, which can improve the image resolution. The maximum accelerating voltage achieved 200 keV in a CM200 FEG TEM.[305]

The principle of TEM imaging relies on the transmission of the electron beam through a thin specimen. The scattering of thick and high density parts produces the dark features on the viewing screen.[299] The overall configuration of the TEM column shares some similar components with SEM. As shown in Fig. 2.29, the electron beam can be generated from the thermionic or FE source and then converged by the condenser lens. After passing through the specimen, the number of transmitted electrons is controlled by the objective aperture, which can efficiently block the scattered electrons. In the meantime, the objective lens focuses the electron beam and constructs an intermediate image. Such an image is magnified by the following intermediate and projector lens. Finally, the image is projected on the fluorescent phosphor viewing screen or converted to a digital form using the electron detector.[307–309]

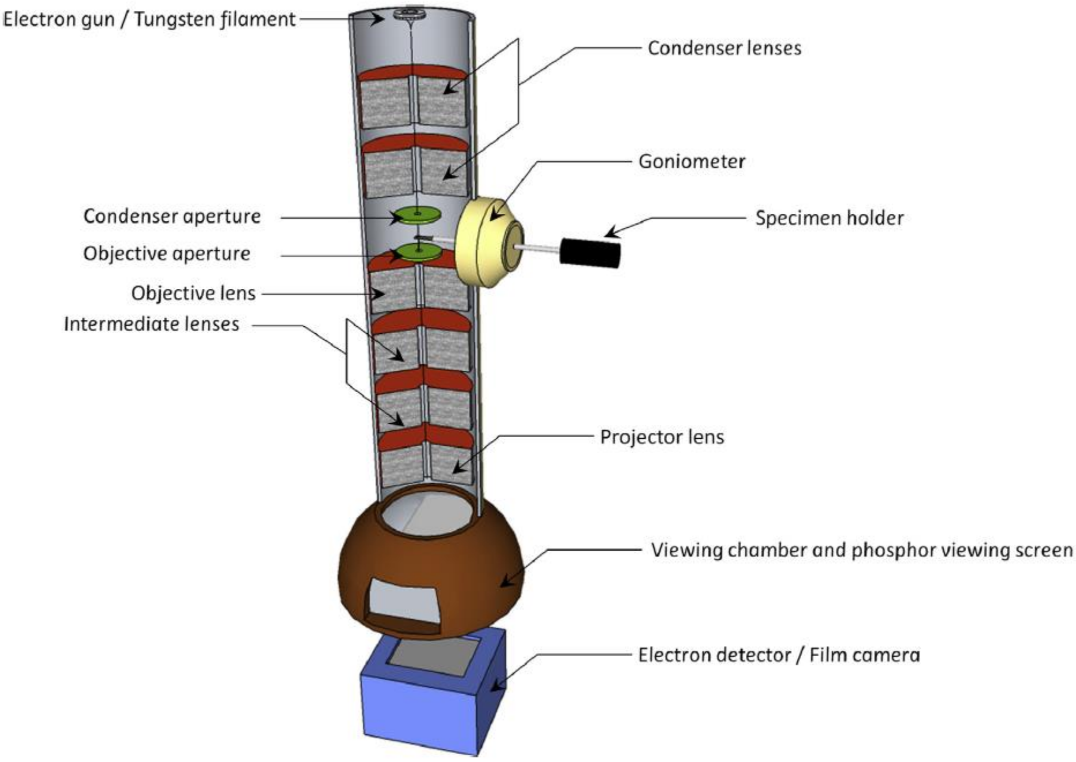

Figure 2.29 The schematic diagram of a transmission electron microscope.[310]

TEM is a powerful imaging method in analysing the core-shell structure with high contrast materials. In an example of a Au-Ag core-shell study, the particles showed a strong contrast difference in imaging.[311] The stability of these particles could be enhanced by a light silica layer, which had a lower density compared to a bimetallic core. The final decoration of small Au NPs covered the whole structure and form "satellites". As shown in Fig. 2.30(A), the image clearly demonstrated this growth of core-shell-satellite particles in the synthesis. Such a complex design was used to increase the electromagnetic coupling for the biological detection. TEM has the excellent performance in identifying small structural changes, including the study of shell thickness. As shown in Fig. 2.30(B), 13 nm Au NPs were used to synthesise the core-shell particles by an electrostatic layer-by-layer strategy.[312] Poly(allylamine hydrochloride) and poly(styrene sulfonate) were selected as a growing pair, which tuned the shell thickness based on the number of deposition steps. TEM clearly proved precise control of shell growth with a well-define core-shell structure. For a swellable poly(NIPAM) MGs, their swollen and collapsed morphologies can be also estimated in TEM.[313] As shown in Fig. 2.30(C), Au nanorods decorated poly(NIPAM) MGs had a larger diameter below lower critical solution temperature. The swelling dependent orientation and interparticle distance were observed for these Au NRs by TEM. The temperature change may give an impact on the plasmon coupling effect. The volume density of Au NRs could be tuned and used as a strong contrast agent due to their thermo-responsive swelling. In this thesis, TEM is used to identify core-shell structures, shell thicknesses, and pH-dependent changes in Chapter 3 and Chapter 4.

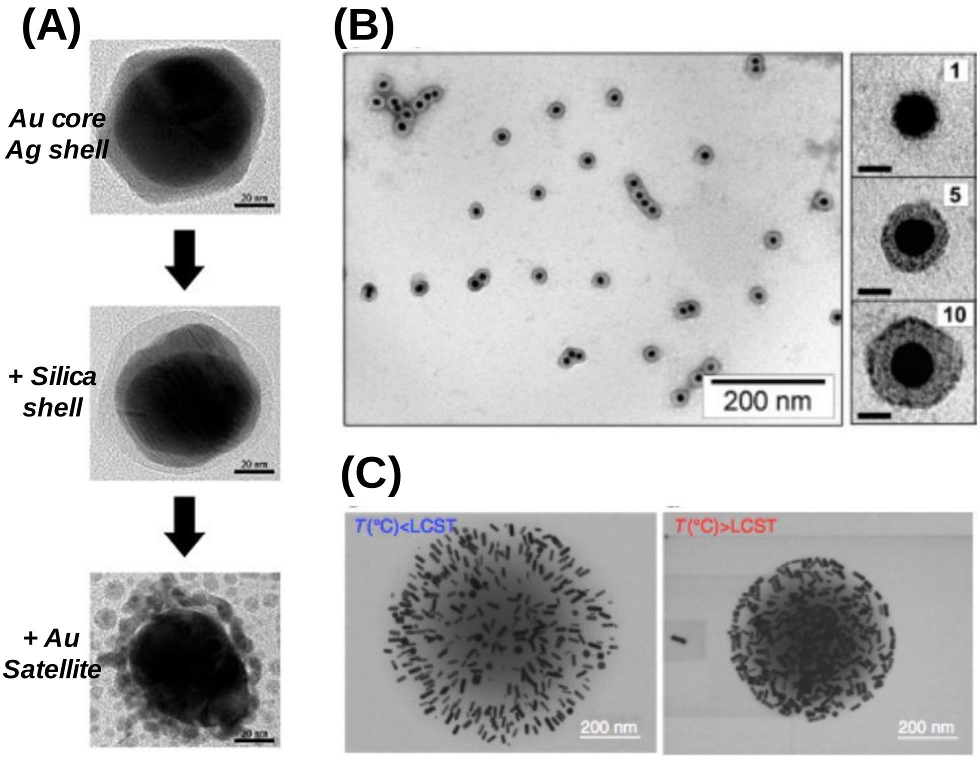

Figure 2.30 (A) TEM images of the core-shell-satellite construction.[311] (B) TEM images of core-shell particles prepared by a layer-by-layer growth. The number represents the grown pairs of the polymer layer.[312] (C) TEM images of Au nanorods decorated poly(NIPAM) MG in a swollen or collapsed state.[313]

2.5 References

1. Yao, J.; Yang, M.; Duan, Y. Chemistry, Biology, and Medicine of Fluorescent Nanomaterials and Related Systems: New Insights into Biosensing, Bioimaging, Genomics, Diagnostics, and Therapy. *Chem. Rev.* **2014**, *114*, 6130–6178.

2. Georgakilas, V.; Tiwari, J. N.; Kemp, K. C.; Perman, J. A.; Bourlinos, A. B.; Kim, K. S.; Zboril, R. Noncovalent Functionalization of Graphene and Graphene Oxide for Energy Materials, Biosensing, Catalytic, and Biomedical Applications. *Chem. Rev.* **2016**, *116*, 5464–5519.

3. Lee, H.; Shin, T. H.; Cheon, J.; Weissleder, R. Recent Developments in Magnetic Diagnostic Systems. *Chem. Rev.* **2015**, *115*, 10690–10724.

4. Tuantranont, A. *Applications of Nanomaterials in Sensors and Diagnostics*; Springer Berlin Heidelberg, 2013; Vol. 14.

5. Wittenberg, N. J.; Haynes, C. L. Using Nanoparticles to Push the Limits of Detection. *Wiley Interdiscip. Rev.: Nanomed. Nanobiotechnol.* **2009**, *1*, 237–254.

6. Krishnamoorthy, S. Nanostructured Sensors for Biomedical Applications-a Current Perspective. *Curr. Opin. Biotechnol.* **2015**, *34*, 118–124.

7. Zhang, S.; Geryak, R.; Geldmeier, J.; Kim, S.; Tsukruk, V. V. Synthesis, Assembly, and Applications of Hybrid Nanostructures for Biosensing. *Chem. Rev.* **2017**, *117*, 12942–13038.

8. Reddy, B.; Salm, E.; Bashir, R. Electrical Chips for Biological Point-of-Care Detection. *Annu. Rev. Biomed. Eng.* **2016**, *18*, 329–355.

9. Zhang, A.; Lieber, C. M. Nano-Bioelectronics. *Chem. Rev.* **2016**, *116*, 215–257.

10. Ray, T. R.; Choi, J.; Bandodkar, A. J.; Krishnan, S.; Gutruf, P.; Tian, L.; Ghaffari, R.; Rogers, J. A. Bio-Integrated Wearable Systems: A Comprehensive Review. *Chem. Rev.* **2019**, *119*, 5461–5533.

11. Shao, C.; Wang, M.; Meng, L.; Chang, H.; Wang, B.; Xu, F.; Yang, J.; Wan, P. Mussel-Inspired Cellulose Nanocomposite Tough Hydrogels with Synergistic Self-Healing, Adhesive, and Strain-Sensitive Properties. *Chem. Mater.* **2018**, *30*, 3110–3121.

12. Zhang, J.; Wan, L.; Gao, Y.; Fang, X.; Lu, T.; Pan, L.; Xuan, F. Highly Stretchable and Self-Healable MXene/Polyvinyl Alcohol Hydrogel Electrode for Wearable Capacitive Electronic Skin. *Adv. Electron. Mater.* **2019**, *1900285*, 1–10.

13. Chen, D.; Pei, Q. Electronic Muscles and Skins: A Review of Soft Sensors and Actuators. *Chem. Rev.* **2017**, *117*, 11239–11268.

14. Yang, J. C.; Mun, J.; Kwon, S. Y.; Park, S.; Bao, Z.; Park, S. Electronic Skin: Recent Progress and Future Prospects for Skin-Attachable Devices for Health Monitoring, Robotics, and Prosthetics. *Adv. Mater.* **2019**, *31*, 1–50.

15. Langford, G. J.; Raeburn, J.; Ferrier, D. C.; Hands, P. J. W.; Shaver, M. P. Morpholino Oligonucleotide Cross-Linked Hydrogels as Portable Optical Oligonucleotide Biosensors. *ACS Sensors* **2019**, *4*, 185–191.

16. Ferrier, D. C.; Shaver, M. P.; Hands, P. J. W. Conductive Composites for Oligonucleotide Detection. *Sens. Bio-Sensing Res.* **2018**, *17*, 1–6.

17. De La Escosura-Muñiz, A.; Sánchez-Espinel, C.; Díaz-Freitas, B.; González-Fernández, Á.; Maltez-Da Costa, M.; Merkoçi, A. Rapid Identification and Quantification of Tumor Cells Using an Electrocatalytic Method Based on Gold Nanoparticles. *Anal. Chem.* **2009**, *81*, 10268–10274.

18. Cui, L.; Wang, M.; Sun, B.; Ai, S.; Wang, S.; Zhang, C. Y. Substrate-Free and Label-Free Electrocatalysis-Assisted Biosensor for Sensitive Detection of MicroRNA in Lung Cancer Cells. *Chem. Commun.* **2019**, *55*, 1172–1175.

19. Maltez-Da Costa, M.; De La Escosura-Muñiz, A.; Nogués, C.; Barrios, L.; Ibáñez, E.; Merkoçi, A. Detection of Circulating Cancer Cells Using Electrocatalytic Gold Nanoparticles. *Small* **2012**, *8*, 3605–3612.

20. Ghoneim, M. T.; Nguyen, A.; Dereje, N.; Huang, J.; Moore, G. C.; Murzynowski, P. J.; Dagdeviren, C. Recent Progress in Electrochemical PH-Sensing Materials and Configurations for Biomedical Applications. *Chem. Rev.* **2019**, *119*, 5248–5297.

21. Estelrich, J.; Sánchez-Martín, M. J.; Busquets, M. A. Nanoparticles in Magnetic Resonance Imaging: From Simple to Dual Contrast Agents. *Int. J. Nanomed.* **2015**, *10*, 1727–1741.

22. Huang, J.; Li, Y.; Orza, A.; Lu, Q.; Guo, P.; Wang, L.; Yang, L.; Mao, H. Magnetic Nanoparticle Facilitated Drug Delivery for Cancer Therapy with Targeted and Image-Guided Approaches. *Adv. Funct. Mater.* **2016**, *26*, 3818–3836.

23. Fazal, S.; Paul-Prasanth, B.; Nair, S. V.; Menon, D. Theranostic Iron Oxide/Gold Ion Nanoprobes for MR Imaging and Noninvasive RF Hyperthermia. *ACS Appl. Mater. Interfaces* **2017**, *9*, 28260–28272.

24. Tamanaha, C. R.; Mulvaney, S. P.; Rife, J. C.; Whitman, L. J. Magnetic Labeling, Detection, and System Integration. *Biosens. Bioelectron.* **2008**, *24*, 1–13.

25. Zhang, F.; Braun, G. B.; Pallaoro, A.; Zhang, Y.; Shi, Y.; Cui, D.; Moskovits, M.; Zhao, D.; Stucky, G. D. Mesoporous Multifunctional Upconversion Luminescent and Magnetic “Nanorattle” Materials for Targeted Chemotherapy. *Nano Lett.* **2012**, *12*, 61–67.

26. Wei, H.; Bruns, O. T.; Kaul, M. G.; Hansen, E. C.; Barch, M.; Wiśniowska, A.; Chen, O.; Chen, Y.; Li, N.; Okada, S.; et al. Exceedingly Small Iron Oxide

Nanoparticles as Positive MRI Contrast Agents. *Proc. Natl. Acad. Sci. U. S. A.* **2017**, *114*, 2325–2330.

27. Kumagai, M.; Sarmat, T. K.; Cabral, H.; Kaida, S.; Sekino, M.; Herlambang, N.; Osada, K.; Kano, M. R.; Nishiyama, N.; Kataoka, K. Enhanced in Vivo Magnetic Resonance Imaging of Tumors by PEGylated Iron-Oxide-Gold Core-Shell Nanoparticles with Prolonged Blood Circulation Properties. *Macromol. Rapid Commun.* **2010**, *31*, 1521–1528.

28. Fatima, H.; Kim, K. S. Iron-Based Magnetic Nanoparticles for Magnetic Resonance Imaging. *Adv. Powder Technol.* **2018**, *29*, 2678–2685.

29. Lim, E. K.; Kim, T.; Paik, S.; Haam, S.; Huh, Y. M.; Lee, K. Nanomaterials for Theranostics: Recent Advances and Future Challenges. *Chem. Rev.* **2015**, *115*, 327–394.

30. Yang, J.; Lee, C. H.; Ko, H. J.; Suh, J. S.; Yoon, H. G.; Lee, K.; Huh, Y. M.; Haam, S. Multifunctional Magneto-Polymeric Nanohybrids for Targeted Detection and Synergistic Therapeutic Effects on Breast Cancer. *Angew. Chemie - Int. Ed.* **2007**, *46*, 8836–8839.

31. Lin, L. Sen; Yang, X.; Zhou, Z.; Yang, Z.; Jacobson, O.; Liu, Y.; Yang, A.; Niu, G.; Song, J.; Yang, H. H.; et al. Yolk–Shell Nanostructure: An Ideal Architecture to Achieve Harmonious Integration of Magnetic–Plasmonic Hybrid Theranostic Platform. *Adv. Mater.* **2017**, *29*.

32. Xu, W.; Wang, D.; Li, D.; Liu, C. C. Recent Developments of Electrochemical and Optical Biosensors for Antibody Detection. *Int. J. Mol. Sci.* **2020**, *21*.

33. Damborský, P.; Švitel, J.; Katrlík, J. Optical Biosensors. *Essays Biochem.* **2016**, *60*, 91–100.

34. Ghaffari, R.; Choi, J.; Raj, M. S.; Chen, S.; Lee, S. P.; Reeder, J. T.; Aranyosi, A. J.; Leech, A.; Li, W.; Schon, S.; et al. Soft Wearable Systems for Colorimetric and Electrochemical Analysis of Biofluids. *Adv. Funct. Mater.* **2019**, *1907269*, 1–10.

35. Sabela, M.; Balme, S.; Bechelany, M.; Janot, J. M.; Bisetty, K. A Review of Gold and Silver Nanoparticle-Based Colorimetric Sensing Assays. *Adv. Eng. Mater.* **2017**, *19*, 1–24.

36. Tang, L.; Li, J. Plasmon-Based Colorimetric Nanosensors for Ultrasensitive Molecular Diagnostics. *ACS Sensors* **2017**, *2*, 857–875.

37. Chen, L. Y.; Wang, C. W.; Yuan, Z.; Chang, H. T. Fluorescent Gold Nanoclusters: Recent Advances in Sensing and Imaging. *Anal. Chem.* **2015**, *87*, 216–229.

38. Li, H.; Mu, Y.; Lu, J.; Wei, W.; Wan, Y.; Liu, S. Target-Cell-Specific Fluorescence Silica Nanoprobes for Imaging and Theranostics of Cancer Cells. *Anal. Chem.* **2014**, *86*, 3602–3609.

39. Chambre, L.; Degirmenci, A.; Sanyal, R.; Sanyal, A. Multi-Functional Nanogels as Theranostic Platforms: Exploiting Reversible and Nonreversible Linkages for Targeting, Imaging, and Drug Delivery. *Bioconjug. Chem.* **2018**, *29*, 1885–1896.

40. Feng, G.; Liu, B. Aggregation-Induced Emission (AIE) Dots: Emerging Theranostic Nanolights. *Acc. Chem. Res.* **2018**, *51*, 1404–1414.

41. Vanden-Hehir, S.; Cairns, S. A.; Lee, M.; Zoupi, L.; Shaver, M. P.; Brunton, V. G.; Williams, A.; Hulme, A. N. Alkyne-Tagged PLGA Allows Direct Visualization of Nanoparticles in Vitro and Ex Vivo by Stimulated Raman Scattering Microscopy. *Biomacromolecules* **2019**, *20*, 4008–4014.

42. Huang, Z.; Zhang, A.; Zhang, Q.; Cui, D. Nanomaterial-Based SERS Sensing Technology for Biomedical Application. *J. Mater. Chem. B* **2019**, *7*, 3755–3774.

43. Wang, J.; Liang, D.; Jin, Q.; Feng, J.; Tang, X. Bioorthogonal SERS Nanotags as a Precision Theranostic Platform for in Vivo SERS Imaging and Cancer Photothermal Therapy . *Bioconjug. Chem.* **2020**.

44. Zhu, M.; Lu, D.; Wu, S.; Lian, Q.; Wang, W.; Milani, A. H.; Cui, Z.; Nguyen, N. T.; Chen, M.; Lyon, L. A.; et al. Responsive Nanogel Probe for Ratiometric Fluorescent Sensing of PH and Strain in Hydrogels. *ACS Macro Lett.* **2017**, *6*, 1245–1250.

45. Wang, D.; Liu, T.; Yin, J.; Liu, S. Stimuli-Responsive Fluorescent Poly(N-Isopropylacrylamide) Microgels Labeled with Phenylboronic Acid Moieties as Multifunctional Ratiometric Probes for Glucose and Temperatures. *Macromolecules* **2011**, *44*, 2282–2290.

46. Nam, J.; Won, N.; Jin, H.; Chung, H.; Kim, S. PH-Induced Aggregation of Gold Nanoparticles for Photothermal Cancer Therapy. *J. Am. Chem. Soc.* **2009**, *131*, 13639–13645.

47. Peng, H. S.; Stolwijk, J. A.; Sun, L. N.; Wegener, J.; Wolfbeis, O. S. A Nanogel for Ratiometric Fluorescent Sensing of Intracellular PH Values. *Angew. Chemie - Int. Ed.* **2010**, *49*, 4246–4249.

48. Tang, L.; Li, J. Plasmon-Based Colorimetric Nanosensors for Ultrasensitive Molecular Diagnostics. *ACS Sensors* **2017**, *2*, 857–875.

49. Szunerits, S.; Boukherroub, R. Sensing Using Localised Surface Plasmon Resonance Sensors. *Chem. Commun.* **2012**, *48*, 8999–9010.

50. Mirkin, C. A.; Letsinger, R. L.; Mucic, R. C.; Storhoff, J. J. A DNA-Based Method for Rationally Assembling Nanoparticles into Macroscopic Materials. *Nature* **1996**, *382*, 607–609.

51. Ghosh, S. K.; Pal, T. Interparticle Coupling Effect on the Surface Plasmon Resonance of Gold Nanoparticles: From Theory to Applications. *Chem. Rev.* **2007**, *107*, 4797–4862.

52. Jazayeri, M. H.; Aghaie, T.; Avan, A.; Vatankhah, A.; Ghaffari, M. R. S. Colorimetric Detection Based on Gold Nano Particles (GNPs): An Easy, Fast, Inexpensive, Low-Cost and Short Time Method in Detection of Analytes (Protein, DNA, and Ion). *Sens. Bio-Sensing Res.* **2018**, *20,* 1–8.

53. Li, H.; Rothberg, L. Colorimetric Detection of DNA Sequences Based on Electrostatic Interactions with Unmodified Gold Nanoparticles. *Proc. Natl. Acad. Sci. U. S. A.* **2004**, *101,* 14036–14039.

54. Piriya V.S, A.; Joseph, P.; Daniel S.C.G., K.; Lakshmanan, S.; Kinoshita, T.; Muthusamy, S. Colorimetric Sensors for Rapid Detection of Various Analytes. *Mater. Sci. Eng. C* **2017**, *78,* 1231–1245.

55. Choe, A.; Yeom, J.; Shanker, R.; Kim, M. P.; Kang, S.; Ko, H. Stretchable and Wearable Colorimetric Patches Based on Thermoresponsive Plasmonic Microgels Embedded in a Hydrogel Film. *NPG Asia Mater.* **2018**, *10,* 912–922.

56. Rosi, N. L.; Mirkin, C. A. Nanostructures in Biodiagnostics. *Chem. Rev.* **2005**, *105,* 1547–1562.

57. Bujalowski, W. M. *Spectroscopic Methods of Analysis*; Humana Press, **2012**.

58. Li, C.; Liu, S. Polymeric Assemblies and Nanoparticles with Stimuli-Responsive Fluorescence Emission Characteristics. *Chem. Commun.* **2012**, *48,* 3262–3278.

59. Dennis, A. M.; Rhee, W. J.; Sotto, D.; Dublin, S. N.; Bao, G. Quantum Dot-Fluorescent Protein Fret Probes for Sensing Intracellular PH. *ACS Nano* **2012**, *6,* 2917–2924.

60. Dulkeith, E.; Ringler, M.; Klar, T. A.; Feldmann, J.; Javier, A. M.; Parak, W. J. Gold Nanoparticles Quench Fluorescence by Phase Induced Radiative Rate Suppression. *Nano Lett.* **2005**, *5,* 585–589.

61. Anger, P.; Bharadwaj, P.; Novotny, L. Enhancement and Quenching of Single-Molecule Fluorescence. *Phys. Rev. Lett.* **2006**, *96,* 3–6.

62. Kang, K. A.; Wang, J.; Jasinski, J. B.; Achilefu, S. Fluorescence Manipulation by Gold Nanoparticles: From Complete Quenching to Extensive Enhancement. *J. Nanobiotechnol.* **2011**, *9,* 1–13.

63. Lin, Z.; Zhang, G.; Yang, W.; Qiu, B.; Chen, G. CEA Fluorescence Biosensor Based on the FRET between Polymer Dots and Au Nanoparticles. *Chem. Commun.* **2012**, *48,* 9918–9920.

64. Li, M.; Cushing, S. K.; Wang, Q.; Shi, X.; Hornak, L. A.; Hong, Z.; Wu, N. Size-Dependent Energy Transfer between CdSe/ZnS Quantum Dots and Gold Nanoparticles. *J. Phys. Chem. Lett.* **2011**, *2,* 2125–2129.

65. Samanta, A.; Zhou, Y.; Zou, S.; Yan, H.; Liu, Y. Fluorescence Quenching of Quantum Dots by Gold Nanoparticles: A Potential Long Range Spectroscopic Ruler. *Nano Lett.* **2014**, *14,* 5052–5057.

66. Acuna, G. P.; Bucher, M.; Stein, I. H.; Steinhauer, C.; Kuzyk, A.; Holzmeister, P.; Schreiber, R.; Moroz, A.; Stefani, F. D.; Liedl, T.; et al. Distance Dependence of Single-Fluorophore Quenching by Gold Nanoparticles Studied on DNA Origami. *ACS Nano* **2012**, *6*, 3189–3195.

67. Griffin, J.; Singh, A. K.; Senapati, D.; Rhodes, P.; Mitchell, K.; Robinson, B.; Yu, E.; Ray, P. C. Size- and Distance-Dependent Nanoparticle Surface-Energy Transfer (NSET) Method for Selective Sensing of Hepatitis C Virus RNA. *Chem. - A Eur. J.* **2009**, *15*, 342–351.

68. Oishi, M.; Tamura, A.; Nakamura, T.; Nagasaki, Y. A Smart Nanoprobe Based on Fluorescence-Quenching PEGylated Nanogels Containing Gold Nanopartlcles for Monitoring the Response to Cancer Therapy. *Adv. Funct. Mater.* **2009**, *19*, 827–834.

69. Carnevale, K. J. F.; Riskowski, R. A.; Strouse, G. F. A Gold Nanoparticle Bio-Optical Transponder to Dynamically Monitor Intracellular PH. *ACS Nano* **2018**, *12*, 5956–5968.

70. Park, S. Y.; Lee, S. M.; Kim, G. B.; Kim, Y. P. Gold Nanoparticle-Based Fluorescence Quenching via Metal Coordination for Assaying Protease Activity. *Gold Bull.* **2012**, *45*, 213–219.

71. Saunders, J. M.; Tong, T.; Le Maitre, C. L.; Freemont, T. J.; Saunders, B. R. A Study of PH-Responsive Microgel Dispersions: From Fluid-to-Gel Transitions to Mechanical Property Restoration for Load-Bearing Tissue. *Soft Matter* **2007**, *3*, 486–494.

72. Milani, A. H.; Freemont, A. J.; Hoyland, J. A.; Adlam, D. J.; Saunders, B. R. Injectable Doubly Cross-Linked Microgels for Improving the Mechanical Properties of Degenerated Intervertebral Discs. *Biomacromolecules* **2012**, *13*, 2793–2801.

73. Jones, C. D.; McGrath, J. G.; Lyon, L. A. Characterization of Cyanine Dye-Labeled Poly(N-Isopropylacrylamide) Core/Shell Microgels Using Fluorescence Resonance Energy Transfer. *J. Phys. Chem. B* **2004**, *108*, 12652–12657.

74. Lei, J.; Wang, L.; Zhang, J. Ratiometric PH Sensor Based on Mesoporous Silica Nanoparticles and Förster Resonance Energy Transfer. *Chem. Commun.* **2010**, *46*, 8445–8447.

75. Shanks, H. R.; Milani, A. H.; Lu, D.; Saunders, B. R.; Carney, L.; Adlam, D. J.; Hoyland, J. A.; Blount, C.; Dickinson, M. Core-Shell-Shell Nanoparticles for NIR Fluorescence Imaging and NRET Swelling Reporting of Injectable or Implantable Gels. *Biomacromolecules* **2019**, *20*, 2694–2702.

76. Wang, H.; Zhang, P.; Hong, Y.; Zhao, B.; Yi, P.; Chen, J. Ratiometric Imaging of Lysosomal Hypochlorous Acid Enabled by FRET-Based Polymer Dots. *Polym. Chem.* **2017**, *8*, 5795–5802.

77. Tang, J.; Kong, B.; Wu, H.; Xu, M.; Wang, Y.; Wang, Y.; Zhao, D.; Zheng, G. Carbon Nanodots Featuring Efficient FRET for Real-Time Monitoring of Drug Delivery and Two-Photon Imaging. *Adv. Mater.* **2013**, *25*, 6569–6574.

78. Wei, W.; Xu, C.; Ren, J.; Xu, B.; Qu, X. Sensing Metal Ions with Ion Selectivity of a Crown Ether and Fluorescence Resonance Energy Transfer between Carbon Dots and Graphene. *Chem. Commun.* **2012**, *48*, 1284–1286.

79. Tokarev, I.; Tokareva, I.; Gopishetty, V.; Katz, E.; Minko, S. Specific Biochemical-to-Optical Signal Transduction by Responsive Thin Hydrogel Films Loaded with Noble Metal Nanoparticles. *Adv. Mater.* **2010**, *22*, 1412–1416.

80. Li, L.; Hutter, T.; Li, W.; Mahajan, S. Single Nanoparticle-Based Heteronanojunction as a Plasmon Ruler for Measuring Dielectric Thin Films. *J. Phys. Chem. Lett.* **2015**, *6*, 2282–2286.

81. Yang, X.; Yang, M.; Pang, B.; Vara, M.; Xia, Y. Gold Nanomaterials at Work in Biomedicine. *Chem. Rev.* **2015**, *115*, 10410–10488.

82. Huang, J. Y.; Lin, H. T.; Chen, T. H.; Chen, C. A.; Chang, H. T.; Chen, C. F. Signal Amplified Gold Nanoparticles for Cancer Diagnosis on Paper-Based Analytical Devices. *ACS Sensors* **2018**, *3*, 174–182.

83. Alkilany, A. M.; Murphy, C. J. Toxicity and Cellular Uptake of Gold Nanoparticles: What We Have Learned so Far? *J. Nanoparticle Res.* **2010**, *12*, 2313–2333.

84. Dreaden, E. C.; Alkilany, A. M.; Huang, X.; Murphy, C. J.; El-Sayed, M. A. The Golden Age: Gold Nanoparticles for Biomedicine. *Chem. Soc. Rev.* **2012**, *41*, 2740–2779.

85. Connor, E. E.; Mwamuka, J.; Gole, A.; Murphy, C. J.; Wyatt, M. D. Gold Nanoparticles Are Taken up by Human Cells but Do Not Cause Acute Cytotoxicity. *Small* **2005**, *1*, 325–327.

86. Mieszawska, A. J.; Mulder, W. J. M.; Fayad, Z. A.; Cormode, D. P. Multifunctional Gold Nanoparticles for Diagnosis and Therapy of Disease. *Mol. Pharm.* **2013**, *10*, 831–847.

87. Mayer, K. M.; Hafner, J. H. Localized Surface Plasmon Resonance Sensors. *Chem. Rev.* **2011**, *111*, 3828–3857.

88. Pellegrotti, J. V.; Acuna, G. P.; Puchkova, A.; Holzmeister, P.; Gietl, A.; Lalkens, B.; Stefani, F. D.; Tinnefeld, P. Controlled Reduction of Photobleaching in DNA Origami-Gold Nanoparticle Hybrids. *Nano Lett.* **2014**, *14*, 2831–2836.

89. He, H.; Xie, C.; Ren, J. Nonbleaching Fluorescence of Gold Nanoparticles and Its Applications in Cancer Cell Imaging. *Anal. Chem.* **2008**, *80*, 5951–5957.

90. Song, Y.; Wei, W.; Qu, X. Colorimetric Biosensing Using Smart Materials. *Adv. Mater.* **2011**, *23*, 4215–4236.

91. Reineck, P.; Gómez, D.; Ng, S. H.; Karg, M.; Bell, T.; Mulvaney, P.; Bach, U. Distance and Wavelength Dependent Quenching of Molecular Fluorescence by Au@SiO2 Core-Shell Nanoparticles. *ACS Nano* **2013**, *7*, 6636–6648.

92. Li, J. F.; Zhang, Y. J.; Ding, S. Y.; Panneerselvam, R.; Tian, Z. Q. Core-Shell Nanoparticle-Enhanced Raman Spectroscopy. *Chem. Rev.* **2017**, *117*, 5002–5069.

93. Wu, Y.; Ali, M. R. K.; Chen, K.; Fang, N.; El-Sayed, M. A. Gold Nanoparticles in Biological Optical Imaging. *Nano Today* **2019**, *24*, 120–140.

94. Huang, X.; El-Sayed, I. H.; Qian, W.; El-Sayed, M. A. Cancer Cell Imaging and Photothermal Therapy in the Near-Infrared Region by Using Gold Nanorods. *J. Am. Chem. Soc.* **2006**, *128*, 2115–2120.

95. Liang, S.; Zhao, Y.; Xu, S.; Wu, X.; Chen, J.; Wu, M.; Zhao, J. X. A Silica-Gold-Silica Nanocomposite for Photothermal Therapy in the near-Infrared Region. *ACS Appl. Mater. Interfaces* **2015**, *7*, 85–93.

96. Sperling, R. A.; Parak, W. J. Surface Modification, Functionalization and Bioconjugation of Colloidal Inorganic Nanoparticles. *Philos. Trans. R. Soc. A Math. Phys. Eng. Sci.* **2010**, *368*, 1333–1383.

97. Zhang, Y.; Cui, X.; Shi, F.; Deng, Y. Nano-Gold Catalysis in Fine Chemical Synthesis. *Chem. Rev.* **2012**, *112*, 2467–2505.

98. Erwin, W. R.; Zarick, H. F.; Talbert, E. M.; Bardhan, R. Light Trapping in Mesoporous Solar Cells with Plasmonic Nanostructures. *Energy Environ. Sci.* **2016**, *9*, 1577–1601.

99. Chen, G.; Roy, I.; Yang, C.; Prasad, P. N. Nanochemistry and Nanomedicine for Nanoparticle-Based Diagnostics and Therapy. *Chem. Rev.* **2016**, *116*, 2826–2885.

100. Fox, M. *Optical Properties of Solids*; Oxford University press, **2001**.

101. Pyykko, P.; Desclaux, J. P. Relativity and the Periodic System of Elements. *Acc. Chem. Res.* **1979**, *12*, 276–281.

102. Boriskina, S. V.; Cooper, T. A.; Zeng, L.; Ni, G.; Tong, J. K.; Tsurimaki, Y.; Huang, Y.; Meroueh, L.; Mahan, G.; Chen, G. Losses in Plasmonics: From Mitigating Energy Dissipation to Embracing Loss-Enabled Functionalities. *Adv. Opt. Photonics* **2017**, *9*, 775.

103. Faraday, M. X. The Bakerian Lecture. —Experimental Relations of Gold (and Other Metals) to Light. *Philos. Trans. R. Soc. London* **1857**, *147*, 145–181.

104. Mie, G. Beiträge Zur Optik Trüber Medien, Speziell Kolloidaler Metallösungen. *Ann. Phys.* **1908**, *330*, 377–445.

105. Petryayeva, E.; Krull, U. J. Localized Surface Plasmon Resonance: Nanostructures, Bioassays and Biosensing-A Review. *Anal. Chim. Acta* **2011**, *706*, 8–24.

106. Xia, Y.; Halas, N. J. Shape-Controlled Synthesis and Surface Plasmonic Properties of Metallic Nanostructures. *MRS Bull.* **2005**, *30*, 338–348.

107. Ajdari, N.; Vyas, C.; Bogan, S. L.; Lwaleed, B. A.; Cousins, B. G. Gold Nanoparticle Interactions in Human Blood: A Model Evaluation. *Nanomedicine (N. Y., NY, U. S.)* **2017**, *13*, 1531–1542.

108. Juan, M. L.; Righini, M.; Quidant, R. Plasmon Nano-Optical Tweezers. *Nat. Photonics* **2011**, *5*, 349–356.

109. Link, S.; El-Sayed, M. A. Spectral Properties and Relaxation Dynamics of Surface Plasmon Electronic Oscillations in Gold and Silver Nanodots and Nanorods. *J. Phys. Chem. B* **1999**, *103*, 8410–8426.

110. Wang, S. H.; Lee, C. W.; Chiou, A.; Wei, P. K. Size-Dependent Endocytosis of Gold Nanoparticles Studied by Three-Dimensional Mapping of Plasmonic Scattering Images. *J. Nanobiotechnol.* **2010**, *8*, 1–13.

111. Senut, M. C.; Zhang, Y.; Liu, F.; Sen, A.; Ruden, D. M.; Mao, G. Size-Dependent Toxicity of Gold Nanoparticles on Human Embryonic Stem Cells and Their Neural Derivatives. *Small* **2016**, *12*, 631–646.

112. Sonavane, G.; Tomoda, K.; Makino, K. Biodistribution of Colloidal Gold Nanoparticles after Intravenous Administration: Effect of Particle Size. *Colloids Surf., B* **2008**, *66*, 274–280.

113. Jain, P. K.; Lee, K. S.; El-Sayed, I. H.; El-Sayed, M. A. Calculated Absorption and Scattering Properties of Gold Nanoparticles of Different Size, Shape, and Composition: Applications in Biological Imaging and Biomedicine. *J. Phys. Chem. B* **2006**, *110*, 7238–7248.

114. Li, M.; Cushing, S. K.; Wu, N. Plasmon-Enhanced Optical Sensors: A Review. *Analyst* **2015**, *140*, 386–406.

115. Johnson, P. B.; Christy, R. W. Optical Constants of the Noble Metals. *Phys. Rev. B* **1972**, *6*, 4370–4379.

116. Willets, K. A.; Van Duyne, R. P. Localized Surface Plasmon Resonance Spectroscopy and Sensing. *Annu. Rev. Phys. Chem.* **2007**, *58*, 267–297.

117. Huang, X.; El-Sayed, M. A. Gold Nanoparticles: Optical Properties and Implementations in Cancer Diagnosis and Photothermal Therapy. *J. Adv. Res.* **2010**, *1*, 13–28.

118. Koh, A. L.; Bao, K.; Khan, I.; Smith, W. E.; Kothleitner, G.; Nordlander, P.; Maier, S. A.; Mccomb, D. W. Electron Energy-Loss Spectroscopy (EELS) of Surface Plasmons in Single Silver Nanoparticles and Dimers: Influence of Beam Damage and Mapping of Dark Modes. *ACS Nano* **2009**, *3*, 3015–3022.

119. Scholl, J. A.; Koh, A. L.; Dionne, J. A. Quantum Plasmon Resonances of Individual Metallic Nanoparticles. *Nature* **2012**, *483*, 421–427.

120. Bernasconi, G. D.; Butet, J. my; Flauraud, V.; Alexander, D.; Brugger, J.; Martin, O. J. F. Where Does Energy Go in Electron Energy Loss Spectroscopy of Nanostructures? *ACS Photonics* **2017**, *4*, 156–164.

121. Nelayah, J.; Kociak, M.; Stéphan, O.; De Abajo, F. J. G.; Tencé, M.; Henrard, L.; Taverna, D.; Pastoriza-Santos, I.; Liz-Marzán, L. M.; Colliex, C. Mapping Surface Plasmons on a Single Metallic Nanoparticle. *Nat. Phys.* **2007**, *3*, 348–353.

122. Zhan, C.; Chen, X. J.; Yi, J.; Li, J. F.; Wu, D. Y.; Tian, Z. Q. From Plasmon-Enhanced Molecular Spectroscopy to Plasmon-Mediated Chemical Reactions. *Nat. Rev. Chem.* **2018**, *2*, 216–230.

123. Yockell-Lelièvre, H.; Lussier, F.; Masson, J. F. Influence of the Particle Shape and Density of Self-Assembled Gold Nanoparticle Sensors on LSPR and SERS. *J. Phys. Chem. C* **2015**, *119*, 28577–28585.

124. Chen, J.; Jin, Y.; Fahruddin, N.; Zhao, J. X. Development of Gold Nanoparticle-Enhanced Fluorescent Nanocomposites. *Langmuir* **2013**, *29*, 1584–1591.

125. Jain, P. K.; Huang, X.; El-Sayed, I. H.; El-Sayed, M. A. Noble Metals on the Nanoscale: Optical and Photothermal Properties and Some Applications in Imaging, Sensing, Biology, and Medicine. *Acc. Chem. Res.* **2008**, *41*, 1578–1586.

126. Templeton, A. C.; Pietron, J. J.; Murray, R. W.; Mulvaney, P. Solvent Refractive Index and Core Charge Influences on the Surface Plasmon Absorbance of Alkanethiolate Monolayer-Protected Gold Clusters. *J. Phys. Chem. B* **2000**, *104*, 564–570.

127. Ghosh, S. K.; Nath, S.; Kundu, S.; Esumi, K.; Pal, T. Solvent and Ligand Effects on the Localized Surface Plasmon Resonance (LSPR) of Gold Colloids. *J. Phys. Chem. B* **2004**, *108*, 13963–13971.

128. Turkevich, J.; Stevenson, P. C.; Hillier, J. A Study of the Nucleation and Growth Processes in the Synthesis of Colloidal Gold. *Discuss. Faraday Soc.* **1951**, *11*, 55–75.

129. Enüstün, B. V.; Turkevich, J. Coagulation of Colloidal Gold. *J. Am. Chem. Soc.* **1963**, *85*, 3317–3328.

130. Biggs, S.; Mulvaney, P.; Zukoski, C. F.; Grieser, F. Study of Anion Adsorption at the Gold-Aqueous Solution Interface by Atomic Force Microscopy. *J. Am. Chem. Soc.* **1994**, *116*, 9150–9157.

131. Park, J. W.; Shumaker-Parry, J. S. Strong Resistance of Citrate Anions on Metal Nanoparticles to Desorption under Thiol Functionalization. *ACS Nano* **2015**, *9*, 1665–1682.

132. Park, J. W.; Shumaker-Parry, J. S. Structural Study of Citrate Layers on Gold Nanoparticles: Role of Intermolecular Interactions in Stabilizing Nanoparticles. *J. Am. Chem. Soc.* **2014**, *136*, 1907–1921.

133. Al-Johani, H.; Abou-Hamad, E.; Jedidi, A.; Widdifield, C. M.; Viger-Gravel, J.; Sangaru, S. S.; Gajan, D.; Anjum, D. H.; Ould-Chikh, S.; Hedhili, M. N.; et al. The Structure and Binding Mode of Citrate in the Stabilization of Gold Nanoparticles. *Nat. Chem.* **2017**, *9*, 890–895.

134. Curry, D.; Cameron, A.; MacDonald, B.; Nganou, C.; Scheller, H.; Marsh, J.; Beale, S.; Lu, M.; Shan, Z.; Kaliaperumal, R.; et al. Adsorption of Doxorubicin on Citrate-Capped Gold Nanoparticles: Insights into Engineering Potent Chemotherapeutic Delivery Systems. *Nanoscale* **2015**, *7*, 19611–19619.

135. FRENS, G. Controlled Nucleation for the Regulation of the Particle Size in Monodisperse Gold Suspensions. *Nat. Phys. Sci.* **1973**, *241*, 20–22.

136. Ji, X.; Song, X.; Li, J.; Bai, Y.; Yang, W.; Peng, X. Size Control of Gold Nanocrystals in Citrate Reduction: The Third Role of Citrate. *J. Am. Chem. Soc.* **2007**, *129*, 13939–13948.

137. Polte, J.; Ahner, T. T.; Delissen, F.; Sokolov, S.; Emmerling, F.; Thünemann, A. F.; Kraehnert, R. Mechanism of Gold Nanoparticle Formation in the Classical Citrate Synthesis Method Derived from Coupled in Situ XANES and SAXS Evaluation. *J. Am. Chem. Soc.* **2010**, *132*, 1296–1301.

138. Thanh, N. T. K.; Maclean, N.; Mahiddine, S. Mechanisms of Nucleation and Growth of Nanoparticles in Solution. *Chem. Rev.* **2014**, *114*, 7610–7630.

139. Ghosh Chaudhuri, R.; Paria, S. Core/Shell Nanoparticles: Classes, Properties, Synthesis Mechanisms, Characterization, and Applications. *Chem. Rev.* **2012**, *112*, 2373–2433.

140. Chen, Y.-S.; Frey, W.; Kim, S.; Homan, K.; Kruizinga, P.; Sokolov, K.; Emelianov, S. Enhanced Thermal Stability of Silica-Coated Gold Nanorods for Photoacoustic Imaging and Image-Guided Therapy. *Opt. Express* **2010**, *18*, 8867.

141. Liz-Marzán, L. M.; Giersig, M.; Mulvaney, P. Synthesis of Nanosized Gold−Silica Core−Shell Particles. *Langmuir* **1996**, *12*, 4329–4335.

142. Wu, C.; Xu, Q.-H. Stable and Functionable Mesoporous Silica-Coated Gold Nanorods as Sensitive Localized Surface Plasmon Resonance (LSPR) Nanosensors. *Langmuir* **2009**, *25*, 9441–9446.

143. Kim, D. J.; Kang, S. M.; Kong, B.; Kim, W.-J.; Paik, H.; Choi, H.; Choi, I. S. Formation of Thermoresponsive Gold Nanoparticle/PNIPAAm Hybrids by Surface-Initiated, Atom Transfer Radical Polymerization in Aqueous Media. *Macromol. Chem. Phys.* **2005**, *206*, 1941–1946.

144. Fernández-López, C.; Pérez-Balado, C.; Pérez-Juste, J.; Pastoriza-Santos, I.; de Lera, Á. R.; Liz-Marzán, L. M. A General LbL Strategy for the Growth of PNIPAM Microgels on Au Nanoparticles with Arbitrary Shapes. *Soft Matter* **2012**, *8*, 4165–4170.

145. Cayre, O. J.; Chagneux, N.; Biggs, S. Stimulus Responsive Core-Shell Nanoparticles: Synthesis and Applications of Polymer Based Aqueous Systems. *Soft Matter* **2011**, *7*, 2211–2234.

146. Li, G. L.; Möhwald, H.; Shchukin, D. G. Precipitation Polymerization for Fabrication of Complex Core-Shell Hybrid Particles and Hollow Structures. *Chem. Soc. Rev.* **2013**, *42*, 3628–3646.

147. Contreras-Cáceres, R.; Pacifico, J.; Pastoriza-Santos, I.; Pérez-Juste, J.; Fernández-Barbero, A.; Liz-Marzán, L. M. Au@pNIPAM Thermosensitive Nanostructures: Control over Shell Cross-Linking, Overall Dimensions, and Core Growth. *Adv. Funct. Mater.* **2009**, *19*, 3070–3076.

148. Contreras-Cáceres, R.; Sánchez-Iglesias, A.; Karg, M.; Pastoriza-Santos, I.; Pérez-Juste, J.; Pacifico, J.; Hellweg, T.; Fernández-Barbero, A.; Liz-Marzán, L. M. Encapsulation and Growth of Gold Nanoparticles in Thermoresponsive Microgels. *Adv. Mater.* **2008**, *20*, 1666–1670.

149. Rauh, A.; Honold, T.; Karg, M. Seeded Precipitation Polymerization for the Synthesis of Gold-Hydrogel Core-Shell Particles: The Role of Surface Functionalization and Seed Concentration. *Colloid Polym. Sci.* **2016**, *294*, 37–47.

150. Karg, M.; Jaber, S.; Hellweg, T.; Mulvaney, P. Surface Plasmon Spectroscopy of Gold-Poly-N-Isopropylacrylamide Core-Shell Particles. *Langmuir* **2011**, *27*, 820–827.

151. Dulle, M.; Jaber, S.; Rosenfeldt, S.; Radulescu, A.; Förster, S.; Mulvaney, P.; Karg, M. Plasmonic Gold-Poly(N-Isopropylacrylamide) Core-Shell Colloids with Homogeneous Density Profiles: A Small Angle Scattering Study. *Phys. Chem. Chem. Phys.* **2015**, *17*, 1354–1367.

152. Thanh, N. T. K.; Green, L. A. W. Functionalisation of Nanoparticles for Biomedical Applications. *Nano Today* **2010**, *5*, 213–230.

153. Guarrotxena, N.; Quijada-Garrido, I. Optical and Swelling Stimuli-Response of Functional Hybrid Nanogels: Feasible Route to Achieve Tunable Smart Core@Shell Plasmonic@Polymer Nanomaterials. *Chem. Mater.* **2016**, *28*, 1402–1412.

154. Saunders, B. R.; Vincent, B. Microgel Particles as Model Colloids: Theory, Properties and Applications. *Adv. Colloid Interface Sci.* **1999**, *80*, 1–25.

155. Lyon, L. A.; Meng, Z.; Singh, N.; Sorrell, C. D.; St. John, A. Thermoresponsive Microgel-Based Materials. *Chem. Soc. Rev.* **2009**, *38*, 865–874.

156. Lyon, L. A.; Fernandez-Nieves, A. The Polymer/Colloid Duality of Microgel Suspensions. *Annu. Rev. Phys. Chem.* **2012**, *63*, 25–43.

157. Baker, W. O. Microgel, A New Macromolecule. *Ind. Eng. Chem.* **1949**, *41*, 511–520.

158. Saunders, B. R.; Crowther, H. M.; Morris, G. E.; Mears, S. J.; Cosgrove, T.; Vincent, B. Factors Affecting the Swelling of Poly(N-Isopropylacrylamide) Microgel Particles: Fundamental and Commercial Implications. *Colloids Surf., A* **1999**, *149*, 57–64.

159. Dalmont, H.; Pinprayoon, O.; Saunders, B. R. Study of PH-Responsive Microgels Containing Methacrylic Acid: Effects of Particle Composition and Added Calcium. *Langmuir* **2008**, *24*, 2834–2840.

160. Pinprayoon, O.; Groves, R.; Saunders, B. R. A Study of Poly(Butadiene/Methacrylic Acid) Dispersions: From PH-Responsive Behaviour to the Effects of Added Ca2+. *J. Colloid Interface Sci.* **2008**, *321*, 315–322.

161. Gnan, N.; Rovigatti, L.; Bergman, M.; Zaccarelli, E. In Silico Synthesis of Microgel Particles. *Macromolecules* **2017**, *50*, 8777–8786.

162. Shi, S.; Wang, Q.; Wang, T.; Ren, S.; Gao, Y.; Wang, N. Thermo-, PH-, and Light-Responsive Poly(N -Isopropylacrylamide- Co -Methacrylic Acid)-Au Hybrid Microgels Prepared by the in Situ Reduction Method Based on Au-Thiol Chemistry. *J. Phys. Chem. B* **2014**, *118*, 7177–7186.

163. Klinger, D.; Landfester, K. Stimuli-Responsive Microgels for the Loading and Release of Functional Compounds: Fundamental Concepts and Applications. *Polymer (Guildf).* **2012**, *53*, 5209–5231.

164. Hoare, T.; Pelton, R. Highly PH and Temperature Responsive Microgels Functionalized with Vinylacetic Acid. *Macromolecules* **2004**, *37*, 2544–2550.

165. Karg, M.; Pich, A.; Hellweg, T.; Hoare, T.; Lyon, L. A.; Crassous, J. J.; Suzuki, D.; Gumerov, R. A.; Schneider, S.; Potemkin, I. I.; et al. Nanogels and Microgels: From Model Colloids to Applications, Recent Developments, and Future Trends. *Langmuir* **2019**, *35*, 6231–6255.

166. Plamper, F. A.; Richtering, W. Functional Microgels and Microgel Systems. *Acc. Chem. Res.* **2017**, *50*, 131–140.

167. Naseem, K.; Hussain Farooqi, Z.; Zia Ur Rehman, M.; Atiq Ur Rehman, M.; Ghufran, M. Microgels as Efficient Adsorbents for the Removal of Pollutants from Aqueous Medium. *Rev. Chem. Eng.* **2019**, *35*, 285–309.

168. Dickinson, E. Microgels - An Alternative Colloidal Ingredient for Stabilization of Food Emulsions. *Trends Food Sci. Technol.* **2015**, *43*, 178–188.

169. Saunders, B. R.; Laajam, N.; Daly, E.; Teow, S.; Hu, X.; Stepto, R. Microgels: From Responsive Polymer Colloids to Biomaterials. *Adv. Colloid Interface Sci.* **2009**, *147–148*, 251–262.

170. Chen, M.; Mokhtar, M. Z.; Whittaker, E.; Lian, Q.; Hamilton, B.; O’Brien, P.; Zhu, M.; Cui, Z.; Haque, S. A.; Saunders, B. R. Reducing Hole Transporter Use and Increasing Perovskite Solar Cell Stability with Dual-Role Polystyrene Microgel Particles. *Nanoscale* **2017**, *9*, 10126–10137.

171. Ekkelenkamp, A. E.; Elzes, M. R.; Engbersen, J. F. J.; Paulusse, J. M. J. Responsive Crosslinked Polymer Nanogels for Imaging and Therapeutics Delivery. *J. Mater. Chem. B* **2018**, *6*, 210–235.

172. Newsom, J. P.; Payne, K. A.; Krebs, M. D. Microgels: Modular, Tunable Constructs for Tissue Regeneration. *Acta Biomater.* **2019**, *88,* 32–41.

173. Jiang, W.; Li, M.; Chen, Z.; Leong, K. W. Cell-Laden Microfluidic Microgels for Tissue Regeneration. *Lab Chip* **2016**, *16*, 4482–4506.

174. Smith, M. H.; South, A. B.; Lyon, L. A. Microgels and Biological Interactions. *Hydrogel Micro and Nanoparticles* **2012**, 209–235.

175. Gu, Z.; Dang, T. T.; Ma, M.; Tang, B. C.; Cheng, H.; Jiang, S.; Dong, Y.; Zhang, Y.; Anderson, D. G. Glucose-Responsive Microgels Integrated with Enzyme Nanocapsules for Closed-Loop Insulin Delivery. *ACS Nano* **2013**, *7*, 6758–6766.

176. Das, M.; Mardyani, S.; Chan, W. C. W.; Kumacheva, E. Biofunctionalized PH-Responsive Microgels for Cancer Cell Targeting: Rational Design. *Adv. Mater.* **2006**, *18*, 80–83.

177. Thaiboonrod, S.; Milani, A. H.; Saunders, B. R. Doubly Crosslinked Poly(Vinyl Amine) Microgels: Hydrogels of Covalently Inter-Linked Cationic Microgel Particles. *J. Mater. Chem. B* **2014**, *2*, 110–119.

178. Liu, R.; Milani, A. H.; Freemont, T. J.; Saunders, B. R. Doubly Crosslinked PH-Responsive Microgels Prepared by Particle Inter-Penetration: Swelling and Mechanical Properties. *Soft Matter* **2011**, *7*, 4696–4704.

179. Cui, Z.; Wang, W.; Obeng, M.; Chen, M.; Wu, S.; Kinloch, I.; Saunders, B. R. Using Intra-Microgel Crosslinking to Control the Mechanical Properties of Doubly Crosslinked Microgels. *Soft Matter* **2016**, *12*, 6985–6994.

180. Milani, A. H.; Bramhill, J.; Freemont, A. J.; Saunders, B. R. Swelling and Mechanical Properties of Hydrogels Composed of Binary Blends of Inter-Linked PH-Responsive Microgel Particles. *Soft Matter* **2015**, *11*, 2586–2595.

181. Milani, A. H.; Saunders, J. M.; Nguyen, N. T.; Ratcliffe, L. P. D.; Adlam, D. J.; Freemont, A. J.; Hoyland, J. A.; Armes, S. P.; Saunders, B. R. Synthesis of Polyacid Nanogels: PH-Responsive Sub-100 Nm Particles for Functionalisation and Fluorescent Hydrogel Assembly. *Soft Matter* **2017**, *13*, 1554–1560.

182. Smith, L. J.; Nerurkar, N. L.; Choi, K. S.; Harfe, B. D.; Elliott, D. M. Degeneration and Regeneration of the Intervertebral Disc: Lessons from Development. *DMM Dis. Model. Mech.* **2011**, *4*, 31–41.

183. Whatley, B. R.; Wen, X. Intervertebral Disc (IVD): Structure, Degeneration, Repair and Regeneration. *Mater. Sci. Eng. C* **2012**, *32*, 61–77.

184. Chan, S. C. W.; Gantenbein-Ritter, B. Intervertebral Disc Regeneration or Repair with Biomaterials and Stem Cell Therapy - Feasible or Fiction? *Swiss Med. Wkly.* **2012**, *142*, 1–12.

185. Wang, Q.; Chen, D. Synthesis and Characterization of a Chitosan Based Nanocomposite Injectable Hydrogel. *Carbohydr. Polym.* **2016**, *136*, 1228–1237.

186. Peroglio, M.; Grad, S.; Mortisen, D.; Sprecher, C. M.; Illien-Jünger, S.; Alini, M.; Eglin, D. Injectable Thermoreversible Hyaluronan-Based Hydrogels for Nucleus Pulposus Cell Encapsulation. *Eur. Spine J.* **2012**, *21*, 839–849.

187. Freemont, T. J.; Saunders, B. R. PH-Responsive Microgel Dispersions for Repairing Damaged Load-Bearing Soft Tissue. *Soft Matter* **2008**, *4*, 919–924.

188. Mohd Isa, I. L.; Abbah, S. A.; Kilcoyne, M.; Sakai, D.; Dockery, P.; Finn, D. P.; Pandit, A. Implantation of Hyaluronic Acid Hydrogel Prevents the Pain Phenotype in a Rat Model of Intervertebral Disc Injury. *Sci. Adv.* **2018**, *4*, 1–20.

189. Wang, W.; Lu, D.; Zhu, M.; Saunders, J. M.; Milani, A. H.; Armes, S. P.; Saunders, B. R. Highly Deformable Hydrogels Constructed by PH-Triggered Polyacid Nanoparticle Disassembly in Aqueous Dispersions. *Soft Matter* **2018**, *14*, 3510–3520.

190. Hu, J.; Kurokawa, T.; Hiwatashi, K.; Nakajima, T.; Wu, Z. L.; Liang, S. M.; Gong, J. P. Structure Optimization and Mechanical Model for Microgel-Reinforced Hydrogels with High Strength and Toughness. *Macromolecules* **2012**, *45*, 5218–5228.

191. Duan, J.; Liang, X.; Guo, J.; Zhu, K.; Zhang, L. Ultra-Stretchable and Force-Sensitive Hydrogels Reinforced with Chitosan Microspheres Embedded in Polymer Networks. *Adv. Mater.* **2016**, *28*, 8037–8044.

192. Treloar, L. R. G. The Elasticity of a Network of Long-Chain Molecules. I. *Trans. Faraday Soc.* **1943**, *39*, 36–41.

193. Smith, K. J. Rubber Elasticity. *Am. Chem. Soc. Polym. Prepr. Div. Polym. Chem.* **1984**, *25*, 898.

194. Treloar, L. R. G. Rubber Elasticity. *Contemp. Phys.* **1971**, *12*, 33–56.

195. Flory, P. J.; Rehner, J. Statistical Mechanics of Cross-Linked Polymer Networks I. Rubberlike Elasticity. *J. Chem. Phys.* **1943**, *11*, 512–520.

196. Brazel, C. S.; Rosen, S. L. *Fundamental Principles of Polymeric Materials*; Wiley, **2012**.

197. Capek, I. Nature and Properties of Ionomer Assemblies. II. *Adv. Colloid Interface Sci.* **2005**, *118*, 73–112.

198. Richtering, W.; Saunders, B. R. Gel Architectures and Their Complexity. *Soft Matter* **2014**, *10*, 3695–3702.

199. Song, Q.; Yin, Y.; Shang, L.; Wu, T.; Zhang, D.; Kong, M.; Zhao, Y.; He, Y.; Tan, S.; Guo, Y.; et al. Tumor Microenvironment Responsive Nanogel for the Combinatorial Antitumor Effect of Chemotherapy and Immunotherapy. *Nano Lett.* **2017**, *17*, 6366–6375.

200. Argentiere, S.; Blasi, L.; Morello, G.; Gigli, G. A Novel PH-Responsive Nanogel for the Controlled Uptake and Release of Hydrophobic and Cationic Solutes. *J. Phys. Chem. C* **2011**, *115*, 16347–16353.

201. Halacheva, S. S.; Adlam, D. J.; Hendow, E. K.; Freemont, T. J.; Hoyland, J.; Saunders, B. R. Injectable Biocompatible and Biodegradable PH-Responsive Hollow Particle Gels Containing Poly(Acrylic Acid): The Effect of Copolymer Composition on Gel Properties. *Biomacromolecules* **2014**, *15*, 1814–1827.

202. Yang, H.; Wang, Q.; Huang, S.; Xiao, A.; Li, F.; Gan, L.; Yang, X. Smart PH/Redox Dual-Responsive Nanogels for On-Demand Intracellular Anticancer Drug Release. *ACS Appl. Mater. Interfaces* **2016**, *8*, 7729–7738.

203. Cuggino, J. C.; Molina, M.; Wedepohl, S.; Igarzabal, C. I. A.; Calderón, M.; Gugliotta, L. M. Responsive Nanogels for Application as Smart Carriers in Endocytic PH-Triggered Drug Delivery Systems. *Eur. Polym. J.* **2016**, *78*, 14–24.

204. Gao, Y.; Ahiabu, A.; Serpe, M. J. Controlled Drug Release from the Aggregation-Disaggregation Behavior of PH-Responsive Microgels. *ACS Appl. Mater. Interfaces* **2014**, *6*, 13749–13756.

205. Ding, J.; Zhuang, X.; Xiao, C.; Cheng, Y.; Zhao, L.; He, C.; Tang, Z.; Chen, X. Preparation of Photo-Cross-Linked PH-Responsive Polypeptide Nanogels as Potential Carriers for Controlled Drug Delivery. *J. Mater. Chem.* **2011**, *21*, 11383–11391.

206. Lee, M. J.; Oh, N. M.; Oh, K. T.; Youn, Y. S.; Lee, E. S. Functional Poly(l-Lysine) Derivative Nanogels with Acidic PH-Pulsed Antitumor Drug Release Properties. *J. Pharm. Investig.* **2014**, *44*, 351–356.

207. Li, M.; Song, W.; Tang, Z.; Lv, S.; Lin, L.; Sun, H.; Li, Q.; Yang, Y.; Hong, H.; Chen, X. Nanoscaled Poly(l-Glutamic Acid)/Doxorubicin-Amphiphile Complex as PH-Responsive Drug Delivery System for Effective Treatment of Nonsmall Cell Lung Cancer. *ACS Appl. Mater. Interfaces* **2013**, *5*, 1781–1792.

208. Knipe, J. M.; Strong, L. E.; Peppas, N. A. Enzyme- and PH-Responsive Microencapsulated Nanogels for Oral Delivery of SiRNA to Induce TNF-α Knockdown in the Intestine. *Biomacromolecules* **2016**, *17*, 788–797.

209. Pikabea, A.; Villar-Álvarez, E.; Forcada, J.; Taboada, P. PH-Controlled Doxorubicin Delivery from PDEAEMA-Based Nanogels. *J. Mol. Liq.* **2018**, *266*, 321–329.

210. Aguirre, G.; Villar-Alvarez, E.; González, A.; Ramos, J.; Taboada, P.; Forcada, J. Biocompatible Stimuli-Responsive Nanogels for Controlled Antitumor Drug Delivery. *J. Polym. Sci. Part A Polym. Chem.* **2016**, *54*, 1694–1705.

211. Wu, W.; Aiello, M.; Zhou, T.; Berliner, A.; Banerjee, P.; Zhou, S. In-Situ Immobilization of Quantum Dots in Polysaccharide-Based Nanogels for Integration of Optical PH-Sensing, Tumor Cell Imaging, and Drug Delivery. *Biomaterials* **2010**, *31*, 3023–3031.

212. Flory, P. *Principle of Polymer Chemistry*; Cornell University Press, **1953**.

213. Nigro, V.; Angelini, R.; Bertoldo, M.; Ruzicka, B. Swelling Behavior in Multi-Responsive Microgels. *Colloids Surf., A* **2017**, *532*, 389–396.

214. Fernández-Nieves, A.; Fernández-Barbero, A.; Vincent, B.; De Las Nieves, F. J. Osmotic De-Swelling of Ionic Microgel Particles. *J. Chem. Phys.* **2003**, *119*, 10383–10388.

215. Hoare, T.; Pelton, R. Functionalized Microgel Swelling: Comparing Theory and Experiment. *J. Phys. Chem. B* **2007**, *111*, 11895–11906.

216. Fernández-Nieves, A.; Fernández-Barbero, A.; Vincent, B.; De Las Nieves, F. J. Charge Controlled Swelling of Microgel Particles. *Macromolecules* **2000**, *33*, 2114–2118.

217. Hirotsu, S. *Static and Time-Dependent Properties of Polymer Gels around the Volume Phase Transition*; **1994**; Vol. 47.

218. Graeme, M. *The Chemistry of Radical Polymerization*; Elsevier, **2005**.

219. Phaniendra, A.; Jestadi, D. B.; Periyasamy, L. Free Radicals: Properties, Sources, Targets, and Their Implication in Various Diseases. *Indian J. Clin. Biochem.* **2015**, *30*, 11–26.

220. Young, R. J.; Lovell, P. A. *Introduction to Polymers : Third Edition*; **2011**.

221. Shalaby, S. W.; Salz, U. *Polymers for Dental and Orthopedic Applications*; CRC Press, **2007**.

222. Atai, M.; Solhi, L.; Nodehi, A.; Mirabedini, S. M.; Kasraei, S.; Akbari, K.; Babanzadeh, S. PMMA-Grafted Nanoclay as Novel Filler for Dental Adhesives. *Dent. Mater.* **2009**, *25*, 339–347.

223. Wei, W.; Abdullayev, E.; Hollister, A.; Mills, D.; Lvov, Y. M. Clay Nanotube/Poly(Methyl Methacrylate) Bone Cement Composites with Sustained Antibiotic Release. *Macromol. Mater. Eng.* **2012**, *297*, 645–653.

224. Park, S. E.; Chao, M.; Raj, P. A. Mechanical Properties of Surface-Charged Poly(Methyl Methacrylate) as Denture Resins. *Int. J. Dent.* **2009**, *2009*, 1–6.

225. Saunders, B. R.; Crowther, H. M.; Vincent, B. Poly[(Methyl Methacrylate)-Co-(Methacrylic Acid)] Microgel Particles: Swelling Control Using PH, Cononsolvency, and Osmotic Deswelling. *Macromolecules* **1997**, *30*, 482–487.

226. Lovell, P. A.; El-Aasser, M. S. *Emulsion Polymerization And Emulsion Polymers*; Wiley, **1997**.

227. Shouldice, G. T. D.; Vandezande, G. A.; Rudin, A. Practical Aspects of the Emulsifier-Free Emulsion Polymerization of Styrene. *Eur. Polym. J.* **1994**, *30*, 179–183.

228. Blackburn, W. H.; Lyon, L. A. Size-Controlled Synthesis of Monodisperse Core/Shell Nanogels. *Colloid Polym. Sci.* **2008**, *286*, 563–569.

229. I; Yu, C.; Chen, R.; Li, J. J.; Li, J. J.; Drahansky, M.; Paridah, M. .; Moradbak, A.; Mohamed, A. .; Owolabi, FolaLi, H. abdulwahab taiwo; et al. We Are IntechOpen , the World ' s Leading Publisher of Open Access Books Built by Scientists , for Scientists TOP 1 %. *Intech* **2012**, *i*, 13.

230. Rahman, M. M.; Elaissari, A. Multi-Stimuli Responsive Magnetic Core–Shell Particles: Synthesis, Characterization and Specific RNA Recognition. *J. Colloid Sci. Biotechnol.* **2012**, *1*, 3–15.

231. Deng, Z.; Guo, Y.; Zhao, X.; Ma, P. X.; Guo, B. Multifunctional Stimuli-Responsive Hydrogels with Self-Healing, High Conductivity, and Rapid Recovery through Host-Guest Interactions. *Chem. Mater.* **2018**, *30*, 1729–1742.

232. Wang, C.; Liu, X.; Wulf, V.; Vázquez-González, M.; Fadeev, M.; Willner, I. DNA-Based Hydrogels Loaded with Au Nanoparticles or Au Nanorods: Thermoresponsive Plasmonic Matrices for Shape-Memory, Self-Healing, Controlled Release, and Mechanical Applications. *ACS Nano* **2019**, *13*, 3424–3433.

233. Li, J.; Celiz, A. D.; Yang, J.; Yang, Q.; Wamala, I.; Whyte, W.; Seo, B. R.; Vasilyev, N. V.; Vlassak, J. J.; Suo, Z.; et al. Tough Adhesives for Diverse Wet Surfaces. *Science (80-.).* **2017**, *357*, 378–381.

234. Sun, S.; Hu, J.; Tang, H.; Wu, P. Spectral Interpretation of Thermally Irreversible Recovery of Poly(N-Isopropylacrylamide-Co-Acrylic Acid) Hydrogel. *Phys. Chem. Chem. Phys.* **2011**, *13*, 5061–5067.

235. Değirmenci, I.; Eren, Ş.; Aviyente, V.; De Sterck, B.; Hemelsoet, K.; Van Speybroeck, V.; Waroquier, M. Modeling the Solvent Effect on the Tacticity in the Free Radical Polymerization of Methyl Methacrylate. *Macromolecules* **2010**, *43*, 5602–5610.

236. Odian, G. *Principles of Polymerization Fourth Edition*; John Wiley & Sons, Inc., **2004**.

237. Günaydin, H.; Salman, S.; Tüzün, N. Ş.; Avci, D.; Aviyente, V. Modeling the Free Radical Polymerization of Acrylates. *Int. J. Quantum Chem.* **2005**, *103*, 176–189.

238. Colombani, D. Driving Forces in Free Radical Addition-Fragmentation Processes. *Prog. Polym. Sci.* **1999**, *24*, 425–480.

239. Chern, C. S. Emulsion Polymerization Mechanisms and Kinetics. *Prog. Polym. Sci.* **2006**, *31*, 443–486.

240. Thickett, S. C.; Gilbert, R. G. Emulsion Polymerization: State of the Art in Kinetics and Mechanisms. *Polymer (Guildf).* **2007**, *48*, 6965–6991.

241. Rao, J. P.; Geckeler, K. E. Polymer Nanoparticles: Preparation Techniques and Size-Control Parameters. *Prog. Polym. Sci.* **2011**, *36*, 887–913.

242. Everett, D. H. Chapter 1. What Are Colloids?; Royal Society of Chemistry, **2007**; pp 1–15.

243. Vincent, B. Introduction to Colloidal Dispersions. *Colloid Sci. Princ. Methods Appl.* **2009**, 1–13.

244. Thorne, J. B.; Vine, G. J.; Snowden, M. J. Microgel Applications and Commercial Considerations. *Colloid Polym. Sci.* **2011**, *289*, 625–646.

245. Lal, S. N. D.; O'Connor, C. J.; Eyres, L. Application of Emulsifiers/Stabilizers in Dairy Products of High Rheology. *Adv. Colloid Interface Sci.* **2006**, *123–126*, 433–437.

246. Guzey, D.; McClements, D. J. Formation, Stability and Properties of Multilayer Emulsions for Application in the Food Industry. *Adv. Colloid Interface Sci.* **2006**, *128–130*, 227–248.

247. Keddie, J. L.; Routh, A. F. *Fundamentals of Latex Film Formation Processes and Properties*; Springer, **2010**.

248. Shaw, D. J. *Introduction to Colloid and Surface Chemistry*; ButterworthHeinemann, **1996**.

249. Derjaguin, B.; Landau, L. Theory of the Stability of Strongly Charged Lyophobic Sols and of the Adhesion of Strongly Charged Particles in Solutions of Electrolytes. *Prog. Surf. Sci.* **1993**, *43*, 30–59.

250. Ohshima, H. The Derjaguin-Landau-Verwey-Overbeek (DLVO) Theory of Colloid Stability. In *Electrical Phenomena at Interfaces and Biointerfaces*; John Wiley & Sons, Inc.: Hoboken, NJ, USA, **2012**; pp 27–34.

251. Hotze, E. M.; Phenrat, T.; Lowry, G. V. Nanoparticle Aggregation: Challenges to Understanding Transport and Reactivity in the Environment. *J. Environ. Qual.* **2010**, *39*, 1909.

252. Adair, J. H.; Suvaci, E.; Sindel, J. Surface and Colloid Chemistry. In *Encyclopedia of Materials: Science and Technology*; Elsevier, **2001**; Vol. 3, pp 1–10.

253. Eastman, J. Colloid Stability. In *Colloid Science*; Blackwell Publishing Ltd.: Oxford, UK, **1966**; pp 36–49.

254. Hamaker, H. C. The London-van Der Waals Attraction between Spherical Particles. *Physica* **1937**, *4,* 1058–1072.

255. De Boer, J. H. The Influence of van Der Waals' Forces and Primary Bonds on Binding Energy, Strength and Orientation, with Special Reference to Some Artificial Resins. *Trans. Faraday Soc.* **1936**, *32*, 10–37.

256. Ohshima, H. Interaction of Colloidal Particles. In *Colloid and Interface Science in Pharmaceutical Research and Development*; Elsevier, **2014**; pp 1–28.

257. Liang, Y.; Hilal, N.; Langston, P.; Starov, V. Interaction Forces between Colloidal Particles in Liquid: Theory and Experiment. *Adv. Colloid Interface Sci.* **2007**, *134–135*, 151–166.

258. Lai, H.; Fang, H.; Huang, L.; He, G.; Reible, D. A Review on Sediment Bioflocculation: Dynamics, Influencing Factors and Modeling. *Sci. Total Environ.* **2018**, *642*, 1184–1200.

259. Stern, O. The Theory of the Electrolytic Double Shift. *Zeitschrift fur elecktrochemie ind Angew. Phys. chemie* **1924**, *30*, 508–516.

260. Park, S.-J.; Seo, M.-K. Intermolecular Force. In *Interface Science and Technology*; **2011**; Vol. 18, pp 1–57.

261. Bhardwaj, R.; Fang, X.; Somasundaran, P.; Attinger, D. Self-Assembly of Colloidal Particles from Evaporating Droplets: Role of DLVO Interactions and Proposition of a Phase Diagram. *Langmuir* **2010**, *26*, 7833–7842.

262. Tavacoli, J. W.; Dowding, P. J.; Routh, A. F. The Polymer and Salt Induced Aggregation of Silica Particles. *Colloids Surf., A* **2007**, *293*, 167–174.

263. Napper, D. . Steric Stabilization. *J. Colloid Interface Sci.* **1977**, *58*, 390–407.

264. Russel, W. B.; Saville, D. A.; Schowalter, W. R. *Colloidal Dispersions*; Cambridge University Press, **1992**.

265. Tadros, F. Steric Stabilisation and Flocculation by Polymers. *Polym. J.* **1991**, *23*, 683–696.

266. Fritz, G.; Schdler, V.; Willenbacher, N.; Wagner, N. J. Electrosteric Stabilization of Colloidal Dispersions Electrosteric Stabilization of Colloidal Dispersions. *Langmuir* **2002**, *18*, 6381–6390.

267. Lee, A.; Tsai, H. Y.; Yates, M. Z. Steric Stabilization of Thermally Responsive N-Isopropylacrylamide Particles by Poly(Vinyl Alcohol). *Langmuir* **2010**, *26*, 18055–18060.

268. Routh, A. F.; Vincent, B. Salt-Induced Homoaggregation of Poly(N-Isopropylacrylamide) Microgels. *Langmuir* **2002**, *18*, 5366–5369.

269. Di, L.; Kerns, E. H.; Di, L.; Kerns, E. H. Chapter 6 – PKa. *Drug-Like Prop.* **2016**, 51–59.

270. Po, H. N.; Senozan, N. M. The Henderson-Hasselbalch Equation: Its History and Limitations. *J. Chem. Educ.* **2001**, *78*, 1499.

271. Nelson, D. L.; Lehninger, A. L.; Cox, M. M. *Lehninger Principles of Biochemistry*; **2008**.

272. Borukhov, I.; Andelman, D.; Borrega, R.; Cloitre, M.; Leibler, L.; Orland, H. Polyelectrolyte Titration: Theory and Experiment. **2000**, 1–13.

273. Richardson, R. Scattering and Reflection Techniques. In *Colloid Science*; Blackwell Publishing Ltd.: Oxford, UK, **2009**; pp 228–254.

274. Hassan, P. A.; Rana, S.; Verma, G. Making Sense of Brownian Motion: Colloid Characterization by Dynamic Light Scattering. *Langmuir* **2015**, *31*, 3–12.

275. Frisken, B. J. Revisiting the Method of Cumulants for the Analysis of Dynamic Light-Scattering Data. *Appl. Opt.* **2001**, *40*, 4087.

276. Bhattacharjee, S. DLS and Zeta Potential – What They Are and What They Are Not? *J. Control. Release* **2016**, *235*, 337–351.

277. Stetefeld, J.; McKenna, S. A.; Patel, T. R. Dynamic Light Scattering: A Practical Guide and Applications in Biomedical Sciences. *Biophys. Rev.* **2016**, *8*, 409–427.

278. Kratz, K.; Hellweg, T.; Eimer, W. Structural Changes in PNIPAM Microgel Particles as Seen by SANS, DLS, and EM Techniques. *Polymer (Guildf).* **2001**, *42*, 6631–6639.

279. Naiim, M.; Boualem, A.; Ferre, C.; Jabloun, M.; Jalocha, A.; Ravier, P. Multiangle Dynamic Light Scattering for the Improvement of Multimodal Particle Size Distribution Measurements. *Soft Matter* **2015**, *11*, 28–32.

280. Jans, H.; Liu, X.; Austin, L.; Maes, G.; Huo, Q. Dynamic Light Scattering as a Powerful Tool for Gold Nanoparticle Bioconjugation and Biomolecular Binding Studies. *Anal. Chem.* **2009**, *81*, 9425–9432.

281. Shim, J. Y.; Gupta, V. K. Reversible Aggregation of Gold Nanoparticles Induced by PH Dependent Conformational Transitions of a Self-Assembled Polypeptide. *J. Colloid Interface Sci.* **2007**, *316*, 977–983.

282. Khlebtsov, B. N.; Khlebtsov, N. G. On the Measurement of Gold Nanoparticle Sizes by the Dynamic Light Scattering Method. *Colloid J.* **2011**, *73*, 118–127.

283. Durand-Gasselin, C.; Capelot, M.; Sanson, N.; Lequeux, N. Tunable and Reversible Aggregation of Poly(Ethylene Oxide-St-Propylene Oxide) Grafted Gold Nanoparticles. *Langmuir* **2010**, *26*, 12321–12329.

284. Dutta, A. Fourier Transform Infrared Spectroscopy. In *Spectroscopic Methods for Nanomaterials Characterization*; Elsevier, **2017**; Vol. 2, pp 73–93.

285. Ismail, A. A.; van de Voort, F. R.; Sedman, J. Chapter 4 Fourier Transform Infrared Spectroscopy: Principles and Applications. In *Techniques and Instrumentation in Analytical Chemistry*; **1997**; Vol. 18, pp 93–139.

286. Griffiths, P. R.; De Haseth, J. A. Introduction to Vibrational Spectroscopy. In *Fourier Transform Infrared Spectrometry*; John Wiley & Sons, Inc.: Hoboken, NJ, USA, **2007**; pp 1–18.

287. Chen, Y.; Zou, C.; Mastalerz, M.; Hu, S.; Gasaway, C.; Tao, X. Applications of Micro-Fourier Transform Infrared Spectroscopy (FTIR) in the Geological Sciences—A Review. *Int. J. Mol. Sci.* **2015**, *16*, 30223–30250.

288. Bhattacharya, S.; Phatake, R.; Barnea, S. N.; Zerby, N.; Zhu, J.; Shikler, R.; Lemcoff, N. G.; Jelinek, R. Fluorescent Self-Healing Carbon Dot / Polymer Gels. *ACS Nano* ***2019***, *13*, 1433-1442.

289. McCann, J.; Behrendt, J. M.; Yan, J.; Halacheva, S.; Saunders, B. R. Poly(Vinylamine) Microgel-Dextran Composite Hydrogels: Characterisation; Properties and PH-Triggered Degradation. *J. Colloid Interface Sci.* **2015**, *449*, 21–30.

290. Farley, R.; Saunders, B. R. A General Method for Functionalisation of Microgel Particles with Primary Amines Using Click Chemistry. *Polymer (Guildf).* **2014**, *55*, 471–480.

291. Milosavljević, N. B.; Ristić, M. D.; Perić-Grujić, A. A.; Filipović, J. M.; Štrbac, S. B.; Rakočević, Z. L.; Krušić, M. T. K. Removal of Cu2+ Ions Using Hydrogels of Chitosan, Itaconic and Methacrylic Acid: FTIR, SEM/EDX, AFM, Kinetic and Equilibrium Study. *Colloids Surf., A* **2011**, *388*, 59–69.

292. Hwangbo, S.; Jeong, H.; Heo, J.; Lin, X.; Kim, Y.; Chang, M.; Hong, J. Antibacterial Nanofilm Coatings Based on Organosilicate and Nanoparticles. *React. Funct. Polym.* **2016**, *102*, 27–32.

293. Liang, B.; He, M. L.; Xiao, Z. P.; Li, Y.; Chan, C. yan; Kung, H. F.; Shuai, X. T.; Peng, Y. Synthesis and Characterization of Folate-PEG-Grafted-Hyperbranched-PEI for Tumor-Targeted Gene Delivery. *Biochem. Biophys. Res. Commun.* **2008**, *367*, 874–880.

294. Huang, C. W.; Wu, P. W.; Su, W. H.; Zhu, C. Y.; Kuo, S. W. Stimuli-Responsive Supramolecular Materials: Photo-Tunable Properties and Molecular Recognition Behavior. *Polym. Chem.* **2016**, *7*, 795–806.

295. Yu, Y.; Yiling, N.; Kou, O.; Takuzo, A. Mechanically Robust, Readily Repairable Polymers via Tailored Noncovalent Cross-Linking. *Science (80-.).* **2018**, *359*, 72–76.

296. Li, J.; Su, Z.; Xu, H.; Ma, X.; Yin, J.; Jiang, X. Supramolecular Networks of Hyperbranched Poly(Ether Amine) (HPEA) Nanogel/Chitosan (CS) for the Selective Adsorption and Separation of Guest Molecules. *Macromolecules* **2015**, *48*, 2022–2029.

297. Peniche, C.; Argüelles-Monal, W.; Davidenko, N.; Sastre, R.; Gallardo, A.; San Román, J. Self-Curing Membranes of Chitosan/PAA IPNs Obtained by Radical Polymerization: Preparation, Characterization and Interpolymer Complexation. *Biomaterials* **1999**, *20*, 1869–1878.

298. Zhao, X.; Wu, H.; Guo, B.; Dong, R.; Qiu, Y.; Ma, P. X. Antibacterial Anti-Oxidant Electroactive Injectable Hydrogel as Self-Healing Wound Dressing with

Hemostasis and Adhesiveness for Cutaneous Wound Healing. *Biomaterials* **2017**, *122*, 34–47.

299. Davis, S. Electron Microscopy. In *Colloid Science*; Blackwell Publishing Ltd.: Oxford, UK, **2013**; Vol. 5, pp 266–282.

300. Zhou, W.; Wang, Z. L. *Scanning Microscopy for Nanotechnology*; Zhou, W., Wang, Z. L., Eds.; Springer New York: New York, NY, **2007**.

301. Scheu, C.; Kaplan, W. D. Introduction to Scanning Electron Microscopy. In *In-Situ Electron Microscopy*; Wiley-VCH Verlag GmbH & Co. KGaA: Weinheim, Germany, **2012**; pp 1–37.

302. Yang, Y.; Wang, X.; Yang, F.; Wang, L.; Wu, D. Highly Elastic and Ultratough Hybrid Ionic–Covalent Hydrogels with Tunable Structures and Mechanics. *Adv. Mater.* **2018**, *30*, 1–9.

303. Cui, Z.; Zhou, M.; Greensmith, P. J.; Wang, W.; Hoyland, J. A.; Kinloch, I. A.; Freemont, T.; Saunders, B. R. A Study of Conductive Hydrogel Composites of PH-Responsive Microgels and Carbon Nanotubes. *Soft Matter* **2016**, *12*, 4142–4153.

304. Hu, M.-S.; Chen, H.-L.; Shen, C.-H.; Hong, L.-S.; Huang, B.-R.; Chen, K.-H.; Chen, L.-C. Photosensitive Gold-Nanoparticle-Embedded Dielectric Nanowires. *Nat. Mater.* **2006**, *5*, 102–106.

305. Joseph, C. L.; Bernal, S. Optical and Electron Microscopy. In *Modern Devices*; John Wiley & Sons, Inc: Hoboken, NJ, **2016**; pp 259–276.

306. Tanaka, N. Structure and Imaging of a Transmission Electron Microscope (TEM). In *Electron Nano-Imaging*; Springer Japan: Tokyo, **2017**; pp 17–28.

307. Bozzola, J. J. Electron Microscopy. In *Encyclopedia of Life Sciences*; John Wiley & Sons, Ltd: Chichester, UK, **2001**; Vol. 5, pp 275–317.

308. Kleebe, H.-J.; Lauterbach, S.; Müller, M. M. Transmission Electron Microscopy. In *Methods in Physical Chemistry*; Wiley-VCH Verlag GmbH & Co. KGaA: Weinheim, Germany, **2012**; pp 797–821.

309. Lei, C. Transmission Electron Microscopy. In *Nanotechnology Research Methods for Foods and Bioproducts*; Wiley-Blackwell: Oxford, UK, **2012**; Vol. 36, pp 127–144.

310. Paredes, A. M. MICROSCOPY | Transmission Electron Microscopy. In *Encyclopedia of Food Microbiology*; Elsevier, **2014**; Vol. 2, pp 711–720.

311. Yang, Y.; Zhu, J.; Zhao, J.; Weng, G. J.; Li, J. J.; Zhao, J. W. Growth of Spherical Gold Satellites on the Surface of Au@Ag@SiO 2 Core-Shell Nanostructures Used for an Ultrasensitive SERS Immunoassay of Alpha-Fetoprotein. *ACS Appl. Mater. Interfaces* **2019**, *11*, 3617–3626.

312. Schneider, G.; Decher, G.; Nerambourg, N.; Praho, R.; Werts, M. H. V.; Blanchard-Desce, M. Distance-Dependent Fluorescence Quenching on Gold Nanoparticles Ensheathed with Layer-by-Layer Assembled Polyelectrolytes. *Nano Lett.* **2006**, *6*, 530–536.

313. Chen, Y. S.; Yoon, S. J.; Frey, W.; Dockery, M.; Emelianov, S. Dynamic Contrast-Enhanced Photoacoustic Imaging Using Photothermal Stimuli-Responsive Composite Nanomodulators. *Nat. Commun.* **2017**, *8*, 1–10.

Chapter 3: Exploring and enhancing the colloidal stability of gold nanoparticles using a poly(MMA-MAA-EGDMA) nanogel shell[1]

3.1 Abstract

The multifunctionality of gold nanoparticles (Au NPs) expands the interdisciplinary research for a wide range of biomedical applications, such as catalysis, contrast agents, photothermal therapy and signal amplification. However, the poor colloidal stability of citrate stabilised Au NPs is the weakness to maintain the performance of these particles in practical use. An irreversible aggregation of Au NPs can be easily triggered in an electrolyte solution due to their electrostatic stabilising citrate layers. Au NPs could be potentially applied to a hydrogel system because they are capable of reporting the change of local environment. An initial study discussed here show Au NPs become colloidally unstable when they were directly incorporated into a gel based on poly(ethyl acrylate-methacrylic acid-divinylbenzene) (poly(EA-MAA-DVB)) microgels (MGs). The growth of the core-shell structure using precipitation polymerisation was selected to provide additional stabilisation for the Au NPs. After summarizing three approaches for shell growth, a new soft core-shell structure consisted of poly(methyl methacrylate-methacrylic acid-ethylene glycol dimethacrylate) (poly(MMA-MAA-EGDMA)) and Au NPs was synthesised through a facile method without any pre-functionalisation steps. The core-shell particles exhibited an expected enhanced colloidal stability to the

---

[1] The results are published in (1). Wu, S.; Zhu, M et al. Plasmonic and Colloidal Stability Behaviours of Au-Acrylic Core-Shell Nanoparticles with Thin pH-Responsive Shells. *Nanoscale* **2018**, 10, 18565–18575, and (2). Schmidt, M. M.; Wu, S et al. How Gold Nanoparticles Can Be Used to Probe the Structural Changes of a pH-Responsive Hydrogel. *Phys. Chem. Chem. Phys.* **2017**, 19, 5102–5112.

electrolyte. The results show localised surface plasmon resonance (LSPR) properties and the colloidal dispersion of core-shell particles was restorable in a saturated NaCl solution. Furthermore, the swellable copolymer shell enabled a facile redispersion of core-shell particles from a completely dried state.

3.2 Introduction

Gold nanoparticles (Au NPs) act as a multifunctional and powerful “tool”, which has been applied to numerous cutting-edge research and continuously attracts considerable attention for practical use.[1-10]. The high extinction coefficient, localised surface plasmon resonance (LSPR) and inertness of Au NPs enlarge the possibility of improvement in a range of therapeutic, diagnostic and functional techniques[11-13]. These applications include imaging,[14-16] catalysis,[17-18] optical sensors[19-20] and photovoltaics.[21-22] Unfortunately, limited colloidal stability is an issue which inhibits some new applications of Au NPs in different environments.[23-24]

As introduced in Chapter 2, localised surface plasmon resonance (LSPR) is a characteristic property of Au NPs. This property describes the interaction between the conduction electrons of metallic nanoparticles and the incident electromagnetic wave. LSPR is sensitive to the local medium around Au NPs, and the change of LSPR acts as one of the indications for unstable Au NP dispersions.[25-26] Although this change can be used in detection and sensing,[13, 19] it is necessary to control the stability of these nanoparticles in applications, especially in physiological conditions,[23, 27] which require consistent and durable performance.

The Turkvich method is a citrate reduction process widely used for the preparation of Au NPs.[28-29] These Au NPs are stabilised through electrostatic repulsion of negatively charged citrate ions.[28, 30] High ionic strength medium can easily disrupt such stabilisation.[31] The construction of the core-shell structure is a natural solution to endow Au NPs with the additional protection and functionality.[23, 32] Inorganic SiO_2 has been widely studied and reported as an effective shell for Au NPs stabilisation and subsequent functionalisation.[5-6, 32-33] However, the rigidity of SiO_2 limits the flexibility of core-shell particles. In contrast to the soft crosslinked polymer shell, these SiO_2 shells are not swellable. The commonly used synthesis of Au-polymer core-shell requires either in situ Au NPs preparation using preformed polymer particles[34] or growth of the polymer shell with preformed Au NPs.[4, 8, 35-36] Free-radical precipitation polymerisation has been used to successfully synthesise temperature-responsive poly(*N*-isopropylacrylamide) (polyNIPAM) hydrogel shells through hydrophobically modified Au NPs.[7-8, 37] A similar core-shell synthesis was also achieved by mimicking the surface of the colloidal seed using sulphur containing copolymer (Au NPs self-assembly) to facilitate the following precipitation polymerisation.[35] Other studies also showed the capability of the core-shell synthesis through oxidative polymerisation[38] and controlled reversible addition fragmentation chain transfer (RAFT) emulsion polymerisation[39].

In this chapter, the morphology, LSPR and colloidal stability of Au NPs and core-shell products were intensively characterised and analysed. Scheme 3.1(i) illustrates the synthesis of Au NPs through citrate reduction using the Turkvich method.[28-29] After exploring the aggregation of Au NPs in the aqueous dispersion and hydrogel medium, a new nanogel shell composed of poly(methyl methacrylate-methacrylic acid-ethylene glycol dimethacrylate) (poly(MMA-MAA-EGDMA))[40] (Scheme 3.1(ii)) was synthesised through a facile precipitation polymerisation without any pre-functionalisation steps. The polymerisation was thermally initiated using ammonium persulfate (APS). This new core-shell synthesis was established by carefully evaluating three routines (Scheme 3.1(iii)) with different surface modifications and monomer feeding modes. The resultant colloidal stability of this core-shell system was strongly improved in the electrolyte solution (Scheme 3.1(iv)) with good redispersion after aggregation.

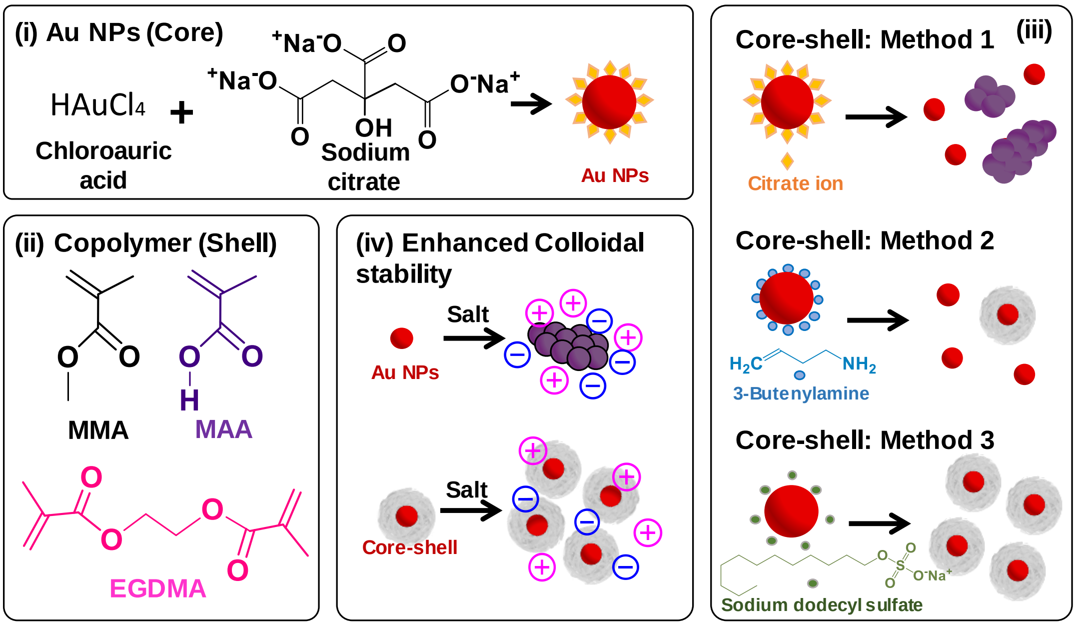

Scheme 3.1 (i) Schematic depiction of the Au NPs synthesis using Turkvich method and the copolymer shell growth using (ii) MMA, MAA and EGDMA through three approaches (iii). The enhanced colloidal stability of core-shell particles is depicted in (iv).

3.3 Experimental

3.3.1 Materials

MMA (99%), MAA (99%), EGDMA (98%), EA (99%), DVB (80%), glycidyl methacrylate (GMA, 97%), *N*,*N*,*N′*,*N′*-tetramethylethylenediamine (TEMED, 99%), ammonium persulfate (APS, 98%), sodium dodecyl sulfate (SDS, 99%), potassium phosphate dibasic (98%), 3-Butenylamine hydrochloride (B-en-A, 97%), phosphate buffered saline (PBS), NaCl (99%), NaOH (97%), sodium citrate dihydrate ($Na_3Cit{\cdot}2H_2O$, ≥99%), and $HAuCl_4{\cdot}3H_2O$ (>99.9%) were purchased from Sigma-Aldrich and used as received. The water used was doubly filtered and deionised.

3.3.2 Synthesis of citrate stabilised Au NPs

The synthesis of citrate stabilised Au NPs was achieved using the Turkvich method.[28-29] $Na_3Cit{\cdot}2H_2O$ solution (5.0 mL, 19 mM) was rapidly added into $HAuCl_4{\cdot}3H_2O$ solution (95 mL, 0.25 mM) which was kept boiling and vigorously stirred (950 rpm) in a 250 mL three-necked flask equipped with a reflux condenser (cooled to 4 °C using water circulation). The flask was heated in a paraffin oil bath using a magnetic hotplate stirrer. The reaction temperature was monitored by immersing a temperature probe in the bath. The reaction was allowed to proceed for 40 min before cooling to room temperature. The final dispersion (2.97 nM) was collected in a glass bottle and stored at 4 °C in the fridge. The salt stability was tested by adding Au NPs to 0 – 55 mM NaCl solution.

3.3.3 Synthesis of poly(EA-MAA-DVB) MGs

The synthesis of poly(EA-MAA-DVB) microgels (MGs) was performed using the seed-feed emulsion polymerisation.[41] SDS (1.80 g) was added to water (518 mL) in a 1 L five-necked round bottom reactor equipped with a mechanical stirrer (300 rpm) and a reflux condenser (cooled to 4 °C using water circulation). The solution was purged with nitrogen for 30 min and heated to 80 °C in a water bath. The inlet nitrogen was guided by a needle through a rubber stopper. Comonomer solution (31.5 g) containing EA (66.0 wt%), MAA (32.7 wt%) and DVB (1.3 wt%) was prepared and transferred to the reactor. The seed formation was proceeded by addition of K_2HPO_4 (3.15 g of a 7.0 wt% solution) and APS (10 g of a 2 wt% solution). After 30 min, comonomer (218.5 g) mixture was fed into the reactor using a peristaltic pump at a uniform rate (2.4 g min^{-1}) over 90 min. The copolymerisation proceeded for a further hour. The flask was finally cooled in an ice bath. Large aggregates of the product were removed by filtration using film mesh (0.2 mm pore size). The product was sealed in the cellulose dialysis tubing (14 kDa cut off) and dialysed against water for 14 days. The dialysis water was changed once per day.

Vinyl functionalisation was conducted by mixing the 400 g MGs (5 wt%) with 30 g GMA in a 1 L flask equipped with a reflux condenser (cooled to 4 °C using water circulation).[41] The mixture was magnetically stirred at 400 rpm and heated at 50 °C for 4 hr in a paraffin oil bath using a magnetic hotplate stirrer. The reaction temperature was monitored by immersing a temperature probe in the bath. The functionalised MG dispersion was finally cooled in an ice bath, and the aggregates were removed using film mesh (0.2 mm pore size). The unreacted GMA was subsequently removed by washing with chloroform twice using a separated funnel. The chloroform was extracted in a rotary evaporator (160 mbar), and functionalised MGs was then concentrated to 13.7 wt% (20 mbar).

3.3.4 DX MG preparation

The preparation of double crosslinked (DX) MG preparation followed a previous method from the Saunders group.[41-42] The GMA-functionalised MG dispersion (1.465 mL) was diluted with water (0.265 mL) using a micropipette (100 – 1000 μL range). Then, aqueous NaOH solution (0.150 mL, 4M) was added to make the physical gel using a micropipette (100 – 1000 μL range), and the pH was adjusted to ~ 7.6. An APS solution (0.050 mL, 3.3 wt%) and TEMEDA solution (0.050 mL, 4.0 wt%) were immediately added to the physical gel using a micropipette (100 – 1000 μL range) and mixed with a vortex mixer. The mixture was then sealed by two pieces of glass slides and clips using an O-ring spacer (inner diameter = 15 mm and wall diameter = 2.5 mm). The sample was heated at 37 °C in oven overnight.

3.3.5 DX MG/Au NP preparation

1 mL Au NPs solution was centrifuged ~ 25 min at 10000 rpm at room temperature. The volume was reduced to 0.265 mL using a micropipette (100 – 1000 μL range). The preparation of DX MG/Au NP using the same protocol in Section 3.3.4 except 0.265 mL water was replaced by the concentrated Au NPs. The mixture was vigorously stirred using a spatula.

3.3.6 Synthesis of poly(MMA-MAA-EGDMA) NGs

The nanogels (NGs) were formed by the surfactant-free emulsion polymerisation. The synthesis was performed in a 100 mL three-necked flask with 26 mL water. The water was purged with nitrogen for 30 min and heated to 80 °C equipped with a reflux condenser (4 °C water circulation). The inlet nitrogen was guided by a needle through a rubber stopper. The flask was heated in a paraffin oil bath using a magnetic hotplate stirrer. The reaction temperature was monitored by immersing a temperature probe in the bath. A comonomer mixture (49.5 mg) of MMA (80.5 wt%), MAA (17.5 wt%) and EGDMA (2.0 wt%) was simultaneously added into the flask using a micropipette (1 – 10 μL range) and magnetically stirred at a speed around 290 rpm. This was followed by adding aqueous K_2HPO_4 (80 μL, 1M) into the solution using a micropipette (10 – 100 μL range). The mixture was equilibrated for 10 min. Under a nitrogen atmosphere, the reaction was initiated by adding APS (100 μL, 19 mM) using a micropipette (10 – 100 μL range). The whole polymerisation process lasted for 2 hr. At the end of reaction, the flask was cooled in an ice bath. The product was sealed in the cellulose dialysis tubing (8 kDa cut off) and dialysed against water for 7 days. The dialysis water was changed once per day.

3.3.7 Synthesis of core-shell particles: Method 1

Citrate stabilised Au NPs (20 mL, synthesised in Section 3.3.2) were diluted with water (6 mL) and added into a 100 mL three-necked flask. The flask was magnetically stirred at a speed of around 290 rpm. The solution was purged with nitrogen for 30 min and heated to 80 °C equipped with a reflux condenser (4 °C water circulation). The inlet nitrogen was guided by a needle through a rubber stopper. The flask was heated in a paraffin oil bath and controlled by a temperature probe. The growth of NG shells used the same protocol as shown in Section 3.3.6. A comonomer mixture (49.5 mg) of MMA (80.5 wt%), MAA (17.5 wt%) and EGDMA (2.0 wt%) was simultaneously added into the flask using a micropipette (1 – 10 μL range). This was followed by adding aqueous K_2HPO_4 (80 μL, 1M) into the solution using a micropipette (10 – 100 μL range). The mixture was equilibrated for 10 min. Under a nitrogen atmosphere, the reaction was initiated by adding APS (100 μL, 19 mM) using a micropipette (10 – 100 μL range).

The polymerisation was continued for 2 hr. At the end of reaction, the flask was cooled in an ice bath. The characterisations were immediately carried on the product (in Section 3.4.4.2).

3.3.8 Synthesis of core-shell particles: Method 2

Pre-functionalisation process of citrate stabilised Au NPs was performed before the synthesis. An aqueous solution of SDS (20 μL, 10 mg mL^{-1}) was added into citrate stabilised Au NP dispersions (20 mL, synthesised in Section 3.3.2) using a micropipette (10 – 100 μL range) with 20 mins magnetic stirring (190 rpm). B-en-A (2 mL, 0.005 mg mL^{-1} in ethanol) was subsequently added dropwise in 1 min using a micropipette (100 – 1000 μL range), and the mixture was magnetically stirred overnight (190 rpm). After finishing these procedures, the solution was uniformly separated into four tubes and centrifuged at 4800 rpm (2680 rcf) for 4 hr. The supernatant was discarded using a micropipette (100 – 1000 μL range). The sediment of functionalised Au NPs was collected and redispersed in water (25 mL). An aqueous SDS solution (1 mL, 2.06 mg mL^{-1}) was then added to the dispersion using a micropipette (100 – 1000 μL range) with magnetic stirring (~ 290 rpm) in a 100 mL three-necked flask. The flask was equipped with a reflux condenser (4 °C water circulation). The mixture was purged with nitrogen for 30 min and heated to 80 °C. The inlet nitrogen was guided by a needle through a rubber stopper. The flask was heated in a paraffin oil bath and controlled by a temperature probe. The polymerisation steps used the same protocol as shown in Section 3.3.6. A comonomer mixture (49.5 mg) of MMA (80.5 wt%), MAA (17.5 wt%) and EGDMA (2.0 wt%) was simultaneously added into the flask using a micropipette (1 – 10 μL range). This was followed by adding aqueous K_2HPO_4 (80 μL, 1M) into the solution using a micropipette (10 – 100 μL range). The mixture was equilibrated for 10 min. Under a nitrogen atmosphere, the reaction was initiated by adding APS (100 μL, 19 mM) using a micropipette (10 – 100 μL range). The polymerisation was continued for 2 hr. At the end of reaction, the flask was cooled in an ice bath. The characterisations were immediately carried out on the product (in Section 3.4.4.3).

3.3.9 Synthesis of core-shell particles: Method 3

An aqueous solution of SDS (20 μL, 10 mg mL^{-1}) was added into citrate stabilised Au NP dispersions (20 mL, synthesised in Section 3.3.2) using a micropipette (10 – 100 μL range) with 20 min magnetic stirring (190 rpm). The mixture was uniformly separated into four tubes and centrifuged at 4800 rpm (2680 rcf) for 4 hr. The supernatant was discarded using a micropipette (100 – 1000 μL range). The sediment of Au NPs was collected and redispersed in water (20 mL). The dispersion was transferred to a three-necked flask with magnetic stirring (290 rpm), and an aqueous SDS solution (1 mL, 4.12 mg mL^{-1}) was subsequently added using a micropipette (100 – 1000 μL range). The flask was equipped with a reflux condenser (4 °C water circulation). The mixture was purged with nitrogen for 30 min and heated to 80°C. The inlet nitrogen was guided by a needle through a rubber stopper. The flask was heated in a paraffin oil bath and controlled by a temperature probe. A comonomer mixture (49.5 mg) of MMA (80.5 wt%), MAA (17.5 wt%) and EGDMA (2.0 wt%) was added to a glass vial using a micropipette (1 – 10 μL range) and dissolved in water (5 mL) on a vortex mixer. This solution was then collected by a 5 mL syringe and added to a syringe pump. Aqueous K_2HPO_4 (80 μL, 1M) was added to the flask using a micropipette (10 – 100 μL range) and the mixture was equilibrated for 10 min. Under a nitrogen atmosphere, the reaction was initiated by aqueous APS (100 μL, 19 mM) using a micropipette (10 – 100 μL range) and a syringe pump was used to feed the comonomer solution into the flask at a uniform rate (0.083 mL min^{-1}) over 1 hr. The reaction was continued for a further 1 hr and finally cooled in an ice bath. The product was uniformly separated into twelves tubes and centrifuged for 1 hr at 10000 rpm. The supernatant was discarded, and the sediment was redispersed with water using a micropipette (100 – 1000 μL range). The centrifugation was repeated four times to remove unreacted monomers, buffer and excess NGs.

3.3.10 Large scale core-shell particle synthesis

The synthesis followed the same protocol of method as shown in Section 3.3.9, except 10 mL and 30 mL citrate stabilised Au NP dispersions were selected and centrifuged to a volume of 20 mL in water. The growth of the shells was performed using these two dispersions.

3.3.11 Colloidal stability experiments

PBS and different concentrations of NaCl (0.5 mL) solutions were mixed with core-shell particles (0.5 mL, 1.4 nM) or Au NPs (0.5 mL, 1.1 nM). The mixture was held for 10 min before taking any further measurements. Both particle types were also tested in a saturated NaCl solution (≥ 6.1 M) to trigger the severe aggregation. These mixtures were allowed to sediment overnight.

A drop of core-shell dispersion (0.7 nM) was placed on an aluminium disk and heated in the oven at 80 °C for 2 hr. The redispersion was achieved by adding a drop of water on the surface of dried particles.

3.3.12 Physical measurements

All the UV spectra were measured on a PerkinElmer Lambda 25 UV-Visible spectrometer. The z-average diameter (d_z) was obtained using a 50 mW He-Ne laser operating at 633 nm in a Malvern Zetasizer Nano ZS instrument. All TEM samples were prepared by drop-casting the dispersion (10 μL) onto a 300-mesh copper grid with a holey carbon film. The grid was held by a tweezer and allowed to dry overnight in a desiccator containing silica gel at room temperature. TEM images were inspected using a Philips CM20 TEM instrument at 200 kV. SEM was conducted on a Philips FEGSEM instrument and a FEI Magellan 400 X-treme High Resolution FEGSEM. All SEM samples were air-dried/freeze-dried and coated with carbon except the Au NPs. An Everhart-Thornley detector was used for secondary electron imaging mode and a circular backscattered detector operated in atomic number contrast mode.

3.4 Results and discussion

3.4.1 Au NP synthesis

As introduced in Chapter 2, the synthesis of Au NPs was achieved using the Turkvich method.[28-29] This is a standard method for producing Au NPs in a water-based reaction. The citrate reduction follows the nucleation and growth processes, which converted the Au^{III} to Au^{0}.[30, 43] In this synthesis, the colour of the solution changed from colourless to ruby red during the first 10 min of reaction (Fig. 3.1(A)). The colour change proved the formation of gold nanoparticles by its pronounced LSPR. Here, the molar ratio of HAuCl$_4$ and Na$_3$Ct was constrained at 4.1 to ensure that the size of nanoparticles was less than 20 nm.[30] The stirring speed was kept high (~ 950 rpm) during the rapid injection of Na$_3$Ct to minimise size dispersity and avoid the formation of aggregates as shown in Fig. 3.1(B).

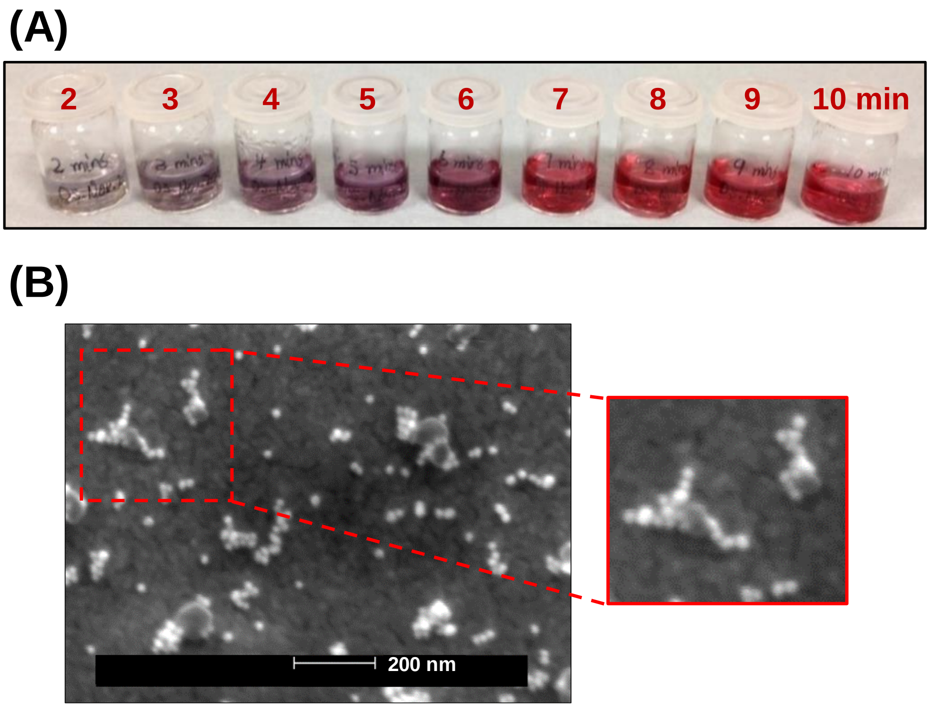

Figure 3.1 (A) The variation of colour during the synthesis of Au NPs, from 2 min to 10 min. (B) SEM images of Au NPs obtained with poor control of reaction. The aggregates are highlighted by a red border.

3.4.2 Au NP characterisation

3.4.2.1 Size and morphology

As shown in Fig. 3.2(A), a ruby red transparent dispersion was obtained without showing any sediments. SEM (Fig. 3.2(B)) was conducted on the prepared Au NPs, and the images show the uniform distribution of the spherical nanoparticles on the substrate. In contrast to Fig 3.1(B), there was no indication of any obvious Au NP aggregates. This result is consistent with the observation from TEM in Fig. 3.2(C). Black circular nanoparticles were visualised due to the high contrast arising from its atomic number and density. These nanoparticles efficiently stop the electron beam from transmitting to the detector. The number-average diameter of Au NPs was measured as 15 ± 1 nm. In Fig. 3.2(D), the DLS distribution also showed a low size dispersity for the Au NP dispersion. The d_z value (19 nm) was slightly greater than the size measured from the EM techniques. After the synthesis, the citrate stabilizing layer was formed around Au NPs. It acts as an electrostatic protection cover to maintain the stability of Au NPs in the dispersion.

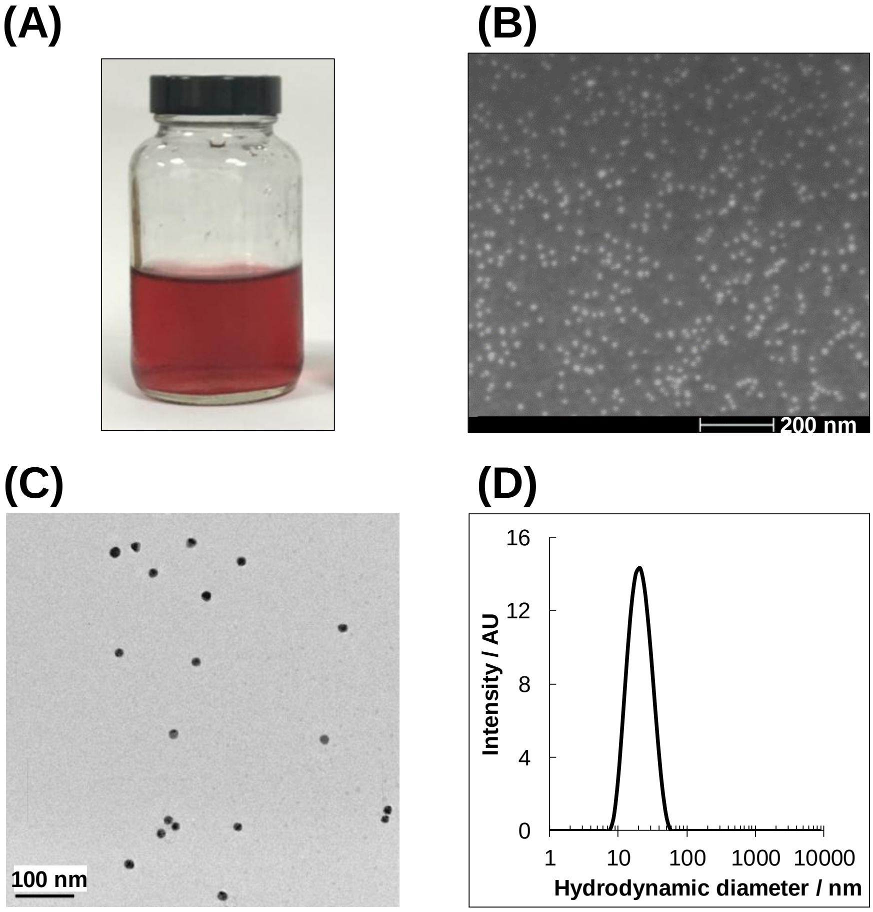

Figure 3.2 (A) The picture of Au NP dispersion after the synthesis. (B) SEM and (C) TEM images of dried Au NPs. (D) DLS size distribution of Au NP dispersion.

3.4.2.2 Molar particle concentration estimation

The theoretical molar concentration of Au NPs can be predicted by counting the number of Au atoms in the dispersion.[44-45] Assuming all atoms were arranged in the face-centred cubic structure, the density of Au NPs is 19.3×10^{-21} g nm^{-3}. The number of Au atoms per particle (N_p) was calculated from its measured diameter (D_p = nm^{-1}) using the following equation (3.1):

$$N_p = \frac{4\pi}{3}\left(\frac{D_p}{2}\right)^3 \times \frac{\rho_{Au}\, N_A}{M_{Au}} = \frac{\pi}{6} \times \frac{\rho_{Au} N_A {D_p}^3}{M_{Au}} \qquad (3.1)$$

$$N_p = 30.89602{D_p}^3 \qquad (3.2)$$

Where ρ_{Au} *is density of Au NPs and* M_{Au} *is the molar mass of Au* (197 g mol^{-1}). N_A is the Avogadro constant. Then the molar particle concentration of Au NPs (C_{Au}) can be obtained:

$$C_{Au} = \frac{N_{SUM}}{N_p V_d N_A} \qquad (3.3)$$

Where N_{SUM} is the total number of Au atoms in the dispersion and V_d is the total volume of the dispersion.

The final concentration is described as the number of particles per volume. However, this theoretical estimation is not accurate enough since a reliable particle concentration is required to manipulate the synthesis. The size of nanoparticles was considered as perfectly monodisperse and it also assumed all Au atoms were consumed to form particles. Here, the UV-Vis spectroscopy was applied to measure a particle concentration based on the Beer-Lambert Law, which showed a linear relationship between the absorbance and concentration of absorbents (Fig. 3.3(A)-(B)). As synthesised particle concentration was calculated as 2.97 nM using the Haiss's calibration table.[46]

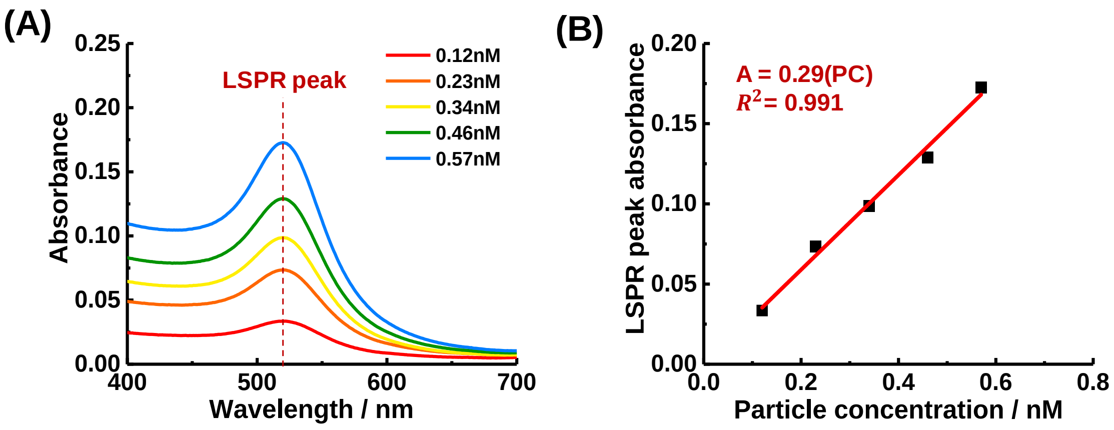

Figure 3.3 (A) UV-Vis spectra of Au NPs with different particle concentrations. (B) The calibration curve of Au NPs was constructed using LSPR peak absorbances.

3.4.3 Studying Au NP aggregation

3.4.3.1 UV-Vis spectroscopy

In order to understand the LSPR properties, the UV-Vis spectra of Au NPs were monitored. As shown in Fig. 3.4(A-D)**,** Au NPs were mixed with NaCl solutions and studied by UV-Vis spectroscopy over the time period of 15 min to 120 min. LSPR absorbance peak (Labelled by the red arrow) gradually decreased with time and this effect became more dominant when the NaCl concentration increased. The decrease of the absorbance could imply that number of isolated Au NPs decreased in the solution.[25-26] The addition of NaCl solution provided an ionic medium, which has a strong screening effect on the surface charge of Au NPs. The citrate protection layer was less functional under such conditions. As a result, it accelerated the formation of Au NPs aggregates as shown in Fig. 3.4(A-D). In the higher wavelength region of Fig. 3.4(D), an additional LSPR peak started to emerge with a broad area (Labelled by the blue arrow) and this process accelerated with a stronger ionic strength. This is an indication of the aggregation process of spherical Au NPs. During aggregation, Au NPs were bridged together to form an anisotropic shape which induces the irregular plasmon coupling effect with the change of the local effective electric field.[47-48] Then, the aggregates of Au NPs appeared as two bands of LSPR in the UV-Vis spectra. The emergence of new bands at higher wavelength is also found in a rod-like nanoparticle (transverse and longitudinal modes of LSPR).[26, 49-50]

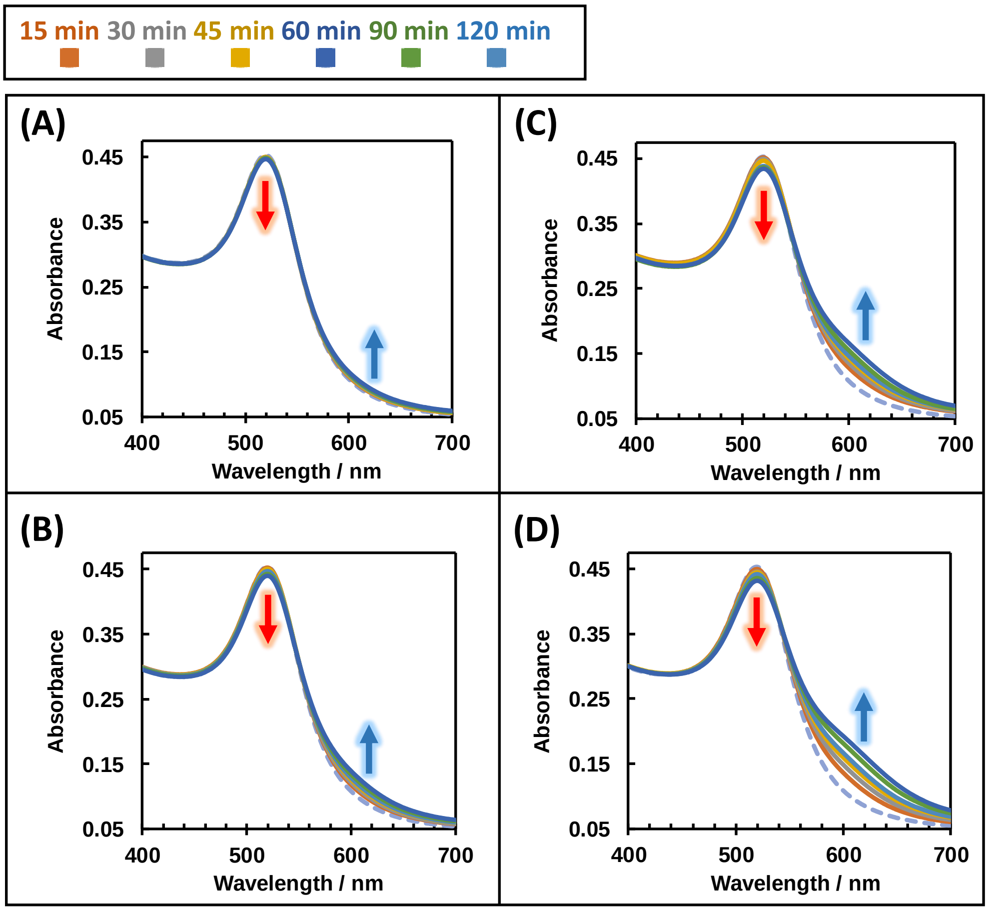

Figure 3.4 UV-Vis spectra of Au NPs measured in a NaCl medium from 15 min to 120 min. The salt concentrations were prepared as (A) 30 mM (B) 35 mM (C) 40 mM (D) 45 mM. The dashed line represented the spectrum of original Au NPs in water.

The kinetic process of aggregation was analysed after 10 min in a range of 12.5 mM – 50 mM NaCl solutions with 0.55 nM Au NPs. In Fig. 3.5(A), the second band of LSPR increased with the increase of NaCl concentration. The characteristic LSPR absorbance peak (at 519 nm) continuously decreased, and a new absorbance peak (at ~ 650 nm) gradually rose as expected. The change of absorbance significantly increased when more salt was introduced into the dispersion (Fig. 3.5(B)). This trend presented an upturn between 30 mM and 50 mM. The critical coagulation concentration (CCC) of Au NPs was determined in this region, and followed reaction limited aggregation. The shift of the characteristic LSPR peak was also observed when the salt concentration exceeded 35 mM and quickly moved from 519 nm to 527 nm at 50 mM (Fig. 3.5(C)).

This shift proved the aggregation occurred across the whole population of Au NPs at this ionic strength. In summary, 50 mM concentration of NaCl is strong enough to trigger an effective aggregation process of Au NPs and cause the dominant change of LSPR properties. This degree of ionic strength is almost unavoidable in most polymer syntheses, gel preparation and practical applications.

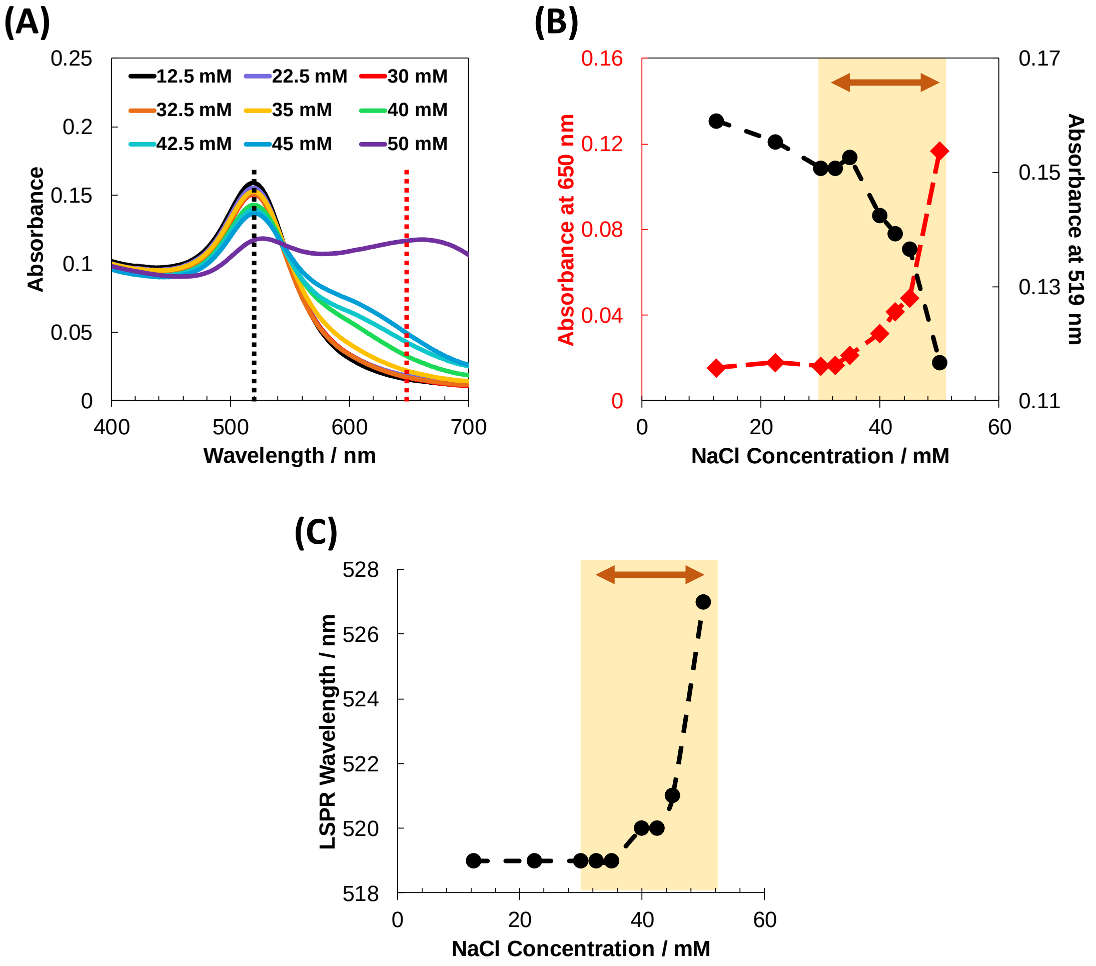

Figure 3.5 (A) UV-Vis spectra of Au NP dispersion in a NaCl solution with different concentrations (12.5 mM – 50 mM). (B) $A_{519\text{nm}}$ (Black) and $A_{650\text{nm}}$ (Red) are plotted against NaCl concentrations. (C) The red-shift of characteristic LSPR peak (from 519 nm) with NaCl concentrations. The CCC was located inside the brown areas.

3.4.3.2 DX MG and Au NP system

In this section, the study of DX MG and Au NP system has been published in Maximilian Schmidt's paper.[51] The included experimental works and analysis were contributed by Shanglin Wu. Poly(EA-MAA-DVB) MGs was synthesised using emulsion polymerisation as reported in a previous study.[41] MGs had a d_z value of 73 nm at pH 4.0, which was much larger than the d_z of Au NPs as shown in Fig. 3.6(A(i) and A(iii)). The mixing of diluted Au NPs and MGs generated two ranges of DLS size distributions. In Fig. 3.6(A(ii)), two individual peaks represented the size distributions of Au NPs and MGs, respectively. The position of the mixing peaks closely matched their original distributions of d_z. Both Au NPs and MGs were electrostatic stabilised and negatively charged.[41, 51] There was no strong attractive interaction among these different particles, which could potentially cause bridging. A soft DX MG was prepared by chemically crosslinking the concentrated GMA-functionalised MGs (13.7 wt%) (Fig. 3.6(B(i))). This gel could be potentially applied in repairing degenerated intervertebral discs.[44, 52] The mixing system of DX MGs and Au NPs (DX MG/Au NP) was transparent and expected to maintain the stability and functionality of both particles (Fig. 3.6(B(ii))).

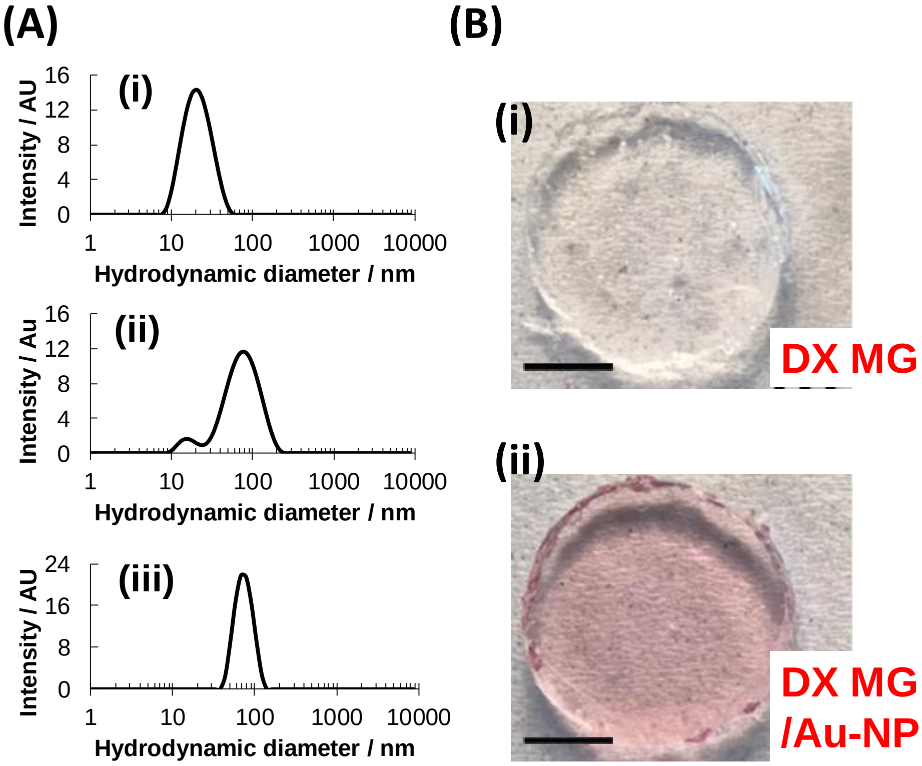

Figure 3.6 (A) DLS size distributions of (i) Au NP dispersion, (ii) Mixed MG/Au NP dispersion and (iii) MG dispersion. (B) Pictures of (i) DX MG and (ii) DX MG/Au NP gels. Scale bars = 0.5 mm.

High resolution SEM images of freeze-dried DX MG/Au NP gel are shown in Fig. 3.7(A-D). The images indicated the aggregates of particles were present in the matrix of the gel. In Fig. 3.7(A-B), secondary electron mode revealed some small clusters of particles from the topography of the gel. When the camera switched to backscattered electron mode (Fig. 3.7(C-D)), these clusters of particles were extensively brightened due to the high contrast of different components in the gel. This bright feature (as highlighted in the red dashed square) proved these clusters belonged to the particles with a high atomic number, which were recognised as Au NPs. The dispersity of these embedded Au NPs was comparable to the SEM images in Fig. 3.1(B). The strong aggregation of Au NPs still occurred broadly through the gel. Although the gelation process could trap Au NPs into the gel network, the high ionic strength (from NaOH or APS solution) still induced the instantaneous aggregation of Au NPs during the gel preparation. An unusual shift of the LSPR absorbance peak from 519 nm to 529 nm was also found in the UV-Vis spectrum after the formation of DX MG/Au NP gel from Schmidt's study.[51]

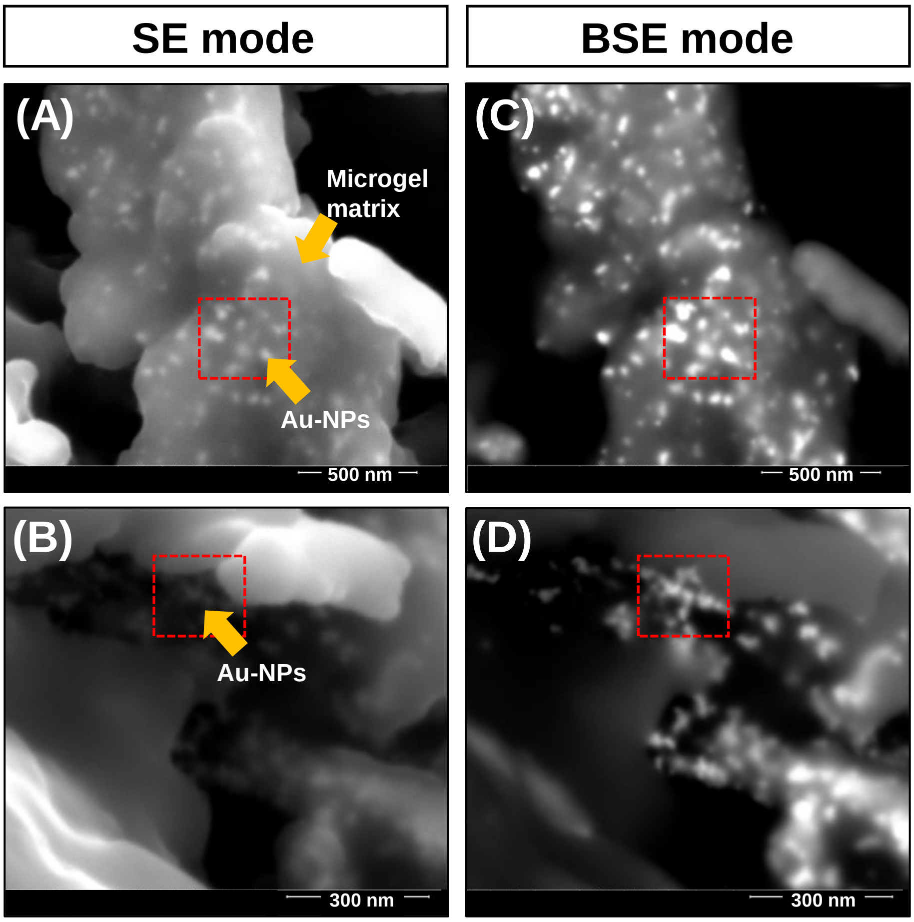

Figure 3.7 SEM images of DX MG/Au NP gels were observed under the ((A) and (B)) secondary electron mode, or ((C) and (D)) backscattered mode. Au NPs were distinguished by the brightness of materials and highlighted by the red dashed square in the microgel matrix.

3.4.4 Core-shell particle approach

The core-shell structure is a favourable form of Au NPs to avoid aggregation in various environments. The growth of a shell could maintain the separation of Au NPs, which endowed the stability of Au NPs and their LSPR properties. Hence, the core-shell Au NPs was proposed and studied by different routes. We used precipitation polymerisation, which required the deposition of monomers/oligomers on the surface of particles. A low monomer concentration was used because the particle concentration of Au NPs is limited in solution. The target shell structure comprised poly(MMA-MAA-EDGMA), which matched the composition of polyacid NGs as previously reported.[40]

3.4.4.1 Low concentration poly(MMA-MAA-EDGMA) particle characterisation

The synthesis of NGs was applied to examine the particle growth at a low monomer concentration. The product was a transparent and clear dispersion (Fig. 3.8(A)). Poly(MMA-MAA-EGDMA) particles were confirmed as a spherical shape in SEM (Fig. 3.8(B)), and they were dispersed due to the carboxylic groups from MAA.[40] TEM also confirmed the presence of poly(MMA-MAA-EGDMA) particles, and the number-average diameter was measured as 37 ± 5 nm (Fig. 3.8(C)). In comparison to Au NPs, poly(MMA-MAA-EGDMA) particles had less contrast in the background due to their much lower density and average atomic number. This large difference of contrast facilitated the observation of core-shell structure by TEM later. In Fig. 3.8(D), DLS size measurement showed the d_z value was 35 nm with a low polydispersity. Overall, the results confirmed the feasibility of the synthesis of poly(MMA-MAA-EGDMA) particles at the low monomer concentration and surfactant-free state.

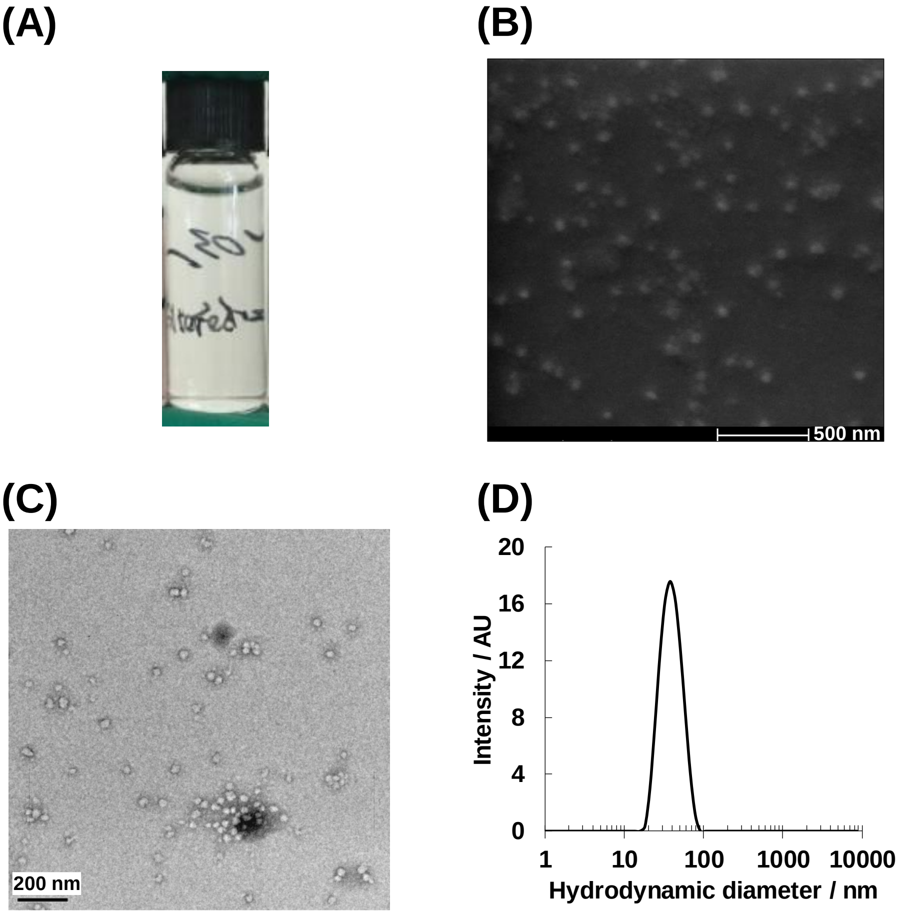

Figure 3.8 (A) The picture of poly(MMA-MAA-EGDMA) NGs. (B) SEM and (C) TEM images of dried poly(MMA-MAA-EGDMA) NGs. (D) DLS size distributions of poly(MMA-MAA-EGDMA) NG dispersion.

3.4.4.2 Core-shell particle approach using Method 1

Citrate-stabilised Au NPs were directly introduced to the synthesis of low concentration poly(MMA-MAA-EGDMA) particles in Method 1 (Fig. 3.9(A)). In Fig. 3.9(B), the normalised UV-Vis spectra showed a characteristic absorbance peak of Au NP aggregates at a higher wavelength region, accompanied a shift of main LSPR peak from 519 nm to 521 nm. The inset picture (Fig. 3.9(B)) shows the colour of the dispersion changed from red to purple after this core-shell synthesis. Again, the evidence of aggregation was also found in DLS (Fig. 3.9(C)) which showed the multiple size distributions of particles across a range of 1 nm and 10000 nm.

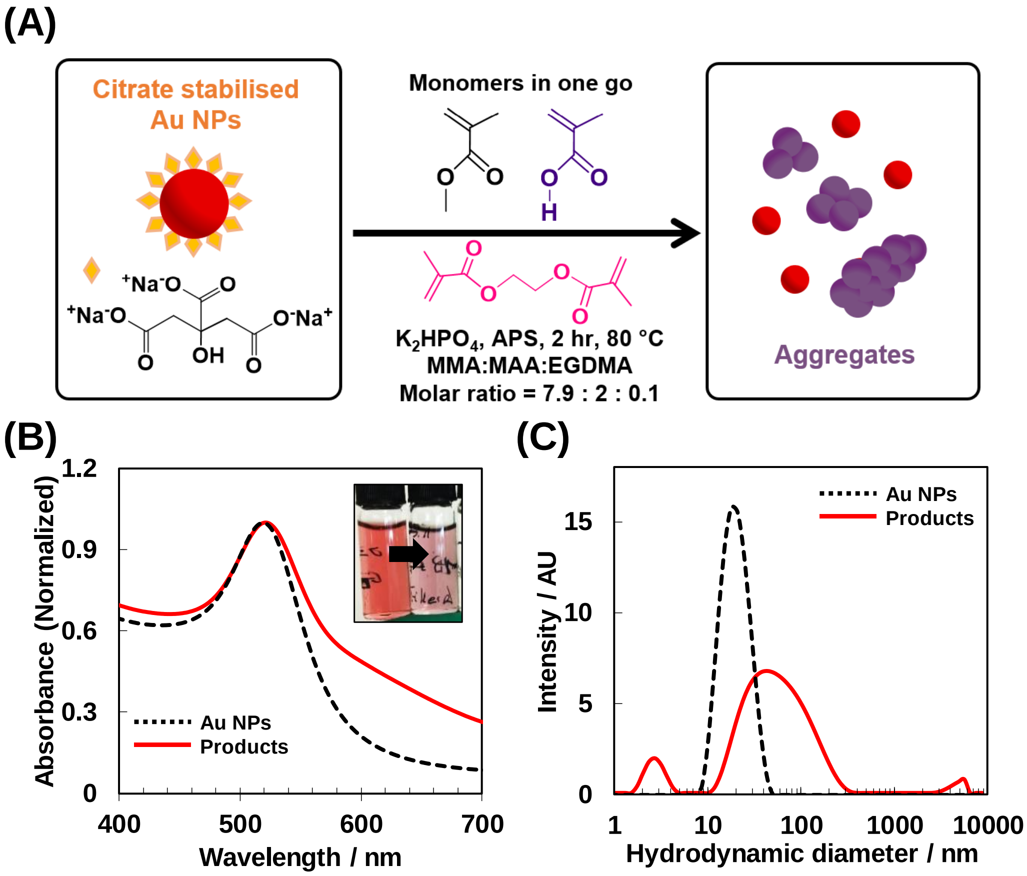

Figure 3.9 (A) Schematic depiction of the copolymer shell growth using MMA, MAA, EGDMA from Method 1. (B) UV-Vis spectra of Au NPs and core-shell particle products. The inset picture showed a transition of colour in the dispersion after the synthesis. (C) DLS size distributions of Au NPs and core-shell particle products.

Although the Au NPs were electrostatic stabilised by the citrate ions, these results indicated they were still able to form aggregates during the synthesis. The design of electrolyte concentration was lower than 50 mM in the synthesis, however, it was heated at 80°C. The probability of collisions and thermal energy among the nanoparticles would increase. The monomer/oligomers also had the potential to bridge Au NPs through a hydrophobic interaction during the growth. TEM images confirmed large aggregates of Au NPs (~ 17 particles, labelled by the yellow arrow in Fig. 3.10(A)) were present in the product. Some discrete poly(MMA-MAA-EGDMA) particles were also found with a range around 70 – 160 nm as shown in SEM (Fig. 3.10(B)). There was no direct evidence which could prove the formation of core-shell particles by Method 1.

The results implied that the negatively charged citrate layer was not a favourable surface for any adsorption of monomers/oligomers. The aggregation process also inhibited and disturbed the synthesis of poly(MMA-MAA-EGDMA) NGs/shells.

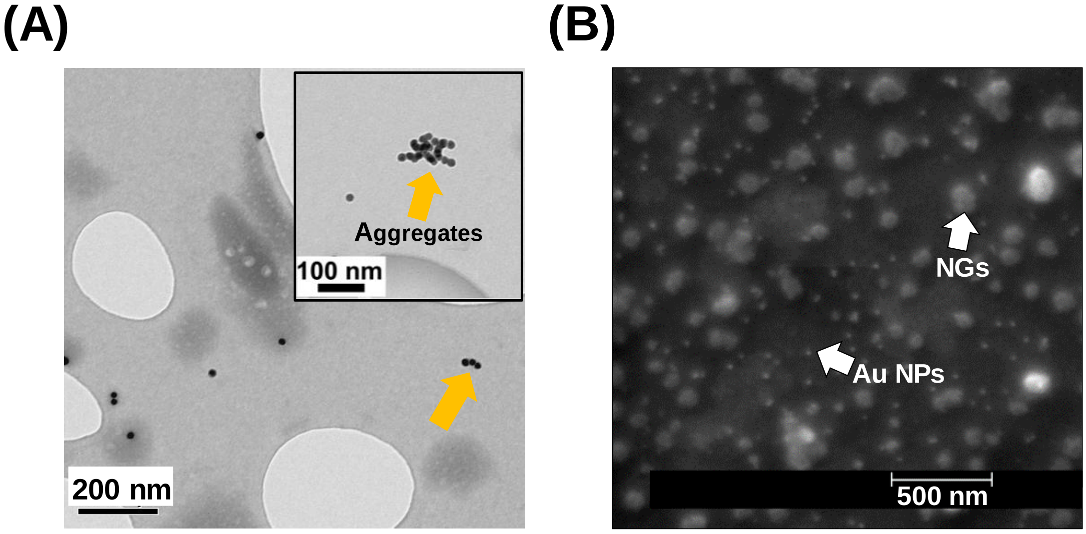

Figure 3.10 EM images of particles from Method 1. (A) TEM images of dried core-shell particle products. Aggregates were observed and identified with a yellow arrow. (B) SEM images of dried core-shell particle products.

3.4.4.3 Core-shell particle approach using Method 2

Here, the pre-functionalisation step was used to modify the surface property of Au NPs based on Rauh’s study of Au-poly(NIPAM) core-shell particles.[8] In addition, a small dose of SDS was added to keep the stabilisation of Au NPs during the shell growth (Fig. 3.11(A)), which was inspired by Method 1. The dispersion did not show any evidence of aggregation from the UV-Vis spectra in Fig. 3.11(B). A LSPR peak shift was observed, which slightly moved from 519 nm to 523 nm. This shift could be mostly attributed by the change of refractive index around the Au NPs. However the shift was small for an expected crosslinked copolymer shell based on the Drude model.[53] DLS measurement showed that shift was caused by the presence of two size distributions of particles (Fig. 3.11(C)). The large peak had a similar size distribution compared to Au

NPs, which indicated an inhomogeneous shell growth (bare Au NPs left) after the synthesis. The small peak resided at a position larger than 100 nm.

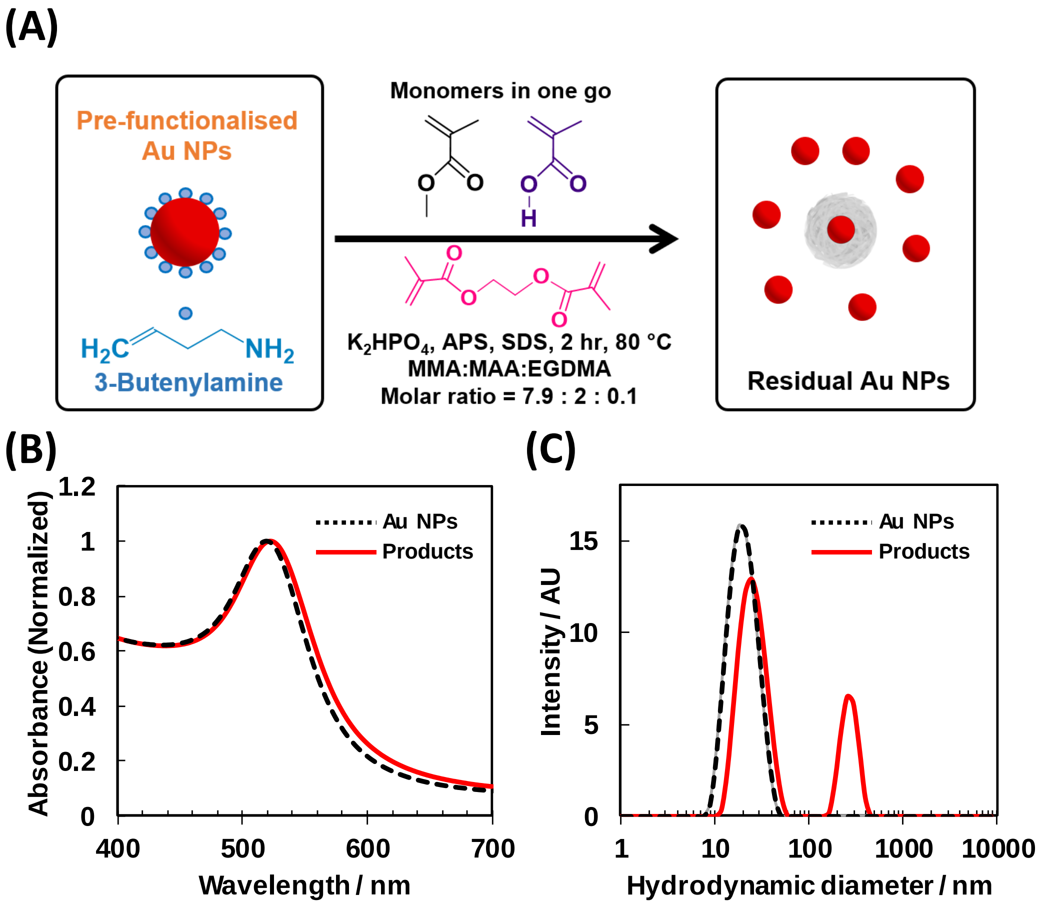

Figure 3.11 (A) Schematic depiction of the copolymer shell growth using MMA, MAA, EGDMA from Method 2. (B) UV-Vis spectra of Au NPs and core-shell particle products. (C) DLS size distributions of Au NPs and core-shell particle products.

TEM could clearly distinguish two species based on the high contrast of these materials. A core-shell structure was well-defined in Fig. 3.12(A). A thick copolymer shell (Yellow arrow) wrapped around the Au NPs (Red arrow) in the image. The diameter of core-shell particles was distributed in a broad range of 130 – 350 nm, which has a comparable size with the poly(NIPAM) shell from Rauh's study.[8] This value was much larger than the expected diameter based on the synthesis of poly(MMA-MAA-EGDMA) NGs, and the growth of the shell was less homogenous in this low concentration system. The distribution of many discrete bare Au NPs and large core-shell particles supported this statement in SEM (Fig. 3.12(B)). Overall, the result suggested the functionalised surface was not as good as expected for the homogenous shell growth in this polyacid system.

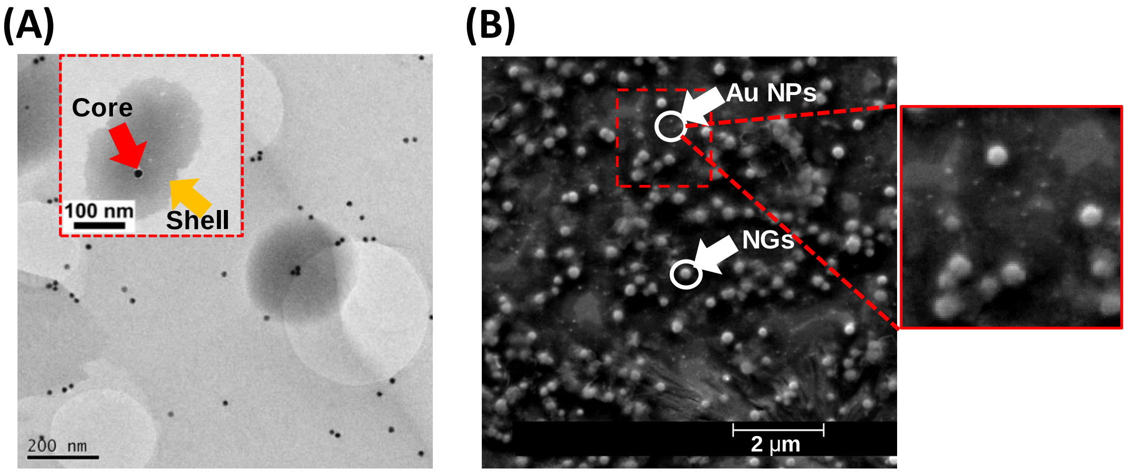

Figure 3.12 EM images of particles from Method 2. (A) TEM images of dried core-shell particle products. The inset picture showed a core-shell particle. The Au core was identified with a red arrow, and the copolymer shell was identified with a yellow arrow. (B) SEM images of dried core-shell particle products with a magnified area.

3.4.4.4 Core-shell particle approach using Method 3

As described in Section 3.3.9, a monomer feeding process of MMA, MAA and EGDMA mixtures was applied at a constant speed over 1 hr, and the pre-functionalisation step was removed compared to Method 2. Instead, the citrate stabilising ions of Au NPs were removed by centrifugation and stabilised by a small dose of SDS during the growth of shells (Fig. 3.13(A)). As shown in Fig. 3.13(B), a transparent and red-pink product was obtained from the synthesis. The UV-Vis spectra showed a uniform red-shift of LSPR peak from 519 nm to 529 nm (Fig. 3.13(C)), without showing any characteristic peaks or evidences of aggregation. The 10 nm red-shift could represent a significant refractive index change in proximity of Au NPs.

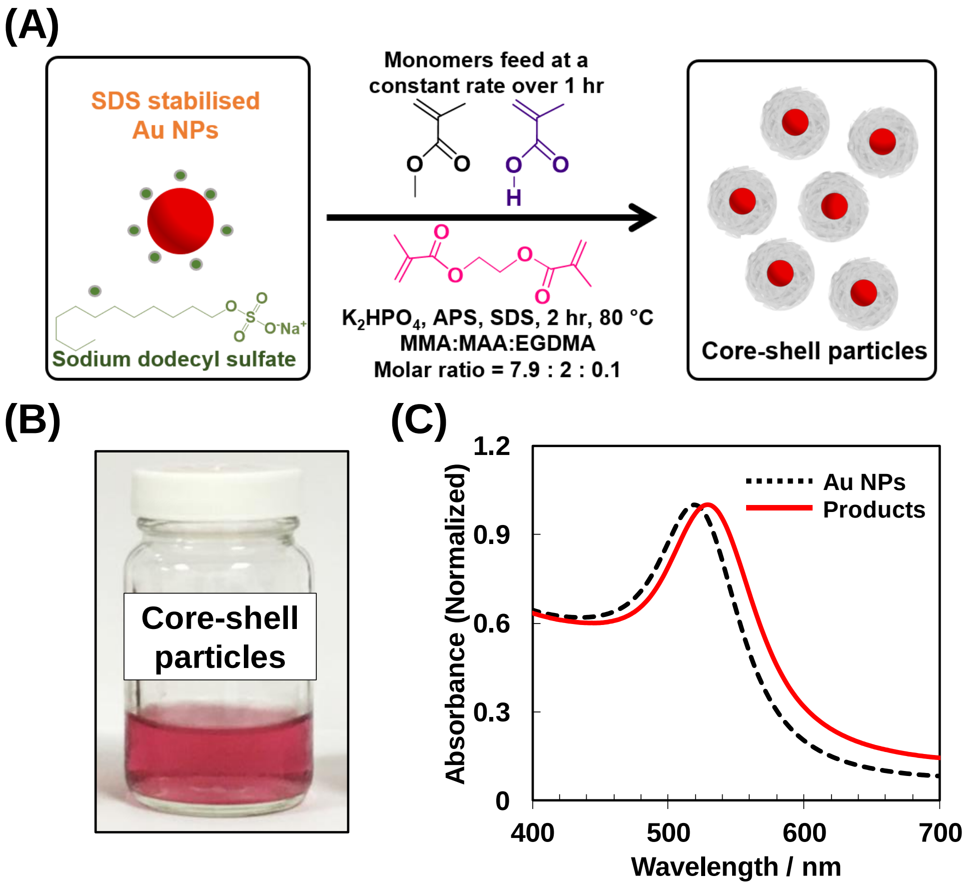

Figure 3.13 (A) Schematic depiction of the copolymer shell growth using MMA, MAA, EGDMA from Method 3. (B) The picture of a core-shell dispersion with a visible colour change. (C) UV-Vis spectra of Au NPs and core-shell particle products.

The d_z also consistently increased to 38 nm compared to Au NPs in Fig. 3.14(A). These results indicated the synthesis of poly(MMA-MAA-EGDMA) shell was more homogenous and grew simultaneously on all of the Au NPs, which contrasts to the previous methods. TEM showed the core-shell particles were successfully prepared at a high yield using this approach (Fig. 3.14(B)). A well-defined structure of Au NPs core (Red arrow) and copolymer shell (Yellow arrow) was clearly revealed. Bare Au NPs could not be found after checking > 30 positions over the carbon film coated copper grid. The TEM diameter of core-shell particles was measured as 35 ± 3 nm which has a similar size compared to poly(MMA-MAA-EGDMA) NGs (Fig. 3.8(C)). It strongly supported that poly(MMA-MAA-EGDMA) copolymer shell was permanently added to the surface of Au NPs. Summarising these results, Method 3 provided a new pathway of polyacid shell growth through the precipitation polymerisation without any pre-functionalisation steps. The deposition of monomers or oligomers was facilitated by the direct contact with Au using the successive monomer feeding and the aid of SDS stabilisation.

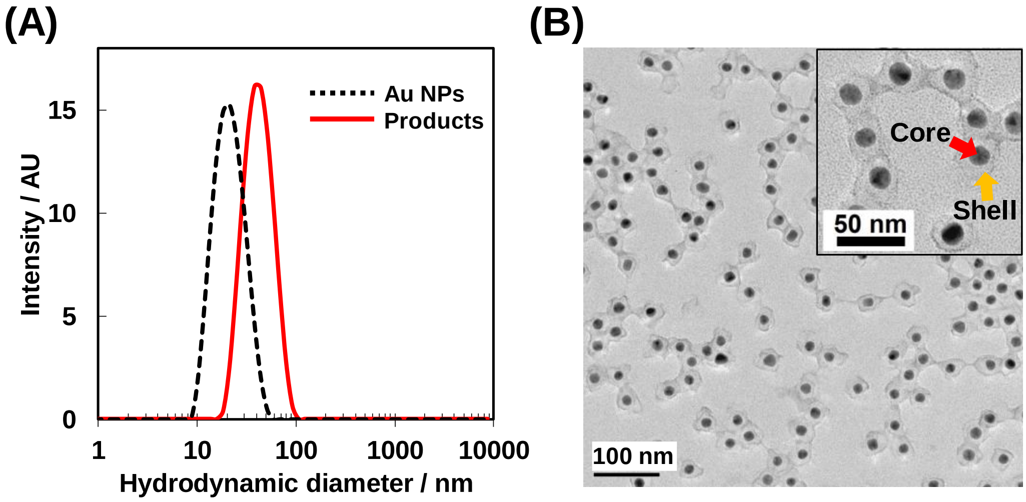

Figure 3.14 Particle characterisation from method 3. (A) DLS size distributions of Au NPs and core-shell particle products. (B) TEM images of dried core-shell particle products. The inset picture highlighted multiple core-shell particles. The Au core was identified with a red arrow, and the copolymer shell was identified with a yellow arrow.

3.4.5 Enhanced stability of core-shell particles

3.4.5.1 Colloidal stability to electrolyte

The electrolyte stability of core-shell particle dispersions (from method 3) and Au NP dispersions were tested in various concentrations of NaCl solution from 0 mM to 50 mM, and a PBS buffer using UV-Vis spectroscopy (Fig. 3.15(A(i)) and Fig. 3.15(B(i))). As shown in Fig. 3.15(B(ii)), 50 mM NaCl medium was strong enough to trigger the visible aggregation of Au NPs due to the strong plasmon coupling effect. Fig. 3.15(A(i-ii)) showed that the core-shell particles brought the additional stability of the LSPR property in the salt solution. The colour/spectral responses did not change which contrasts to the Au NP dispersion. The latter showed the emergence of a new absorbance peak near 650 nm with a significant colour change. In addition, both core-shell particles and Au NPs were mixed in PBS buffer. The results showed a great enhancement of the stability of core-shell particles at physiological pH condition (Fig. 3.15(A(i)) and Fig 3.15(B(i))). This stability could enable the potential application of the core-shell particles in vivo, where the salt concentration (~ 0.15 M) would immediately cause the irreversible aggregation of Au NPs.

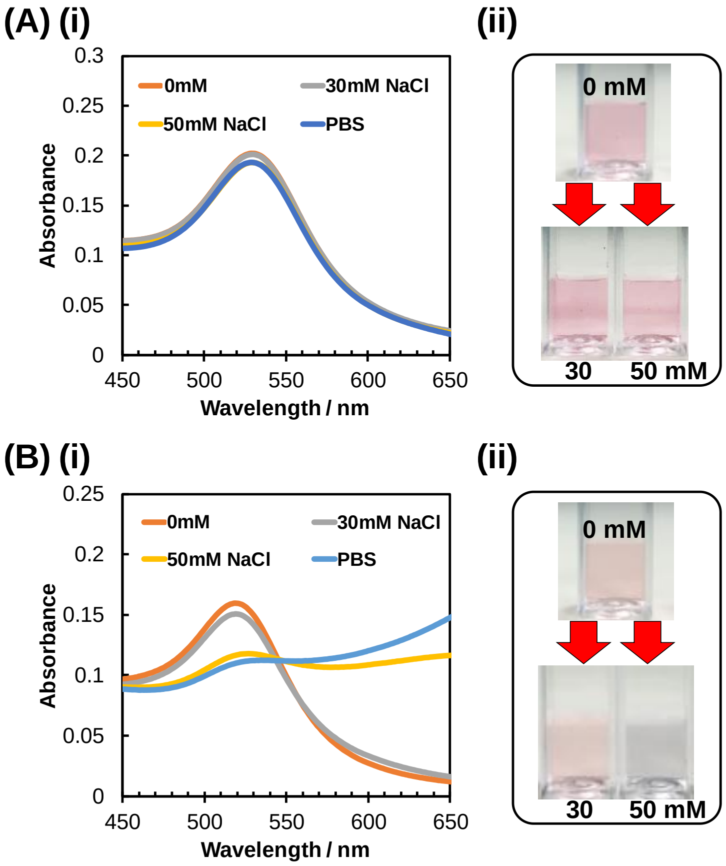

Figure 3.15 (A) (i) UV-Vis spectra of core-shell particles (Method 3) dispersed in the solution with different NaCl concentrations and also PBS. (ii) The picture showed the transition of colour in the dispersion. (B) (i) UV-Vis spectra of Au NPs were tested in the same way and used as the control data. (ii) The picture showed the transition of colour in the dispersion.

3.4.5.2 Reversible aggregation

The reversibility of Au NPs and core-shell particle aggregates was tested in a saturated aqueous NaCl solution. This ultra-strong ionic medium triggered aggregation and sedimentation of core-shell particles after 1 day. The inset picture and UV-Vis spectra of red sediment were shown in Fig. 3.16(A(i-ii)), and the characteristic absorbance peak of core-shell particles was still observable at 529 nm in the spectrum. This robust encapsulation of copolymer endowed the ultra-strong colloidal stability to Au NPs. The LSPR of sediments was little affected and remained a red-pink colour even after aggregation. In comparison, Au NPs completely lost their LSPR properties without a good protection shell (Fig. 3.16(B(i-ii))). After a slight agitation of the aggregates, a pronounced LSPR absorbance peak of core-shell particles and red dispersions were regained in Fig. 3.16(A(iii)). The LSPR peak wavelength only red-shifted ~ 3 nm compared to the original spectrum (Fig. 3.16(A(i))). The LSPR property of Au NPs was permanently lost and non-redispersible in water as shown in Fig. 3.16(B(iii)).

The van der Waals attraction should be responsible for this difference of stability. The volume fraction of Au NPs core and poly(MMA-MAA-EGDMA) shell were calculated as ~ 7.9 vol% and 92.1 vol% respectively based on their TEM diameters (Au NPs = 15 nm, Core-shell particles = 35 nm). The van der Waals attraction of gold could be less dominant in this structure. The thick copolymer shell ($A_{eff} = 5.5 \times 10^{-20}$ J) has a much lower effective Hamaker (A_{eff}) constant in water compared to the Au NPs ($A_{eff} = 95 \times 10^{-20}$ J) which were calculated from equation 3.4:[54]

$$A_{eff} = (\sqrt{A_1} - \sqrt{A_2})^2 \qquad (3.4)$$

Where the materials ($A_{1(Au)} = 25 \times 10^{-20}$ J or $A_{1(MMA)} = 7.1 \times 10^{-20}$ J)[55-56] were dispersed in the water phase ($A_{2(water)} = 3.7 \times 10^{-20}$ J)[57]. The particle-particle attractive interaction energy is proportional to A_{eff},[54] which explained why the stability of the core-shell system is much better than Au NPs.

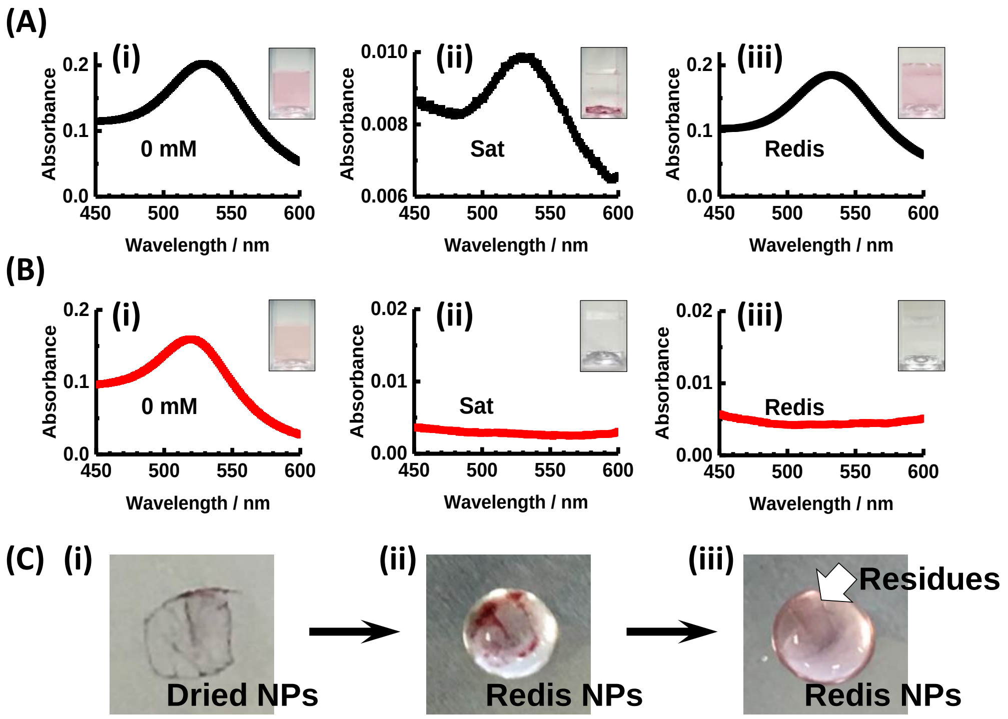

Figure 3.16 UV-Vis spectra of (A) core-shell particles (Method 3) and (B) Au NPs dispersed in the saturated NaCl solution. (i)-(iii) showed start, aggregation and redispersion stages of the experiment, respectively. The inset pictures showed the state of the dispersion at different stages. (C) Pictures of oven dried core-shell particles (Method 3). (i)-(iii) showed the redispersion process with a drop of water.

The photographs showed the redispersibility of core-shell particles which were completely pre-dried in the oven (Fig. 3.16(C(i-iii))). The dried core-shell particles became a black solid film in appearance. The loss of water caused the complete collapse and shrinkage of copolymer shells. Particles tended to accumulate intensively under the heat, and it could not maintain a well-defined distance among Au NP cores. A strong plasmon coupling effect would occur in adjacent Au NPs. The latter was the reason for a colour change, however, the original red colour was easily restored by a drop of water

(~ 10s). This indicated the crosslinked poly(MMA-MAA-EGDMA) shell quickly swelled back to a hydrated state and hindered the plasmon coupling. The observation highlighted the advantage of this robust poly(MMA-MAA-EGDMA) shell in the enhancement of colloidal stability, and it also provided a method to determine whether the core-shell structure was successfully synthesised with the similar composition of copolymer.

3.4.6 Large scale core-shell particle synthesis

The feasibility of large scale synthesis was studied by varying the particle concentration of Au NPs in the synthesis based on Method 3. UV-Vis spectra of the products were recorded separately in Fig. 3.17(A). An increasing trend of the absorbance was observed following an order of 1.14 nM < 2.28 nM < 3.42 nM Au NPs, which were seeded in the synthesis. The red shift of LSPR absorbance peaks was confirmed from 519 nm to 529 nm in all three concentrations. Fig. 3.17(B) showed a linear trend when the concentration of Au NPs was plotted against the absorbance of the corresponding core-shell particles. They showed a proportional relationship which indicated an efficient synthesis by varying the concentrations of Au NP seeding. In addition, a saturated NaCl solution was added into three core-shell dispersions respectively. Red sediments were obtained in all the solutions (Fig. 3.17(C)) and clearly became denser from 1.14 nM to 3.42 nM Au NP seeding. These results supported the observation from the UV-Vis spectra and confirmed the strong colloidal stability of this new core-shell system.

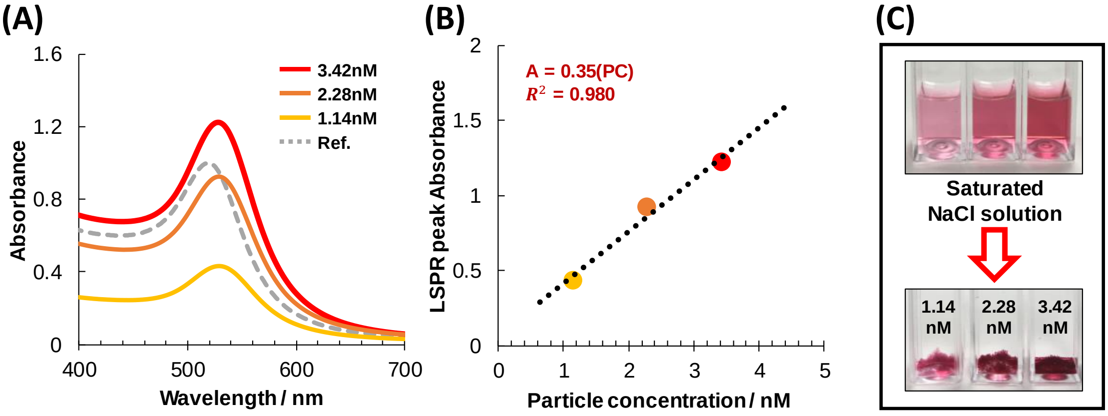

Figure 3.17 (A) UV-Vis spectra of three core-shell samples (Method 3) were prepared with 1.14 nM, 2.28 nM and 3.42 nM Au NPs seeding. Normalised UV-Vis spectra of Au NPs were used as the reference. (B) The LSPR absorbance peaks of core-shell samples are plotted against the particle concentration of Au NPs used in the synthesis. (C) The images showed three core-shell samples were triggered to form red sediments in a saturated NaCl solution.

3.5 Conclusions

The colloidal stability of citrated stabilised Au NPs was extensively explored in this study. The critical coagulation concentration of Au NPs was defined as ~ 50 mM in the NaCl medium. The SEM images confirmed this stabilisation was not strong enough to maintain their original dispersity (and their LSPR properties) in the application of DX MG system. A new and efficient core-shell synthesis was developed here without requiring any pre-functionalisation steps. The evaluation of three different core-shell structure approaches finally enabled the growth of a protective poly(MMA-MAA-EGDMA) NG shell around Au NPs. This new synthesis is facile and controllable by the monomer feeding process, which has the potential for the large-scale production. Poly(MMA-MAA-EGDMA) copolymer shells endowed the ultra-strong colloidal stability to Au NPs. The LSPR property of core-shell particles can be maintained in a saturated aqueous NaCl solution and restorable from the solid state. These features are beneficial for the storage and design of the microgel or hydrogel applications.

3.6 References

1. Daniel, M. C.; Astruc, D., Gold nanoparticles: assembly, supramolecular chemistry, quantum-size-related properties, and applications toward biology, catalysis, and nanotechnology. *Chem Rev* **2004,** *104*, 293-346.

2. Saha, K.; Agasti, S. S.; Kim, C.; Li, X.; Rotello, V. M., Gold nanoparticles in chemical and biological sensing. *Chem Rev* **2012,** *112*, 2739-79.

3. Pelaz, B.; Alexiou, C.; Alvarez-Puebla, R. A.; Alves, F.; Andrews, A. M.; Ashraf, S.; Balogh, L. P.; Ballerini, L.; Bestetti, A.; Brendel, C.; et al., Diverse Applications of Nanomedicine. *ACS Nano* **2017,** *11*, 2313-2381.

4. Yilmaz, G.; Demir, B.; Timur, S.; Becer, C. R., Poly(methacrylic acid)-Coated Gold Nanoparticles: Functional Platforms for Theranostic Applications. *Biomacromolecules* **2016,** *17*, 2901-11.

5. Liz-Marzán, L. M.; Giersig, M.; Mulvaney, P., Synthesis of Nanosized Gold−Silica Core−Shell Particles. *Langmuir* **1996,** *12*, 4329-4335.

6. Reineck, P.; Gomez, D.; Ng, S. H.; Karg, M.; Bell, T.; Mulvaney, P.; Bach, U., Distance and wavelength dependent quenching of molecular fluorescence by Au@SiO2 core-shell nanoparticles. *ACS Nano* **2013,** *7*, 6636-48.

7. Karg, M.; Jaber, S.; Hellweg, T.; Mulvaney, P., Surface plasmon spectroscopy of gold-poly-N-isopropylacrylamide core-shell particles. *Langmuir* **2011,** *27*, 820-7.

8. Rauh, A.; Honold, T.; Karg, M., Seeded precipitation polymerization for the synthesis of gold-hydrogel core-shell particles: the role of surface functionalization and seed concentration. *Colloid Polym. Sci.* **2015,** *294*, 37-47.

9. Man, R. W. Y.; Li, C. H.; MacLean, M. W. A.; Zenkina, O. V.; Zamora, M. T.; Saunders, L. N.; Rousina-Webb, A.; Nambo, M.; Crudden, C. M., Ultrastable Gold Nanoparticles Modified by Bidentate N-Heterocyclic Carbene Ligands. *J Am Chem Soc* **2018,** *140*, 1576-1579.

10. Steiner, A. M.; Mayer, M.; Seuss, M.; Nikolov, S.; Harris, K. D.; Alexeev, A.; Kuttner, C.; Konig, T. A. F.; Fery, A., Macroscopic Strain-Induced Transition from Quasi-infinite Gold Nanoparticle Chains to Defined Plasmonic Oligomers. *ACS Nano* **2017,** *11*, 8871-8880.

11. Anker, J. N.; Hall, W. P.; Lyandres, O.; Shah, N. C.; Zhao, J.; Van Duyne, R. P., Biosensing with plasmonic nanosensors. *Nat Mater* **2008,** *7*, 442-53.

12. Mieszawska, A. J.; Mulder, W. J.; Fayad, Z. A.; Cormode, D. P., Multifunctional gold nanoparticles for diagnosis and therapy of disease. *Mol Pharm* **2013,** *10*, 831-47.

13. Huang, X.; Liu, Y.; Yung, B.; Xiong, Y.; Chen, X., Nanotechnology-Enhanced No-Wash Biosensors for in Vitro Diagnostics of Cancer. *ACS Nano* **2017,** *11*, 5238-5292.

14. Huang, X.; El-Sayed, I. H.; Qian, W.; El-Sayed, M. A., Cancer cell imaging and photothermal therapy in the near-infrared region by using gold nanorods. *J Am Chem Soc* **2006,** *128*, 2115-20.

15. Jin, R.; Zeng, C.; Zhou, M.; Chen, Y., Atomically Precise Colloidal Metal Nanoclusters and Nanoparticles: Fundamentals and Opportunities. *Chem Rev* **2016,** *116*, 10346-413.

16. Mosquera, J.; Henriksen-Lacey, M.; Garcia, I.; Martinez-Calvo, M.; Rodriguez, J.; Mascarenas, J. L.; Liz-Marzan, L. M., Cellular Uptake of Gold Nanoparticles Triggered by Host-Guest Interactions. *J Am Chem Soc* **2018,** *140*, 4469-4472.

17. Lin, C.-H.; Liu, X.; Wu, S.-H.; Liu, K.-H.; Mou, C.-Y., Corking and Uncorking a Catalytic Yolk-Shell Nanoreactor: Stable Gold Catalyst in Hollow Silica Nanosphere. *J. Phys. Chem. Lett.* **2011,** *2*, 2984-2988.

18. Yin, Z.; Wang, Y.; Song, C.; Zheng, L.; Ma, N.; Liu, X.; Li, S.; Lin, L.; Li, M.; Xu, Y.; Li, W.; Hu, G.; Fang, Z.; Ma, D., Hybrid Au-Ag Nanostructures for Enhanced Plasmon-Driven Catalytic Selective Hydrogenation through Visible Light Irradiation and Surface-Enhanced Raman Scattering. *J Am Chem Soc* **2018,** *140*, 864-867.

19. Mayer, K. M.; Hafner, J. H., Localized surface plasmon resonance sensors. *Chem Rev* **2011,** *111*, 3828-57.

20. Thacker, V. V.; Herrmann, L. O.; Sigle, D. O.; Zhang, T.; Liedl, T.; Baumberg, J. J.; Keyser, U. F., DNA origami based assembly of gold nanoparticle dimers for surface-enhanced Raman scattering. *Nat Commun* **2014,** *5*, 3448.

21. Du, J.; Qi, J.; Wang, D.; Tang, Z., Facile synthesis of Au@TiO2 core–shell hollow spheres for dye-sensitized solar cells with remarkably improved efficiency. *Energy Environ. Sci.* **2012,** *5*.

22. Lu, L.; Luo, Z.; Xu, T.; Yu, L., Cooperative plasmonic effect of Ag and Au nanoparticles on enhancing performance of polymer solar cells. *Nano Lett* **2013,** *13*, 59-64.

23. Molina, M.; Asadian-Birjand, M.; Balach, J.; Bergueiro, J.; Miceli, E.; Calderón, M., Stimuli-responsive nanogel composites and their application in nanomedicine. *Chem. Soc. Rev.* **2015,** *44*, 6161-6186.

24. Liu, Y.; Shipton, M. K.; Ryan, J.; Kaufman, E. D.; Franzen, S.; Feldheim, D. L., Synthesis, stability, and cellular internalization of gold nanoparticles containing mixed peptide-poly(ethylene glycol) monolayers. *Anal Chem* **2007,** *79*, 2221-9.

25. Chegel, V.; Rachkov, O.; Lopatynskyi, A.; Ishihara, S.; Yanchuk, I.; Nemoto, Y.; Hill, J. P.; Ariga, K., Gold Nanoparticles Aggregation: Drastic Effect of Cooperative Functionalities in a Single Molecular Conjugate. *J. Phys. Chem. C* **2012,** *116*, 2683-2690.

26. Yang, Y.; Matsubara, S.; Nogami, M.; Shi, J., Controlling the aggregation behavior of gold nanoparticles. *Mater. Sci. Eng., B* **2007,** *140*, 172-176.

27. Yang, X.; Yang, M.; Pang, B.; Vara, M.; Xia, Y., Gold Nanomaterials at Work in Biomedicine. *Chem Rev* **2015,** *115*, 10410-88.

28. Enustun, B. V.; Turkevich, J., *J Am Chem Soc* **1963,** *85*, 3317-3328.

29. Turkevich, J.; Stevenson, P. C.; Hillier, J., A study of the nucleation and growth processes in the synthesis of colloidal gold. *Discuss. Faraday Soc.* **1951,** *11*.

30. Ji, X.; Song, X.; Li, J.; Bai, Y.; Yang, W.; Peng, X., Size control of gold nanocrystals in citrate reduction: the third role of citrate. *J Am Chem Soc* **2007,** *129*, 13939-48.

31. Wang, G.; Sun, W., Optical limiting of gold nanoparticle aggregates induced by electrolytes. *J Phys Chem B* **2006,** *110*, 20901-5.

32. Wu, C.; Xu, Q. H., Stable and functionable mesoporous silica-coated gold nanorods as sensitive localized surface plasmon resonance (LSPR) nanosensors. *Langmuir* **2009,** *25*, 9441-6.

33. Kwon, N. K.; Lee, T. K.; Kwak, S. K.; Kim, S. Y., Aggregation-Driven Controllable Plasmonic Transition of Silica-Coated Gold Nanoparticles with Temperature-Dependent Polymer-Nanoparticle Interactions for Potential Applications in Optoelectronic Devices. *ACS Appl Mater Interfaces* **2017,** *9*, 39688-39698.

34. Kim, J. H.; Lee, T. R., Hydrogel-templated growth of large gold nanoparticles: synthesis of thermally responsive hydrogel-nanoparticle composites. *Langmuir* **2007,** *23*, 6504-9.

35. Guarrotxena, N.; Quijada-Garrido, I., Optical and Swelling Stimuli-Response of Functional Hybrid Nanogels: Feasible Route to Achieve Tunable Smart Core@Shell Plasmonic@Polymer Nanomaterials. *Chem. Mater.* **2016,** *28*, 1402-1412.

36. Kang, Y.; Taton, T. A., Core/Shell gold nanoparticles by self-assembly and crosslinking of micellar, block-copolymer shells. *Angew Chem Int Ed Engl* **2005,** *44*, 409-12.

37. Dulle, M.; Jaber, S.; Rosenfeldt, S.; Radulescu, A.; Forster, S.; Mulvaney, P.; Karg, M., Plasmonic gold-poly(N-isopropylacrylamide) core-shell colloids with homogeneous density profiles: a small angle scattering study. *Phys Chem Chem Phys* **2015,** *17*, 1354-67.

38. Zhou, J.; Jeon, J.-W.; Ponder, J. F.; Geldmeier, J. A.; Mahmoud, M. A.; El-Sayed, M.; Reynolds, J. R.; Tsukruk, V. V., Electrochromic tuning of transparent gold nanorods with poly[(3,4-propylenedioxy)pyrrole] shells in the near-infrared region. *J. Mater. Chem. C* **2017,** *5*, 12571-12584.

39. Pereira, S. O.; Barros-Timmons, A.; Trindade, T., A Comparative Study of Chemical Routes for Coating Gold Nanoparticles via Controlled RAFT Emulsion Polymerization. *Part. Part. Syst. Charact.* **2017,** *34*.

40. Milani, A. H.; Saunders, J. M.; Nguyen, N. T.; Ratcliffe, L. P. D.; Adlam, D. J.; Freemont, A. J.; Hoyland, J. A.; Armes, S. P.; Saunders, B. R., Synthesis of polyacid

nanogels: pH-responsive sub-100 nm particles for functionalisation and fluorescent hydrogel assembly. *Soft Matter* **2017,** *13*, 1554-1560.

41. Cui, Z.; Wang, W.; Obeng, M.; Chen, M.; Wu, S.; Kinloch, I.; Saunders, B. R., Using intra-microgel crosslinking to control the mechanical properties of doubly crosslinked microgels. *Soft Matter* **2016,** *12*, 6985-94.

42. Liu, R.; Milani, A. H.; Freemont, T. J.; Saunders, B. R., Doubly crosslinked pH-responsive microgels prepared by particle inter-penetration: swelling and mechanical properties. *Soft Matter* **2011,** *7*.

43. Polte, J.; Ahner, T. T.; Delissen, F.; Sokolov, S.; Emmerling, F.; Thunemann, A. F.; Kraehnert, R., Mechanism of gold nanoparticle formation in the classical citrate synthesis method derived from coupled in situ XANES and SAXS evaluation. *J Am Chem Soc* **2010,** *132*, 1296-301.

44. Liu, X.; Atwater, M.; Wang, J.; Huo, Q., Extinction coefficient of gold nanoparticles with different sizes and different capping ligands. *Colloids Surf., B* **2007,** *58*, 3-7.

45. Lu, Y.; Wang, L.; Chen, D.; Wang, G., Determination of the concentration and the average number of gold atoms in a gold nanoparticle by osmotic pressure. *Langmuir* **2012,** *28*, 9282-7.

46. Haiss, W.; Thanh, N. T.; Aveyard, J.; Fernig, D. G., Determination of size and concentration of gold nanoparticles from UV-vis spectra. *Anal Chem* **2007,** *79*, 4215-21.

47. Ghosh, S. K.; Pal, T., Interparticle coupling effect on the surface plasmon resonance of gold nanoparticles: from theory to applications. *Chem Rev* **2007,** *107*, 4797-862.

48. Karg, M.; Pastoriza-Santos, I.; Perez-Juste, J.; Hellweg, T.; Liz-Marzan, L. M., Nanorod-coated PNIPAM microgels: thermoresponsive optical properties. *Small* **2007,** *3*, 1222-9.

49. Link, S.; El-Sayed, M. A., Shape and size dependence of radiative, non-radiative and photothermal properties of gold nanocrystals. *Int Rev Phys Chem* **2000,** *19*, 409-453.

50. Ruan, Q.; Fang, C.; Jiang, R.; Jia, H.; Lai, Y.; Wang, J.; Lin, H. Q., Highly enhanced transverse plasmon resonance and tunable double Fano resonances in gold@titania nanorods. *Nanoscale* **2016,** *8*, 6514-26.

51. Schmidt, M. M.; Wu, S.; Cui, Z.; Nguyen, N. T.; Faulkner, M.; Saunders, B. R., How gold nanoparticles can be used to probe the structural changes of a pH-responsive hydrogel. *Phys Chem Chem Phys* **2017,** *19*, 5102-5112.

52. Milani, A. H.; Freemont, A. J.; Hoyland, J. A.; Adlam, D. J.; Saunders, B. R., Injectable doubly cross-linked microgels for improving the mechanical properties of degenerated intervertebral discs. *Biomacromolecules* **2012,** *13*, 2793-801.

53. Ghosh, S. K.; Nath, S.; Kundu, S.; Esumi, K.; Pal, T., Solvent and Ligand Effects on the Localized Surface Plasmon Resonance (LSPR) of Gold Colloids. *J. Phys. Chem. B* **2004,** *108*, 13963-13971.

54. Shaw, D. J., Introduction to Colloid and Surface Chemistry. *Butterworth-Heinemann* **1996**.

55. Biggs, S.; Mulvaney, P., Measurement of the forces between gold surfaces in water by atomic force microscopy. *J. Chem. Phys.* **1994,** *100*, 8501-8505.

56. Schimpf, M. E.; Semenov, S. N., Mechanism of Polymer Thermophoresis in Nonaqueous Solvents. *J. Phys. Chem. B* **2000,** *104*, 9935-9942.

57. Israelachvili, J., *Intermolecular and surface forces*. Academic Press **1991**.

Chapter 4: Plasmonic behaviours of Au-acrylic core–shell nanoparticles: The study of various shell thicknesses and their pH-responsive properties[2]

4.1 Abstract

Following the previous established core-shell synthesis method in Chapter 3, five acrylic-based Au core-shell particles were synthesised using a facile precipitation polymerisation with tuneable shell thicknesses. Core-shell particles composed of Au core and temperature-responsive copolymer shell have been reported in many studies. However, few of these studies focused on the construction of pH-responsive copolymer shells. A pH-triggered swelling property was introduced here by controlling the composition of acrylic-based monomers used to construct the shell. The shell thickness of these particles measured by TEM was varied in a range of 2 – 18 nm (δ_{TEM}), which showed relatively thinner shells compared with other reported systems. The localised surface plasmon resonance (LSPR) wavelength was characterised and compared to the simulated spectral data. Au-CEA particles with the thinnest shell showed pH-triggered reversible aggregation and a pronounced spectral shift. Those particles were biocompatible and showed the potential in intracellular pH sensing in HeLa cells.

---

[2] The results are published in (1). Wu, S.; Zhu, M et al. Plasmonic and Colloidal Stability Behaviours of Au-Acrylic Core-Shell Nanoparticles with Thin pH-Responsive Shells. *Nanoscale* **2018**, 10, 18565–18575.

4.2 Introduction

Core-shell gold nanomaterials are attractive structures, which promote thriving research in optical,[1–6] catalytical[7–11] and biomedical areas.[12–16] During the design stage, flexible control of the morphology and structure can have a great impact on the LSPR property.[13,17] This property contributes to a wide range of bio-applicable areas.[18–22] The combination of various nanomaterials with Au can overcome some weaknesses or provide an additional functionality,[23,24] such as strengthening of signal[25] and enhancement of colloidal stability.[26] As reported in Chapter 3, the formation of an acrylic-based copolymer shell around gold nanoparticles (Au NPs) maintained their original LSPR. In the meantime, this core-shell structure endowed them with improved colloidal stability.

A facile controllable core-shell approach could provide a favourable platform,[27–32] which contributes a broad diversity to the development of functional Au nanomaterials. The synthesis of Au-poly(*N*-isopropylacrylamide) (poly(NIPAM)) core-shell particles is a well-known example of stimuli-responsive copolymer shell with the high tunability.[33–35] The change of LSPR was sensitive to the local composition of materials around Au NPs.[33] Studies of core-shell structures support the understanding of their unique properties in the nano-sized range, such as fluorescence quenching,[31,36] LSPR,[37,38] and surface-enhanced Raman spectroscopy.[25,39] However, few studies have examined the generation of a tuneable pH-swellable shell.

pH-responsive particles are potentially useful nanomaterials due to their adaptive performance. pH-dependent targeting, drug delivery and imaging provides an alternative solution in the treatment of disease.[40–42] The treatment of cancer is a beneficial area for the application of pH-responsive components,[41,43–45] because cancer cells show an abnormal pH condition (~ 6.5 – 6.9) compared to healthy cells.[45–49] Intracellular pH (e.g. endosomes, pH 5.0 – 7.2) is also more acidic than the physiological pH.[40,50,51] Au nanomaterials provide potential in photothermal therapy and bio-imaging.[14,15,52] A facile design of pH-dependent Au core-shell structures could open new directions in biomedical research.

The acrylic-based nanogels (NGs) and microgels (MGs) have been used to prepare pH-responsive biocompatible gels for a wide range of applications, such as strain reporting,[53,54] load-bearing[55,56] and drug release[57]. Here, a series of acrylic-based Au core-shell particles were synthesised with different shell thicknesses following the method established in Chapter 3. As shown in Scheme 4.1, the copolymer shells were composed of methyl methacrylate (MMA), methacrylic acid (MAA) or 2-carboxyethyl acrylate (CEA), and ethylene glycol dimethacrylate (EGDMA) as the crosslinker. The shell thickness dependent and pH-responsive properties were characterised and analysed for all core-shell particles. The LSPR wavelength shift was well explained with the aid of the finite difference time domain (FDTD) simulated data of Au core and MMA shells. The pH dependent LSPR changes were observed with a highly swellable MAA containing copolymer shell. In addition, the CEA containing particles had an ultrathin and pH-responsive copolymer shell, which was further investigated to explore potential biomedical use.

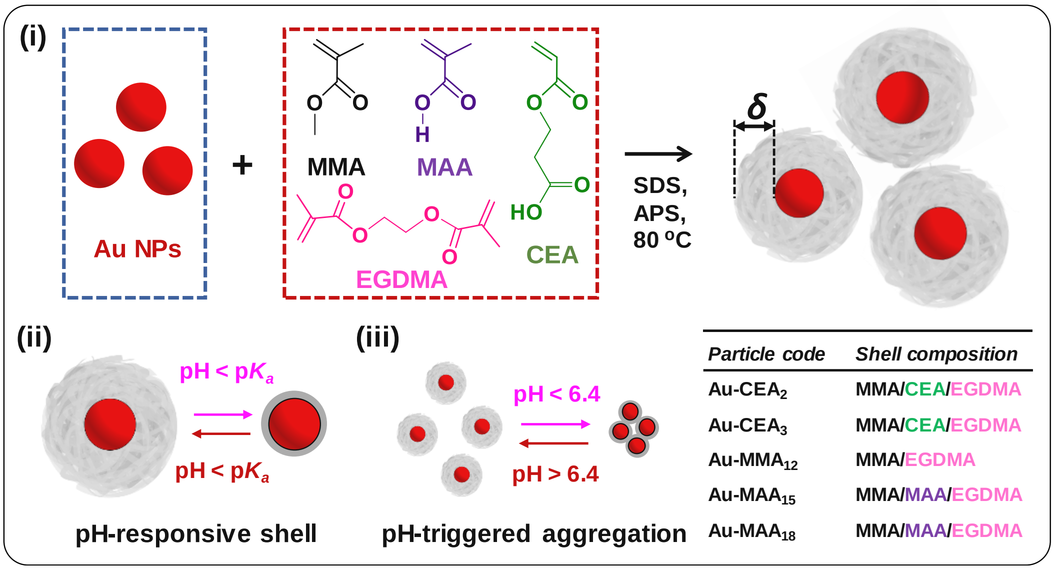

Particle code	*Shell composition*
Au-CEA$_2$	MMA/CEA/EGDMA
Au-CEA$_3$	MMA/CEA/EGDMA
Au-MMA$_{12}$	MMA/EGDMA
Au-MAA$_{15}$	MMA/MAA/EGDMA
Au-MAA$_{18}$	MMA/MAA/EGDMA

Scheme 4.1 (i) Schematic depiction of five types of acrylic core-shell syntheses using precipitation polymerisation. The particle codes are listed in the table. δ is the subscript and denotes the shell thickness. (ii) The core-shell particles show swellable copolymer shells by varying the pH. (iii) A pH-triggered reversible aggregation is established for CEA containing particles.

4.3 Experimental

4.3.1 Materials

MMA (99%), MAA (99%), CEA (Product Number: 552348), EGDMA (98%), ammonium persulfate (APS, 98%), sodium dodecyl sulfate (SDS, 99%), potassium phosphate dibasic (98%), phosphate buffered saline (PBS), NaCl (99%), sodium citrate dihydrate ($Na_3Cit·2H_2O$, ≥99%), and $HAuCl_4·3H_2O$ (>99.9%) were purchased from Sigma-Aldrich and used as received. The water used was doubly filtered and deionised.

4.3.2 Pre-treatment of Au NPs

The synthesis of Au NPs was achieved using the method described in Chapter 3. An aqueous SDS solution (20 μL, 10 mg mL^{-1}) was added to the Au NP dispersion (20 mL, 2.97 nM) using a micropipette (10 – 100 μL range) with magnetic stirring (190 rpm). The mixture was uniformly separated into four tubes and centrifuged at 4800 rpm (2680 rcf) for 4 hr. The sediment was collected and redispersed in water (20 mL in total) to maintain the original concentration of Au NPs.

4.3.3 Synthesis of Au-acrylic core–shell particles containing MMA-MAA

The Au-MAA synthesis followed the protocol of shell growth (Method 3) in Chapter 3. Here, an example of Au-MAA_{18} particles is described. The subscript represents the shell thickness of core-shell particles based on measurements from TEM. The details of the synthesis are listed in Table 4.1. The Au NP dispersion (20 mL, pre-treated as described in Section 4.3.2) was transferred to a 100 mL three-necked flask with magnetic stirring (290 rpm), and an aqueous SDS solution (1.0 mL, 4.12 mg mL^{-1}) was subsequently added using a micropipette (100 – 1000 μL range). The flask was equipped with a reflux condenser (4 °C water circulation). The mixture was purged with nitrogen for 30 min and heated to 80°C. The inlet nitrogen was guided by a needle through a rubber stopper. The flask was heated in a paraffin oil using a magnetic hotplate stirrer. The reaction temperature was monitored by immersing a temperature probe in the bath. A comonomer mixture (49.5 mg) of MMA (80.5 wt%), MAA (17.5 wt%) and EGDMA (2.0 wt%) was added to a glass vial using a micropipette (1 – 10 μL range) and dissolved in water (5.0 mL) on a vortex mixer. This solution was then collected by a 5.0 mL syringe and set in a syringe pump. Aqueous K_2HPO_4 (80 μL, 1M) was added to the flask using a micropipette (10 – 100 μL range), and the mixture was equilibrated for 10 min. Under a nitrogen atmosphere, this was followed by addition of APS (100 μL, 19 mM) using a micropipette (10 – 100 μL range) and a syringe pump was used to feed the comonomer solution into the flask at a uniform rate (0.083 mL min^{-1}) over 1 hr. The reaction continued for a further 3 hr, and was finally cooled in an ice bath. The product was uniformly separated into twelves tubes and centrifuged for 1 hr at 10000 rpm. The supernatant was discarded, and the sediment was redispersed with water (26 mL in total) using a micropipette (100 – 1000 μL range). The centrifugation was repeated four times to remove unreacted monomers, buffer and excess NGs.

Au-MAA_{15} particles were synthesised using the same protocol as shown above. However, a higher MAA concentrations (33.0 wt%) was included in the feed. The comonomer ratio was varied to MMA (65.0 wt%), MAA (33.0 wt%) and EGDMA (2.0 wt%) with K_2HPO_4 (140 μL, 1.0 M) in solution (Table 4.1).

Table 4.1 Materials used to prepare Au-acrylic core-shell particles.

Particle Codes	$C_{Au\,NP}^{a}$ **/ nM**	**MMA / wt.% (mol.%)**^{a}	**MAA or CEA/ wt.% (mol.%)** ^{a}	**EGDMA / wt.% (mol.%)** ^{a}	**SDS / wt. %**^{b}	**APS / wt. %**^{b}	**Mon / g**^{c}	**Water / g**
Au NPs	2.97	-	-	-	-	-	-	-
Au-CEA$_2$	1.14	53.2 (62.3)	45.2 (36.7)	1.6 (1.0)	0.016	0.002	0.0600	26
Au-CEA$_3$	1.14	53.2 (62.3)	45.2 (36.7)	1.6 (1.0)	0.016	0.002	0.0600	26
Au-MMA$_{12}$	1.14	98.0 (99.0)	0 (0)	2.0 (1.0)	0.016	0.002	0.0491	26
Au-MAA$_{15}$	2.29	65.0 (62.3)	33.0 (36.7)	2.0 (1.0)	0.016	0.002	0.0491	26
Au-MAA$_{18}$	2.29	80.5 (79.0)	17.5 (20.0)	2.0 (1.0)	0.016	0.002	0.0491	26

^{a} Initial molar concentration. ^{b} Dissolved in water phase. ^{c} Total mass of all monomers added

4.3.4 Synthesis of Au-acrylic core–shell particles containing MMA-CEA

The Au-CEA synthesis followed the same protocol as described in Section 4.3.3 for Au-MAA. However, MAA was substituted by CEA (53.2 wt%), which was mixed with MMA (45.2 wt%) and EDGMA (1.6 wt%) to give a comonomer mixture (60 mg). The mixture was dissolved in water (5.0 mL) using a vortex mixer and collected by a 5.0 mL syringe. Au NPs (10 mL, 2.97 nM, pre-treated as described in Section 4.3.2) and water (10 mL) were added to a 100 mL three-necked flask with magnetic stirring (290 rpm). An aqueous SDS solution (1.0 mL, 4.12 mg mL^{-1}) was subsequently added using a micropipette (100 – 1000 μL range). The flask was equipped with a reflux condenser (4 °C water circulation). The mixture was purged with nitrogen for 30 min and heated to 80°C. The inlet nitrogen was guided by a needle through a rubber stopper. The flask was heated in a paraffin oil bath and controlled by a temperature probe. Different volumes of K_2HPO_4 (150 μL for Au-CEA$_2$ or 120 μL for Au-CEA$_3$, 1.0 M) were used in the synthesis using a micropipette (100 – 1000 μL range), and the solution pH was prepared at ~ 5.8 (for Au-CEA$_2$) and 5.3 (for Au-CEA$_3$). The details of the preparation are listed in Table 4.1. Under a nitrogen atmosphere, the reaction was initiated by APS (100 μL, 19 mM) using a micropipette (10 – 100 μL range) and a syringe pump was used to feed the comonomer solution into the flask at a uniform rate (0.083 mL min^{-1}) over 1 hr. The reaction continued for a further 3 hr, and was finally cooled in an ice bath. The product was uniformly separated into twelves tubes and centrifuged for 1 hr at 10000 rpm. The supernatant was discarded, and the sediment was redispersed with water (26 mL in total) using a micropipette (100 – 1000 μL range). The centrifugation was repeated four times to remove unreacted monomers, buffer and excess NGs. The pH of the dispersion was kept above 6.4 to avoid the formation of aggregates.

4.3.5 Synthesis of Au-acrylic core–shell particles containing MMA

The Au-MMA synthesis followed the same protocol as described in Section 4.3.3 for Au-MAA. The details of the preparation are listed in Table 4.1. Au NPs (10 mL, 2.97 nM, pre-treated as described in Section 4.3.2) and water (10 mL) were added to a 100 mL three-necked flask with magnetic stirring (290 rpm). SDS solution (1.0 mL, 4.12 mg mL^{-1}) was added using a micropipette (100 – 1000 μL range). The flask was equipped with a reflux condenser (4 °C water circulation). The mixture was purged with nitrogen for 30 min and heated to 80°C. The inlet nitrogen was guided by a needle through a rubber stopper. The flask was heated in a paraffin oil bath and controlled by a temperature probe. A comonomer mixture (49.5 mg) of MMA (98 wt%) and EGDMA (2 wt%) was dissolved in water (5.0 mL) using a vortex mixer. This solution was then collected by a 5.0 mL syringe and set in a syringe pump. Under a nitrogen atmosphere, aqueous APS (100 μL, 19 mM) was subsequently added to the flask using a micropipette (10 – 100 μL range) and a syringe pump was used to feed the comonomer solution into the flask at a uniform rate (0.083 mL min^{-1}) over 1 hr. The reaction continued for a further 3 hr, and was finally cooled in an ice bath. The product was uniformly separated into twelves tubes and centrifuged for 1 hr at 10000 rpm. The supernatant was discarded, and the sediment was redispersed with water (26 mL in total) using a micropipette (100 – 1000 μL range). The centrifugation was repeated four times to remove unreacted monomers, buffer and excess NGs.

4.3.6 Physical measurements

All the UV spectra were measured on a PerkinElmer Lambda 25 UV-Visible spectrometer. The z-average diameter (d_z) and zeta potential were obtained from DLS measurements using a 50 mW He-Ne laser operating at 633 nm using a Malvern Zetasizer Nano ZS instrument. The swelling experiments were held for 10 min at different pH values before taking any further measurements. All TEM samples were prepared by drop-casting the dispersion (10 μL) onto a 300-mesh copper grid with a holey carbon film. The grid was held by tweezers and allowed to dry overnight in a desiccator containing silica gel at room temperature. TEM images were inspected using a Philips CM20 TEM instrument at 200 kV. Number-average diameters were determined by measuring at least 100 particles. X-ray photoelectron spectroscopy (XPS) data were obtained by Ben Spencer (The University of Manchester) using an Axis Ultra DLD spectrometer (Kratos) which used a monochromated Al Kα X-ray source (1486.6 eV, 10 mA emission). Survey spectra were acquired with a pass energy of 80 eV while high resolution narrow scans of the important atomic core levels were acquired using a pass energy of 20 eV. The experiments were performed under high vacuum at pressures $< 3 \times 10^{-8}$ mbar. Data were analysed using CasaXPS, where photoelectron peaks are fit with product-approximation Voigt functions (Gaussian–Lorentzian peaks with a mixing ratio of 0.3).

4.3.7 Finite difference time domain simulations

The experimental details and results of finite difference time domain **(**FDTD) simulation were provided by Kirsten Volk and Prof. Matthias Karg (Heinrich-Heine-Universität Düsseldorf). FDTD calculations were performed using commercial software from Lumerical Solutions, Inc. (FDTD Solutions, Version 8.18.1332). A single, spherical Au NP (radius: r = 6.5 nm) was used with varying PMMA shell sizes (thicknesses (δ) = 0 – 24 nm) in water, which was placed in the centre of the FDTD simulation, with perfectly matched layer (PML) boundary conditions in the x, y and z directions. A total-field scattered-field source (TFSF) surrounding the nanoparticle (x-, y-, z-span = 118 nm) was used as light source (incident wavelengths: λ = 300 – 800 nm). There were two analysis groups employed, each of which consisted of a box of power monitors: one in the total field region (x-, y-, z-span = 83 nm) and one in the scattered field region (x-, y-, z-span = 143 nm). These analysis groups were used to calculate absorption and scattering. For the broadband source simulation the FDTD software was allowed to approximate the refractive index (*n*) of Au to literature values[58] using a polynomial function. For water and the PMMA shells constant n values of 1.332[59] and 1.4934[60,61] were used, respectively, since they hardly change over the investigated spectral range. An overwrite region with a uniform mesh of 5×10^{-3} nm in the near-field region (x-, y-, z-span 23 nm) of the Au NP was chosen additionally to the non-uniform mesh. All simulations reached the auto shut-off level of 10^{-9} before reaching 1000 fs simulation time.

4.3.8 Cell culture and internalisation studies

The experimental details and results of cell culture were provided by Daman Adlam (The University of Manchester). HeLa cells, cell line derived from human cervical cancer, were cultured in Dulbecco’s modified Eagle’s medium (DMEM) supplemented with 10% fetal bovine serum, Glutamax (Life Technologies, UK) and antibiotic/antimycotic (Sigma-Aldrich, UK) at 37 °C in a humidified 5% CO_2 atmosphere. Cells were seeded at a density of 2×10^4 per well onto 13 mm sterile glass coverslips in 24 well cell culture plates and allowed to attach overnight. Media was replenished and Au-CEA$_2$ particles introduced at a concentration of 1.0 nM. Control wells received an equal volume of phosphate buffered saline (two samples per time point). Cells were cultured up to ten days and viability was determined at appropriate time points by live/dead assay (Life Technologies, UK) according to the supplier instructions. The cells were fixed with 4% paraformaldehyde in PBS and mounted onto slides at day 10. Images were obtained with an Olympus BX51 fluorescence microscope and a Leitz Diavert inverted phase contrast light microscope.

4.4 Results and discussion

4.4.1 Au-poly(MMA-(MAA)-EGDMA) core-shell particle characterisation

The average diameter of Au NPs (d_{TEM}) was measured as around 15 ± 1 nm using TEM as shown in Fig. 4.1(A(i)-(ii)). Three core-shell particles were synthesised using the previously method established in Chapter 3. They all possessed a well-defined circular core-shell structure in TEM (Fig.4.1(B(i)-D(i))). These particles had a low size dispersity. TEM images indicated the presence of variable shell thicknesses among the three poly(MMA-(MAA)-EGDMA) core-shell samples with an increasing order: Au-MAA$_{18}$ > Au-MAA$_{15}$ > Au-MMA$_{12}$. In Fig. 4.1(B(ii)-D(ii)), d_{TEM} was counted and averaged over more than 100 particles. The data showed that δ_{TEM} ranged between 12 nm and 18 nm (Table 4.2). These diameters were recorded in the dried state due to the drop-casting preparation and high vacuum of TEM chamber. Therefore, the water was not expected to be present in the collapsed shell (pH 6) during imaging.

DLS size measurements (d_z) showed a clear increasing trend of d_z from Fig. 4.1(A(iii)) to Fig. 4.1(D(iii)). They had a slightly larger diameter (d_z, pH 6) compared to d_{TEM}. Here, d_z gave the diameter of a hydrated particle based on the measurement of diffusion coefficient (Chapter 2). On the other hand, d_{TEM} obtained the information from a direct inspection on dried particles. The primary dimension and volume of materials (Au NPs or copolymer shells) could be straightforwardly calculated without considering other factors (hydrated parts, adsorbed layers, outspread polymer chains). For example, Au NPs had a d_z ~ 19 nm which was 4 nm larger than $d_{TEM.}$ The DLS measurement could also include the citrate stabilising layer in the size measurement. Here, d_{TEM} of Au NPs is considered more reliable for analysis due to a direct visualisation of the shell thickness. Table 4.2 shows a list of properties for a series of Au-poly(MMA-(MAA)-

EGDMA) core-shell particles. These particles had a high shell volume fraction in a range of 92.5 – 97.9 vol% based on the d_{TEM} calculation.

Table 4.2 Properties of Au-poly(MMA-(MAA)-EGDMA) core-shell particles studied.

Particle codes	**d_{TEM} /nm**	**δ_{TEM} ^{a}/ nm**	**$\phi_{shell}{}^b$/ vol%**	**d_z /nm (pH 6)**	**d_z /nm (pH 10)**	**δ_{DLS} ^{a}/ nm (pH 6)**	**ζ^c/ mV (pH 6)**	**LSPR λ (nm) (pH 6)**
Au NPs	15 ± 1	-	0	19	-	-	-42.5	519
Au-MMA_{12}	39 ± 3	12	92.5	44	44	15	-17.6	528
Au-MAA_{15}	45 ± 4	15	97.0	61	121	23	-17.6	529
Au-MAA_{18}	51 ± 5	18	97.9	68	66	27	-17.8	529

[a] Values calculated using $\delta = (d_{cs} - d_c)/2$ where d_{cs} and d_c are the diameters of the core-shell particles and core particles, respectively. δ_{DLS} was calculated by the DLS diameter of core-shell particles and the TEM diameter of core particles. [b] Shell volume fraction calculated from the TEM data using: $\phi_{sh} = [(d_c + 2\delta)^3 - d_c^3]/[(d_c + 2\delta)^3]$. [c] Zeta potential.

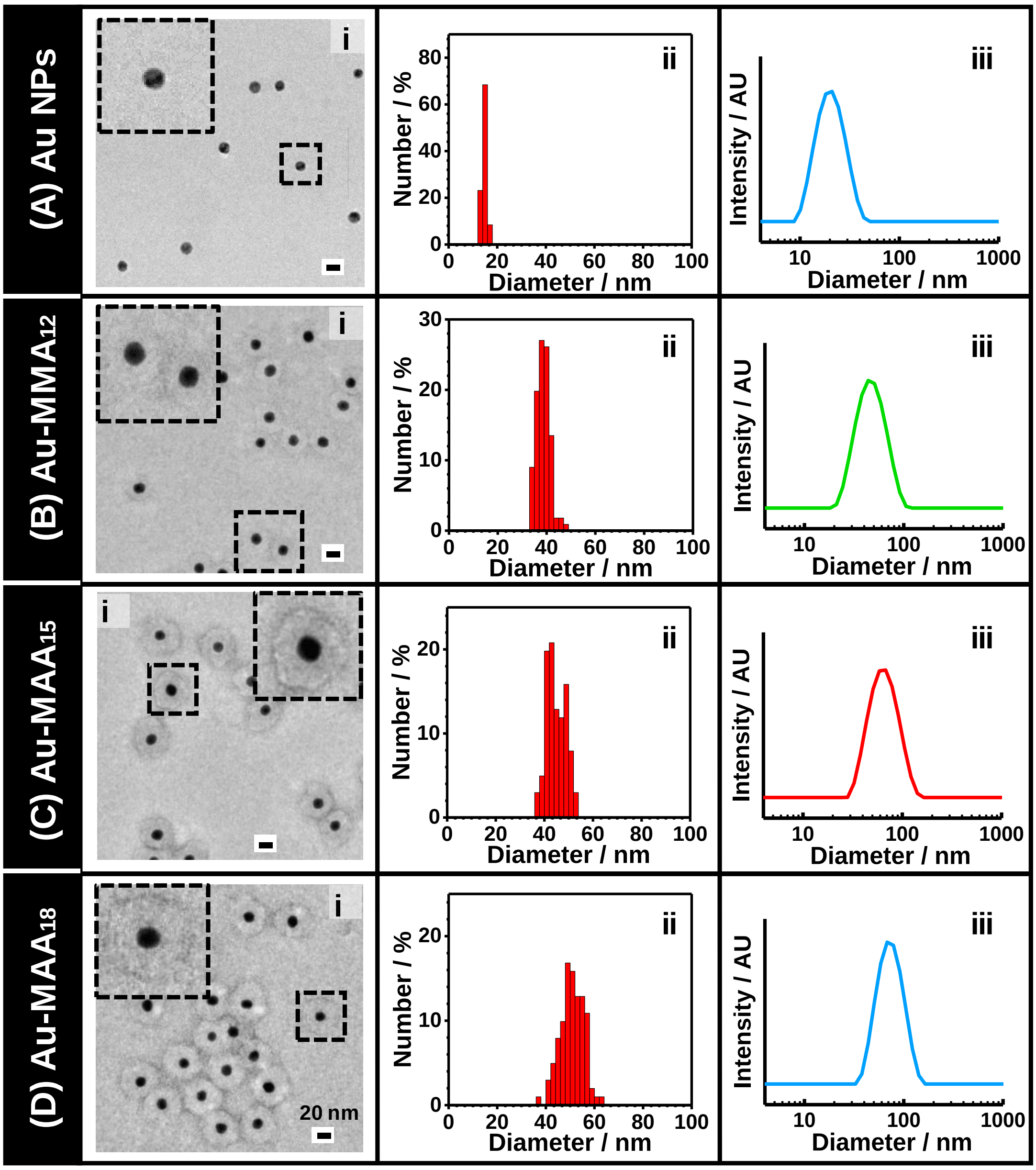

Figure 4.1 (A) Au NPs, (B) Au-MMA$_{12}$, (C) Au-MAA$_{15}$ and (D) Au-MAA$_{18}$ dispersions were inspected at a dried state by (i) TEM and (ii) size distributions from the TEM were recorded. (iii) The DLS size distribution of core-shell particles measured at pH 6 in water.

Au-MAA$_{15}$ and Au-MAA$_{18}$ core-shell particles contained negatively charged carboxylic acid groups, which had the similar composition compared to pH-responsive NGs.[62] Therefore, the swelling of shells should be found by increasing pH in the dispersions. This swelling behaviour was beneficial for the formation of physical gel or sensing.[53,56] As shown in Fig. 4.2(A), DLS measurements of Au NPs were used as a control in various pH conditions. The d_z was constant at ~ 19 nm from pH 5 to pH 11. In comparison to Fig.4.2(B), the change of d_z showed the same trend in Au-MAA$_{18}$, which had a steady diameter (d_z ~ 68 nm) with increasing pH. This was caused by a low MAA content (17.5 wt%) used in the synthesis (Table 4.1). When the MAA content increased to 33 wt%, a pronounced swelling appeared in Fig. 4.2(C). Au-MAA$_{15}$ had a d_z ~ 61 nm at pH 6 and gradually swelled to 121 nm at pH 10 due to the deprotonation of carboxylic groups. The zeta potential of these particles was recorded simultaneously in a range of pH (Fig. 4.2(E)-(G)). The negative charge suggests there is an electrostatic repulsion (carboxylic acid groups) between particles. The increase of the magnitude of the zeta potential was also found at higher pH conditions. This change of Au-MAA$_{15}$ (Fig. 4.2(G)) closely followed its swelling trend, which exhibited a significant increase in a range of pH 8-10. It suggested the pK_a existed in this range.[56,63]

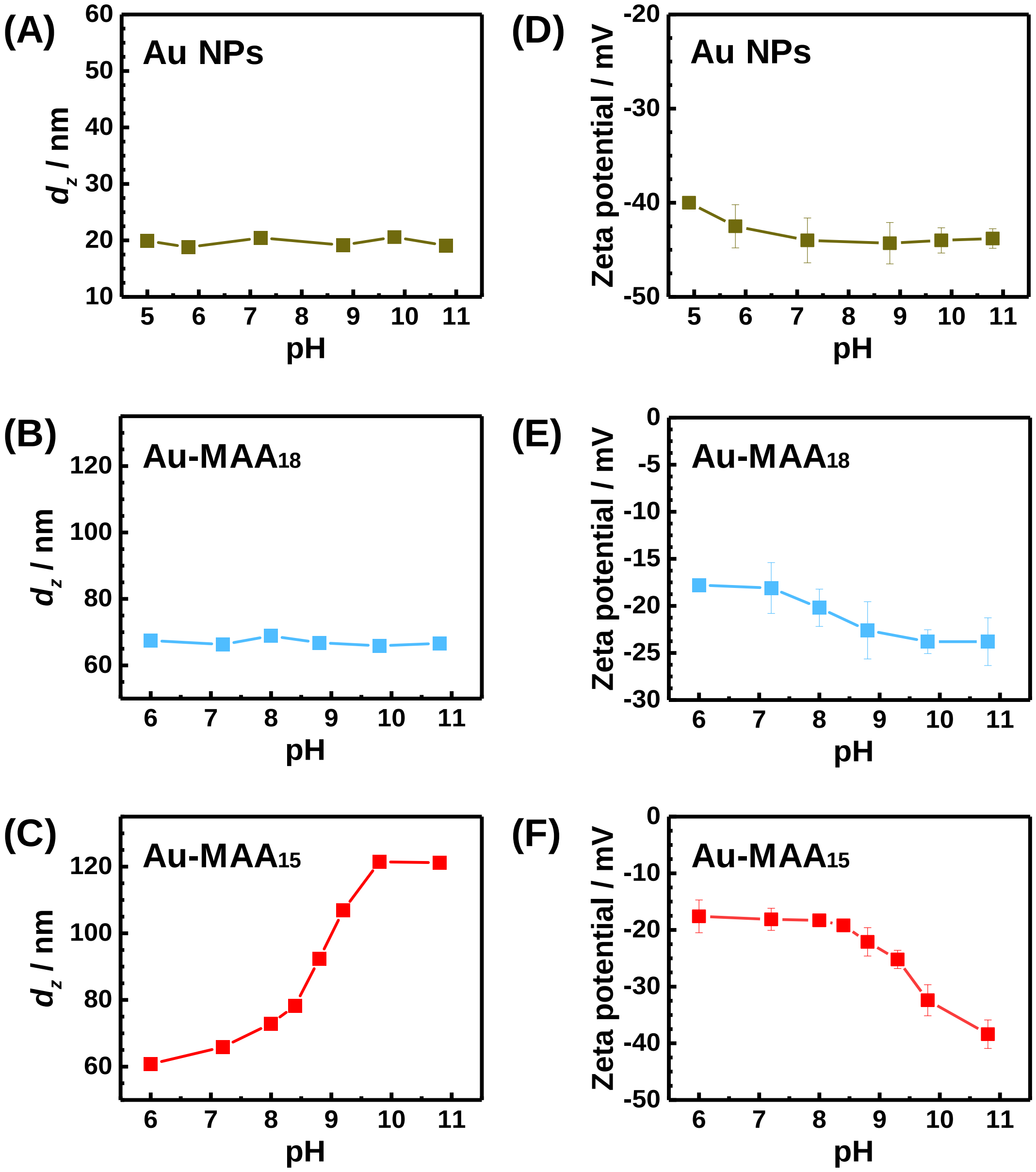

Figure 4.2 The z-average diameter and zeta potential of (A and D) Au NPs, (B and E) Au-MAA$_{18}$, (C and F) Au-MAA$_{15}$ as a function of pH. The identities are labelled.

4.4.2 Au-poly(MMA-CEA-EGDMA) core-shell particle characterisation

A new type of core-shell particles was synthesised here by replacing the same mol% MAA of Au-MAA_{15} with CEA. Based on the experimental observation, CEA is a more acidic monomer which involved a larger concentration of buffers to fix the pH of the solution. Two kinds of CEA-based core-shell particles (Au-CEA_2 and Au-CEA_3) were prepared by tuning the pH of the synthesis using K_2HPO_4. In Fig. 4.3(A(i)-B(i)), TEM showed both Au-CEA particles had a much smaller size than Au-MAA/MMA particles (Fig. 4.1(B(i)-D(i)). TEM images highlighted an ultrathin copolymer shell was formed in both Au-CEA_2 and Au-CEA_3 dispersions. DLS size measurements agreed with this observation, which also showed a uniform size distribution in Fig 4.3(A(iii)-B(iii)). According to the study in Chapter 3 Section 3.4.4, the core-shell synthesis was proceeded in the continuous phase by the hydrophobic adsorption of monomers/oligomers on the surface of Au NPs. CEA has a factor of three lower oil-water partition coefficient compared to MAA and the polarity of CEA is similar to acrylic acid.[64] This difference means CEA is a relatively hydrophilic monomer in the core-shell synthesis. Therefore, the synthesis was expected to have less adsorption of monomers/oligomers from the aqueous phase and finally contributed to the formation of such a thin copolymer shell. Table 4.3 shows the summary of properties in Au-CEA_2 and Au-CEA_3 particles. In comparison to Au-MAA/MMA particles (Table 4.2), they showed a smaller shell volume fraction in a range of 43.6 – 71.9 vol% based on the d_{TEM} calculation.

Table 4.3 Properties of Au-poly(MMA-CEA-EGDMA) core-shell particles studied.

Particle codes	d_{TEM} **/nm**	δ_{TEM} ^{a}**/ nm**	ϕ_{shell}^{b}/ *vol%*	d_z **/nm (pH 6)**	d_z **/nm (pH 10)**	δ_{DLS} ^{a}**/ nm (pH 6)**	ζ^{c}**/ mV (pH 6)**	**LSPR λ (nm) (pH 6)**
Au-CEA$_2$	18 ± 1	2	43.6	22	28	4	-9.2	522
Au-CEA$_3$	21 ± 2	3	71.9	28	31	7	-11.4	526

^{a} Values calculated using $\delta = (d_{cs} - d_c)/2$ where d_{cs} and d_c are the diameters of the core-shell particles and core particles, respectively. δ_{DLS} was calculated by the DLS diameter of core-shell particles and the TEM diameter of core particles. t^b Shell volume fraction calculated from the TEM data using: $\phi_{sh} = [(d_c + 2\delta)^3 - d_c^3]/[(d_c + 2\delta)^3]$. ^{c} Zeta potential.

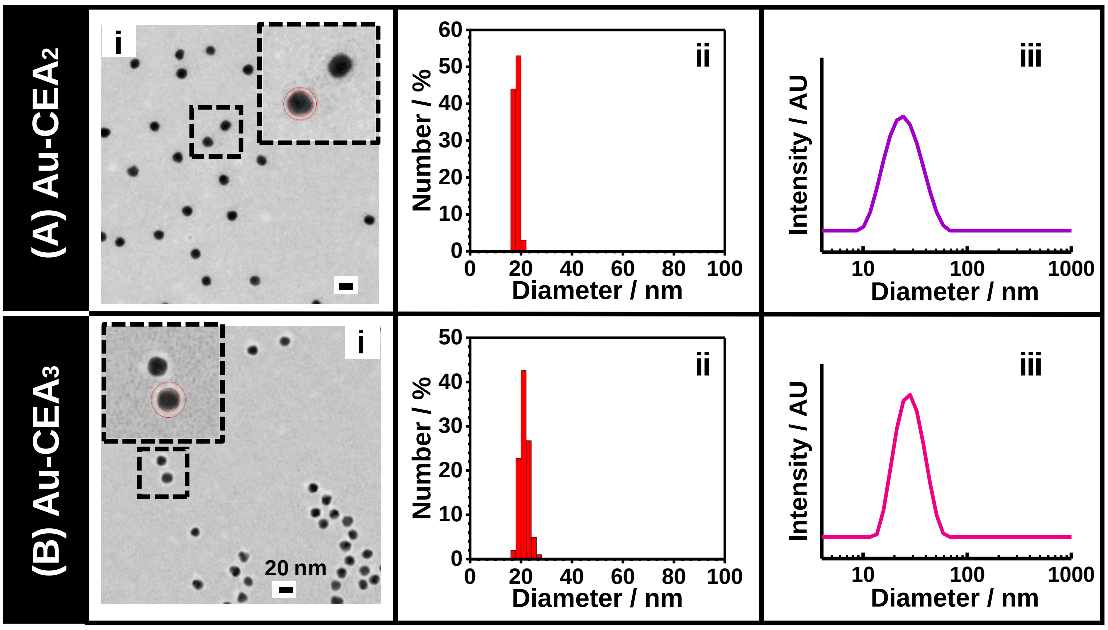

Figure 4.3 (A) Au-CEA$_2$ and (B) Au-CEA$_3$ dispersions were inspected at a dried state by (i) TEM and (ii) size distributions from the TEM were recorded. (iii) The DLS size distribution of core-shell particles measured at pH 6 in water.

CEA also possesses an acidic carboxylic group. Therefore, the copolymer shell of Au-CEA particles could perform a swelling behaviour when the pH increases beyond its pK_a. As shown in Fig. 4.4(A)-(B), the d_z of Au-CEA particles increased from pH 6 and levelled off around pH 7.2. The d_z of Au-CEA$_2$ was measured as 22 nm at pH 6 and finally reached to 28 nm at pH 11. The change of d_z was less significant than Au-MAA$_{15}$

due to its thin shell and low monomer/oligomer adsorption in the synthesis. However, the pH swelling range of Au-CEA met the physiological pH requirement in the human body, especially for tumours (pH 5.5 – 7.0) and normal tissues (pH 7.3 – 7.4).[45–48,65] The zeta potential data (Fig. 4.4(C)-(D)) also supported the increase of the absolute charge beyond pH 6, which coincided with the swelling trend in size measurement. It should be noted that the magnitude of zeta potential is quite small in the low pH region (Fig. 4.4(C)-(D)), which suggests an unstable colloidal state of Au-CEA particles. The aggregation might then occur with time when the pH drops to 6.

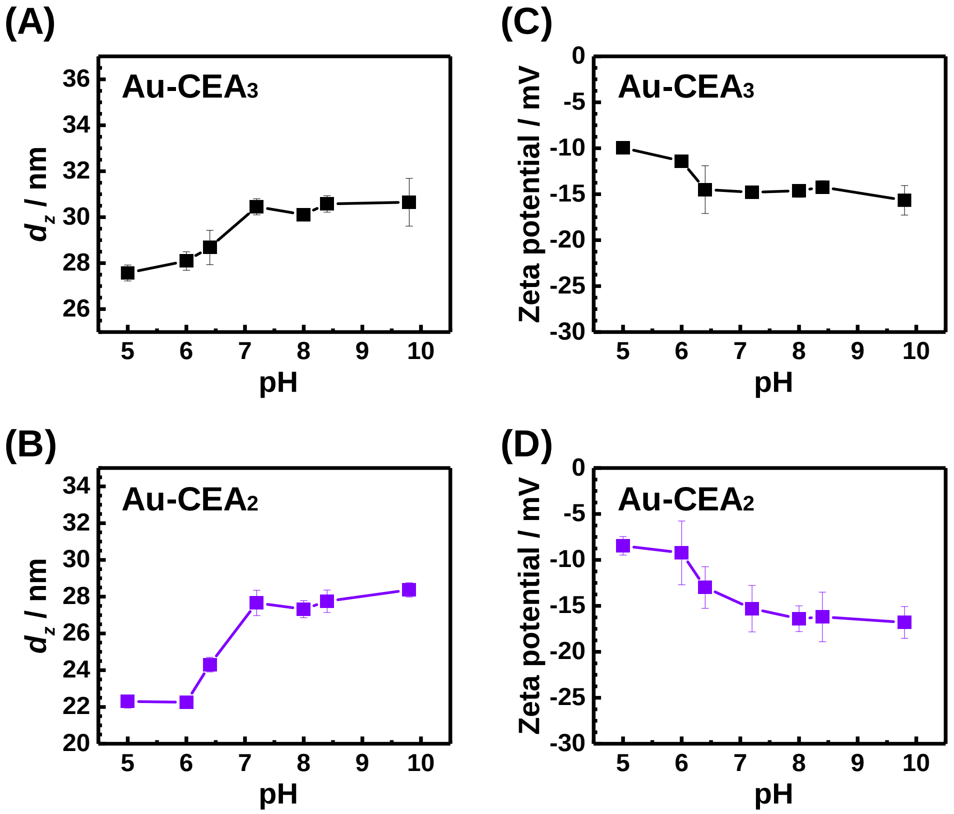

Figure 4.4 The z-average diameter and zeta potential of Au-CEA$_3$ (A and C) and Au-CEA$_2$ (B and D) as a function of pH. The identities are labelled inside the graph.

4.4.3 XPS characterisation of core-shell particles

In order to confirm the composition of the core-shell particles, high-resolution XPS spectra were obtained to probe the dried Au-CEA$_2$, Au-MMA$_{12}$, Au-MAA$_{15}$ and Au-MAA$_{18}$ particles. In Fig. 4.5(A)-(D), the C 1s spectra were well fitted with three individual peaks using the CasaXPS software, which showed three binding energies of ~ 284.8, 286.2 and 289.0 eV due to C−C, C−O and O=C−O, respectively.[66] These data prove the presence of the copolymer shells. XPS spectroscopy is a surface analysis technique, which is limited to several nanometres detection depth (~ 10 nm).[67] In the Au 4f spectra (Fig. 4.5(E)-(H)), the signal of energy peaks was featureless and noisy for Au-MMA$_{12}$, Au-MAA$_{15}$ and Au-MAA$_{18}$ samples. The thick copolymer shells of those particles (δ_{TEM} = 12 − 18 nm) hindered the detection of Au core in the centre. Here, two peaks are weakly resolved between 80 eV and 90 eV. In contrast, Au-CEA$_2$ particles had a δ_{TEM} ~ 2 nm and a spin-orbit splitting pair was found with a clear difference ~ 3.8 eV in the Au 4f spectra (Fig. 4.5(E)). The binding energies showed similar values ~ 83.8 and 86.8 eV which are reported elsewhere for Au NPs.[68] Hence, the XPS results supported the observation of the core-shell structure from TEM. Much thinner shell thicknesses of Au-CEA$_2$ particles is confirmed compared to Au-MMA/MAA particles.

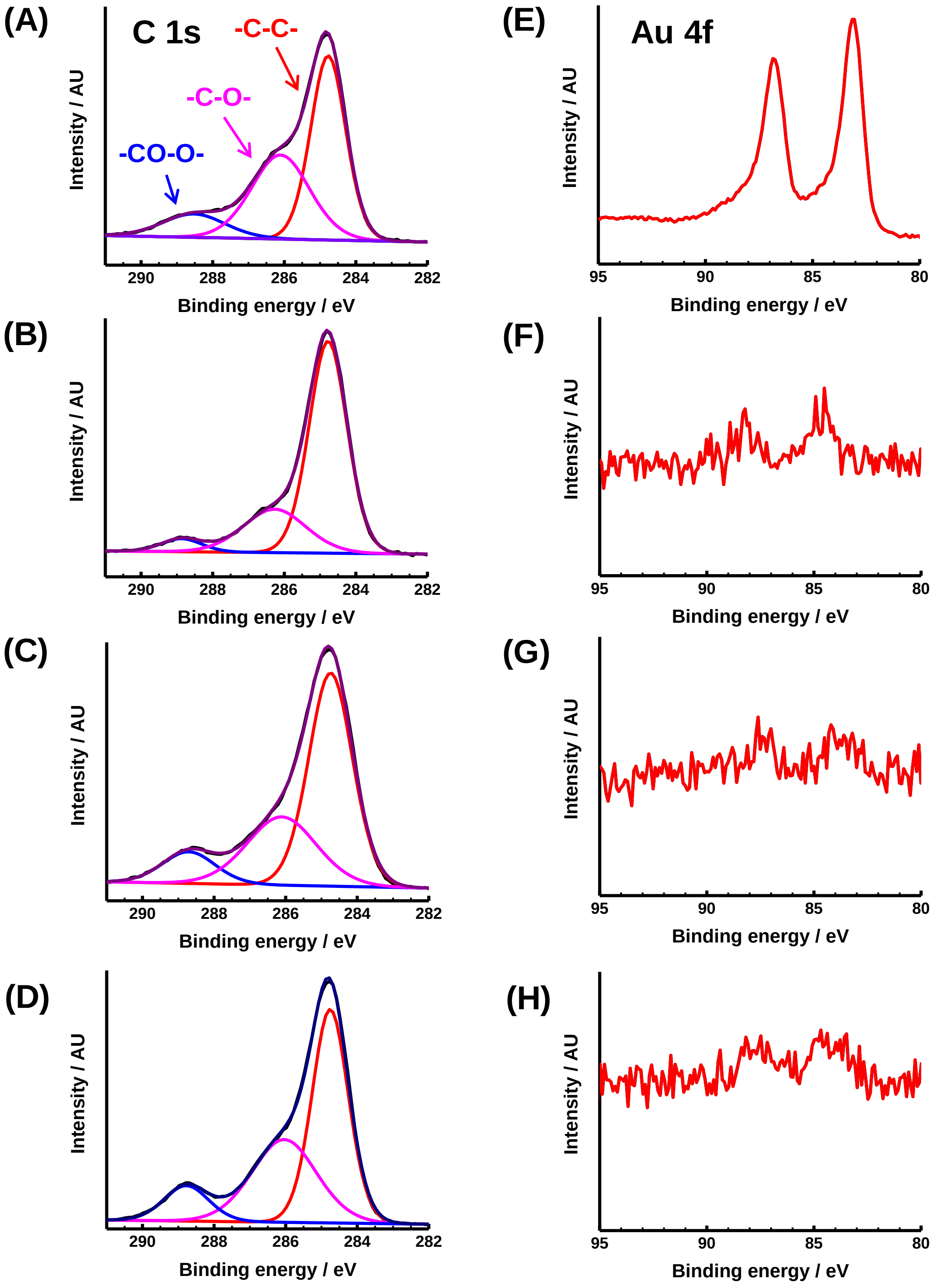

Figure 4.5 C 1s and Au 4f XPS spectra for Au-CEA$_2$ (A and E), Au-MMA$_{12}$ (B and F), Au-MAA$_{15}$ (C and G) and Au-MAA$_{18}$ (D and H) core-shell particles.

4.4.4 Effects of shell thicknesses on LSPR

As described above, five acrylic-based Au core-shell particles were introduced with variable shell thicknesses and volume fractions. The size used for the LSPR analysis was obtained based on their d_{TEM} (Table 4.2 and 4.3) as discussed in Section 4.4.1. The spectra show a clear difference among their LSPR peak wavelength in Fig. 4.6(A). The red-shift performance was observed from the normalised UV-Vis spectra of core-shell particles (collapsed at pH 6) with the increase of δ_{TEM}. There was a ~ 10 nm difference of LSPR wavelength between the largest (Au-MAA$_{18}$, δ_{TEM} ~ 18 nm) and smallest (Au NPs) particles (Table 4.2 and 4.3). The LSPR peak wavelength is plotted as a function of δ_{TEM} in Fig. 4.6(B). A steep increase of wavelength was found at δ_{TEM} below 5 nm (Au-CEA$_2$ and Au-CEA$_3$). The wavelength continuously increased from 519 nm and reached to a plateau around 529 nm when the shell thickness exceeded ~ 10 nm. The change of effective refractive index in the proximity of Au cores accounted for this red shift.[4,69] Overall, these core-shell particles had a relatively thin shell (less than 20 nm) compared to other studies.[33–35] Therefore, the LSPR property can be intensively varied by the surrounding medium including both copolymer and water. Fig. 4.6(C) is plotted to correlate the LSPR wavelength shift to shell volume fraction. A linear trend was observed. This change indicated the dielectric environment was effectively varied by the copolymer shell, which suggested the major contribution to the red-shift for core-shell particles. The polymer-to-water volume ratio increased with the δ_{TEM} and led to a higher refractive index in the near field.

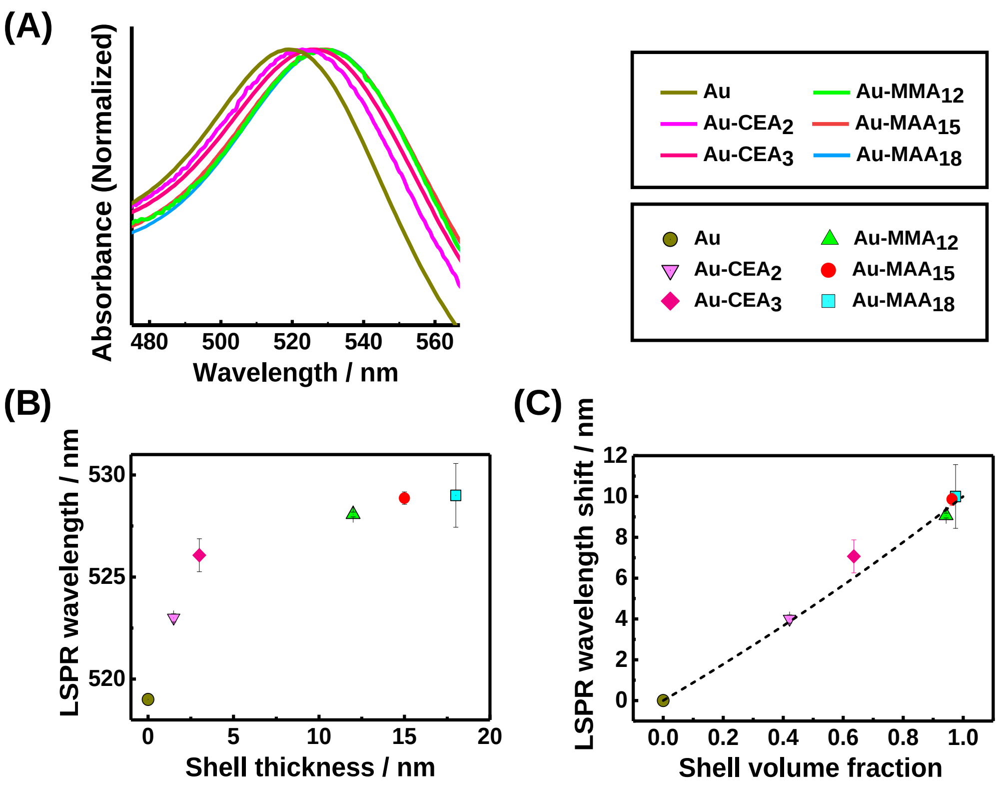

Figure 4.6 (A) Normalised UV-visible absorbance spectra for Au NPs and core–shell particles. The dispersion pH was 6.0. (B) Variation of the measured LSPR wavelength with δ_{TEM}. (C) Variation of the LSPR wavelength shift with shell volume fraction.

In order to understand the shell thickness dependent change of LSPR, an FDTD simulation was performed on Au NPs with tuneable poly(MMA) shell thicknesses in water (Fig. 4.7(A)-(B)). A slightly smaller diameter of Au NPs (13 nm) was used in the simulation and could provide a better agreement with the experimental value of Au NPs. This difference could be caused by the idealised morphology of particles in the simulation, which assumed a perfectly spherical shape with a homogenous surface. However, the synthesis should provide the slightly polydisperse Au NPs (Fig 4.1(A)). As shown in Fig. 4.7(A), the simulation provided a whole near-field map of a single Au NP in the water. A strong near-field was observed at a place < 5 nm from the surface of Au NP, which could explain the steep change of LSPR wavelength over 0 – 3 nm copolymer shell thicknesses (Fig. 4.6(B)). In comparison, the highlighted 15 nm shell was far from the near-field zone, and particles could be less sensitive to that region. This caused that the further increase of δ_{TEM} showed a constant LSPR wavelength around 529 nm (Fig. 4.6(B)). A similar LSPR wavelength shift was confirmed by numerical simulations of the LSPR spectra in Fig. 4.7(B). Here, the poly(MMA) shell was applied to a single Au NP with the variable shell thicknesses and the refractive index recognised as 1.49.[60,61] The shell thickness was plotted against the LSPR peak wavelength in Fig. 4.7(C), which had a comparable trend with the experimental data. The figures showed the LSPR wavelength was shifted to 528 nm with a 5 nm shell (poly(MMA)) and was constant around 531 nm beyond a thickness of 15 nm. The simulation overestimated the shell thickness above 5 nm, which had a 1 – 2 nm LSPR wavelength difference compared to the experimental data. When the *n* of shells decreased to 1.46, the simulation provided a much closer fit as shown in Fig. 4.7(C). In this case, it suggested the true *n* of these copolymer shells could be slightly smaller than the expected value of poly(MMA). The core-shell particles were expected to contain some residual water in the hydrated copolymer shell (even at pH 6), which can reasonably be attributed to a lower *n* around the Au cores. In comparison to other core-shell particles, the new synthesis used a range of thin pH-responsive copolymers shells, which gave a strong impact on LSPR properties. The thickness regime (2 – 18 nm) coincided well with the most sensitive near-field position as shown in Fig. 4.7(A). A systematic study of thin pH-responsive shells has rarely been reported in previous research. Until recently, intracellular therapies and plasmonic sensing promoted development of pH-responsive nanohybrids, such as Au-polyaniline[70,71] and Au-poly(4-vinylpridines)[72–74] core-shell particles. However, these particles either lack swellable NG phases or have too large core size (> 50 nm), which makes them unable to be compared to the present Au-acrylic system. Extensive NG or MG shell research has focused on thermo-responsive compositions (e.g. poly(NIPAM)), and those shells were thick.[34,75–78] The synthesis of such core-shell systems usually requires surface functionalisation or coating prior to the shell growth. The present Au-acrylic particles were established without using any complex surface modifications through the study of Chapter 3 and 4. Their thin shells provide a highly tuneable LSPR platform for pH controllable smart designs.

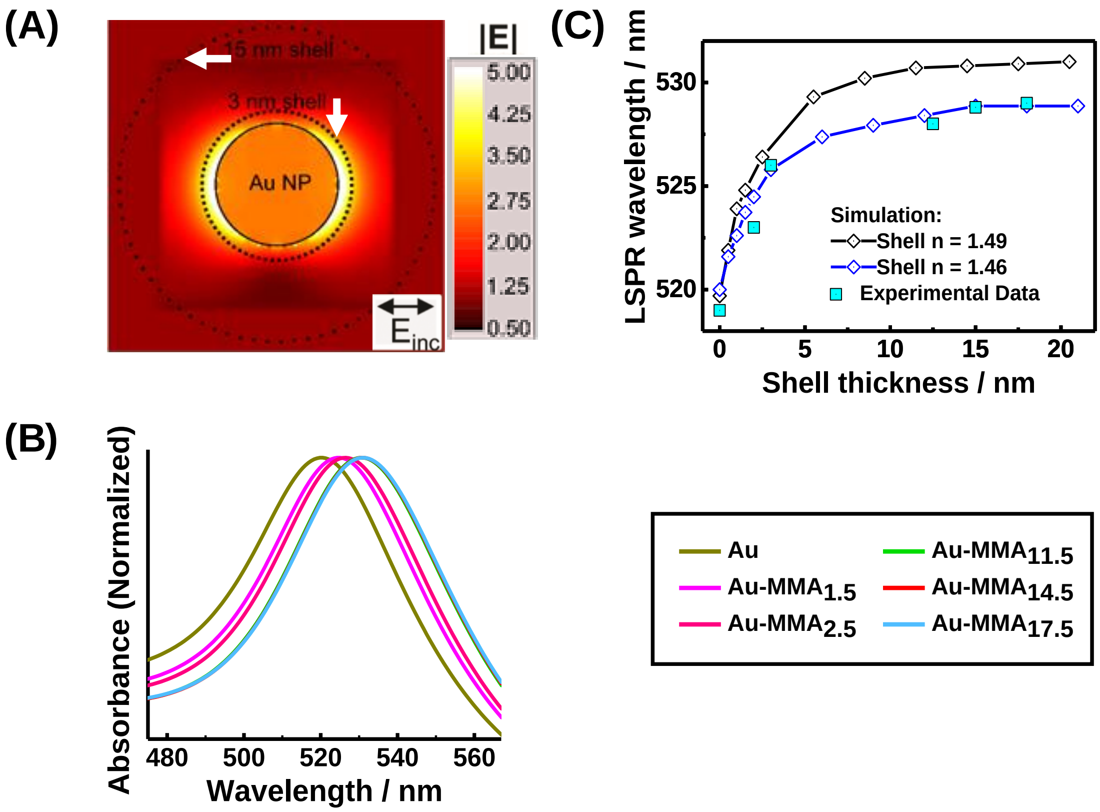

Figure 4.7 (A) Simulated near-field map of a single Au NP in water with an outline (solid line), the thin 3 nm polymer shell for Au-CEA$_3$ (dotted line) and the 15 nm polymer shell for Au-MAA$_{15}$ (wide dotted line). The colour code showed the magnitude of the electric field at the LSPR maximum. (B) Simulated absorbance spectra for Au-MMA core–shell particles with a range of shell thicknesses. (C) Simulated data showed the dependence of the LSPR wavelength on the shell thickness (δ_{TEM}) for polymer shell with refractive index, n = 1.49 (black open diamonds), and n = 1.46 (purple open diamonds) compared to experimental data (blue closed squares).

4.4.5 pH-triggered LSPR changes

As shown in Fig. 4.2 and Fig. 4.4, the MAA/CEA containing core-shell particles exhibited pH-dependent changes in d_z when the pH of solution approached the pK_a. The swelling of the shell could affect the local refractive index around the Au cores. Therefore, it was expected to observe a change of LSPR properties with pH. In Fig. 4.8, the pH of the solution is plotted against the characteristic LSPR wavelength for selected core-shell dispersions. There is no observable LSPR peak wavelength shift in Au NPs and Au-MAA$_{18}$ particles, which is reasonable due to their non-swellable behaviour (Fig. 4.2). However, both Au-CEA$_2$ and Au-CEA$_3$ particles also maintained a constant LSPR wavelength in their pH swelling region, i.e. at pH > 6.0. The refractive index surrounding Au cores was expected to change with the expansion of the copolymer shell. This effect might be attenuated due to their very thin shell thicknesses. In the simulated near-field map (Fig. 4.7(A)), the CEA containing shell was closely located inside the near-field area, which also accompanied a large contribution of the surrounding water ($n \approx 1.33$). The overall effective medium refractive index should be lower than the value of poly(MMA) shell. The swelling process could cause a slight reduction of n in shell, and the shell was further propagated in the near-field zone. Therefore, these very thin shells of Au-CEA$_2$ and Au-CEA$_3$ particles could not provide any strong shifts with a significant change of the effective n value.

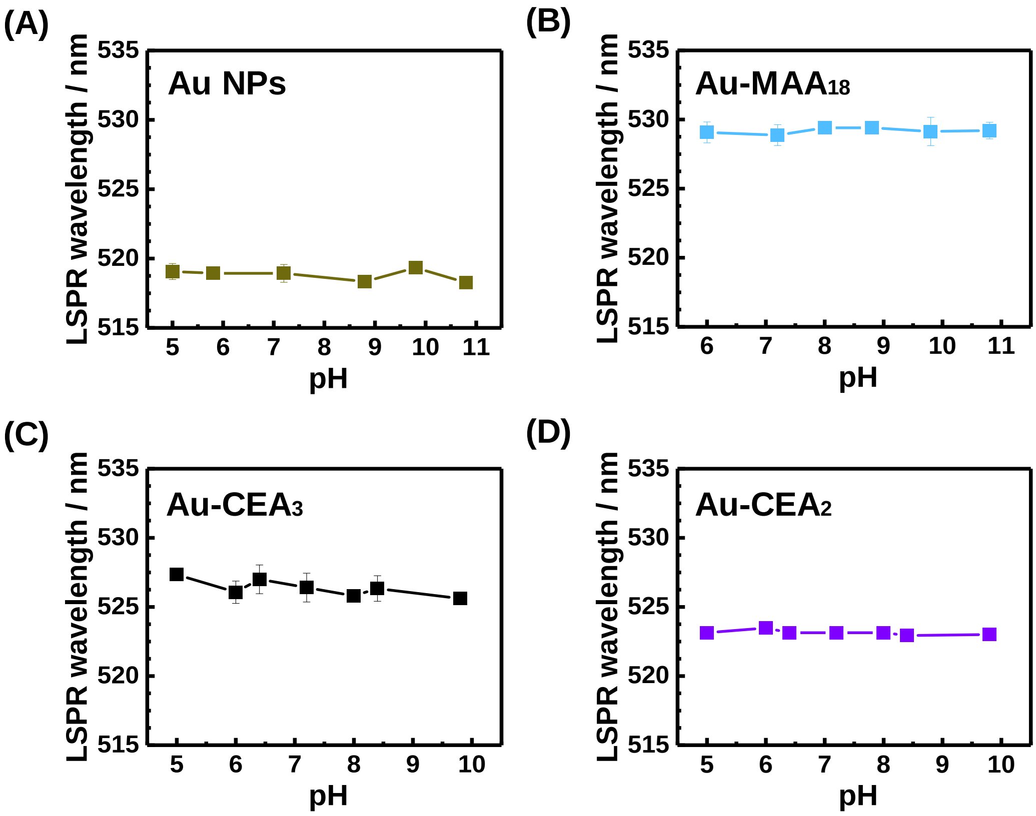

Figure 4.8 The variation of LSPR wavelengths for (A) Au NPs (B) Au-MAA$_{18}$ (C) Au-CEA$_3$ and (D) Au-CEA$_2$ as a function of pH. The identities are labelled.

In comparison to other core-shell particles, an obvious LSPR wavelength shift was found in the Au-MAA$_{15}$ particles inside its swelling pH regime (Fig. 4.9(A)). The LSPR showed a pronounced change from ~ 529 nm to ~ 524 nm at pH 6 and 10.8. This blue shift occurred when the pH exceeded 8 (Fig. 4.9(B)), which was consistent with its swelling behaviour (Fig. 4.2). Here, the thick shell of Au-MAA$_{15}$ occupied the whole area of the near-field zone in the simulated map (Fig. 4.7(A)). When the shell was swollen, water could effectively penetrate through the near-field zone and finally dilute the effective refractive index value around Au cores. As a result, the characteristic LSPR wavelength of Au-MAA$_{15}$ could shift toward the position of Au NPs. In Fig. 4.9(C), a visible transition of colour from deep magenta to pink was observed in solution with increasing pH. These pH-responsive results supported the outcomes from the simulation, and showed the potential as an optical colorimetric probe in pH sensing.[79] On the other hand, the shift of wavelength could reflect the variation of the effective refractive index value change as a consequence of the shell swelling. Such particles could be potentially used as a remote method to reflect the size change.[80,81]

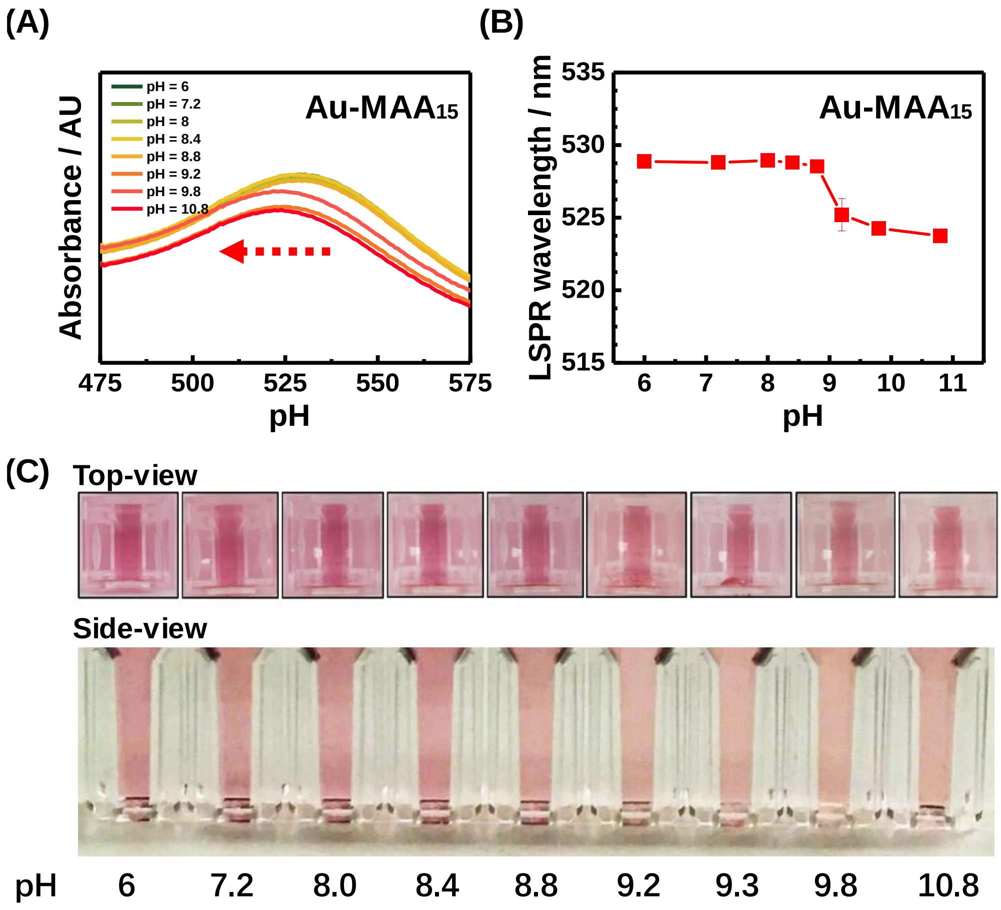

Figure 4.9 (A) UV-Vis spectra of Au-MAA$_{15}$ were recorded at a range of pH values. (B) The variation of LSPR wavelengths in Au-MAA$_{15}$ as a function of pH. The identities are labelled. (C) The pictures (Top-view (intensive colour) and side-view) of Au-MAA$_{15}$ containing cuvettes were captured for a range of pH values.

4.4.6 Reversible pH-triggered aggregation and pH sensing

4.4.6.1 Au-CEA$_2$ core-shell particle aggregation

The Au-CEA particles showed a very thin copolymer and low zeta potentials below pH 6 (Fig. 4.4), which suggested poor colloidal stability of the dispersion at low pH. However, DLS measurements showed a fascinating pH-dependent swelling of these particles was present in the physiological pH range. Here, Au-CEA$_2$ particles were chosen to explore their potential for biomedical applications. As shown in Fig. 4.10(A(i)-(ii)), Au-CEA$_2$ particles were covered by a ~ 2 nm thin shell at pH 5. When the pH reached 7.4, these shells expanded to ~ 5 nm due to the presence of negatively charged carboxylic groups (Fig. 4.10(B(i)-(ii))). This swelling change was visualised under TEM, which agreed with the data in the DLS measurements (Fig. 4.4).

A pH-triggered aggregation can be achieved by fixing the pH of Au-CEA$_2$ particles below 6.4. Subsequently, the centrifugation process or the physiological ionic strength were applied to accelerate the aggregation of particles. The electrostatic and steric repulsion were weakened in the electrolyte with low pH and the collapsed thin shell was no longer able to maintain good colloidal stability. As a result, aggregates of particles were built up and this is highlighted in the pictures (Fig. 4.10(A(iii))). This aggregate was not redispersible with the addition of buffer less than pH 6.4. In contrast, the physiological pH conditions (~ 7.4) easily redispersed the particles (after 2 s) and restored the colour of the solution due to the shell swelling as shown in Fig. 4.10(B(iii)). The results suggested the aggregation of Au-CEA$_2$ particles could be manipulated using pH.

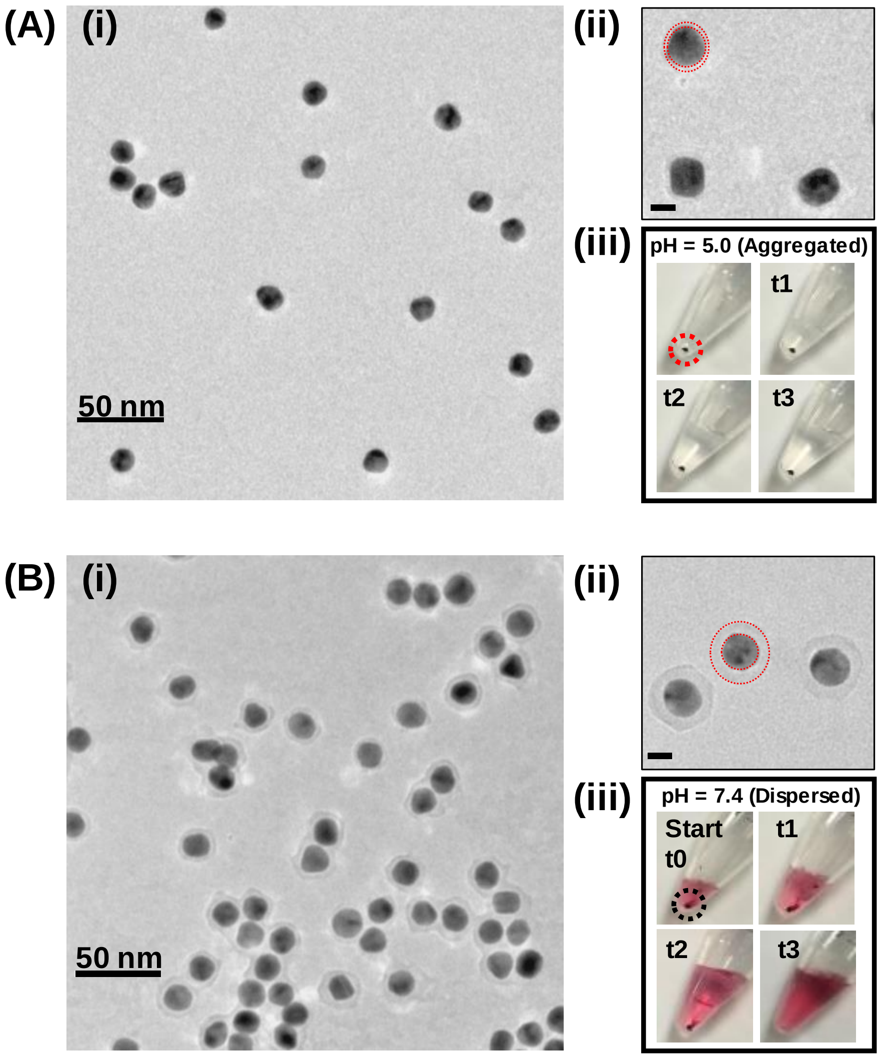

Figure 4.10 Au-CEA$_2$ particles were dispersed at (A) pH 5 and (B) pH 7.4, respectively. (i) The TEM images and (ii) highlighted shells (red dotted line, scale bars = 10 nm) are shown in both dispersions. (iii) The redispersion experiments of pH-triggered aggregates were performed using different pH buffers. The pictures were recorded simultaneously at different time points of the addition process (t_0 to t_3, interval ~ 0.5 s).

4.4.6.2 Reversible aggregation and UV-Vis spectral changes

A reversible aggregation of Au-CEA$_2$ particles was established by cyclic changing of the pH in the dispersion. In Fig. 4.11(A), the colour of the solution showed a pronounced difference between pH < 6.4 and pH > 6.4 (with the buffer or PBS adjustment). A reversible transition of violet to pink was observed by tuning the pH. The UV-Vis spectra (Fig. 4.11(B)) revealed the shift of LSPR wavelength from 522 nm to 542 nm with a broader absorption after aggregation. The spectral shift could be returned to its original position by redispersing the Au-CEA$_2$ aggregates in PBS. After repeated cycles of this process, the change of LSPR peak wavelength showed a reasonably good reversibility (Fig. 4.11(C)). In Chapter 3 (Fig. 3.15 and Fig. 3.16), Au NPs with thick shells could avoid this kind of spectral changes by reducing the probability of LSPR coupling. According to the simulated near-field map (Fig. 4.7(A)), this ~ 2 nm collapsed thin shell was located inside the strong near-field surrounding the Au core. A near-field coupling effect could be unavoidable when Au-CEA$_2$ particles started to get closer to each other. Therefore, the aggregation of Au-CEA$_2$ particles accompanied the visible change of colour, which could be beneficial in the sensing area, especially for pH detection. In addition, this reversible aggregation occurred within the physiological pH range, which suggests a favourable application for in vitro/vivo studies.

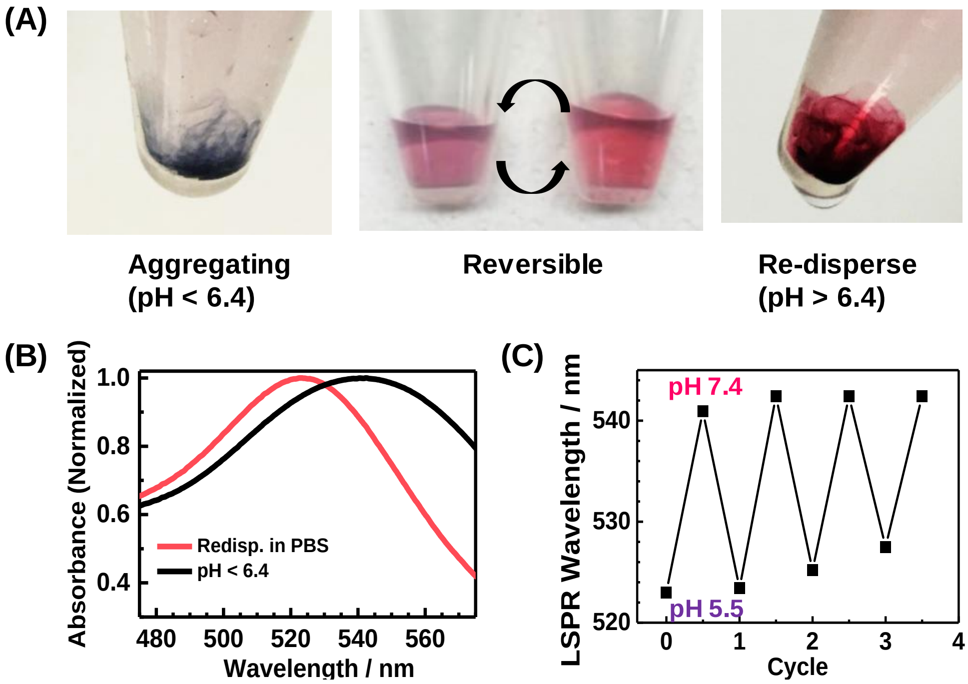

Figure 4.11 (A) The pictures showed the reversible aggregation of Au-CEA$_2$ particles occurred by varying the pH of dispersions. (B) The spectral change of the aggregated Au-CEA$_2$ particles. (C) Reversible red-shifts with pH cycling.

4.4.6.3 HeLa cells culture and internalisation study

The cellular study of Au nanomaterials can be directly visualised and located in a dark field microscope without involving complex sample preparation and instrumentation.[82,83] Cheap and simple operation makes Au-acrylic particles highly desirable as an intracellular probe for cancer cells. HeLa cells are a cell line, which is commonly used in cell culture and cancer research.[41,84,85] These cells were selected to culture with Au-CEA$_2$ particles to examine the potential of particles to be used in biomedical research. In Fig. 4.12, the live/dead images showed the cytotoxicity results of HeLa cells in the presence of Au-CEA$_2$ particles (1.0 nM). In comparison to the control images, there were few red stained cells under the fluorescent microscope. Au-CEA$_2$ particles were confirmed as not cytotoxic at days 3 and 6.

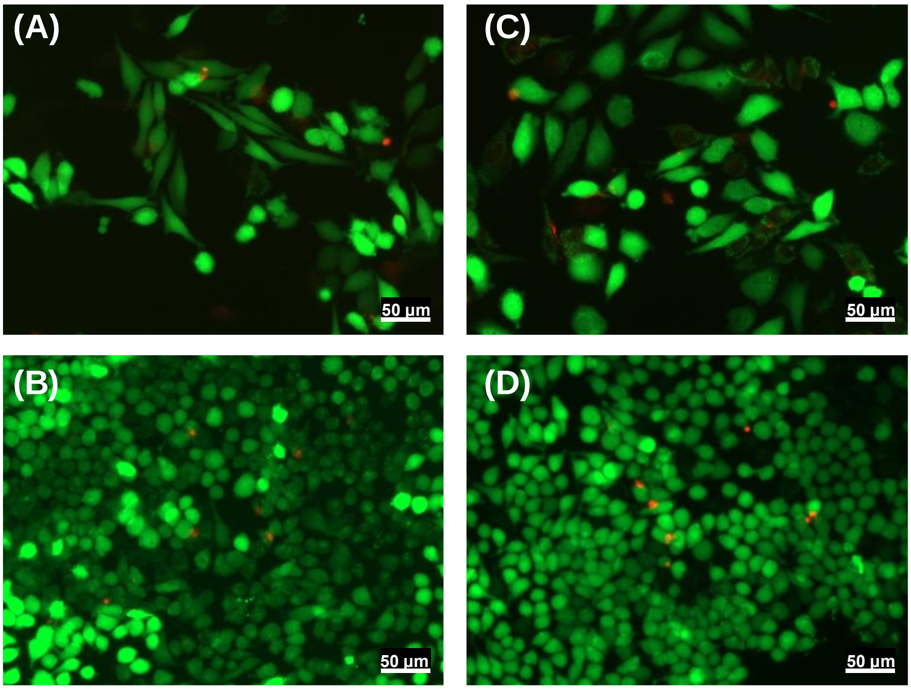

Figure 4.12 Live/dead assay images of HeLa cell line in the (A and B) presence and (C and D) absence of Au-CEA$_2$ particles (1 nM) after 3 days and 6 days culture, respectively.

HeLa cells (Control and Au-CEA$_2$ particles) were further cultured after 10 days to examine the cell internalisation of particles. Then, the cells were observed in dark field mode as shown in Fig. 4.13. It is apparent that, many bright dots are only found inside the HeLa cells, which were cultured in the presence of Au-CEA$_2$ particles. The difference between cell studies of the control and Au-CEA$_2$ particles is caused by the formation of aggregates.[86,87] These particles were very small (d_{TEM} ~ 18 nm) and should not be observable under the optical microscopy. However, when the HeLa cells internalised Au-CEA$_2$ particles, pH-triggered aggregation occurred due to the low pH environment of the endosomal/lysosomal lumen[42,48,87] The scattering cross section of the Au aggregates significantly increased and could be visualised as numerous bright features in the dark field mode.[86,87] The image shows a high incidence of granular deposits within the cell membrane of Au-CEA$_2$ treated cultures. These particles were effectively locked inside the cell even after 10 days. Overall, the results show the capability of Au-CEA$_2$ particles in reporting pH environments within the cells. This new structure of the thin pH-responsive copolymer shell with a Au NP core has the potential for applications in biomedical imaging research. In contrast to pH-sensitive fluorescent probes, pH-triggered aggregation of Au-CEA$_2$ particles can significantly increase the scattering signal. The signal can be ~ 5 orders of magnitude stronger than ordinary fluorescent molecules.[88] Intracellular fluorescent probes also suffer from photobleaching effects, which limit their long-term and reliable detection.[89–91] In comparison to the present Au-acrylic system, similar pH-triggered protocols have been reported in other intracellular dark field imaging studies. Nam et al. reported a citraconic amide functionalised Au NP system.[87] The hydrolysis of the citraconic amide produced mixed charged Au surfaces at pH 5.5. As a result of the electrostatic interaction, dark field imaging revealed pH-triggered intracellular aggregation. Song et al. reported a construction of the plasmonic vesicles by self-assembling amphiphilic Au NPs.[92] These Au NPs were grafted by pH-sensitive poly(methyl methacrylate-4-vinylpyridine) brushes, which showed a hydrophobic to hydrophilic transition at pH 5.4. Therefore, the late endosomes or lysosomes could drive the disruption of the plasmonic vesicles. The decoupling of assembled gold nanoparticles resulted in a reduction of scattering signal in the dark field imaging. Most studies of Au NPs have relied on polyethylene glycol coating and ligand functionalisation to construct their designs with built-in pH-responsiveness and colloidal stability.[86,87,92–97] However, potentially useable pH-responsive NG shells have been rarely reported for the intracellular studies. Strong plasmonic coupling is sensitive to a distance ~ 6 nm between the surfaces of Au NPs as shown in Fig. 4.7(A), which highlights the robustness of new Au-CEA$_2$ particles (~ 2 nm shell). Simple Au-acrylic core-shell platforms offer an alternative intracellular solution due to their inherent non-cytotoxicity, tuneable diameter, tailorable optical property, strong colloidal stability, swellable shell and physiological pH working domain (5.5 – 7.4). These plasmonic particles may further simplify the future theranostic design (e.g colloidosomes) for pH-regulated drug release,[98–100] photoacoustic imaging[101–104] and photothermal therapy[103,105–107]. Moreover, the composition of Au-acrylic core-shell is compatible with pH-responsive MG or NG gels. They should be capable of reporting internal gel environments based on LSPR changes, e.g. aggregated Au-CEA$_2$ in mechanical tests.[108,109]

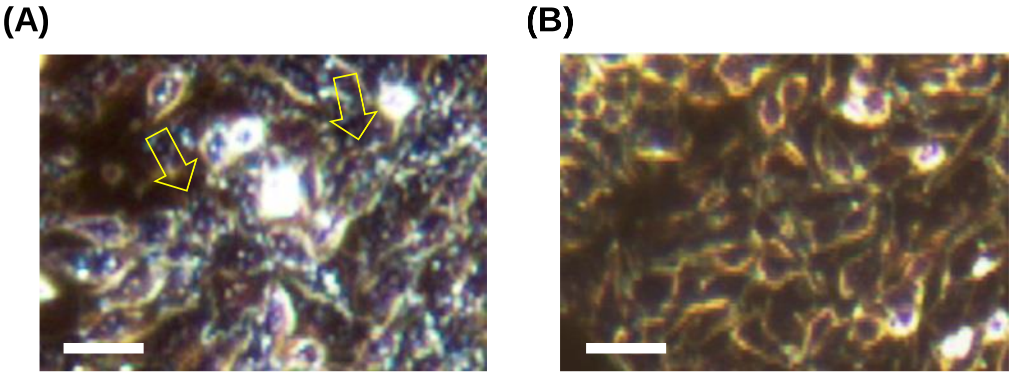

Figure 4.13 Dark field optical images of HeLa cell line in the (A) presence and (B) absence of Au-CEA$_2$ particles (1 nM) after 10 days culture. The bright dots are highlighted by yellow arrows. Scale bars = 50 µm.

4.5 Conclusions

Five kinds of Au core-shell particles were successfully synthesised with tuneable shell thicknesses and swelling through the precipitation polymerisation. Either a thick (δ_{TEM} ~ 12 – 18 nm) or a very thin (δ_{TEM} ~ 2 – 3 nm) copolymer shell was achievable using an acrylic-based formulation based on MMA-(CEA/MAA)-EGDMA. The thin shells were investigated by both TEM and XPS analysis. All these particles were well-dispersed with a pronounced LSPR wavelength. The LSPR wavelength was red shifted with the increase of the shell thickness, and a maximum wavelength was found at 529 nm. The change was caused by the variation of the effective refractive index of the medium, with the supporting evidence from the simulated spectral data and near-field maps. The LSPR wavelength shift of Au-MMA (simulated) closely fitted the experimental results of the five Au core-shell particles, when the refractive index of the shell was assumed as 1.46. The pH-dependent LSPR wavelength changes and pH-triggered reversible aggregation were found in Au-MAA$_{15}$ and Au-CEA$_2$ core-shell particles, respectively. Such a reversible aggregation can occur within the physiological pH range. The HeLa cell culture and internalisation study highlighted the capability of Au-CEA$_2$ particles in reporting the pH environment within the cell. Those particles may have further potential in tumour treatment or other theranostic development.

4.6 References

1. Krishnendu, S.; Sarit S., A.; Chaekyu, K.; Xiaoning, L.; Vincent M., R. Gold Nanoparticles in Chemical and Biological Sensing. *Chem. Rev.* **2014**, *112*, 2739–2779.

2. Qian, Z.; Ginger, D. S. Reversibly Reconfigurable Colloidal Plasmonic Nanomaterials. *J. Am. Chem. Soc.* **2017**, *139*, 5266–5276.

3. Ruan, Q.; Fang, C.; Jiang, R.; Jia, H.; Lai, Y.; Wang, J.; Lin, H. Q. Highly Enhanced Transverse Plasmon Resonance and Tunable Double Fano Resonances in Gold@titania Nanorods. *Nanoscale* **2016**, *8*, 6514–6526.

4. Said-Mohamed, C.; Niskanen, J.; Lairez, D.; Tenhu, H.; Maioli, P.; Del Fatti, N.; Vallée, F.; Lee, L. T. Polymer-Modulated Optical Properties of Gold Sols. *J. Phys. Chem. C* **2012**, *116*, 12660–12669.

5. Wang, Z.; Quan, X.; Zhang, Z.; Cheng, P. Optical Absorption of Carbon-Gold Core-Shell Nanoparticles. *J. Quant. Spectrosc. Radiat. Transf.* **2018**, *205*, 291–298.

6. Byers, C. P.; Halas, N. J.; Nordlander, P.; Link, S.; Landes, C. F.; Swearer, D. F.; Yorulmaz, M.; Hoener, B. S.; Huang, D.; Hoggard, A.; et al. From Tunable Core-Shell Nanoparticles to Plasmonic Drawbridges: Active Control of Nanoparticle Optical Properties. *Sci. Adv.* **2015**, *1*, 1–10.

7. Zhang, Y.; Cui, X.; Shi, F.; Deng, Y. Nano-Gold Catalysis in Fine Chemical Synthesis. *Chem. Rev.* **2012**, *112*, 2467–2505.

8. Zhang, Q.; Lee, I.; Joo, J. B.; Zaera, F.; Yin, Y. Core-Shell Nanostructured Catalysts. *Acc. Chem. Res.* **2013**, *46*, 1816–1824.

9. Yin, Z.; Wang, Y.; Song, C.; Zheng, L.; Ma, N.; Liu, X.; Li, S.; Lin, L.; Li, M.; Xu, Y.; et al. Hybrid Au-Ag Nanostructures for Enhanced Plasmon-Driven Catalytic Selective Hydrogenation through Visible Light Irradiation and Surface-Enhanced Raman Scattering. *J. Am. Chem. Soc.* **2018**, *140*, 864–867.

10. Lin, C. H.; Liu, X.; Wu, S. H.; Liu, K. H.; Mou, C. Y. Corking and Uncorking a Catalytic Yolk-Shell Nanoreactor: Stable Gold Catalyst in Hollow Silica Nanosphere. *J. Phys. Chem. Lett.* **2011**, *2*, 2984–2988.

11. Gawande, M. B.; Goswami, A.; Asefa, T.; Guo, H.; Biradar, A. V.; Peng, D.-L.; Zboril, R.; Varma, R. S. Core–Shell Nanoparticles: Synthesis and Applications in Catalysis and Electrocatalysis. *Chem. Soc. Rev.* **2015**, *44*, 7540–7590.

12. Mieszawska, A. J.; Mulder, W. J. M.; Fayad, Z. A.; Cormode, D. P. Multifunctional Gold Nanoparticles for Diagnosis and Therapy of Disease. *Mol. Pharm.* **2013**, *10*, 831–847.

13. Yang, X.; Yang, M.; Pang, B.; Vara, M.; Xia, Y. Gold Nanomaterials at Work in Biomedicine. *Chem. Rev.* **2015**, *115*, 10410–10488.

14. Chen, X.; Zhang, Q.; Li, J.; Yang, M.; Zhao, N.; Xu, F. J. Rattle-Structured Rough Nanocapsules with in-Situ-Formed Gold Nanorod Cores for Complementary Gene/Chemo/Photothermal Therapy. *ACS Nano* **2018**, *12*, 5646–5656.

15. Moreira, A. F.; Rodrigues, C. F.; Reis, C. A.; Costa, E. C.; Correia, I. J. Gold-Core Silica Shell Nanoparticles Application in Imaging and Therapy: A Review. *Microporous Mesoporous Mater.* **2018**, *270*, 168–179.

16. Tomitaka, A.; Ota, S.; Nishimoto, K.; Arami, H.; Takemura, Y.; Nair, M. Dynamic Magnetic Characterization and Magnetic Particle Imaging Enhancement of Magnetic-Gold Core–Shell Nanoparticles. *Nanoscale* **2019**, *11*, 6489–6496.

17. Yockell-Lelièvre, H.; Lussier, F.; Masson, J. F. Influence of the Particle Shape and Density of Self-Assembled Gold Nanoparticle Sensors on LSPR and SERS. *J. Phys. Chem. C* **2015**, *119*, 28577–28585.

18. Marino, A.; Arai, S.; Hou, Y.; Degl'Innocenti, A.; Cappello, V.; Mazzolai, B.; Chang, Y. T.; Mattoli, V.; Suzuki, M.; Ciofani, G. Gold Nanoshell-Mediated Remote Myotube Activation. *ACS Nano* **2017**, *11*, 2494–2505.

19. Zhao, R.; Han, X.; Li, Y.; Wang, H.; Ji, T.; Zhao, Y.; Nie, G. Photothermal Effect Enhanced Cascade-Targeting Strategy for Improved Pancreatic Cancer Therapy by Gold Nanoshell@Mesoporous Silica Nanorod. *ACS Nano* **2017**, *11*, 8103–8113.

20. Hirsch, L. R.; Stafford, R. J.; Bankson, J. A.; Sershen, S. R.; Rivera, B.; Price, R. E.; Hazle, J. D.; Halas, N. J.; West, J. L. Nanoshell-Mediated near-Infrared Thermal Therapy of Tumors under Magnetic Resonance Guidance. *Proc. Natl. Acad. Sci.* **2003**, *100*, 13549–13554.

21. Kuzyk, A.; Yang, Y.; Duan, X.; Stoll, S.; Govorov, A. O.; Sugiyama, H.; Endo, M.; Liu, N. A Light-Driven Three-Dimensional Plasmonic Nanosystem That Translates Molecular Motion into Reversible Chiroptical Function. *Nat. Commun.* **2016**, *7*, 1–6.

22. Lin, L. Sen; Yang, X.; Zhou, Z.; Yang, Z.; Jacobson, O.; Liu, Y.; Yang, A.; Niu, G.; Song, J.; Yang, H. H.; et al. Yolk–Shell Nanostructure: An Ideal Architecture to Achieve Harmonious Integration of Magnetic–Plasmonic Hybrid Theranostic Platform. *Adv. Mater.* **2017**, *29*.

23. Ghosh Chaudhuri, R.; Paria, S. Core/Shell Nanoparticles: Classes, Properties, Synthesis Mechanisms, Characterization, and Applications. *Chem. Rev.* **2012**, *112*, 2373–2433.

24. Choueiri, R. M.; Galati, E.; Thérien-Aubin, H.; Klinkova, A.; Larin, E. M.; Querejeta-Fernández, A.; Han, L.; Xin, H. L.; Gang, O.; Zhulina, E. B.; et al.

Surface Patterning of Nanoparticles with Polymer Patches. *Nature* **2016**, *538*, 79–83.

25. Li, J. F.; Zhang, Y. J.; Ding, S. Y.; Panneerselvam, R.; Tian, Z. Q. Core-Shell Nanoparticle-Enhanced Raman Spectroscopy. *Chem. Rev.* **2017**, *117*, 5002–5069.

26. Liu, Y.; Shipton, M. K.; Ryan, J.; Kaufman, E. D.; Franzen, S.; Feldheim, D. L. Synthesis, Stability, and Cellular Internalization of Gold Nanoparticles Containing Mixed Peptide-Poly(Ethylene Glycol) Monolayers. *Anal. Chem.* **2007**, *79*, 2221–2229.

27. Liz-Marzán, L. M.; Giersig, M.; Mulvaney, P. Synthesis of Nanosized Gold−Silica Core−Shell Particles. *Langmuir* **1996**, *12*, 4329–4335.

28. Kang, Y.; Taton, T. A. Core/Shell Gold Nanoparticles by Self-Assembly and Crosslinking of Micellar, Block-Copolymer Shells. *Angew. Chemie - Int. Ed.* **2005**, *44*, 409–412.

29. Contreras-Cáceres, R.; Pacifico, J.; Pastoriza-Santos, I.; Pérez-Juste, J.; Fernández-Barbero, A.; Liz-Marzán, L. M. Au@pNIPAM Thermosensitive Nanostructures: Control over Shell Cross-Linking, Overall Dimensions, and Core Growth. *Adv. Funct. Mater.* **2009**, *19*, 3070–3076.

30. Chen, J.; Jin, Y.; Fahruddin, N.; Zhao, J. X. Development of Gold Nanoparticle-Enhanced Fluorescent Nanocomposites. *Langmuir* **2013**, *29*, 1584–1591.

31. Schneider, G.; Decher, G.; Nerambourg, N.; Praho, R.; Werts, M. H. V.; Blanchard-Desce, M. Distance-Dependent Fluorescence Quenching on Gold Nanoparticles Ensheathed with Layer-by-Layer Assembled Polyelectrolytes. *Nano Lett.* **2006**, *6*, 530–536.

32. Guarrotxena, N.; Quijada-Garrido, I. Optical and Swelling Stimuli-Response of Functional Hybrid Nanogels: Feasible Route to Achieve Tunable Smart Core@Shell Plasmonic@Polymer Nanomaterials. *Chem. Mater.* **2016**, *28*, 1402–1412.

33. Karg, M.; Jaber, S.; Hellweg, T.; Mulvaney, P. Surface Plasmon Spectroscopy of Gold-Poly-N-Isopropylacrylamide Core-Shell Particles. *Langmuir* **2011**, *27*, 820–827.

34. Rauh, A.; Honold, T.; Karg, M. Seeded Precipitation Polymerization for the Synthesis of Gold-Hydrogel Core-Shell Particles: The Role of Surface Functionalization and Seed Concentration. *Colloid Polym. Sci.* **2016**, *294*, 37–47.

35. Dulle, M.; Jaber, S.; Rosenfeldt, S.; Radulescu, A.; Förster, S.; Mulvaney, P.; Karg, M. Plasmonic Gold-Poly(N-Isopropylacrylamide) Core-Shell Colloids with Homogeneous Density Profiles: A Small Angle Scattering Study. *Phys. Chem. Chem. Phys.* **2015**, *17*, 1354–1367.

36. Reineck, P.; Gómez, D.; Ng, S. H.; Karg, M.; Bell, T.; Mulvaney, P.; Bach, U. Distance and Wavelength Dependent Quenching of Molecular Fluorescence by Au@SiO2 Core-Shell Nanoparticles. *ACS Nano* **2013**, *7*, 6636–6648.

37. Hanske, C.; Sanz-Ortiz, M. N.; Liz-Marzán, L. M. Silica-Coated Plasmonic Metal Nanoparticles in Action. *Adv. Mater.* **2018**, *30*, 1–28.

38. Juvé, V.; Cardinal, M. F.; Lombardi, A.; Crut, A.; Maioli, P.; Pérez-Juste, J.; Liz-Marzán, L. M.; Del Fatti, N.; Vallée, F. Size-Dependent Surface Plasmon Resonance Broadening in Nonspherical Nanoparticles: Single Gold Nanorods. *Nano Lett.* **2013**, *13*, 2234–2240.

39. Yang, Y.; Zhu, J.; Zhao, J.; Weng, G. J.; Li, J. J.; Zhao, J. W. Growth of Spherical Gold Satellites on the Surface of Au@Ag@SiO 2 Core-Shell Nanostructures Used for an Ultrasensitive SERS Immunoassay of Alpha-Fetoprotein. *ACS Appl. Mater. Interfaces* **2019**, *11*, 3617–3626.

40. Carnevale, K. J. F.; Riskowski, R. A.; Strouse, G. F. A Gold Nanoparticle Bio-Optical Transponder to Dynamically Monitor Intracellular PH. *ACS Nano* **2018**, *12*, 5956–5968.

41. Tang, H.; Zhao, W.; Yu, J.; Li, Y.; Zhao, C. Recent Development of PH-Responsive Polymers for Cancer Nanomedicine. *Molecules* **2019**.

42. Guo, A.; Wang, Y.; Xu, S.; Zhang, X.; Li, M.; Liu, Q.; Shen, Y.; Cui, D.; Guo, S. Preparation and Evaluation of PH-Responsive Charge-Convertible Ternary Complex FA-PEI-CCA/PEI/DNA with Low Cytotoxicity and Efficient Gene Delivery. *Colloids Surf., B* **2017**, *152*, 58–67.

43. Gao, W.; Chan, J. M.; Farokhzad, O. C. PH-Responsive Nanoparticles for Drug Delivery. *Mol. Pharm.* **2010**, *7*, 1913–1920.

44. Yilmaz, G.; Guler, E.; Geyik, C.; Demir, B.; Ozkan, M.; Odaci Demirkol, D.; Ozcelik, S.; Timur, S.; Remzi Becer, C. PH Responsive Glycopolymer Nanoparticles for Targeted Delivery of Anti-Cancer Drugs. *Mol. Syst. Des. Eng.* **2018**, *3*, 150–158.

45. Ranneh, A. H.; Takemoto, H.; Sakuma, S.; Awaad, A.; Nomoto, T.; Mochida, Y.; Matsui, M.; Tomoda, K.; Naito, M.; Nishiyama, N. An Ethylenediamine-Based Switch to Render the Polyzwitterion Cationic at Tumorous PH for Effective Tumor Accumulation of Coated Nanomaterials. *Angew. Chemie - Int. Ed.* **2018**, *57*, 5057–5061.

46. Zhou, Z.; Shen, Y.; Tang, J.; Fan, M.; Van Kirk, E. A.; Murdoch, W. J.; Radosz, M. Charge-Reversal Drug Conjugate for Targeted Cancer Cell Nuclear Drug Delivery. *Adv. Funct. Mater.* **2009**, *19*, 3580–3589.

47. Zhang, X.; Lin, Y.; Gillies, R. J. Tumor PH and Its Measurement Xiaomeng. *J. Nucl Med.* **2010**, *51*, 1167–1170.

48. Kato, Y.; Ozawa, S.; Miyamoto, C.; Maehata, Y.; Suzuki, A.; Maeda, T.; Baba, Y. Acidic Extracellular Microenvironment and Cancer. *Cancer Cell Int.* **2013**, *13*, 1.

49. Li, J.; Mooney, D. J. Designing Hydrogels for Controlled Drug Delivery. *Nat. Rev. Mater.* **2016**, *1*.

50. Ekkelenkamp, A. E.; Elzes, M. R.; Engbersen, J. F. J.; Paulusse, J. M. J. Responsive Crosslinked Polymer Nanogels for Imaging and Therapeutics Delivery. *J. Mater. Chem. B* **2018**, *6*, 210–235.

51. Dennis, A. M.; Rhee, W. J.; Sotto, D.; Dublin, S. N.; Bao, G. Quantum Dot-Fluorescent Protein Fret Probes for Sensing Intracellular PH. *ACS Nano* **2012**, *6*, 2917–2924.

52. Huang, X.; El-Sayed, I. H.; Qian, W.; El-Sayed, M. A. Cancer Cell Imaging and Photothermal Therapy in the Near-Infrared Region by Using Gold Nanorods. *J. Am. Chem. Soc.* **2006**, *128*, 2115–2120.

53. Zhu, M.; Lu, D.; Wu, S.; Lian, Q.; Wang, W.; Milani, A. H.; Cui, Z.; Nguyen, N. T.; Chen, M.; Lyon, L. A.; et al. Responsive Nanogel Probe for Ratiometric Fluorescent Sensing of PH and Strain in Hydrogels. *ACS Macro Lett.* **2017**, *6*, 1245–1250.

54. Zhu, M.; Lu, D.; Wu, S.; Lian, Q.; Wang, W.; Lyon, L. A.; Wang, W.; Bártolo, P.; Saunders, B. R. Using Green Emitting PH-Responsive Nanogels to Report Environmental Changes within Hydrogels: A Nanoprobe for Versatile Sensing. *Nanoscale* **2019**, *11*, 11484–11495.

55. Milani, A. H.; Freemont, A. J.; Hoyland, J. A.; Adlam, D. J.; Saunders, B. R. Injectable Doubly Cross-Linked Microgels for Improving the Mechanical Properties of Degenerated Intervertebral Discs. *Biomacromolecules* **2012**, *13*, 2793–2801.

56. Liu, R.; Milani, A. H.; Freemont, T. J.; Saunders, B. R. Doubly Crosslinked PH-Responsive Microgels Prepared by Particle Inter-Penetration: Swelling and Mechanical Properties. *Soft Matter* **2011**, *7*, 4696–4704.

57. Lu, D.; Zhu, M.; Wu, S.; Wang, W.; Lian, Q.; Saunders, B. R. Triply Responsive Coumarin-Based Microgels with Remarkably Large Photo-Switchable Swelling. *Polym. Chem.* **2019**, *10*, 2516–2526.

58. Johnson, P. B.; Christy, R. W. Optical Constants of the Noble Metals. *Phys. Rev. B* **1972**, *6*, 4370–4379.

59. Hale, G. M.; Querry, M. R. Optical Constants of Water in the 200-Nm to 200-Mm Wavelength Region. *Appl. Opt.* **1973**, *12*, 555.

60. Sultanova, N.; Kasarova, S.; Nikolov, I. Dispersion Properties of Optical Polymers. *Acta Phys. Pol. A* **2009**, *116*, 585–587.

61. Michel, P.; Dugas, J.; Cariou, J. M.; Martin, L. Thermal Variations of Refractive Index of PMMA, Polystyrene, and Poly (4-Methyl-1-Pentene). *J. Macromol. Sci. Part B* **1986**, *25*, 379–394.

62. Milani, A. H.; Saunders, J. M.; Nguyen, N. T.; Ratcliffe, L. P. D.; Adlam, D. J.; Freemont, A. J.; Hoyland, J. A.; Armes, S. P.; Saunders, B. R. Synthesis of Polyacid Nanogels: PH-Responsive Sub-100 Nm Particles for Functionalisation and Fluorescent Hydrogel Assembly. *Soft Matter* **2017**, *13*, 1554–1560.

63. Milani, A. H.; Bramhill, J.; Freemont, A. J.; Saunders, B. R. Swelling and Mechanical Properties of Hydrogels Composed of Binary Blends of Inter-Linked PH-Responsive Microgel Particles. *Soft Matter* **2015**, *11*, 2586–2595.

64. Fang, C.; Wang, Y.; Lin, Z.; Daniels, E. S.; Klein, A. Partitioning of Monobutyl Itaconate and β-Carboxyethyl Acrylate between Organic and Water Phases. *J. Appl. Polym. Sci.* **2014**, *131*, 1–7.

65. Justus, C. R.; Dong, L.; Yang, L. V. Acidic Tumor Microenvironment and PH-Sensing G Protein-Coupled Receptors. *Front. Physiol.* **2013**, *4 DEC*, 1–9.

66. Alswieleh, A. M.; Cheng, N.; Canton, I.; Ustbas, B.; Xue, X.; Ladmiral, V.; Xia, S.; Ducker, R. E.; El Zubir, O.; Cartron, M. L.; et al. Zwitterionic Poly(Amino Acid Methacrylate) Brushes. *J. Am. Chem. Soc.* **2014**, *136*, 9404–9413.

67. Ma, Z.; Mao, Z.; Gao, C. Surface Modification and Property Analysis of Biomedical Polymers Used for Tissue Engineering. *Colloids Surf., B* **2007**, *60*, 137–157.

68. Kumar, A.; Mandal, S.; Selvakannan, P. R.; Pasricha, R.; Mandale, A. B.; Sastry, M. Investigation into the Interaction between Surface-Bound Alkylamines and Gold Nanoparticles. *Langmuir* **2003**, *19*, 6277–6282.

69. Ghosh, S. K.; Nath, S.; Kundu, S.; Esumi, K.; Pal, T. Solvent and Ligand Effects on the Localized Surface Plasmon Resonance (LSPR) of Gold Colloids. *J. Phys. Chem. B* **2004**, *108*, 13963–13971.

70. Doña, M.; Ortega-Rodriguez, A.; Alarcón-Fernández, C.; López-Romero, J. M.; Contreras-Cáceres, R. Effect of the Cross-Linking Density on the Gold Core Oxidation in Hybrid Core@shell Au@pNIPAM and Janus Au@p4VP Systems. *Colloids Surf., A* **2020**, *584*, 124014.

71. Clara-Rahola, J.; Moscoso, A.; Belén Ruiz-Muelle, A.; Laurenti, M.; Formanek, P.; Lopez-Romero, J. M.; Fernández, I.; Diaz, J. F.; Rubio-Retama, J.; Fery, A.; et al. Au@p4VP Core@shell PH-Sensitive Nanocomposites Suitable for Drug Entrapment. *J. Colloid Interface Sci.* **2018**, *514*, 704–714.

72. Li, Z.; Xia, L.; Li, G.; Hu, Y. Raman Spectroscopic Imaging of PH Values in Cancerous Tissue by Using Polyaniline@gold Nanoparticles. *Microchim. Acta* **2019**, *186*.

73. Jeon, J. W.; Zhou, J.; Geldmeier, J. A.; Ponder, J. F.; Mahmoud, M. A.; El-Sayed, M.; Reynolds, J. R.; Tsukruk, V. V. Dual-Responsive Reversible Plasmonic Behavior of Core-Shell Nanostructures with PH-Sensitive and Electroactive Polymer Shells. *Chem. Mater.* **2016**, *28*, 7551–7563.

74. Lin, H.; Song, L.; Huang, Y.; Cheng, Q.; Yang, Y.; Guo, Z.; Su, F.; Chen, T. Macroscopic Au@PANI Core/Shell Nanoparticle Superlattice Monolayer Film with Dual-Responsive Plasmonic Switches. *ACS Appl. Mater. Interfaces* **2020**, *12*, 11296–11304.

75. Murphy, S.; Jaber, S.; Ritchie, C.; Karg, M.; Mulvaney, P. Laser Flash Photolysis of Au-PNIPAM Core-Shell Nanoparticles: Dynamics of the Shell Response. *Langmuir* **2016**, *32*, 12497–12503.

76. Nguyen, H. H.; Payré, B.; Fitremann, J.; Lauth-De Viguerie, N.; Marty, J. D. Thermoresponsive Properties of PNIPAM-Based Hydrogels: Effect of Molecular Architecture and Embedded Gold Nanoparticles. *Langmuir* **2015**, *31*, 4761–4768.

77. Casado-Rodriguez, M. A.; Sanchez-Molina, M.; Lucena-Serrano, A.; Lucena-Serrano, C.; Rodriguez-Gonzalez, B.; Algarra, M.; Diaz, A.; Valpuesta, M.; Lopez-Romero, J. M.; Perez-Juste, J.; et al. Synthesis of Vinyl-Terminated Au Nanoprisms and Nanooctahedra Mediated by 3-Butenoic Acid: Direct Au@pNIPAM Fabrication with Improved SERS Capabilities. *Nanoscale* **2016**, *8*, 4557–4564.

78. Contreras-Cáceres, R.; Pacifico, J.; Pastoriza-Santos, I.; Pérez-Juste, J.; Fernández-Barbero, A.; Liz-Marzán, L. M. Au@pNIPAM Thermosensitive Nanostructures: Control over Shell Cross-Linking, Overall Dimensions, and Core Growth. *Adv. Funct. Mater.* **2009**, *19*, 3070–3076.

79. Sun, S.; Ning, X.; Zhang, G.; Wang, Y. C.; Peng, C.; Zheng, J. Dimerization of Organic Dyes on Luminescent Gold Nanoparticles for Ratiometric PH Sensing. *Angew. Chemie - Int. Ed.* **2016**, *55*, 2421–2424.

80. Koc, M. A.; Raja, S. N.; Hanson, L. A.; Nguyen, S. C.; Borys, N. J.; Powers, A. S.; Wu, S.; Takano, K.; Swabeck, J. K.; Olshansky, J. H.; et al. Characterizing Photon Reabsorption in Quantum Dot-Polymer Composites for Use as Displacement Sensors. *ACS Nano* **2017**, *11*, 2075–2084.

81. Schmidt, M. M.; Wu, S.; Cui, Z.; Nguyen, N. T.; Faulkner, M.; Saunders, B. R. How Gold Nanoparticles Can Be Used to Probe the Structural Changes of a PH-Responsive Hydrogel. *Phys. Chem. Chem. Phys.* **2017**, *19*, 5102–5112.

82. D'Acunto, M. Detection of Intracellular Gold Nanoparticles: An Overview. *Materials (Basel).* **2018**, *11*.

83. Kumar, A.; Kim, S.; Nam, J. M. Plasmonically Engineered Nanoprobes for Biomedical Applications. *J. Am. Chem. Soc.* **2016**, *138*, 14509–14525.

84. Molina, M.; Asadian-Birjand, M.; Balach, J.; Bergueiro, J.; Miceli, E.; Calderón, M. Stimuli-Responsive Nanogel Composites and Their Application in Nanomedicine. *Chem. Soc. Rev.* **2015**, *44*, 6161–6186.

85. Vaughan, H. J.; Green, J. J.; Tzeng, S. Y. Cancer-Targeting Nanoparticles for Combinatorial Nucleic Acid Delivery. *Adv. Mater.* **2019**, *1901081*, 1–36.

86. Nam, J.; La, W. G.; Hwang, S.; Ha, Y. S.; Park, N.; Won, N.; Jung, S.; Bhang, S. H.; Ma, Y. J.; Cho, Y. M.; et al. PH-Responsive Assembly of Gold Nanoparticles and "Spatiotemporally Concerted" Drug Release for Synergistic Cancer Therapy. *ACS Nano* **2013**, *7*, 3388–3402.

87. Nam, J.; Won, N.; Jin, H.; Chung, H.; Kim, S. PH-Induced Aggregation of Gold Nanoparticles for Photothermal Cancer Therapy. *J. Am. Chem. Soc.* **2009**, *131*, 13639–13645.

88. Jain, P. K.; Lee, K. S.; El-Sayed, I. H.; El-Sayed, M. A. Calculated Absorption and Scattering Properties of Gold Nanoparticles of Different Size, Shape, and Composition: Applications in Biological Imaging and Biomedicine. *J. Phys. Chem. B* **2006**, *110*, 7238–7248.

89. He, H.; Xie, C.; Ren, J. Nonbleaching Fluorescence of Gold Nanoparticles and Its Applications in Cancer Cell Imaging. *Anal. Chem.* **2008**, *80*, 5951–5957.

90. Hoebe, R. A.; Van Oven, C. H.; Gadella, T. W. J.; Dhonukshe, P. B.; Van Noorden, C. J. F.; Manders, E. M. M. Controlled Light-Exposure Microscopy Reduces Photobleaching and Phototoxicity in Fluorescence Live-Cell Imaging. *Nat. Biotechnol.* **2007**, *25*, 249–253.

91. Howes, P.; Thorogate, R.; Green, M.; Jickells, S.; Daniel, B. Synthesis, Characterisation and Intracellular Imaging of PEG Capped BEHP-PPV Nanospheres. *Chem. Commun.* **2009**, No. 18, 2490–2492.

92. Song, J.; Zhou, J.; Duan, H. Self-Assembled Plasmonic Vesicles of SERS-Encoded Amphiphilic Gold Nanoparticles for Cancer Cell Targeting and Traceable Intracellular Drug Delivery. *J. Am. Chem. Soc.* **2012**, *134*, 13458–13469.

93. Zhao, Y.; Cao, L.; Ouyang, J.; Wang, M.; Wang, K.; Xia, X. H. Reversible Plasmonic Probe Sensitive for PH in Micro/Nanospaces Based on i-Motif-Modulated Morpholino-Gold Nanoparticle Assembly. *Anal. Chem.* **2013**, *85*, 1053–1057.

94. Zheng, X. S.; Hu, P.; Cui, Y.; Zong, C.; Feng, J. M.; Wang, X.; Ren, B. BSA-Coated Nanoparticles for Improved SERS-Based Intracellular PH Sensing. *Anal. Chem.* **2014**, *86*, 12250–12257.

95. Jung, S.; Nam, J.; Hwang, S.; Park, J.; Hur, J.; Im, K.; Park, N.; Kim, S. Theragnostic PH-Sensitive Gold Nanoparticles for the Selective Surface Enhanced Raman Scattering and Photothermal Cancer Therapy. *Anal. Chem.* **2013**, *85*, 7674–7681.

96. Dong, B.; Du, S.; Wang, C.; Fu, H.; Li, Q.; Xiao, N.; Yang, J.; Xue, X.; Cai, W.; Liu, D. Reversible Self-Assembly of Nanoprobes in Live Cells for Dynamic Intracellular PH Imaging. *ACS Nano* **2019**.

97. Rosman, C.; Pierrat, S.; Henkel, A.; Tarantola, M.; Schneider, D.; Sunnick, E.; Janshoff, A.; Sönnichsen, C. A New Approach to Assess Gold Nanoparticle Uptake by Mammalian Cells: Combining Optical Dark-Field and Transmission Electron Microscopy. *Small* **2012**, *8*, 3683–3690.

98. Ly, N. H.; Nguyen, T. D.; Joo, S. W. Raman Spectroscopy of PH-Induced Release of Zidovudine from Lactobionic Acid-Conjugated PEGylated Gold Colloids. *Colloids Surf., B* **2018**, *171*, 49–57.

99. Chambre, L.; Degirmenci, A.; Sanyal, R.; Sanyal, A. Multi-Functional Nanogels as Theranostic Platforms: Exploiting Reversible and Nonreversible Linkages for Targeting, Imaging, and Drug Delivery. *Bioconjug. Chem.* **2018**, *29*, 1885–1896.

100. Yang, H.; Wang, Q.; Huang, S.; Xiao, A.; Li, F.; Gan, L.; Yang, X. Smart PH/Redox Dual-Responsive Nanogels for On-Demand Intracellular Anticancer Drug Release. *ACS Appl. Mater. Interfaces* **2016**, *8*, 7729–7738.

101. Chen, Y. S.; Yoon, S. J.; Frey, W.; Dockery, M.; Emelianov, S. Dynamic Contrast-Enhanced Photoacoustic Imaging Using Photothermal Stimuli-Responsive Composite Nanomodulators. *Nat. Commun.* **2017**, *8*, 1–10.

102. Li, W.; Chen, X. Gold Nanoparticles for Photoacoustic Imaging. *Nanomedicine (London, U. K.)* **2015**, *10*, 299–320.

103. Cheng, X.; Sun, R.; Yin, L.; Chai, Z.; Shi, H.; Gao, M. Light-Triggered Assembly of Gold Nanoparticles for Photothermal Therapy and Photoacoustic Imaging of Tumors In Vivo. *Adv. Mater.* **2017**, *29*.

104. Chen, Y. S.; Zhao, Y.; Yoon, S. J.; Gambhir, S. S.; Emelianov, S. Miniature Gold Nanorods for Photoacoustic Molecular Imaging in the Second Near-Infrared Optical Window. *Nat. Nanotechnol.* **2019**, *14*, 465–472.

105. Zhang, Y.; Chang, J.; Huang, F.; Yang, L.; Ren, C.; Ma, L.; Zhang, W.; Dong, H.; Liu, J.; Liu, J. Acid-Triggered in Situ Aggregation of Gold Nanoparticles for Multimodal Tumor Imaging and Photothermal Therapy. *ACS Biomater. Sci. Eng.* **2019**, *5*, 1589–1601.

106. Zhou, W.; Hu, K.; Kwee, S.; Tang, L.; Wang, Z.; Xia, J.; Li, X. J. Gold Nanoparticle Aggregation-Induced Quantitative Photothermal Biosensing Using a Thermometer: A Simple and Universal Biosensing Platform. *Anal. Chem.* **2020**, *92*, 2739–2747.

107. Sun, M.; Liu, F.; Zhu, Y.; Wang, W.; Hu, J.; Liu, J.; Dai, Z.; Wang, K.; Wei, Y.; Bai, J.; et al. Salt-Induced Aggregation of Gold Nanoparticles for Photoacoustic Imaging and Photothermal Therapy of Cancer. *Nanoscale* **2016**, *8*, 4452–4457.

108. Steiner, A. M.; Mayer, M.; Seuss, M.; Nikolov, S.; Harris, K. D.; Alexeev, A.; Kuttner, C.; König, T. A. F.; Fery, A. Macroscopic Strain-Induced Transition from Quasi-Infinite Gold Nanoparticle Chains to Defined Plasmonic Oligomers. *ACS Nano* **2017**, *11*, 8871–8880.

109. Choe, A.; Yeom, J.; Shanker, R.; Kim, M. P.; Kang, S.; Ko, H. Stretchable and Wearable Colorimetric Patches Based on Thermoresponsive Plasmonic Microgels Embedded in a Hydrogel Film. *NPG Asia Mater.* **2018**, *10*, 912–922.

Chapter 5: Self-curing super-stretchable polymer/microgel complex coacervate gels without covalent bond formation[3]

5.1 Abstract

As introduced in Chapter 3, poly(EA-MAA-DVB) double crosslinked MGs could be prepared after the glycidyl methacrylate functionalisation. However, the stretchability and multifunctionality are limited due to the interlinked covalent bonding network. Here, a new system of polymer/microgel complex coacervate (PMCC) gels were created by mixing two preformed oppositely charge polyelectrolytes (poly(EA-MAA-DVB) MGs and branched polyethyleneimine). This method provided a shapeable hydrogel, which could be simply transformed into a highly elastic network after annealing. The whole gelation process did not require in situ free-radical polymerisation and covalent bond formation. After thermal reconfiguration, the dynamic and ionic structure provided super-stretchable, self-healing, highly adhesive, super-swellable performance to the PMCC gel. The gels could be further stiffened with a high concentration of Ca^{2+}. In comparison to other complex coacervate gels, the new PMCC system showed stronger modulus, higher breaking strain and greater functionality with potential for biomedical applications.

---

[3] The results are published in Wu, S.; Zhu, M et al. Self-Curing Super-Stretchable Polymer/Microgel Complex Coacervate Gels without Covalent Bond Formation. *Chem. Sci.* **2019**, *10*, 8832–8839

5.2 Introduction

Hydrogels are favourable water-rich polymer networks, which possesses numerous crosslinks (physical or chemical) to keep the water inside a 3D network structure.[1,2] The mechanical properties of hydrogels can be intentionally tuned by varying the spatial arrangement and crosslinking mechanism[3–5] to fit the requirements of a particular application (e.g. Soft tissue engineering[6,7]). Different designs expand the applicable areas of such materials in drug delivery,[8] water purification,[9] electronic skin,[10,11] wound healing,[12,13] soft robotics,[14,15] CO_2 capture[16,17] and injectability.[18,19]

Hydrogels have potential for biomedical applications based on their stimuli-responsive properties (pH, temperature, solutes or light).[20,21] A macroscopic property of gel networks can be simply controlled by stimuli-triggered crosslinking,[22,23] swelling or degradation of polymer colloids.[24,25] As reported in the previous studies in Saunders's group, a range of pH-responsive microgels (MGs) or nanogels (NGs) particles were prepared using free radical emulsion polymerisation.[25–28] These particles swelled within a physiological pH range. After swelling, the MGs/NGs could form a physical gel and further build up a doubly crosslinked (DX) network based on the glycidyl methacrylate functionalisation.[29,30] These injectable and crosslinked gels have the potential for regeneration in intervertebral disc (IVD) repair. However, the lack of ductility and amine functionalities limit the potential research.

Recent studies reported some outstanding stretchable and tough hydrogels, such as nanocomposite hydrogels,[26,31,32] supramolecular hydrogels,[33–35] double network hydrogels[36,37] and microgel-reinforced hydrogels.[38,39] Such hydrogels required covalent bond formation, accompanying host-guest interactions, hydrogen bonding, electrostatic interactions or physical entanglement. However, the complicated gelation procedures or in situ free-radical polymerisation also reduce their potential for use in industrial/biomedical areas. In this case, physical or dynamic crosslinked gels are preferable candidates, which might exhibit self-healing based on their dynamic network.[40,41]

Polyelectrolyte (PE) complex gels are prepared through the physical crosslinking of oppositely charged PEs.[42–45] Complex coacervation of oppositely charged PEs can drive phase separation, which spontaneously generates solvent-rich and solvent-depleted phases.[46,47] This phase separation process has been widely used for the microencapsulation in the food and pharmaceutical industries due to low-cost, high-scalability and simplicity in preparation.[48,49] The typical hydrogel-like coacervated based materials can be designed using two oppositely charged triblock copolymers, and these materials have potential for bolus-style delivery.[45,50] Here, we introduce a new binary polyelectrolyte combination of an anionic polyacid MG and a cationic branched polyethyleneimine (PEI). PEI has been used in gene transfer[51] and hydrogel network construction.[41]

As shown in Scheme 5.1, dynamic polymer/MG complex coacervate (PMCC) gels were prepared by mixing and kneading MG particles with branched PEI, denoted as the pre-gels. Swellable and pH-responsive MG particles were prepared by copolymerising ethyl acrylate, methacrylic acid, and divinylbenzene using emulsion polymerisation (poly(EA-MAA-DVB) MGs).[26] The pre-gels were highly dynamic and shapeable, and could transform to a highly elastic temperature-cured gel (T-gel) after annealing ≥ 37 °C. The structure rearrangement allows the formation of high-density ionic bonds, which further affects the mechanical properties of the T-gels. This new class of PMCC gels possesses shapeability, super-stretchability, self-healing, high adhesiveness, high swellability and Ca^{2+} stiffened properties. They have strong advantages over other common complex coacervate gels, which suffer from poor mechanical performance and a lack of moldability (e.g. shapeable to elastic).[45,46,52–54]

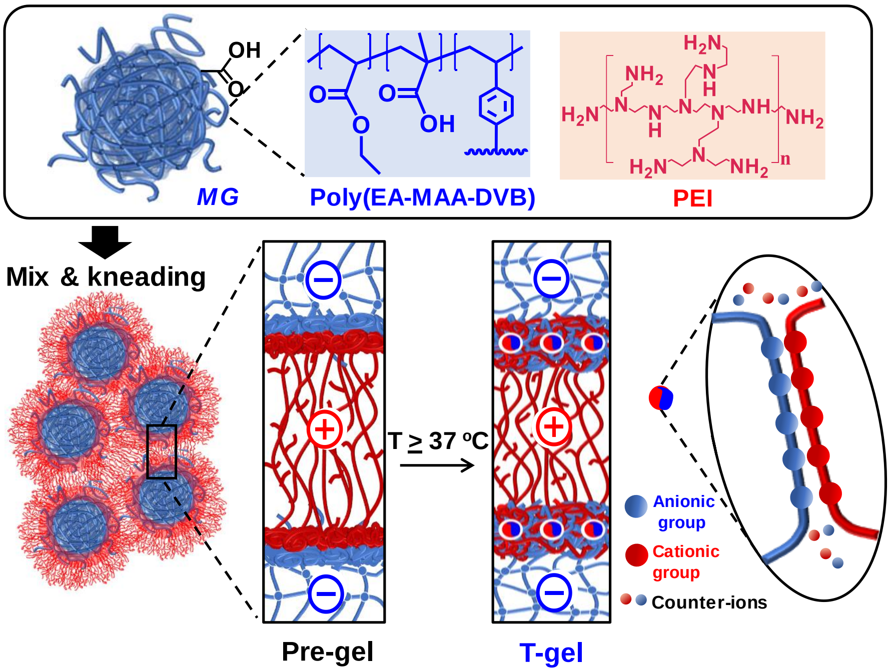

Scheme 5.1 Schematic depiction of PEI/MG pre-gel and T-gel preparation with cooperative ionic bonding using a simple mix and kneading method.

5.3 Experimental

5.3.1 Materials

Ethyl acrylate (EA, 99%), methacrylic acid (MAA, 99%), divinylbenzene (DVB, 80%), ammonium persulfate (98%), sodium dodecyl sulphate (SDS, 99%), potassium phosphate dibasic (98%), phosphate buffered saline (PBS), $CaCl_2$ (≥ 98.0 %) were purchased from Sigma-Aldrich. Branched PEI with molecular weights of 0.60, 10 and 70 kD were purchased from Polysciences, Inc. All materials were used as received. Ultrahigh purity deionised water was used in all experiments.

5.3.2 MG synthesis

The synthesis of anionic MG particles was performed using the seed-feed emulsion polymerisation. SDS (1.80 g) was added to water (518 mL) in a 1 L five-necked round bottom reactor with a mechanical stirrer (300 rpm) and a reflux condenser (5 °C water circulation). The solution was purged with nitrogen for 30 min and heated to 80 °C in a water bath. The inlet nitrogen was guided by a needle through a rubber stopper. Comonomer solution (31.5 g) containing EA (66.0 wt%), MAA (32.7 wt%) and DVB (1.3 wt%) was prepared and transferred to the reactor. The seed formation was proceeded by addition of K_2HPO_4 (3.15 g of a 7.0 wt% solution) and APS (10 g of a 2 wt% solution). After 30 min, the comonomer (218.5 g) mixture was fed into the reactor using a peristaltic pump at a uniform rate (2.4 g min^{-1}) over a period of 90 min. The copolymerisation proceeded for a further hour. The flask was finally cooled in an ice bath. Large aggregates of the product were removed by filtration using film mesh (0.2 mm pore size). The product was sealed in the cellulose dialysis tubing (14 kDa) and soaked in water for 14 days. Dialysis water was changed once per day. The final MG was concentrated to 17.2 wt% by rotary evaporation (20 mbar) at room temperature and stored at 5 °C before use.

5.3.3 PEI/MG gel preparation

The following gives an example of preparation of PEI/MG(50-0.67). 0.67 represents the mass ratio (MR) of PEI to MG and the sample code of gels is further explained in Section 5.4.2.2. The MG dispersion (1.20 mL, 17.2 wt%, pH ~ 4 – 5) was transferred to a vial. PEI solution (10 kD) was diluted to 17.2 wt% with water and the desired quantity (0.80 mL) injected into the MG dispersion. The mixture was mechanically stirred and vigorously mixed by hand using a spatula to form a white pre-gel. The solution pH of this pre-gel was 7.3. The pre-gel was further mechanically mixed using a kneading method similar to "dough making" for a further 5 min until it reached a smooth, uniform state. The gel was then sealed by two pieces of glass slide and clips with a hollow mold. These molds consisted of either an O-ring (inner diameter = 19 mm and wall diameter = 2.5 mm) or a PTFE hollow cylinder (inner diameter = 12 mm and height = 12 mm). Parafilm was used to completely encapsulate the molds to ensure that no evaporation occurred during heating. The gel was heated at the required temperature for 20 hr (T-gel). Other gel MRs were prepared by varying the PEI:MG MR (from 0.40 to 1.0) and molecular weight of PEI. The total volume of initial pre-gel was 2.0 mL. In the Ca^{2+} stiffening experiments, PEI/MG(50-0.67) gels were immersed in saturated aqueous $CaCl_2$ solutions for various times.

5.3.4 Swelling and adhesive experiments

During the gel preparation step, six PEI/MG(50-0.67) gels were separately prepared and placed into different pH buffers. Universal pH indicator was added to each buffer solution. The gels were allowed to swell for 2 days. The change of colour and total mass was recorded. The adhesive ability was examined by a flip experiment with a glass slide. The gel at pH 7.4 was selected for adhesive tests to various materials: rubber, plastic, steel, Teflon, glass and fresh porcine skin.

5.3.5 Self-healing experiments

The disc-like samples were separated into two parts by cutting down the middle. The gels were then re-joined together with some drops of water along the cutting line. They were sealed again and placed for 24 hr at room temperature to allow healing process. The self-healed ability was quantified by uniaxial tensile measurements.

5.3.6 Physical measurements

The z-average diameter (d_z) and zeta potential (ζ) data for the MGs were measured at 25 °C using a Malvern Zetasizer Nano ZS instrument. The swelling experiments were held for 10 min at different pH values before taking measurements. The d_z values were calculated using the Stokes-Einstein equation. The carboxylic acid content and pK_a for the MGs were determined via potentiometric titration using a Mettler Toledo DL15 titrator. TEM samples were prepared by drop-casting MG dispersions (10 μL, 0.001 wt.%) onto copper grids (300 mesh) coated with holey carbon film. MGs were stained with uranyl acetate at room temperature overnight. TEM studies were performed using an FEI Tecnai 12 BioTwin instrument operating at 100 kV. SEM samples were freeze-dried and coated with Au/Pd prior to imaging to prevent sample-charging. All SEM studies were conducted using a FEI Quanta 650 FEG-SEM instrument operating at 20 kV. FTIR spectra were collected using a Nicolet 5700 ATR-FTIR spectrometer (128 scans, 2 cm^{-1} resolution). Mechanical properties were assessed using an Instron series 5569 instrument. Rectangular and cylinder shapes were prepared for tensile and compression tests, respectively. Uniaxial tensile measurements were conducted at a strain rate of 0.055 s^{-1}, while uniaxial compression studies utilised a strain rate of 0.015 s^{-1}. Compression experiments were ceased at ~ 84% strain to avoid damage to the instrument. Gels had still not broken under such conditions. The cyclic tensile test was performed on both tensile and compression measurements. Each sample was allowed to rest for 5 min between each successive cycle unless otherwise stated. The elastic modulus was obtained from the linear part of the stress-strain graph in the low strain region. Engineering stress and strain are reported in this study. The adhesive strength was characterised by lap shear testing. Glass and Teflon substrates (75 mm × 25 mm × 1 mm) were cleaned using sonication in water and ethanol. Excess fat from porcine skins (75 mm × 25 mm × 1 mm) was removed using a scalpel and the skin cleaned with water and soap and rinsed well with water. All samples were cut into the size of 15 mm × 15 mm before attachment. The gel was evenly placed on one surface, then two surfaces were joined together by overlapping the gel for 10 s. The adhesive strength was obtained from the failure point of the gel under uniaxial loading.

5.3.7 Live/Dead and MTT assays.

The experimental details and results of cell culture were provided by Daman Adlam (The University of Manchester). T/C28a2, human chondrocyte cells, were cultured in Dulbecco’s modified Eagle’s medium (DMEM) supplemented with 10% fetal bovine serum and antibiotic/antimycotic (Sigma-Aldrich, UK) at 37 °C in a humidified 5% CO_2 atmosphere. Cells were seeded at a density of 5 x 10^5 onto 35 mm glass bottom dishes (VWR International) containing 5 mm discs of gel (40 mg) and cultured up to 72 hr with daily media changes. Viability of cells adjacent to the gels was determined at 24, 48 and 72 hr time-points versus gel-free controls by live/dead assay (Life Technologies, UK). Images were obtained with an Olympus BX51 fluorescence microscope and a

Lietz Diavert inverted phase contrast light microscope. For a quantitative assay, the T/C28a2 cells were seeded at a density of 5 x 10^4 per well onto 24 well plates containing 0.4 µm cell-culture inserts (BD Biosciences) and allowed to adhere overnight before exposure to 15 mg of gel via the insert (n = 3). Cell viability was determined by the MTT assay (Sigma-Aldrich) using a FLUOstar OMEGA plate reader.

5.4 Results and discussion

5.4.1 Poly(EA-MAA-DVB) MG characterisation

The pH-responsive poly(EA-MAA-DVB) MGs were synthesised using the free-radical emulsion polymerisation. These MG particles were used to prepare more ductile covalently-interlinked MGs, and they had a high particle swelling ratio and appeared transparent that were considered advantages.[26] The poly(EA-MAA-DVB) MGs had a number-average diameter of 55 nm in a dried state (< pH 6) as determined from TEM studies (Fig. 5.1(A)). In Fig. 5.1(B), the potentiometric titration data provided the acid group content ~ 35.8 wt%, which originated from MAA (containing -COOH). The titration also gave a pK_a of 6.5 in poly(EA-MAA-DVB) MG dispersions. From the DLS measurements, the MG particles swelled from 74 nm at pH 4.7 to 502 nm at pH 11 (Fig. 5.1(C)). A steep increase of d_z was found around pH 6.5, which agreed with the pKa. Such a pH change maybe suitable in physiological environments. This strong swelling feature also endowed the higher deformability to the crosslinked hydrogel compared to other reported low swellable MGs.[26]

The pH-dependent change of the zeta potential coincided well with the swelling trend, and indicated a negatively charged surface (from -28 mV to -44 mV) of MG particles (Fig. 5.1(D)). Here, strong electrostatic stabilisation maintained the good colloidal stability of these particles in water. In addition, these highly charged groups were favourable to drive formation of the complex coacervated phase in the study.

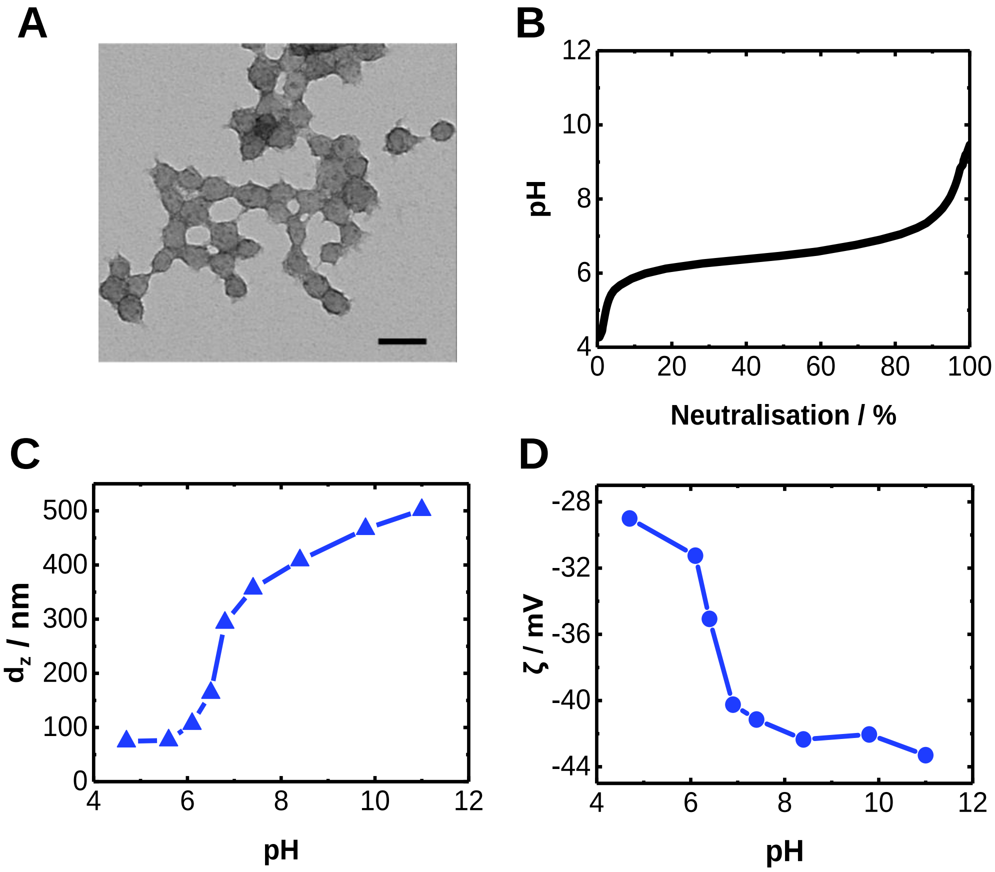

Figure 5.1 (A) The TEM image of poly(EA-MAA-DVB) MGs. Scale bar = 100 nm. (B) Potentiometric titration data of poly(EA-MAA-DVB) MGs. (C) Variation of the z-average diameter and (D) zeta potential as a function of pH.

5.4.2 Formation of PEI/MG complex coacervate

5.4.2.1 Dilute PEI/MG dispersions

Highly-branched PEI is a polycationic polymer with a pK_a of 8.5.[55] As shown in Scheme 5.1, branched PEI (10 kD) contains many primary, secondary and tertiary amine groups, which act as the positively charged groups interacting with anionic MG particles. The diluted PEI/MG dispersion was prepared for different MRs by mixing a low concentration (< 1 wt%) of MGs with PEI. Fig. 5.2(A) does not show any evidence of excessive aggregation. However, a small number of white beads could be observed upon decreasing the MR and became dominant at MR = 0.4. This difference provided a strong indication of MG aggregation at low MR due to the presence of PEI chains. The samples showed a large increase of d_z (> 600 nm) with high polydispersity in a MR range between 0.57 and 0.4 (Fig. 5.2(B)). The DLS measurement also exhibited a slight increase of d_z at high MR. The mixture had an average d_z ~ 250 nm, when MR was tuned between 0.67 and 1 (pH ~ 7.3 - 7.9). Although adsorbed PEI chains might contribute to the size measurement of MGs, the d_z of the mixture was still much smaller than the expected swollen particles according to Fig. 5.1(C) (> 350 nm above pH 7.3). The addition of PEI constrained the spatial expansion of the MGs at high pH. The electrostatic attraction screened the repulsive force of MG particles (among $-COO^-$ groups). This feature indicated a strong interaction between the anionic MGs and cationic PEI after mixing, which could involve the PEI wrapping and interpenetration.

In Fig. 5.2(C), the zeta potential of the dilute PEI/MG dispersion showed a gradual change from +25.9 mV to -1.9 mV with the decrease of MR. Most of the mixtures were positively charged particles and became negatively charged or neutral at MR ~ 0.4. The trend implied that the PEI/MG dispersion became less stable due to the reduction of electrostatic repulsive forces.

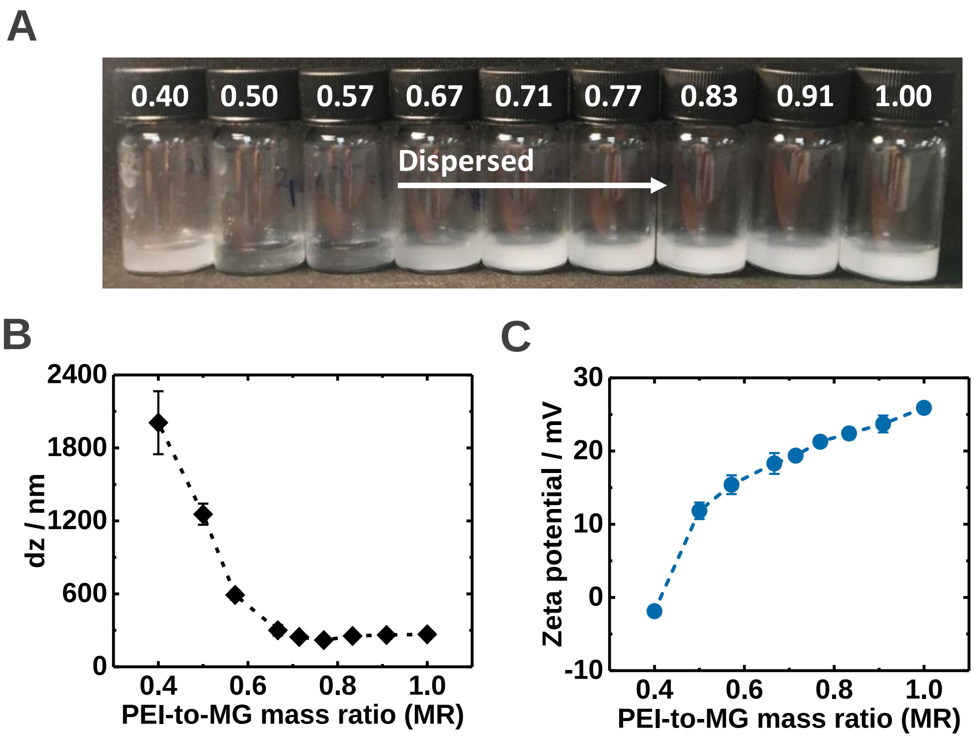

Figure 5.2 (A) The pictures showed the dispersity of dilute PEI/MG, and mass ratios (MRs) are labelled. (B) DLS size measurements and (C) Zeta potentials for dilute PEI/MG mixed dispersions recorded for various MRs.

5.4.2.2 Formation of pre-gels and T-gels

As shown in Fig. 5.3(A), a milky and viscous MG dispersion (17.2 wt%) was prepared to make the complex coacervated gel with branched PEI using the mixing and kneading method. The zeta potential measurement confirmed that these MG particles had a highly negatively charged surface in Fig. 5.1(D). Simply hand-mixing MGs and PEI gave a ‘putty like’ soft gel (pre-gel) within several seconds to minutes. As prepared pre-gels maintained an integral network and deformed plastically with a strong adhesiveness (Fig. 5.3(B)). They could be molded into various shapes and were injectable using a syringe. Such plastic flow gels could adapt to any defects or damage on substrates, which exhibited the capability of gluing, sealing and coating. In addition, this pre-gel can be formed under physiologically relevant conditions (e.g. pH 7.4 and 37 °C).

Remarkably, temperature curing (at 37, 50 or 80 °C for 20 h) transformed the deformable pre-gels into highly elastic T-gels (Fig. 5.3(B) and Fig. 5.3(C)). This property of T-gels was tuneable and they were transparent and stretchable after annealing. Hence, the PMCC pre-gels could be shaped and then set in any desired shape simply by heating. In the following study, a series of polymer/MG complex coacervate (PMCC) gels are prepared by varying the dry weight PEI/MG MR. Each gel is denoted by PEI/MG(T-MR), where T is the annealing temperature (°C) and MR corresponds to the PEI-to-MG mass ratio.

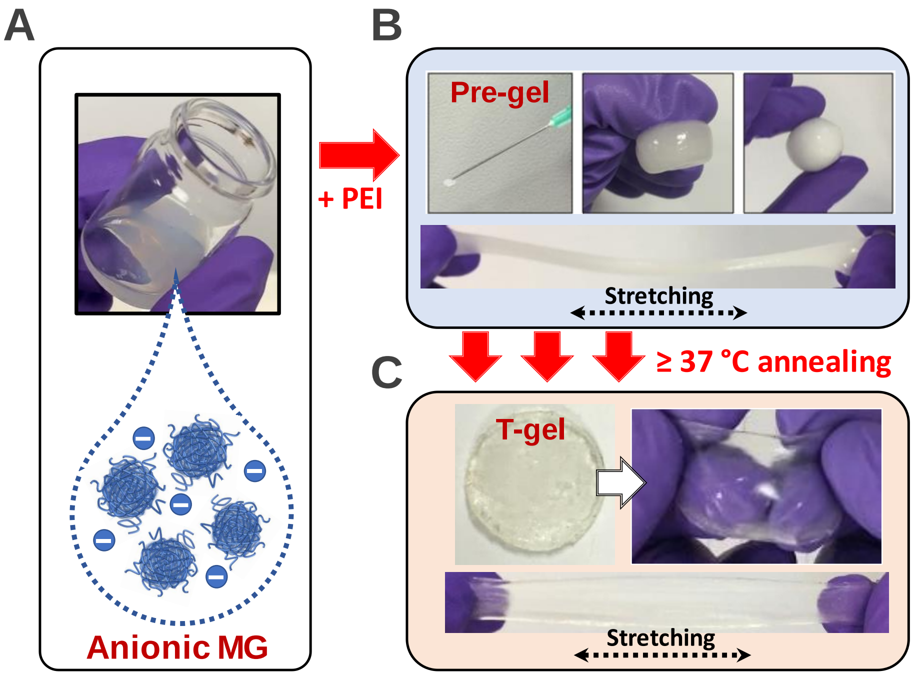

Figure 5.3 (A) The aqueous dispersion of negatively charged MG particles (17.2 wt%). (B) Plastic flow, adhesiveness and injectability of shapeable PEI/MG(0.67) pre-gels. (C) Stretchable behaviours of a PEI/MG(50-0.67) T-gel of 19 mm diameter.

For PEI/MG gels, the formation of a gel phase does not require chemical reaction in the pre-gel and T-gel preparation. This feature is highly desirable for applications in a sensitive environment (e.g. tissue).[7] Most MG studies involve the free radical polymerisation to construct an elastic and robust gel network. In doubly crosslinked (DX) MGs, ammonium persulfate (APS) and tetramethylethylenediamine (TEMED) were used to initiate the crosslinking of vinyl-functionalised MGs.[26,27,30] Similar radical reactions were also applied to construct matrix phases (e.g. polyacrylamide) in MG enhanced or reinforced gel networks.[56–59] In contrast, in situ physical gelation is a more bio-friendly process, which may also provide shapeability, injectability, self-adapting and self-healing properties. For example, pH-responsive swollen MGs (e.g. poly(EA-MAA-EGDMA)) could form an injectable shear-thinning phase at physiological pH.[26] High injectability and self-healing were also found in a zwitterionic microgels system, which could create a malleable cell construct.[60] Similar physical and dynamic covalent platforms are widely used for designing cell-laden constructs, wound healing materials and drug carriers.[12,53,60–63] However, their networks are usually weak and cannot provide satisfactory mechanical performance for load-bearing materials (e.g. a lack of a highly elastic phase). Some studies show elastic physical gels can be constructed by increasing attractive interactions in a salt environment.[64,65] In this thesis, the preparation of PEI/MG gels offers an alternative approach, which exhibits a simple transition from a shapeable phase to an elastic phase upon mixing and annealing.

5.4.3 FTIR spectra of pre-gels and T-gels

In comparison to FTIR spectra of MGs and PEI, pre-gels exhibited new bands at 1552 and 1637 cm^{-1} (Fig. 5.4(A)) which were assigned to -COO$^-$ (asymmetric stretch) and –NH$_3^+$, respectively.[66] These bands indicated the formation of ionic crosslinks between the MG particles and PEI chains within the T-gels. Hydrogen bonding interactions were also indicated by the red shift in the PEI N-H stretch[67,68] from 3450 to 3400 cm^{-1} with a broader band (Fig. 5.4(B)). The shift of corresponding bands remained unchanged for T-gel (37, 50 or 80 ^{o}C) (Fig. 5.4(C)-(D)), and was exactly as same as the pre-gel, which proved the bonding mechanism was independent of the annealing process. There was no evidence for the formation of new covalent amide bonds. Therefore, the PMCC gels were formed as a result of extensive ionic and hydrogen bonding here.

However, different mechanical properties were observed between T-gels and pre-gels (Fig. 5.3). A model has been suggested here, where the MGs acted as nanosized crosslinkers and PEI as flexible bridges between adjacent MGs during the mixing process. A related morphology has been reported for covalent nanostructured hydrogels.[69] The PEI chains initially adsorbed in a flat conformation and then further interpenetrated into the MG peripheries upon annealing (Scheme 5.1).[70] Such interpenetration increased the number of ion pairs which was driven by the entropy increase due to mobile ion release.[70] Hence, a more elastic structure was constructed after annealing.

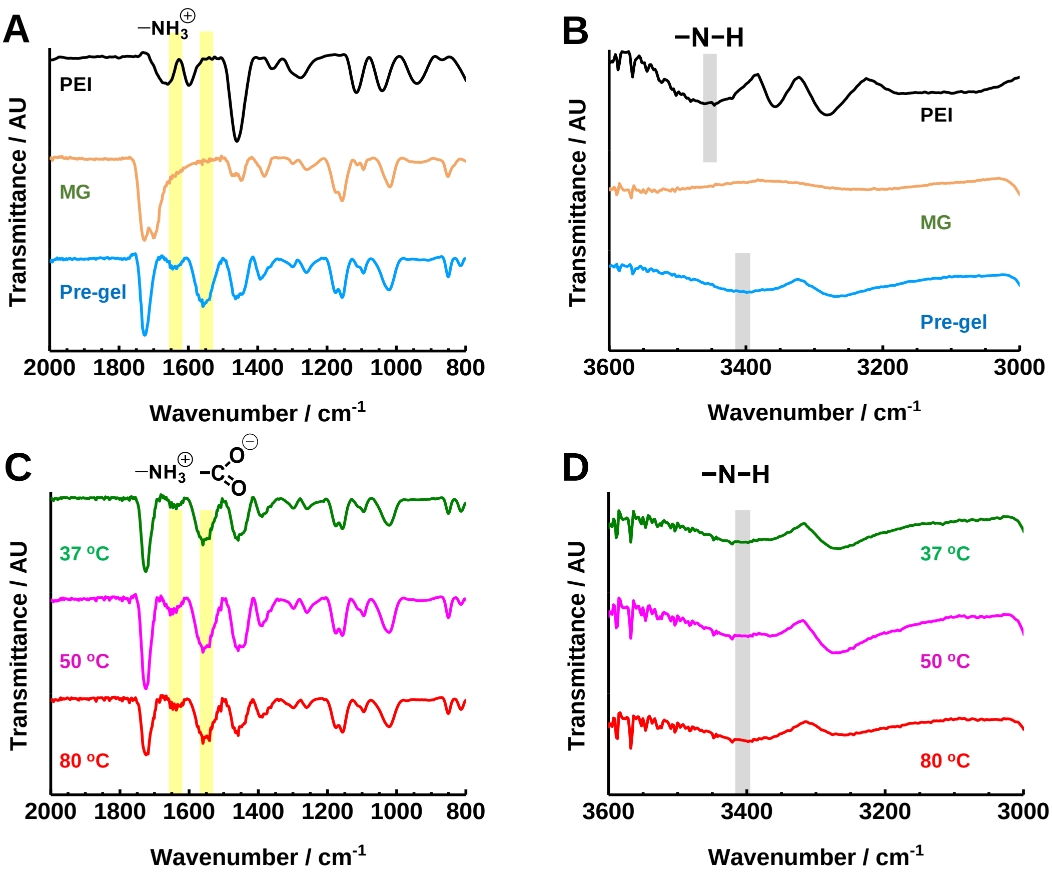

Figure 5.4 FTIR spectra for (A and B) PEI, MG and pre-gels (PEI/MG(0.67)) as well as (C and D) T-gels (PEI/MG(T-0.67)) heated at various temperatures. The spectra for the pre-gel and T-gel showed new bands due to ionic groups (indicated by yellow bars) and a shift of the N-H group (indicated by grey bars). The pH of the gels was 7.3.

5.4.4 Morphologies of pre-gels and T-gels

All the pre-gels and T-gels were freeze-dried and inspected in SEM (Fig 5.5 (A)-(D)). The microstructure uncovered the differences of the polymer network among these gels, which were highly porous as a result of ice sublimation. The number-average pore size distributions are shown in the bar chart (Fig 5.5 (E)-(H)). The pre-gel showed a coarse microstructure with the largest pore size (5.06 μm). After annealing the pre-gel at 37 °C, the pore size largely shrank down to 0.34 μm for PEI/MG(37-0.67) T-gel. The pore size can be further reduced to ~ 0.01 μm by annealing at 80 °C. The reduction of pore size indicated strengthening of the polymer network within the gel,[71] and the feature was easily tuneable using different annealing temperatures.

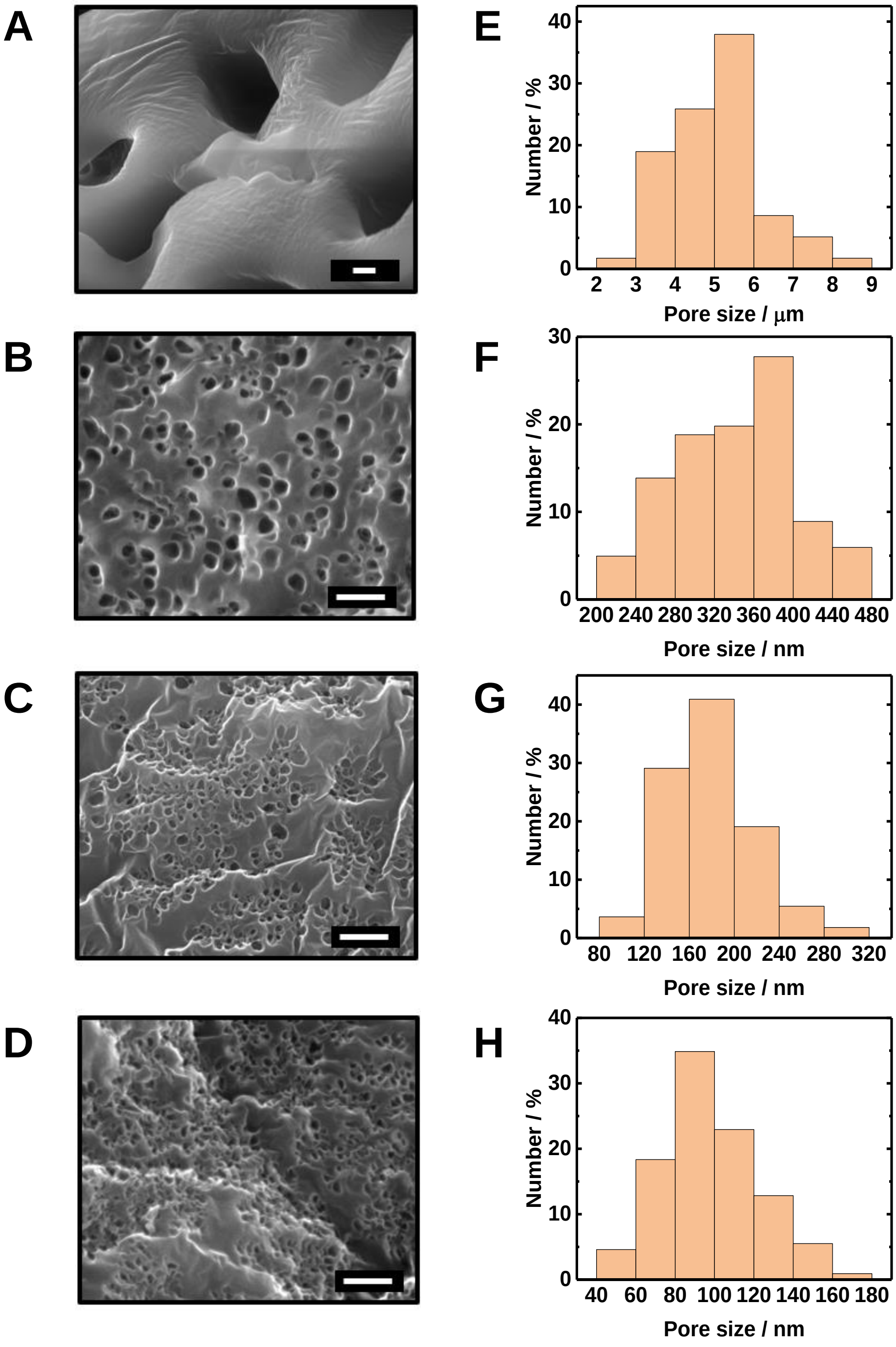

Figure 5.5 SEM images for freeze-dried (A) PEI/MG(0.67) pre-gel, (B) PEI/MG(37-0.67), (C) PEI/MG(50-0.67) and (D) PEI/MG(80-0.67) T-gels. Scale bars = 1 μm. Pore size distributions for (E) PEI/MG(0.67) pre-gel, (F) PEI/MG(37-0.67), (G) PEI/MG(50-0.67) and (H) PEI/MG(80-0.67) T-gels. The average pore sizes were 5.06 ± 1.11 μm, 0.34 ± 0.06 μm, 0.178 ± 0.037 μm and 0.098 ± 0.025 μm, respectively.

5.4.5 Uniaxial tensile tests for T-gels: effects of MR and annealing temperature

A small piece of PEI/MG(50-0.67) T-gel was uniaxially stretched and found to be super-stretchable as shown in Fig. 5.6(A). In Section 5.4.2.1, the tunable dispersity and zeta potential were found by changing the MR of the dilute dispersion. Here, the relationship between the tensile stress-strain properties and MR (Fig. 5.6(B)) was further investigated by studying a series of PEI/MG(50-MR) (MR = 0.40, 0.50, 0.67, 0.8, 1) (Table 5.1). The maximum breaking strain of 1015% was reached for PEI/MG(50-0.67). The highest Young's modulus (39.0 kPa) and tensile strength (64.0 kPa) were obtained for PEI/MG(50-0.40), which had the lowest MR. When the MR increased, MG particles were diluted by PEI and the average separation between MGs increased. Therefore, the PEI bridging length increased, and the proportion of crosslinking centers reduced which lowered the modulus (Fig. 5.6(C)). In other words, MGs make a major contribution to the elastic modulus and strength of PEI/MG T-gels. However, Fig. 5.6(C) showed the breaking strain of PEI/MG(50-MR) passed through a maximum at MR 0.67. In the early stages, the MR increase caused the length of the bridging chains increased. At higher MR values, fewer PEI chains were able to uniformly bridge neighboring MGs which potentially lowered the stretchability.

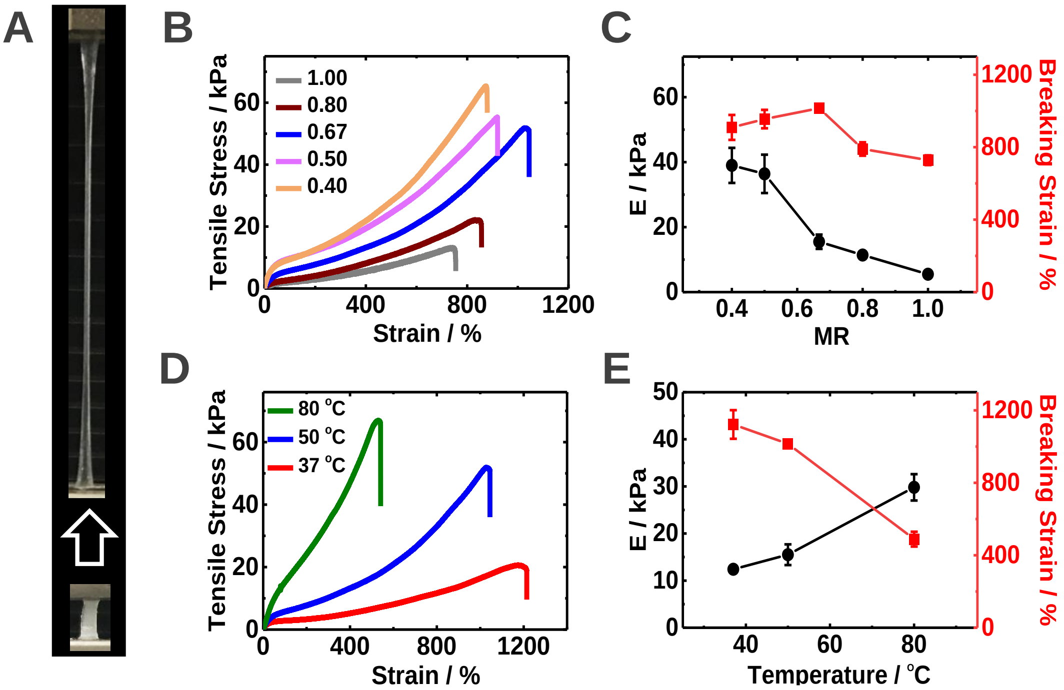

Figure 5.6 (A) A stretched PEI/MG(50-0.67) gel. (B) Uniaxial tensile stress-strain curve and (C) mechanical properties for PEI/MG(50-MR) gels prepared at 50 °C using various mass ratios (MR = 0.40, 0.50, 0.67, 0.80, 1.00). (D) Tensile stress-strain curve and (E) mechanical properties for PEI/MG(T-0.67) gels annealed at various temperatures (T = 37 °C, 50 °C, 80 °C).

Table 5.1 Mechanical properties with different mass ratios for PEI/MG(50-MR) gels.

MR[a]	E / kPa[b]	Tensile strength / kPa	Strain at break / %	Toughness / MJ/m^3
0.40	39.0 ± 5.4	64.0 ± 10.3	909 ± 69	0.267 ± 0.040
0.50	36.4 ± 5.9	59.6 ± 2.8	955 ± 51	0.262 ± 0.025
0.67	15.5 ± 2.2	45.4 ± 7.0	1015 ± 18	0.194 ± 0.029
0.80	11.4 ± 1.0	20.3 ± 1.8	790 ± 37	0.072 ± 0.007
1.00	5.5 ± 0.9	12.3 ± 1.2	728 ± 27	0.041 ± 0.004

[a] PEI-to-MG mass ratio; [b] Young's modulus

The effect of annealing temperature was subsequently investigated at 37 °C, 50 °C and 80 °C (Table 5.2). Tensile measurements (Fig. 5.6(D)) showed that the PEI/MG(37-

0.67) gel exhibited the highest breaking strain of all the gels (1122%) while the PEI/MG(80-0.67) gel possessed the strongest modulus (29.8 kPa) and strength (62.5 kPa) with a relatively high breaking strain (489%). PEI/MG(50-0.67) had the most balanced tensile property and the highest toughness (0.194 MJ m^{-3}) using the area under the stress-strain curve. During the annealing, thermal energy could accelerate/drive the reconfiguration and increase the number-density of elastically effective ionic crosslinks (Scheme 5.1), which could enhance the gel modulus according to rubber elasticity theory.[72] Therefore, the elevated annealing temperature reasonably led to a higher modulus and a lower breaking strain in the T-gel (Fig. 5.6(E)). PEI/MG(50-0.67) T-gel had the best overall mechanical properties and was selected for the following study unless otherwise were stated.

Table 5.2 Mechanical properties of PEI/MG(T-0.67) gels prepared at different temperatures.

Gel	E / kPa[a)]	Tensile strength / kPa	Strain at break / %	Toughness / MJ/m^3
PEI/MG(80-0.67)	29.8 ± 2.8	62.5 ± 5.2	489 ± 41	0.152 ± 0.022
PEI/MG(50-0.67)	15.5 ± 2.2	45.4 ± 7.0	1015 ± 18	0.194 ± 0.029
PEI/MG(37-0.67)	12.4 ± 0.2	19.8 ± 1.2	1122 ± 79	0.104 ± 0.004

[a)] Young's modulus.

5.4.6 Uniaxial tensile tests for PEI/MG(50-0.67) T-gels: effects of PEI molecular weight

The effect of PEI molecular weight on PEI/MG(50-0.67) mechanical properties was investigated via uniaxial tensile tests (Fig. 5.7(A)). Low molecular weight PEI (0.60 kD) could not form a gel network even after annealing at 50 °C (Fig. 5.7(B)). The PEI/MG mixture was a viscous liquid. This observation suggests that 0.60 kD PEI cannot provide effective interpenetration and bridging of the MG particles due to spatial limitations. In contrast, 70 kD PEI was able to form a robust disc-like T gel as shown in Fig. 5.7(B). The tensile stress-strain curve showed the elastic modulus was 14.8 kPa. They had a similar modulus compared to the 10 kD PEI/MG(50-0.67) gel (Table 5.1). As observed in Section 5.4.5, the MGs acts as the major phase to control the modulus with these high molecular weights PEI. However, the stretchability of 70 kD PEI/MG(50-0.67) gel was largely reduced (Fig. 5.7(A)). The macroscopic structure of 70 kD gel was not homogenous due to the high viscosity of its pre-gel. This difference was possibly responsible for the decrease in breaking strain. 10 kD PEI was used for the following study.

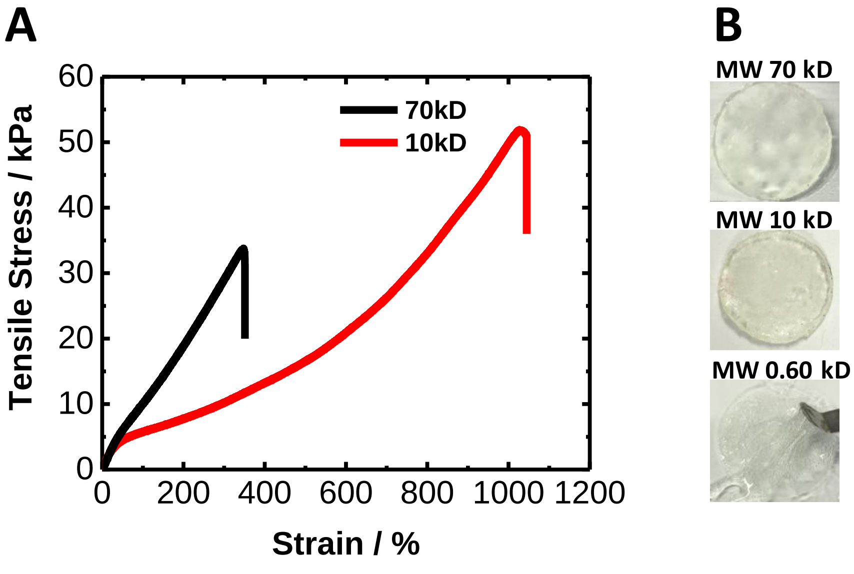

Figure 5.7 (A) Uniaxial tensile stress-strain measurements for PEI/MG(50-0.67) gels with different PEI molecular weights (10 kD and 70 kD) (B) Pictures showed the appearance of PEI/MG(50-0.67) gels. The mixture of branched PEI (0.60 kD) and MGs remained viscous without forming a gel network.

5.4.7 Cyclic uniaxial tensile tests for PEI/MG(50-0.67) T-gels

The dynamic tensile stress-strain data for the PEI/MG(50-0.67) gel was collected and explored at a low strain region (< 400%) as shown in Fig. 5.8(A). A hysteresis loop indicated there was significant energy dissipation during the loading-unloading process, which showed a difference compared to the rigid covalent-bonding network.[73,74] The residual strain and dissipated energy increased linearly with the applied maximum strain (Fig. 5.8(B)-(C)). The presence of plastic deformation proved the change of dynamic networks. However, this deformation should not be permanent due to the lack of covalent bonds and structure disassembly (low strain). As depicted in Scheme 5.1, the network of PEI/MG gel is proposed to be constructed by numerous ionic and hydrogen bonds. In principle, damage will be recovered with long enough resting time.

Multiple cyclic tests (8 times) of PEI/MG(50-0.67) gel were conducted at 200% strain with a 5 min relaxation interval in Fig. 5.8(D). There was a superposition for hysteresis loops after the multiple runs. The maximum stress and dissipated energy rapidly became constant (Fig. 5.8(E)-(F)), with less than 5% difference between each cycle. The lack of change in dissipated energy with cycling implied that chains did not slide past each other. Instead, the sacrificial bonds were gradually reformed in the absence of stress. The dynamic nature of these ionic (and hydrogen) bonds is a likely cause of the excellent stretchability of the T-gels.

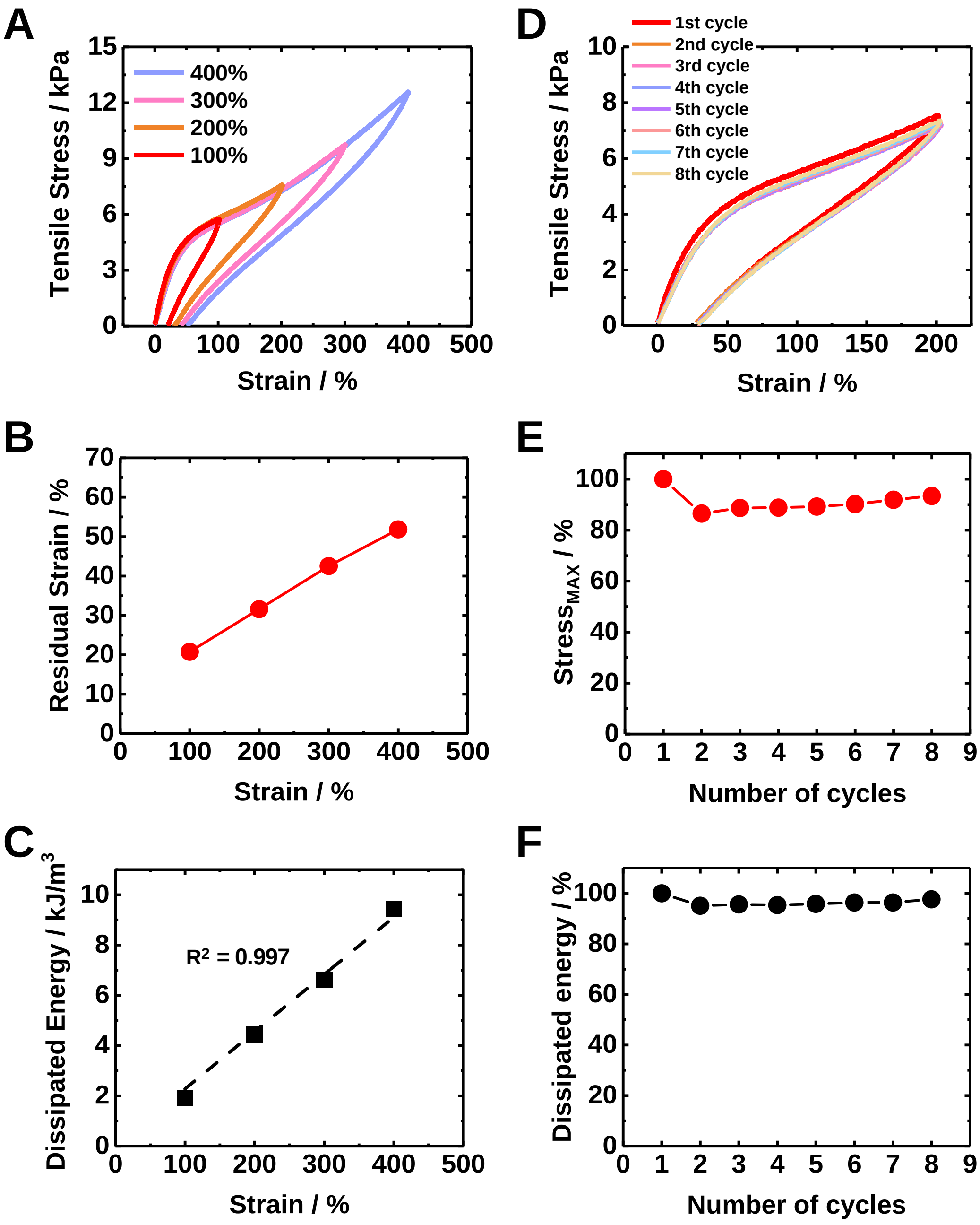

Figure 5.8 (A) The cyclic loading of PEI/MG(50-0.67) gels was tested at four different strains (100%, 200%, 300% and 400%). (B) The residual strain and (C) dissipated energy are acquired from the hysteresis loop and plotted against the applied strain. (D) Multiple cyclic loading of a PEI/MG(50-0.67) gel conducted for eight runs. (E) The percentage change of maximum stress at 200% and (F) dissipated energy were recorded for every loading-unloading cycle.

5.4.8 Uniaxial compression tests for PEI/MG(50-0.67) T-gels

In order to gain insight into the mechanical properties of this complex coacervate gel, uniaxial compression tests are carried out to explore the gel performance. The results are shown in Fig 5.9. Doubly crosslinked (DX) MGs have been reported as potential candidates for the restoration of the mechanical property during degenerated intervertebral disc repair.[29,30] A previous poly(EA-MAA-DVB) DX MGs was prepared using the same MG composition compared to this study. This DX MGs gel had a breaking strain ~ 76%.[26] In comparison, PEI/MG(50-0.67) gel exhibited excellent compressive properties with no defects or failure occurring at 84% (Fig. 5.9(A)). This strain was limited by the instrument, and did not reach the breaking strain of the samples. The gel could be repeatedly compressed (5 min relaxation interval, 84% strain) without showing any observable changes in the stress-strain curve. The Young's modulus was calculated as 11.5 kPa from the linear part at low strain. This value is comparable to that of muscles.[75] However, the modulus was smaller than with poly(EA-MAA-DVB) DX MGs (~ 20 kPa) due to the lack of chemical crosslinks. In Fig. 5.9(B)-(C) cyclic compressive data (30 %, 40 %, 50 %, 60 %, 70%, 80 % strains) showed that the residual strain is proportional to the maximum cycle strain. A large hysteresis loop is observed and increased at higher applied strain. It was caused by the large extent of damage to networks as a result of excessive deformation, however they could recover after resting. These features were consistent with the observations from cyclic tensile measurements.

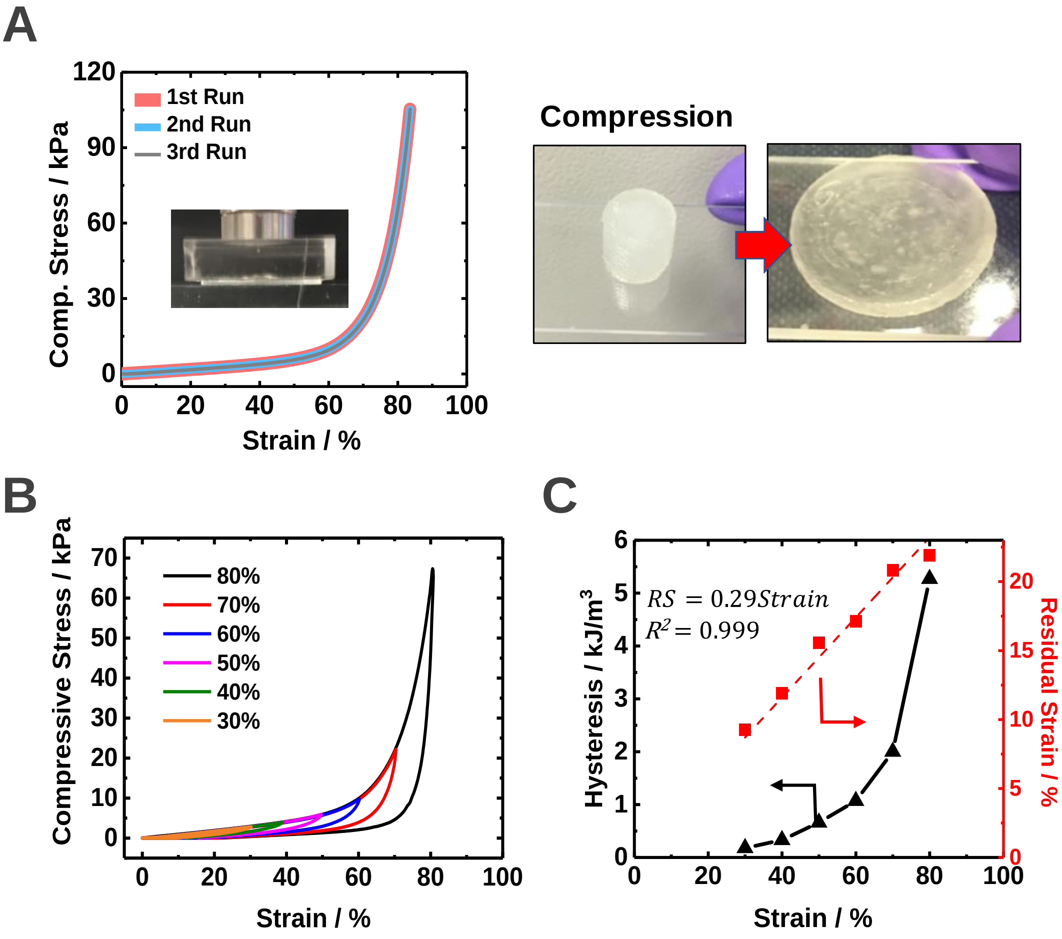

Figure 5.9 (A) Multiple uniaxial compressive stress-strain loading were tested for a PEI/MG(50-0.67) gel. The pictures showed a cylinder gel (12 mm × 12 mm) was compressed into a flat plate without showing damage. (B) The cyclic compression test was conducted at six different strains (30 %, 40 %, 50 %, 60 %, 70% and 80 %). (C) Hysteresis and residual strains from the gels are plotted against the applied strain.

5.4.9 Self-healing experiments for PEI/MG(T-0.67) T-gels

Self-healing is a potentially useful property, which could repair defects and extend the operational lifetimes of hydrogels in practice. Self-healing systems generally rely on the reformation of either physical bonding or dynamic covalent bonding after the failure.[40,41] A highly dynamic of PEI/MG gels was expected to possess such a property. As shown in Fig. 5.10(A), two different dye-stained PEI/MG(50-0.67) gels were prepared and cut into semicircle disks along the black dashed line. The semicircle disks with different colour were rejoined at room temperature. A clear self-healing property was observed after 24 hr. The pictures showed a connective boundary along the self-healed region, which could be easily distinguished by the colour difference. The high stretchability was restored without a sudden interfacial fracture during the stretching. MGs are non-healable cross-linked particles. Therefore, the highly mobile PEI could account for this self-healing.[41,76]

The self-healed property of MG/PEI(T-0.67) gels was further investigated at 37, 50 and 80 °C annealing temperatures. Tensile stress-strain measurements recorded the degree of self-healing from the breaking strain in Fig. 5.10(B)-(D). All the failures occurred at the self-healed interface as expected. In comparison to pristine samples the self-healed stress-strain curve perfectly followed the previous trend. However, the recovery of breaking strain achieved 92%, 64% and 20% for PEI/MG(37-0.67), PEI/MG(50-0.67) and PEI/MG(80-0.67) gels, respectively. Higher annealing temperatures generated more reconfiguration (interpenetration of PEI) and ionic bonds inside the hydrogel network. Therefore, the increase of rigidity limited the self-healing inside PEI/MG(80-0.67) gels.

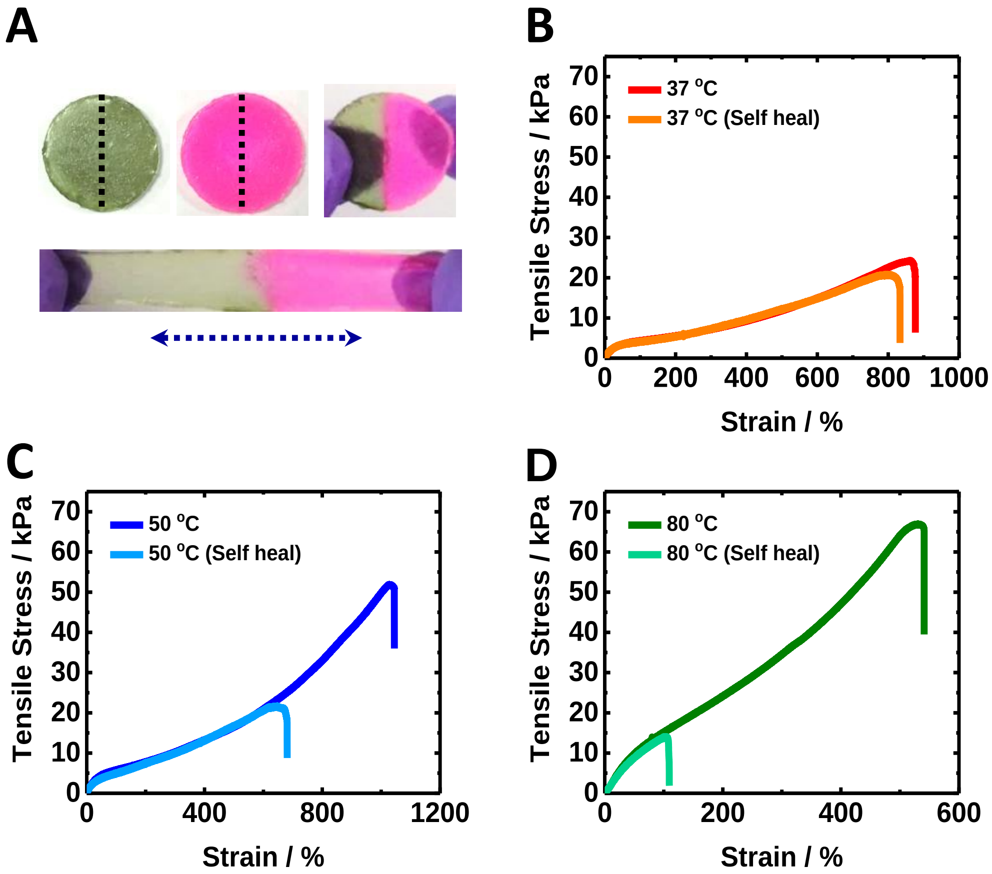

Figure 5.10 (A) Two differently dye-stained PEI/MG(50-0.67) gels were cut along the dashed lines and reciprocally rejoined together. The self-healed gel was stretchable. The uniaxial tensile test showed the extent of self-healing for (B) PEI/MG(37-0.67), (C) PEI/MG(50-0.67) and (D) PEI/MG(80-0.67) after 24 hr. The control gels were stored for a total of 2 days before tensile measurements.

5.4.10 Swelling behaviours of pre-gels and T-gels

The pH-responsiveness of MG particles were studied in Section 5.4.1. After mixing with PEI, the resultant PEI/MG(0.67) pre-gel could show a swelling in pH 11 buffer. The solution gradually penetrated the periphery of a white and soft pre-gel as shown in Fig 5.11(A). The outermost area became relatively transparent and spread after 1 day. Then, the pre-gel gradually expanded to fill all the available space in the vial up to 5 days and did not become fluid-like. The freeform swelling agreed with highly deformable and moldable natures of the pre-gel.

pH swelling of PEI/MG(50-0.67) T-gel is consistent with the observation from the pre-gel, which can swell at high pH, although the network of the T-gel becomes elastic. The swelling of the T-gel was studied across a range of the solution pH values (4.7 – 10.8). These gels could maintain the original shape after swelling due to their elastic nature (Fig. 5.11(B)). The disk-like T-gel expanded to form a giant transparent disk when the pH increased beyond the PEI p*Ka* of ~ 8.5.[55] The swelling degree of T-gel was quantified by the mass ratio (Fig. 5.11(C)), which had a negligible change from pH 4.7 to 8.4 (swelling degree: 102 wt% – 105 wt%). When the solution pH further increased, the swelling degree suddenly increased to 1470 wt% and 2704 wt% at pH 9.8 and 11, respectively. From Fig. 5.2(B), the swelling of the dilute PEI/MG dispersion was suppressed by PEI chains at a low pH condition. This behaviour was consistent with the swelling study of the T-gel discussion here, which could be contributed by the charge screening from electrostatic attraction. The zeta potential (Fig. 5.11(D)) confirmed the presence of strongly negative-charged hybrid particles, only when the pH exceeded 8.4. Therefore, the repulsive force between anionic carboxylate groups probably caused an expansion of MG particles in the T-gels.

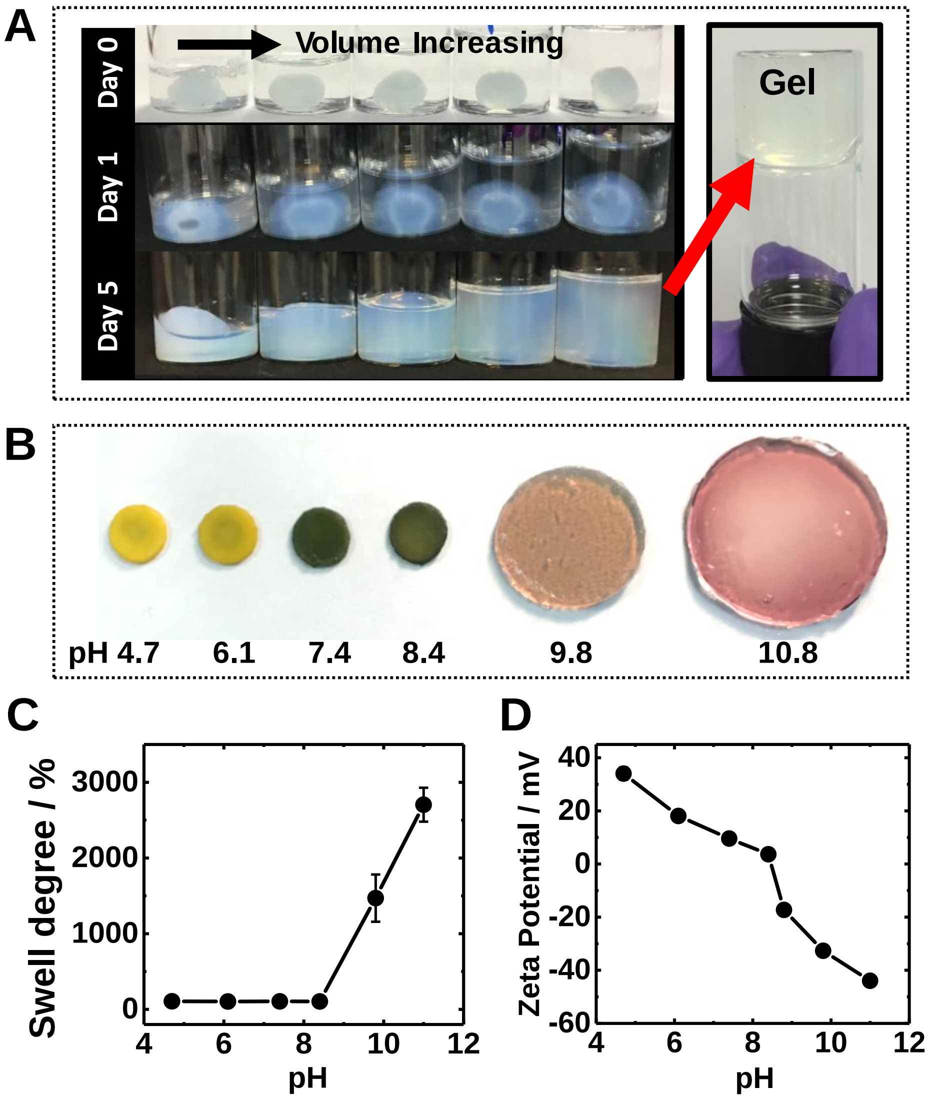

Figure 5.11 (A) Aqueous swelling behaviours of PEI/MG(0.67) pre-gels at pH 11. Such pre-gels swell to fill the available volume. (B) Swelling of PEI/MG(50-0.67) T-gels after immersion in various buffers containing the universal pH-indicator. The pH of the buffers is labelled below the gels. (C) Degree of swelling for the PEI/MG(50-0.67) gels is plotted as a function of solution pH. (D) Zeta potential is plotted against pH for a dilute mixture of PEI/MG(0.67).

The PEI/MG(0.67) pre-gel can be readily dissembled in highly alkaline media (pH ~ 14) as shown in Fig. 5.12(A). The strong base converted a free-standing pre-gel to a weak jelly-like state after 2 hr. The remaining gels was completely dissolved into the solution within 1 day. The breaking of ionic crosslinks at high pH conditions is the major reason for this network disruption. However, all the T-gels remained undegradable under the same conditions in Fig. 5.12(B). The robustness of the T-gel is an unusual observation compared to conventional coacervate gels.[77] The extent of swelling was affected by the annealing temperature of T-gels, which showed descending in the order PEI/MG(37-0.67) > PEI/MG(50-0.67) > PEI/MG(80-0.67). The presence of persistent PEI bridging between MGs could be the reason for their robustness. The annealing process drives or accelerates the interpenetration of PEI chains into the periphery of MG particles. The multiple hydrogen bonding can firmly lock the network, which most likely originated from the primary and secondary amines groups (PEI) interacted with carboxylate and ester groups (MGs).[78]

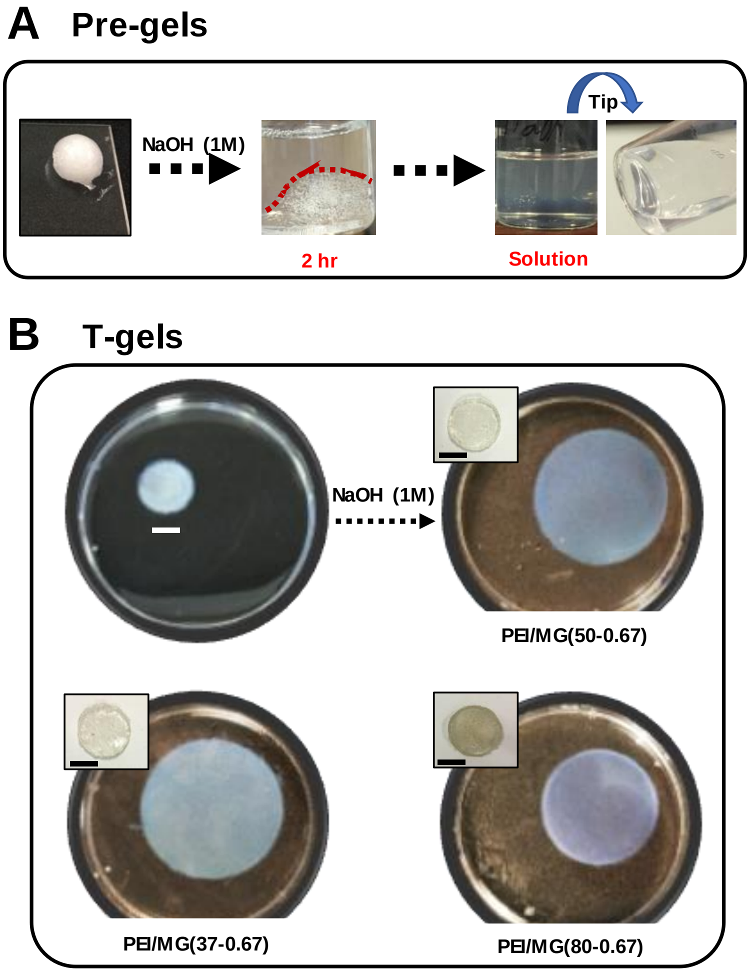

Figure 5.12 (A) Pre-gels and (B) T-gels were placed in aqueous NaOH (1.0 M) for 2 days. The solution pH was ~ 14. (A) PEI/MG(0.67) pre-gels dissolved and formed a solution. (B) PEI/MG(37-0.67), PEI/MG(50-0.67), and PEI/MG(80-0.67) T-gels swelled to different extents but did not dissolve in solution. Scale bar = 10 mm.

5.4.11 Adhesion tests of PEI/MG(50-0.67) T-gels

The adhesiveness of PEI/MG(50-0.67) T-gel was investigated here using a wide range of materials as shown in Fig. 5.13. The disk gel was immersed in pH 7.4 before direct attachment to the various surfaces, such as glass, plastic, rubber, steel and Teflon. The pictures show the T-gels (on nitrile gloves) could adhere to all the selected surfaces and support the relatively heavy glassware or steel (~ 150 g) in air. In addition, the bioadhesive properties were also studied using porcine skin. The magnified interfacial areas revealed a strong adhesive phase between the skin and gel. The flipping force showed the gel was stretched without a sudden failure of adhesion, which was attributed to the high stretchability and energy dissipation of T-gel. Fig. 5.13 showed that the T-gels could adhere to both the solid materials and biological tissue (skin).

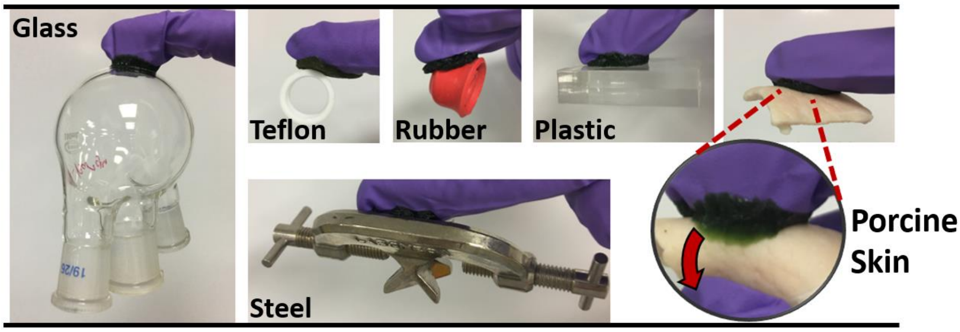

Figure 5.13 PEI/MG(50-0.67) adhered to various materials including glass, Teflon, steel, plastic, rubber and porcine skin. The magnified picture highlighted the adhesion by a flipping process (indicated by the red arrow).

The pH-dependent adhesiveness of PEI/MG(50-0.67) gel was observed after immersion in various buffers (pH 6.1, pH 7.4 and pH 8.4). The change of adhesive strength was visualised using a “flip test”. As shown in Fig. 5.14(A), the gel partially sits on a smooth polypropylene membrane for 10 s. Then, the remaining parts were gently touched and lifted upward by a glass slide. The pictures (Fig. 5.14(B)) of stained gels (universal pH indicator) showed a clear decrease of adhesive strength (on glass) from pH 6.1 to pH

8.4, where the gel was released from the top. The overall surface charge of the gel was positive below pH 8.4 based on Fig. 5.11(D). The adhesion between the glass and gel was weakened when the zeta potential approached negative values. The presence of electrostatic attraction could be verified here and acted as the dominant mechanism of the adhesiveness below pH 8.4. The adhesion strength was subsequently quantified through a standard lap shear test as depicted in Fig. 5.14(C). All the measurements allowed a 10 s contact time between the substrates and gel. The results showed the overall adhesive strength ranged from 7.5 to 17.5 kPa, which were tested on glass, Teflon and porcine skin from pH 6.1 to pH 8.4 (Fig. 5.14(D)). These adhesions are reasonably strong and applicable.[35,79] The decrease of adhesive strength was observed on the glass substrate with the increasing pH, which agreed with the results from "flip test". However, the adhesion of gel to Teflon remained constant. In comparison to the biological tissue, the adhesive strength of porcine skin was measured as 8.9 kPa at pH 7.4 and was also independent of pH. PEI/MG gel had a hydrophobic nature due to the coacervate state.[70] The results are suggestive of a hydrophobic interaction, which has been also reported for a poly(N-isopropylacrylamide) based complex coacervates.[52] Overall, the adhesiveness of PEI/MG(50-0.67) contained both mechanisms of the electrostatic attraction and hydrophobic interaction.

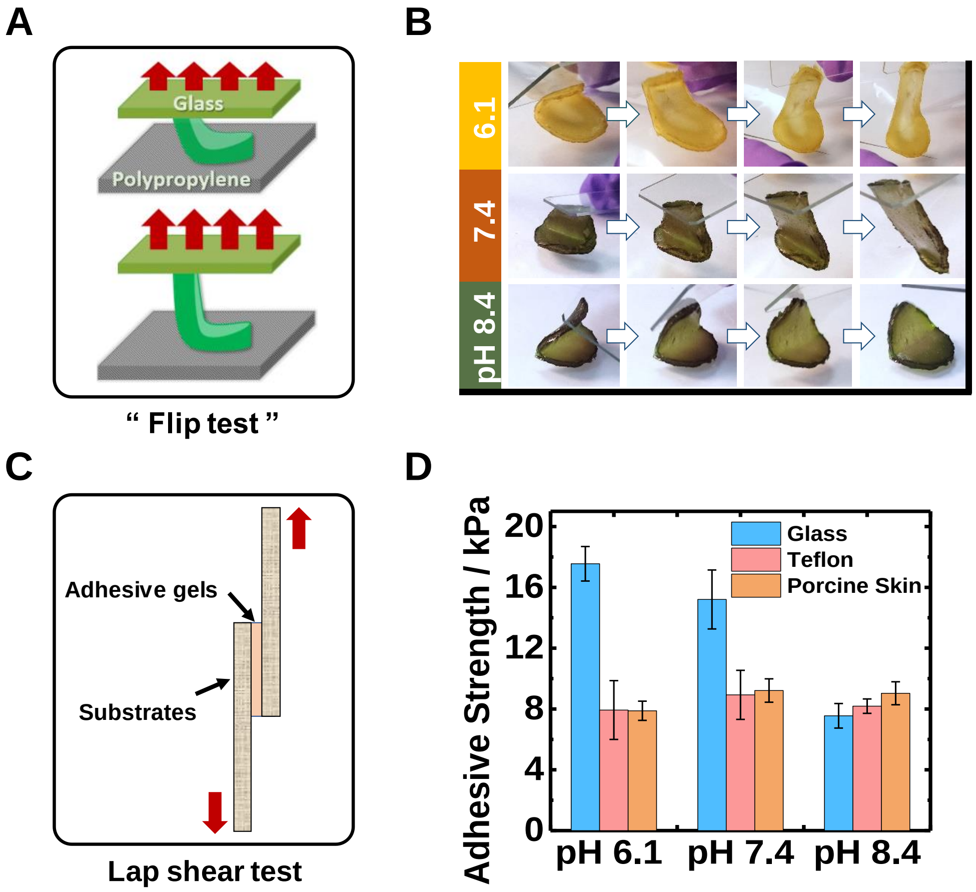

Figure 5.14 (A) Schematic cartoon shows a "flip test" of gel in contact with the glass and polypropylene film, and tested for (B) PEI/MG(50-0.67) gels with the universal pH indicator at different pH values (6.1, 7.4 and 8.4). (C) Schematic cartoon shows a standard lap shear test in a sandwich structure, and (D) the adhesive strength of PEI/MG(50-0.67) gels was tested on glass, Teflon and porcine skin at different pH values (6.1, 7.4 and 8.4).

5.4.12 Ca^{2+} stiffened PEI/MG(50-0.67) T-gels

After immersing PEI/MG(50-0.67) gel in a saturated $CaCl_2$ solution (6.7 M) for 3 hr, the gel network was largely strengthened as shown in Fig. 5.15. Ca^{2+} ions can bridge the negatively charged carboxylate groups and form strong ionic crosslinks (Fig. 5.15(A)). The gel became hard and rigid, which largely constrained the stretchability. However, the multiple-folding process showed there was no observable or permanent damage (Fig. 5.15(B)). The damage tolerance of Ca^{2+} treated gel could allow the small degrees of deformation in practice. Furthermore, a thin fiber-like (1 mm thickness) gel can easily sustain 250 g mass in the air (Fig. 5.15(C)). This dramatic enhancement of load-bearing properties indicated the high ionic crosslinks density within the gel network. In contrast, a NaCl saturated solution could not trigger any strengthening effects on the PEI/MG(50-0.67) gel. Such a saturated solution was also unable to disintegrate the gel after the 3 months immersion at 50 °C, which indicated the irreversible formation of these physical gels.

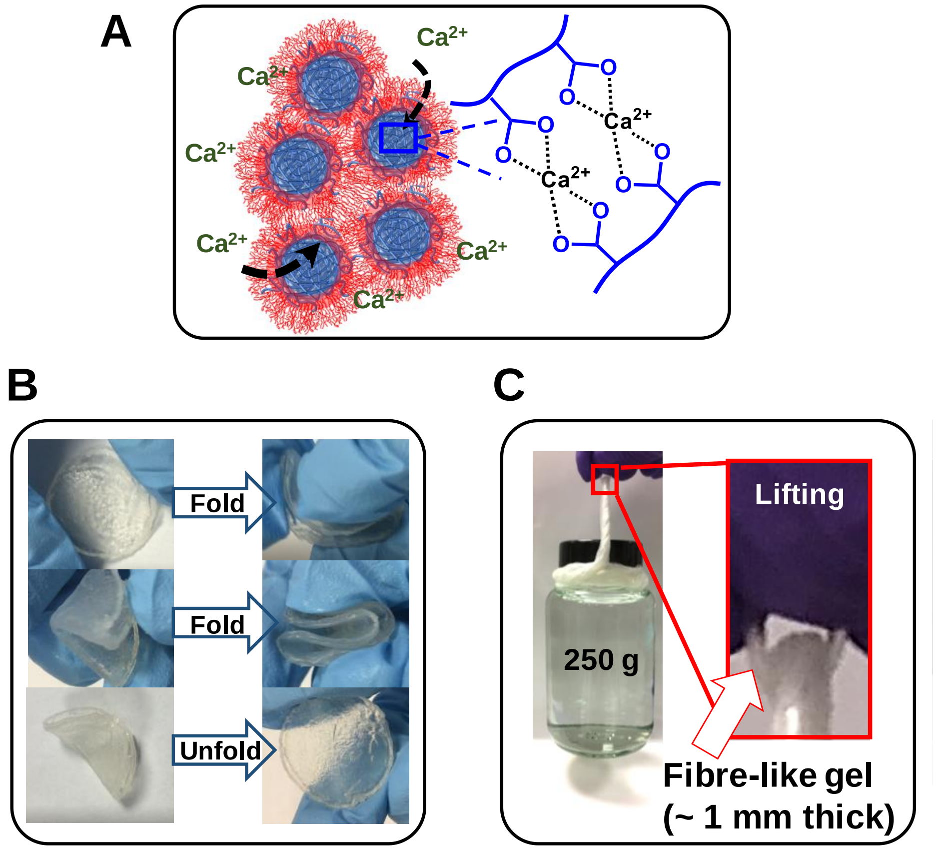

Figure 5.15 (A) Schematic cartoon shows the mechanism for Ca^{2+}-stiffening of the PEI/MG T-gels. (B) A stiffened PEI/MG(50-0.67) disk was foldable without showing damage. (C) A fibre-like stiffened PEI/MG(50-0.67) sustained a heavy mass (~ 250 g).

Uniaxial tensile stress-strain tests of Ca^{2+} stiffened gel were conducted as shown in Fig. 5.16(A). The immersion periods of PEI/MG(50-0.67) were varied for 30 s, 10 min, 60 min and 180 min, respectively. The reduction of breaking strain was observed with the longer immersion period. However, the breaking strain was still above 70 % for 180 min (Fig. 5.16(B)), which could be suitable for a less stretchable load-bearing condition. The modulus of coacervate gel can be quickly increased from 0.016 MPa to 0.30 MPa in a saturated $CaCl_2$ solution for 30 s. It could also be dramatically increased up to 34 MPa after 180 min immersion (Table 5.3). The latter modulus is almost ~ 2000 times the original gel. In a highly elastic hybrid chitosan-polyacrylamide composite gel, the elastic modulus increased from 0.060 MPa to 1.3 MPa after immersing in a saturated sodium citrate solution.[71] This enhancement was contributed by an additional ionic network between multivalent anions and short-chain chitosans. A similar stiffening strategy was also used in a hybrid chitosan-gelatin composite gel.[65] After soaking in a sodium phytate solution, the modulus of the gels increased from 0.030 MPa to 2.47 MPa. Ca^{2+} stiffened physical gels have a maximum elastic modulus of ~ 34 MPa, which is much stiffer than the example ions-stiffened gels discussed above. This tensile elastic modulus is comparable to the modulus of skin (~ 10 – 40 MPa) and some natural elastomers.[80,81]

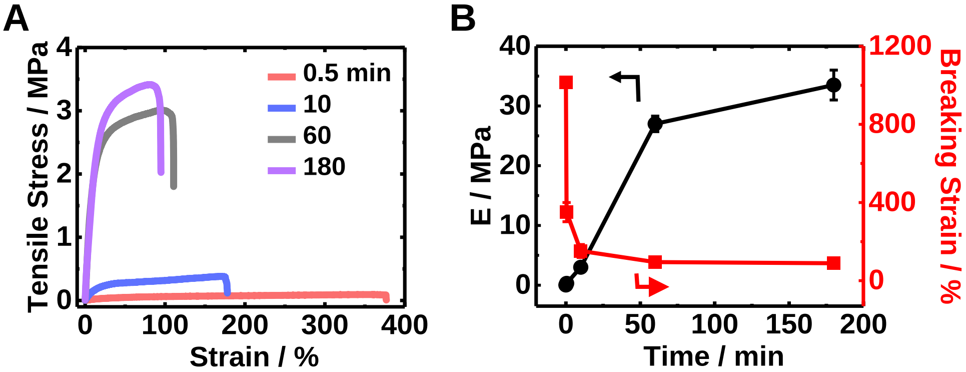

Figure 5.16 (A) Uniaxial tensile stress-strain measurements of PEI/MG(50-0.67) gels immersed in a saturated $CaCl_2$ solution for 0.5, 10, 60, 180 min. (B) The elastic modulus and breaking strain were recorded against the immersing time.

Table 5.3 Comparison of mechanical properties for PEI/MG(50-0.67) gels at different Ca^{2+} equilibration times.

Time / min	E / MPa[a)]	Tensile strength / MPa	Strain at break / %	Toughness / MJ/m^3
0.5	0.30 ± 0.06	0.09 ± 0.02	351 ± 49	0.223 ± 0.035
10	3.00 ± 0.08	0.39 ± 0.02	152 ± 33	0.472 ± 0.063
60	27.0 ± 1.3	3.1 ± 0.2	95 ± 21	2.56 ± 0.46
180	33.5 ± 2.5	3.4 ± 0.1	89 ± 17	3.03 ± 0.44

[a)] Young's modulus

5.4.13 Biocompatibility

The biocompatibility of the new complex coacervate gel (T-gel) was examined with chondrocyte cells. PEI/MG(50-0.50) gel was prepared and washed with PBS for this study. The cells were seeded and grown around the gel inside the medium in a well plate. A control cell culture was also prepared without the gel insert. In Fig. 5.17, the phase-contrast images showed the appearance of the cells was well-defined. After 3 days culture, the images indicated there was a promising proliferation of cells in both control and gel involved system. The live/dead assay was subsequently inspected under a fluorescent microscope. The images revealed (Fig. 5.18) there were mostly living cells (Green staining) during the cell culture with the PEI/MG(50-0.50) gel. The number of living cells increased from day 1 to day 3 as a result of proliferation. However, the overall population slightly dropped compared to the control images.

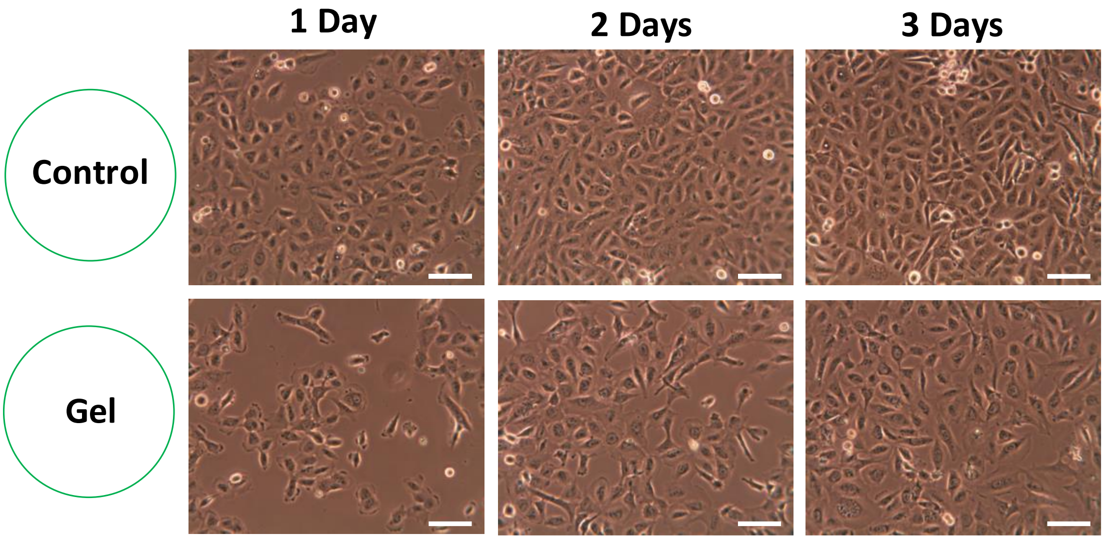

Figure 5.17 Optical microscopy showed the chondrocyte cells were cultured in the presence/absence of PEI/MG(50-0.50) gels from Day 1 to Day 3. Scale bars = 100 μm.

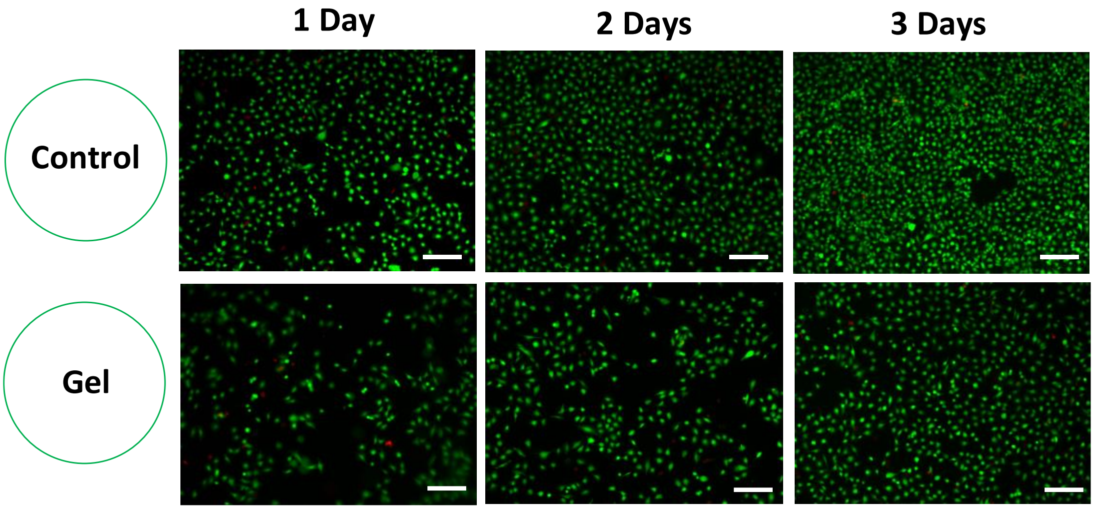

Figure 5.18 Live/dead assay images showed the chondrocyte cells were cultured in the presence/absence of PEI/MG(50-0.50) gels from Day 1 to Day 3. Scale bars = 200 μm.

In order to quantify the cytotoxicity of PEI/MG(50-0.50) gel, the MTT assay was applied to test the metabolic activity during the cell culture (Fig. 5.19). PEI has been applied in transfection and carried the positive charges, which indicated the potential presence of cytotoxicity. PEI aqueous solution (17.2 wt%) was used in the preparation with a high molecular weight (10 kD). The result showed the cell viability was 90%, 78% and 70% after day 1, 2 and 3, respectively. The slight decrease of cell viability supported the decrease of overall population in live-dead assays (Fig. 5.18). The release of some free PEI chains likely occurred during the cell culture due to the physical bonding network which is dynamic. Overall, the gels had relatively low cytotoxicity. In principle, the cell viability could be further improved following the strategies: (1) decreasing the MR in T-gel, (2) chemically functionalising PEI[82] and/or chemically crosslinking PEI.[76]

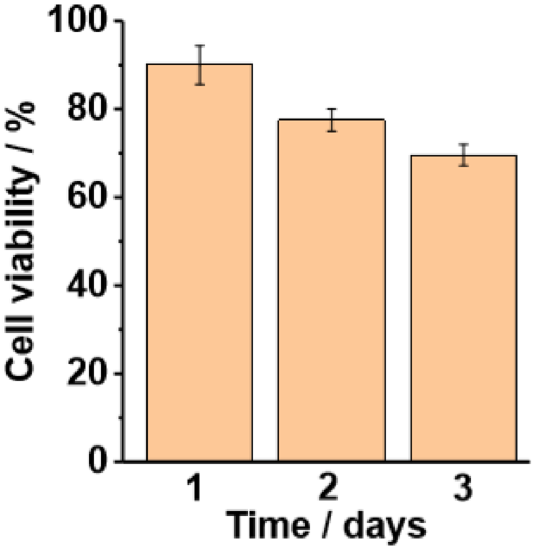

Figure 5.19 MTT assay tests showed the viability of the chondrocyte cells in the presence of PEI/MG(50-0.50) gels relative to the control experiment from Day 1 to Day 3.

5.5 Conclusions

A new class of super-stretchable, self-healable, highly-adhesive and super-swellable complex coacervate hydrogel was developed from the mixture of anionic MGs and cationic PEI components. A highly deformable pre-gel can be transferred into an elastic T-gel annealing at ≥ 37 °C. There was no chemical bonds formation during the gelation, which has been confirmed from FTIR spectra. The interpenetration likely occurred at the annealing process. The mechanical properties were tuneable by controlling the annealing temperature and mass ratio, and the maximum breaking strain can reach 1122%. The multiple cyclic test and self-healing experiment supported the favourable dynamic network of T-gel, which was not degradable at the high pH or strong ionic medium. These gels can adhere to a wide range of materials and have the pH-dependent adhesive strength in contact with a charged substrate. In addition, the mechanical property can be further strengthened by a high concentration of Ca^{2+} ions, with an enhanced elastic modulus ~ 34 MPa. These new gels offer potential applications as engineering gels, structural biomaterials including cartilage repair, wound healing, and also for water purification membranes. This new PMCC gel also opens a wide range of studies in the relevant areas, which expands the application and design of MG particles in the complex coacervate gel.

5.6 References

1. Richtering, W.; Saunders, B. R. Gel Architectures and Their Complexity. *Soft Matter* **2014**, *10*, 3695–3702.

2. Caló, E.; Khutoryanskiy, V. V. Biomedical Applications of Hydrogels: A Review of Patents and Commercial Products. *Eur. Polym. J.* **2015**, *65*, 252–267.

3. Sun, J. Y.; Zhao, X.; Illeperuma, W. R. K.; Chaudhuri, O.; Oh, K. H.; Mooney, D. J.; Vlassak, J. J.; Suo, Z. Highly Stretchable and Tough Hydrogels. *Nature* **2012**, *489*, 133–136.

4. Sun, T. L.; Kurokawa, T.; Kuroda, S.; Ihsan, A. Bin; Akasaki, T.; Sato, K.; Haque, M. A.; Nakajima, T.; Gong, J. P. Physical Hydrogels Composed of Polyampholytes Demonstrate High Toughness and Viscoelasticity. *Nat. Mater.* **2013**, *12*, 932–937.

5. Truong, V. X.; Ablett, M. P.; Richardson, S. M.; Hoyland, J. A.; Dove, A. P. Simultaneous Orthogonal Dual-Click Approach to Tough, in-Situ -Forming Hydrogels for Cell Encapsulation. *J. Am. Chem. Soc.* **2015**, *137*, 1618–1622.

6. Saunders, L.; Ma, P. X. Self-Healing Supramolecular Hydrogels for Tissue Engineering Applications. *Macromol. Biosci.* **2019**, *19*, 1–11.

7. El-Sherbiny, I. M.; Yacoub, M. H. Hydrogel Scaffolds for Tissue Engineering: Progress and Challenges. *Glob. Cardiol. Sci. Pract.* **2013**, *2013*, 38.

8. Hoare, T. R.; Kohane, D. S. Hydrogels in Drug Delivery: Progress and Challenges. *Polymer (Guildf).* **2008**, *49*, 1993–2007.

9. Gao, H.; Sun, Y.; Zhou, J.; Xu, R.; Duan, H. Mussel-Inspired Synthesis of Polydopamine-Functionalized Graphene Hydrogel as Reusable Adsorbents for Water Purification. *ACS Appl. Mater. Interfaces* **2013**, *5*, 425–432.

10. Hammock, M. L.; Chortos, A.; Tee, B. C. K.; Tok, J. B. H.; Bao, Z. 25th Anniversary Article: The Evolution of Electronic Skin (E-Skin): A Brief History, Design Considerations, and Recent Progress. *Adv. Mater.* **2013**, *25*, 5997–6038.

11. Zhang, J.; Wan, L.; Gao, Y.; Fang, X.; Lu, T.; Pan, L.; Xuan, F. Highly Stretchable and Self-Healable MXene/Polyvinyl Alcohol Hydrogel Electrode for Wearable Capacitive Electronic Skin. *Adv. Electron. Mater.* **2019**, *1900285*, 1–10.

12. Griffin, D. R.; Weaver, W. M.; Scumpia, P. O.; Di Carlo, D.; Segura, T. Accelerated Wound Healing by Injectable Microporous Gel Scaffolds Assembled from Annealed Building Blocks. *Nat. Mater.* **2015**, *14*, 737–744.

13. Chouhan, D.; Lohe, T. u.; Samudrala, P. K.; Mandal, B. B. In Situ Forming Injectable Silk Fibroin Hydrogel Promotes Skin Regeneration in Full Thickness Burn Wounds. *Adv. Healthc. Mater.* **2018**, *7*, 1–15.

14. Bauer, S.; Bauer-Gogonea, S.; Graz, I.; Kaltenbrunner, M.; Keplinger, C.; Schwödiauer, R. 25th Anniversary Article: A Soft Future: From Robots and Sensor Skin to Energy Harvesters. *Adv. Mater.* **2014**, *26*, 149–162.

15. Shintake, J.; Cacucciolo, V.; Floreano, D.; Shea, H. Soft Robotic Grippers. *Adv. Mater.* **2018**, *30*.

16. Xu, X.; Pejcic, B.; Heath, C.; Wood, C. D. Carbon Capture with Polyethylenimine Hydrogel Beads (PEI HBs). *J. Mater. Chem. A* **2018**, *6*, 21468–21474.

17. Xu, X.; Heath, C.; Pejcic, B.; Wood, C. D. CO2 Capture by Amine Infused Hydrogels (AIHs). *J. Mater. Chem. A* **2018**, *6,* 4829–4838.

18. Liu, J.; Pang, Y.; Zhang, S.; Cleveland, C.; Yin, X.; Booth, L.; Lin, J.; Lucy Lee, Y. A.; Mazdiyasni, H.; Saxton, S.; et al. Triggerable Tough Hydrogels for Gastric Resident Dosage Forms. *Nat. Commun.* **2017**, *8*, 1–9.

19. Liu, X.; Steiger, C.; Lin, S.; Parada, G. A.; Liu, J.; Chan, H. F.; Yuk, H.; Phan, N. V.; Collins, J.; Tamang, S.; et al. Ingestible Hydrogel Device. *Nat. Commun.* **2019**, *10.*

20. Oliva, N.; Conde, J.; Wang, K.; Artzi, N. Designing Hydrogels for On-Demand Therapy. *Acc. Chem. Res.* **2017**, *50*, 669–679.

21. Koetting, M. C.; Peters, J. T.; Steichen, S. D.; Peppas, N. A. Stimulus-Responsive Hydrogels: Theory, Modern Advances, and Applications. *Mater. Sci. Eng. R Reports* **2015**, *93*, 1–49.

22. Gaulding, J. C.; Smith, M. H.; Hyatt, J. S.; Fernandez-Nieves, A.; Lyon, L. A. Reversible Inter- and Intra-Microgel Cross-Linking Using Disulfides. *Macromolecules* **2012**, *45*, 39–45.

23. Zhu, L.; Zhao, C.; Gong, D. Ca2+ Responsive Microgel-Stabilized Pickering Emulsions. *J. Dispers. Sci. Technol.* **2016**, *37*, 1570–1573.

24. Lu, D.; Zhu, M.; Wu, S.; Wang, W.; Lian, Q.; Saunders, B. R. Triply Responsive Coumarin-Based Microgels with Remarkably Large Photo-Switchable Swelling. *Polym. Chem.* **2019**, *10*, 2516–2526.

25. Wang, W.; Lu, D.; Zhu, M.; Saunders, J. M.; Milani, A. H.; Armes, S. P.; Saunders, B. R. Highly Deformable Hydrogels Constructed by PH-Triggered Polyacid Nanoparticle Disassembly in Aqueous Dispersions. *Soft Matter* **2018**, *14*, 3510–3520.

26. Cui, Z.; Wang, W.; Obeng, M.; Chen, M.; Wu, S.; Kinloch, I.; Saunders, B. R. Using Intra-Microgel Crosslinking to Control the Mechanical Properties of Doubly Crosslinked Microgels. *Soft Matter* **2016**, *12*, 6985–6994.

27. Milani, A. H.; Bramhill, J.; Freemont, A. J.; Saunders, B. R. Swelling and Mechanical Properties of Hydrogels Composed of Binary Blends of Inter-Linked PH-Responsive Microgel Particles. *Soft Matter* **2015**, *11*, 2586–2595.

28. Milani, A. H.; Saunders, J. M.; Nguyen, N. T.; Ratcliffe, L. P. D.; Adlam, D. J.; Freemont, A. J.; Hoyland, J. A.; Armes, S. P.; Saunders, B. R. Synthesis of Polyacid Nanogels: PH-Responsive Sub-100 Nm Particles for Functionalisation and Fluorescent Hydrogel Assembly. *Soft Matter* **2017**, *13*, 1554–1560.

29. Liu, R.; Milani, A. H.; Freemont, T. J.; Saunders, B. R. Doubly Crosslinked PH-Responsive Microgels Prepared by Particle Inter-Penetration: Swelling and Mechanical Properties. *Soft Matter* **2011**, *7*, 4696–4704.

30. Milani, A. H.; Freemont, A. J.; Hoyland, J. A.; Adlam, D. J.; Saunders, B. R. Injectable Doubly Cross-Linked Microgels for Improving the Mechanical Properties of Degenerated Intervertebral Discs. *Biomacromolecules* **2012**, *13*, 2793–2801.

31. Gan, D.; Xing, W.; Jiang, L.; Fang, J.; Zhao, C.; Ren, F.; Fang, L.; Wang, K.; Lu, X. Plant-Inspired Adhesive and Tough Hydrogel Based on Ag-Lignin Nanoparticles-Triggered Dynamic Redox Catechol Chemistry. *Nat. Commun.* **2019**, *10*, 1–10.

32. Jiang, H.; Zhang, G.; Li, F.; Zhang, Y.; Lei, Y.; Xia, Y.; Jin, X.; Feng, X.; Li, H. A Self-Healable and Tough Nanocomposite Hydrogel Crosslinked by Novel Ultrasmall Aluminum Hydroxide Nanoparticles. *Nanoscale* **2017**, *9*, 15470–15476.

33. Wang, Y. J.; Zhang, X. N.; Song, Y.; Zhao, Y.; Chen, L.; Su, F.; Li, L.; Wu, Z. L.; Zheng, Q. Ultrastiff and Tough Supramolecular Hydrogels with a Dense and Robust Hydrogen Bond Network. *Chem. Mater.* **2019**, *31*, 1430–1440.

34. Ding, H.; Liang, X.; Zhang, X. N.; Wu, Z. L.; Li, Z.; Sun, G. Tough Supramolecular Hydrogels with Excellent Self-Recovery Behavior Mediated by Metal-Coordination Interaction. *Polymer (Guildf).* **2019**, *171*, 201–210.

35. Deng, Z.; Guo, Y.; Zhao, X.; Ma, P. X.; Guo, B. Multifunctional Stimuli-Responsive Hydrogels with Self-Healing, High Conductivity, and Rapid Recovery through Host-Guest Interactions. *Chem. Mater.* **2018**, *30*, 1729–1742.

36. Gong, J. P.; Katsuyama, Y.; Kurokawa, T.; Osada, Y. Double-Network Hydrogels with Extremely High Mechanical Strength. *Adv. Mater.* **2003**, *15*, 1155–1158.

37. Jia, H.; Huang, Z.; Fei, Z.; Dyson, P. J.; Zheng, Z.; Wang, X. Unconventional Tough Double-Network Hydrogels with Rapid Mechanical Recovery, Self-Healing, and Self-Gluing Properties. *ACS Appl. Mater. Interfaces* **2016**, *8*, 31339–31347.

38. Hu, J.; Kurokawa, T.; Nakajima, T.; Sun, T. L.; Suekama, T.; Wu, Z. L.; Liang, S. M.; Gong, J. P. High Fracture Efficiency and Stress Concentration Phenomenon for Microgel-Reinforced Hydrogels Based on Double-Network Principle. *Macromolecules* **2012**, *45*, 9445–9451.

39. Hu, J.; Hiwatashi, K.; Kurokawa, T.; Liang, S. M.; Wu, Z. L.; Gong, J. P. Microgel-Reinforced Hydrogel Films with High Mechanical Strength and Their Visible Mesoscale Fracture Structure. *Macromolecules* **2011**, *44*, 7775–7781.

40. Wu, J.; Cai, L. H.; Weitz, D. A. Tough Self-Healing Elastomers by Molecular Enforced Integration of Covalent and Reversible Networks. *Adv. Mater.* **2017**, *29*, 1–8.

41. Yan, B.; Huang, J.; Han, L.; Gong, L.; Li, L.; Israelachvili, J. N.; Zeng, H. Duplicating Dynamic Strain-Stiffening Behavior and Nanomechanics of Biological Tissues in a Synthetic Self-Healing Flexible Network Hydrogel. *ACS Nano* **2017**, *11*, 11074–11081.

42. Luo, F.; Sun, T. L.; Nakajima, T.; Kurokawa, T.; Zhao, Y.; Sato, K.; Ihsan, A. Bin; Li, X.; Guo, H.; Gong, J. P. Oppositely Charged Polyelectrolytes Form Tough, Self-Healing, and Rebuildable Hydrogels. *Adv. Mater.* **2015**, *27*, 2722–2727.

43. Li, W.; Feng, R.; Wang, R.; Li, D.; Jiang, W.; Liu, H.; Guo, Z.; Serpe, M. J.; Hu, L. Polyelectrolyte-Based Physical Adhesive Hydrogels with Excellent Mechanical Properties for Biomedical Applications. *J. Mater. Chem. B* **2018**, *6*, 4799–4807.

44. Ladet, S.; David, L.; Domard, A. Multi-Membrane Hydrogels. *Nature* **2008**, *452*, 76–79.

45. Krogstad, D. V.; Lynd, N. A.; Choi, S. H.; Spruell, J. M.; Hawker, C. J.; Kramer, E. J.; Tirrell, M. V. Effects of Polymer and Salt Concentration on the Structure and Properties of Triblock Copolymer Coacervate Hydrogels. *Macromolecules* **2013**, *46*, 1512–1518.

46. Lalevée, G.; David, L.; Montembault, A.; Blanchard, K.; Meadows, J.; Malaise, S.; Crépet, A.; Grillo, I.; Morfin, I.; Delair, T.; et al. Highly Stretchable Hydrogels from Complex Coacervation of Natural Polyelectrolytes. *Soft Matter* **2017**, *13*, 6594–6605.

47. Shao, H.; Stewart, R. J. Biomimetic Underwater Adhesives with Environmentally Triggered Setting Mechanisms. *Adv. Mater.* **2010**, *22*, 729–733.

48. Timilsena, Y. P.; Akanbi, T. O.; Khalid, N.; Adhikari, B.; Barrow, C. J. Complex Coacervation: Principles, Mechanisms and Applications in Microencapsulation. *Int. J. Biol. Macromol.* **2019**, *121*, 1276–1286.

49. Schmitt, C.; Turgeon, S. L. Protein/Polysaccharide Complexes and Coacervates in Food Systems. *Adv. Colloid Interface Sci.* **2011**, *167*, 63–70.

50. Blocher, W. C.; Perry, S. L. Complex Coacervate-Based Materials for Biomedicine. *Wiley Interdiscip. Rev.: Nanomed. Nanobiotechnol.* **2017**, *9*, 76–78.

51. Gebhart, C. L.; Kabanov, A. V. Evaluation of Polyplexes as Gene Transfer Agents. *J. Control. Release* **2001**, *73*, 401–416.

52. Dompé, M.; Cedano-Serrano, F. J.; Heckert, O.; van den Heuvel, N.; van der Gucht, J.; Tran, Y.; Hourdet, D.; Creton, C.; Kamperman, M. Thermoresponsive Complex Coacervate-Based Underwater Adhesive. *Adv. Mater.* **2019**, *31*.

53. Lee, A. L. Z.; Voo, Z. X.; Chin, W.; Ono, R. J.; Yang, C.; Gao, S.; Hedrick, J. L.; Yang, Y. Y. Injectable Coacervate Hydrogel for Delivery of Anticancer Drug-Loaded Nanoparticles in Vivo. *ACS Appl. Mater. Interfaces* **2018**, *10*, 13274–13282.

54. Nam, H. G.; Nam, M. G.; Yoo, P. J.; Kim, J. H. Hydrogen Bonding-Based Strongly Adhesive Coacervate Hydrogels Synthesized Using Poly(N-Vinylpyrrolidone) and Tannic Acid. *Soft Matter* **2019**, *15*, 785–791.

55. Choosakoonkriang, S.; Lobo, B. A.; Koe, G. S.; Koe, J. G.; Middaugh, C. R. Biophysical Characterization of PEI/DNA Complexes. *J. Pharm. Sci.* **2003**, *92*, 1710–1722.

56. He, X.; Liu, L.; Han, H.; Shi, W.; Yang, W.; Lu, X. Bioinspired and Microgel-Tackified Adhesive Hydrogel with Rapid Self-Healing and High Stretchability. *Macromolecules* **2019**, *52*, 72–80.

57. Duan, J.; Liang, X.; Guo, J.; Zhu, K.; Zhang, L. Ultra-Stretchable and Force-Sensitive Hydrogels Reinforced with Chitosan Microspheres Embedded in Polymer Networks. *Adv. Mater.* **2016**, *28*, 8037–8044.

58. Hu, J.; Kurokawa, T.; Hiwatashi, K.; Nakajima, T.; Wu, Z. L.; Liang, S. M.; Gong, J. P. Structure Optimization and Mechanical Model for Microgel-Reinforced Hydrogels with High Strength and Toughness. *Macromolecules* **2012**, *45*, 5218–5228.

59. Zhao, Y.; Chen, S.; Hu, J.; Yu, J.; Feng, G.; Yang, B.; Li, C.; Zhao, N.; Zhu, C.; Xu, J. Microgel-Enhanced Double Network Hydrogel Electrode with High Conductivity and Stability for Intrinsically Stretchable and Flexible All-Gel-State Supercapacitor. *ACS Appl. Mater. Interfaces* **2018**, *10*, 19323–19330.

60. Sinclair, A.; O'Kelly, M. B.; Bai, T.; Hung, H. C.; Jain, P.; Jiang, S. Self-Healing Zwitterionic Microgels as a Versatile Platform for Malleable Cell Constructs and Injectable Therapies. *Adv. Mater.* **2018**, *30*, 1–8.

61. Rogina, A.; Ressler, A.; Matić, I.; Gallego Ferrer, G.; Marijanović, I.; Ivanković, M.; Ivanković, H. Cellular Hydrogels Based on PH-Responsive Chitosan-Hydroxyapatite System. *Carbohydr. Polym.* **2017**, *166*, 173–182.

62. Gil, M. S.; Thambi, T.; Phan, V. H. G.; Kim, S. H.; Lee, D. S. Injectable Hydrogel-Incorporated Cancer Cell-Specific Cisplatin Releasing Nanogels for Targeted Drug Delivery. *J. Mater. Chem. B* **2017**, *5*, 7140–7152.

63. Li, Y.; Wang, X.; Fu, Y. N.; Wei, Y.; Zhao, L.; Tao, L. Self-Adapting Hydrogel to Improve the Therapeutic Effect in Wound-Healing. *ACS Appl. Mater. Interfaces* **2018**, *10*, 26046–26055.

64. Zhang, J.; Zhu, Y.; Song, J.; Yang, J.; Pan, C.; Xu, T.; Zhang, L. Novel Balanced Charged Alginate/PEI Polyelectrolyte Hydrogel That Resists Foreign-Body Reaction. *ACS Appl. Mater. Interfaces* **2018**, *10*, 6879–6886.

65. Xu, L.; Wang, C.; Cui, Y.; Li, A.; Qiao, Y.; Qiu, D. Conjoined-Network Rendered Stiff and Tough Hydrogels from Biogenic Molecules. *Sci. Adv.* **2019**, *5*.

66. Peniche, C.; Argüelles-Monal, W.; Davidenko, N.; Sastre, R.; Gallardo, A.; San Román, J. Self-Curing Membranes of Chitosan/PAA IPNs Obtained by Radical Polymerization: Preparation, Characterization and Interpolymer Complexation. *Biomaterials* **1999**, *20*, 1869–1878.

67. Yu, Y.; Yiling, N.; Kou, O.; Takuzo, A. Mechanically Robust, Readily Repairable Polymers via Tailored Noncovalent Cross-Linking. *Science (80-.).* **2018**, *359*, 72–76.

68. Hwangbo, S.; Jeong, H.; Heo, J.; Lin, X.; Kim, Y.; Chang, M.; Hong, J. Antibacterial Nanofilm Coatings Based on Organosilicate and Nanoparticles. *React. Funct. Polym.* **2016**, *102*, 27–32.

69. Xia, L. W.; Xie, R.; Ju, X. J.; Wang, W.; Chen, Q.; Chu, L. Y. Nano-Structured Smart Hydrogels with Rapid Response and High Elasticity. *Nat. Commun.* **2013**, *4*, 1–11.

70. Gucht, J. van der; Spruijt, E.; Lemmers, M.; Cohen Stuart, M. A. Polyelectrolyte Complexes: Bulk Phases and Colloidal Systems. *J. Colloid Interface Sci.* **2011**, *361*, 407–422.

71. Yang, Y.; Wang, X.; Yang, F.; Wang, L.; Wu, D. Highly Elastic and Ultratough Hybrid Ionic–Covalent Hydrogels with Tunable Structures and Mechanics. *Adv. Mater.* **2018**, *30*, 1–9.

72. Treloar, L. R. G. *The Physics of Rubber Elasticity, Oxford Univ. Press*; 1975.

73. Yang, C. H.; Wang, M. X.; Haider, H.; Yang, J. H.; Sun, J. Y.; Chen, Y. M.; Zhou, J.; Suo, Z. Strengthening Alginate/Polyacrylamide Hydrogels Using Various Multivalent Cations. *ACS Appl. Mater. Interfaces* **2013**, *5*, 10418–10422.

74. Nguyen, N. T.; Milani, A. H.; Jennings, J.; Adlam, D. J.; Freemont, A. J.; Hoyland, J. A.; Saunders, B. R. Highly Compressive and Stretchable Poly(Ethylene Glycol) Based Hydrogels Synthesised Using PH-Responsive Nanogels without Free-Radical Chemistry. *Nanoscale* **2019**, *11*, 7921–7930.

75. Engler, A. J.; Griffin, M. A.; Sen, S.; Bönnemann, C. G.; Sweeney, H. L.; Discher, D. E. Myotubes Differentiate Optimally on Substrates with Tissue-like Stiffness: Pathological Implications for Soft or Stiff Microenvironments. *J. Cell Biol.* **2004**, *166*, 877–887.

76. Saxena, S.; Lyon, L. A. Enabling Method to Design Versatile Biomaterial Systems from Colloidal Building Blocks. *Mol. Syst. Des. Eng.* **2016**, *1*, 189–201.

77. Lemmers, M.; Sprakel, J.; Voets, I. K.; Van Der Gucht, J.; Cohen Stuart, M. A. Multiresponsive Reversible Gels Based on Chargedriven Assembly. *Angew. Chemie - Int. Ed.* **2010**, *49*, 708–711.

78. Perrin, C. L.; Nielson, J. B. “Strong” Hydrogen Bonds in Chemistry and Biology. *Annu. Rev. Phys. Chem.* **2002**, *48*, 511–544.

79. Zhao, X.; Wu, H.; Guo, B.; Dong, R.; Qiu, Y.; Ma, P. X. Antibacterial Anti-Oxidant Electroactive Injectable Hydrogel as Self-Healing Wound Dressing with Hemostasis and Adhesiveness for Cutaneous Wound Healing. *Biomaterials* **2017**, *122*, 34–47.

80. Li, J.; Illeperuma, W. R. K.; Suo, Z.; Vlassak, J. J. Hybrid Hydrogels with Extremely High Stiffness and Toughness. *ACS Macro Lett.* **2014**, *3*, 520–523.

81. Wegst, U. G. K.; Ashby, M. F. The Mechanical Efficiency of Natural Materials. *Philos. Mag.* **2004**, *84*, 2167–2186.

82. Zintchenko, A.; Philipp, A.; Dehshahri, A.; Wagner, E. Simple Modifications of Branched PEI Lead to Highly Efficient SiRNA Carriers with Low Toxicity. *Bioconjug. Chem.* **2008**, *19*, 1448–1455.

Chapter 6: Conclusions and future work

6.1 Conclusions

This thesis aimed to strengthen and expand the potential of existing pH-responsive microgels (MGs) or nanogels (NGs) in biomedical applications, which could lead to the next generation of therapeutic and diagnostic capabilities. Gold nanoparticles (Au NPs) were successfully applied to construct highly stable core-shell nanoparticles using a new and efficient route of the precipitation polymerisation. The synthesis produced a range of core-shell nanoparticles with tuneable shell thicknesses. Such a system promoted the fundamental understanding of the impact of pH-responsive NG shells on Au NPs. Their characteristic localised surface plasmonic resonance (LSPR) offered pH-triggered responses of the optical property to NGs. Although those studies focused on the particle level, the overall performance of pH-responsive injectable gel was also improved by introducing a cationic polymer to the construction of the network.

At the beginning of the project, the citrate stabilised Au NPs were synthesised with good dispersity. However, the nature of electrostatic stabilisation is strongly sensitive to the concentration of electrolytes. Such stabilisation was not strong enough to maintain the dispersity and LSPR property in the doubly crosslinked MG system. After evaluating different approaches, Chapter 3 established a new core-shell synthesis without requiring any pre-functionalisation steps. A NG shell was successfully constructed around each Au NP through a monomer feeding precipitation polymerisation. The superior efficiency of the core-shell construction was confirmed with scalable particle concentrations. The anionic NG shells endowed Au NPs with the improved colloidal stability by lowering the effective Hamaker constant in water.

Therefore, the LSPR property of core-shell particles was even maintainable in the saturated aqueous NaCl solution or restorable from the oven dried solid state. The facile and new core-shell synthesis expands the design of MG and NG structures toward a new direction.

Following the established core-shell synthesis, Chapter 4 carried on the research of the shell thickness dependent property and pH-responsive behaviour by synthesising five kinds of acrylic-based core-shell particles. Those particles had the shell thickness, ranged from 2 nm to 18 nm. Thin NG shells facilitated the analysis of LSPR sensitive distances. The increase of the shell thickness red-shifted LSPR peak wavelengths. When the shell thickness exceeded 12.5 nm, LSPR peak wavelengths became relatively constant. The simulated spectra and near-field map supported those spectral observations with the refractive index change around Au NPs. Au-MAA$_{15}$ core-shell particles had a pronounced swelling trend from pH 6 to pH 11. The swollen shell caused the blue shift of LSPR peak wavelengths from deep magenta to pink. Therefore, Au-MAA$_{15}$ could be potentially used in a remote method for monitoring the size change or pH variation. In addition, pH-triggered reversible aggregation was also achieved by manipulating electrostatic repulsion in Au-CEA$_2$ core-shell particles. The coupling effect of Au-CEA$_2$ induced the visible colour change due to their thin NG shells. The process can occur in the physiological pH range. The cell culture and internalisation study highlighted the capability of Au-CEA$_2$ for reporting pH environments within the HeLa cells.

Apart from the study at the particle level, a new multifunctional gel was designed using anionic MG particles in Chapter 5. The appropriate addition of the cationic branched polyethyleneimine (PEI) generated robust ionic crosslinks based on the complex coacervation. At the elevated temperature (T ≥ 37 °C), the highly deformable pre-gels converted to the elastic covalent-like T-gels without the formation of covalent inter-crosslinks. The interpenetration occurred and increased the number of ionic crosslinks, which contributed to their extraordinary mechanical properties. The stretchability of T-gels can reach 1122% by controlling the annealing temperature and mass ratio between MGs and PEI. The inherent dynamic network made this super-stretchable gel self-healable in practice. pH-responsive MG particles also endowed the super-swellabiltiy to both pre-gels and T-gels. The T-gels could even maintain their robust physical gel network at pH 14 or in a saturated salt medium. The nature of complex coacervation had both hydrophobic and hydrophilic properties. The gels could adhere to a range of materials, with pH-dependent adhesive strength on a charged surface. The stiffness of T-gels was further improved by Ca^{2+} crosslinking the MG particles. Overall, the new polymer/MGs complex coacervate (PMCC) gel provides a new direction in constructing the robust gel network. The successful design of this super-swellable, super-stretchable, self-healable, adhesive gel could lead to the continuous development of pH-responsive MGs toward a broader biomedical area.

6.2 Future work

The research of Au core-shell particles can be further explored in either compositional or practical studies based on the established protocols. A simple experiment would be the manipulation of crosslinker structure used for the NG shells. A systematic study of the crosslinker concentrations could enable the understanding of swelling behaviours with the corresponding LSPR peak wavelength shift. In addition, the high aspect ratio of Au nanorods can be prepared using the seed-growth method.[1] Au nanorods should provide both transverse and longitudinal modes of LSPR in the core-shell particles. Near-infrared absorption of Au nanorods core shows the potential in photothermal therapy.[2] Based on Chapter 4 and Chapter 5, a simple strain sensor could be constructed by incorporating the pH-triggered core-shell aggregates into PMCC gels at low pH. Super-stretchability should facilitate the observation of de-coupling effect in core-shell aggregates. Theoretically, any blue shifts of LSPR can correlate to the extension ratio of the gel.[3,4]

More investigations of the new PMCC gel are also required in future studies. Other types of pH-responsive MGs could be used to deeply examine their roles in the construction of gel networks. The particle size, swelling degree and crosslinkers density should be manipulated to tune the mechanical and swelling properties of PMCC gels. Cationic branched PEI is also replaceable in the system using commercially available polyallyamine and polylysine. Those alternative polymers may further reduce the cytotoxicity from PEI. Crosslinking chemistry could be partially performed to constrain the release of PEI in cell cultures. In the gel formulation, incorporation of catechol groups might give a solution in improving the tissue adhesion.[5] Moreover, the addition of carbonate or phosphate could produce minerals in Ca^{2+} stiffen gel.[6] The new mineral gel has potential to gain more attentions in biomedical and environmental uses.

6.3 References

1. Pérez-Juste, J.; Pastoriza-Santos, I.; Liz-Marzán, L. M.; Mulvaney, P. Gold Nanorods: Synthesis, Characterization and Applications. *Coord. Chem. Rev.* **2005**, *249*, 1870–1901.

2. Huang, X.; El-Sayed, I. H.; Qian, W.; El-Sayed, M. A. Cancer Cell Imaging and Photothermal Therapy in the Near-Infrared Region by Using Gold Nanorods. *J. Am. Chem. Soc.* **2006**, *128*, 2115–2120.

3. Steiner, A. M.; Mayer, M.; Seuss, M.; Nikolov, S.; Harris, K. D.; Alexeev, A.; Kuttner, C.; König, T. A. F.; Fery, A. Macroscopic Strain-Induced Transition from Quasi-Infinite Gold Nanoparticle Chains to Defined Plasmonic Oligomers. *ACS Nano* **2017**, *11*, 8871–8880.

4. Hill, R. T.; Kozek, K. M.; Hucknall, A.; Smith, D. R.; Chilkoti, A. Nanoparticle-Film Plasmon Ruler Interrogated with Transmission Visible Spectroscopy. *ACS Photonics* **2014**, *1*, 974–984.

5. Gan, D.; Xing, W.; Jiang, L.; Fang, J.; Zhao, C.; Ren, F.; Fang, L.; Wang, K.; Lu, X. Plant-Inspired Adhesive and Tough Hydrogel Based on Ag-Lignin Nanoparticles-Triggered Dynamic Redox Catechol Chemistry. *Nat. Commun.* **2019**, *10*, 1–10.

6. Sun, S.; Mao, L. B.; Lei, Z.; Yu, S. H.; Cölfen, H. Hydrogels from Amorphous Calcium Carbonate and Polyacrylic Acid: Bio-Inspired Materials for "Mineral Plastics." *Angew. Chemie - Int. Ed.* **2016**, *55*, 11765–11769.